AD-A227 018

REPORT DOCUMENTATION PAGE

DTIC FILE COPY

Form Approved
OMB No. 0704-0188

1a. REPORT SECURITY CLASSIFICATION	1b. RESTRICTIVE MARKINGS
Unclassified	

2a. SECURITY CLASSIFICATION AUTHORITY	3. DISTRIBUTION/AVAILABILITY OF REPORT
	Approved for public release,
2b. DECLASSIFICATION/DOWNGRADING SCHEDULE	distribution unlimited
	Approved for public release,

SELECTED
SEP 26 1990
D

4. PERFORMING ORGANIZATION REPORT NUMBER(S)	5. MONITORING ORGANIZATION REPORT NUMBER(S)
	AFOSR-TR- 90 1056

6a. NAME OF PERFORMING ORGANIZATION	6b. OFFICE SYMBOL (If applicable)	7a. NAME OF MONITORING ORGANIZATION
Clarkson University		AFOSR

6c. ADDRESS (City, State, and ZIP Code)	7b. ADDRESS (City, State, and ZIP Code)
Division of Research Potsdam, NY 13676	Building 410 Bolling AFB, DC 20332-6448

8a. NAME OF FUNDING/SPONSORING ORGANIZATION	8b. OFFICE SYMBOL (If applicable)	9. PROCUREMENT INSTRUMENT IDENTIFICATION NUMBER
AFOSR	NA	AFOSR-88-0114

8c. ADDRESS (City, State, and ZIP Code)	10. SOURCE OF FUNDING NUMBERS			
Building 410 Bolling AFB, DC 20332-6448	PROGRAM ELEMENT NO.	PROJECT NO.	TASK NO.	WORK UNIT ACCESSION NO.
	61102F	2302	C1	

11. TITLE (Include Security Classification)

Fundamental Penetration Mechanisms of a Flat-Plate in Saturated Clays

12. PERSONAL AUTHOR(S)

Huang, An-Bin; Bunting, Robert D.; Ahuja, Anurag

13a. TYPE OF REPORT	13b. TIME COVERED	14. DATE OF REPORT (Year, Month, Day)	15. PAGE COUNT
Final	FROM 88/02/15 TO 90/08/2	900828	231

16. SUPPLEMENTARY NOTATION

17. COSATI CODES			18. SUBJECT TERMS (Continue on reverse if necessary and identify by block number)
FIELD	GROUP	SUB-GROUP	Penetration, Flat Plate, Saturated Clay, Strain Path

19. ABSTRACT (Continue on reverse if necessary and identify by block number)

Flat-plate penetrometers, such as the Marchetti Dilatometer and K_o Stepped-Blade, have become an important part of in situ testing in geotechnical engineering. However, the use of flat-plate penetrometers has been highly empirical, mainly due to the lack of knowledge of soil response to the flat-plate penetration. In this research project, a numerical technique capable of computing strain paths for three-dimensional penetrometers was developed. A calibration chamber system for cohesive soils and model flat-plates were fabricated. for the first time, three dimensional strain path analyses were performed for several of the flat-plate penetrometers currently being used in the industry. The results show that flat-plates can induce large strains and strain reversals at levels comparable to those of cone penetration. The characteristics of the strain field during a flat-plate penetration is influenced by both the w/t ratio and the tip apex angle. Regardless of the geometry, the pore pressure and total stress peak at the tip of the penetrometer. The pore pressure and total stress decrease sharply as the
(over

20. DISTRIBUTION/AVAILABILITY OF ABSTRACT	21. ABSTRACT SECURITY CLASSIFICATION
☐ UNCLASSIFIED/UNLIMITED ☒ SAME AS RPT. ☐ DTIC USERS	Unclassified

22a. NAME OF RESPONSIBLE INDIVIDUAL	22b. TELEPHONE (Include Area Code)	22c. OFFICE SYMBOL
Lt Col Steven C. Boyce	(202) 767-6963	AFOSR/NA

DD Form 1473, JUN 86   Previous editions are obsolete.   SECURITY CLASSIFICATION OF THIS PAGE

UNCLASSIFIED

(continued #19)

soil element passes the tip of the flat-plate. The pore pressure and total stress around
the flat-plate do not increase with the plate thickness as some had suggested. For
a simple flat-plate (i.e., the flat Dilatometer), the penetration-induced pore pressure
is positively related to the soil rigidity index in the horizontal direction. The excess
pore pressure dissipation around the flat-plate in an anisotropically consolidated clay
follows an axisymmetric pattern. Interpretation of the pore pressure dissipation data
using an axisymmetric solution resulted a c_h value comparable but lower than those
obtained from reference consolidation tests.

ERRATA

12 September 1990

The following are changes to "Fundamental Penetration Mechanisms of a Flat-Plate in Saturated Clays", the final report for Grant AFOSR-88-0144 by An-Bin Huang, Robert D. Bunting and Anurag Ahuja of Clarkson University.

p 22   Equation 2.39:

  "E_1" not "e_1"

p 28   1st sentence should read:

  "strain path analysis to be performed"

p 33   Section 3.3, 4th line:

  "Eq. ??" should be replaced with its proper value

p 50   3rd line from the bottom:

  "Modified Cam Clay" not "Modefied Cam Clay"

p 51   Section 4.1, 4th line:

  "the irreversible *plastic* strain" not "the reversible *plastic* strain"

p 66   5th line:

  delete "Ix Ix" from "triaxial tests Ix Ixare presented"

p 147 Section 8.1, 2nd line:

  "tied" not "tighed"

p 150 2nd paragraph, 3rd line:

  insert space between "the" and "two"

p 216 18th line:

  "shown in Figure 10.2" not "shown in Figure refkoblade"

FUNDAMENTAL PENETRATION MECHANISMS OF A FLAT-PLATE IN SATURATED CLAYS

by

An-Bin Huang, Robert D. Bunting and Anurag Ahuja

A report on research

sponsored by

The United States Air Force

Office of Scientific Research

Bolling Air Force Base

Accesion For		
NTIS CRA&I		J
DTIC TAB		
Unannounced		
Justification		
By		
Distribution /		
Availability Codes		
Dist	Avail and/or Special	
A-1		

August 28, 1990

Department of Civil and Environmental Engineering

Clarkson University

Potsdam, New York

i

Abstract

Flat-plate penetrometers, such as the Marchetti Dilatometer and K_o Stepped-Blade, have become an important part of in situ testing in geotechnical engineering. However, the use of flat-plate penetrometers has been highly empirical, mainly due to the lack of knowledge of soil response to the flat-plate penetration. In this research project, a numerical technique capable of computing strain paths for three-dimensional penetrometers was developed. A calibration chamber system for cohesive soils and model flat-plates were fabricated. For the first time, three-dimensional strain path analyses were performed for several of the flat-plate penetrometers currently being used in the industry. The results show that flat-plates can induce large strains and strain reversals at levels comparable to those of cone penetration. The characteristics of the strain field during a flat-plate penetration is influenced by both the w/t ratio and the tip apex angle. Regardless of the geometry, the pore pressure and total stress peak at the tip of the penetrometer. The pore pressure and total stress decrease sharply as the soil element passes the tip of the flat-plate. The pore presure and total stress around the flat-plate do not increase with the plate thickness as some had suggested. For a simple flat-plate (i.e., the flat Dilatometer), the penetration induced pore pressure is positively related to the soil rigidity index in the horizontal direction. The excess pore pressure dissipation around the flat-plate in an anisotropically consolidated clay follows an axisymmetric pattern. Interpretation of the pore pressure dissipation data using an axisymmetric solution resulted a c_h value comparable but lower than those obtained from reference consolidation tests.

Acknowledgements

Contents

List of Figures

ix

List of Tables

Chapter 1

INTRODUCTION

1.1 Applications of Flat-Plate Penetrometers in Geotechnical Engineering

The technique of inserting a flat-plate into soil to obtain engineering design parameters has been incorporated in a number of recent insitu soil testing techniques. These include the Marchetti (1975; 1980) Dilatometer (DMT), the K_o-Stepped Blade (Handy et al., 1982; Lutenegger and Timian, 1986), and various push-in spade cells (Massarsch, 1975; Tedd and Charles, 1981). Figure 1.1 presents a general description of some of the commonly used flat-plates. Flat-plate penetrometers offer potentially important advantages over other (i.e. cone penetrometer) penetrometers including:

1. It is possible to reveal directional anisotropy in horizontal stress (Handy et al., 1982);

2. The penetration simulates boundary conditions in the case of a one-dimensional compression, therefore enables a simplified interpretation of the test data (Marchetti,
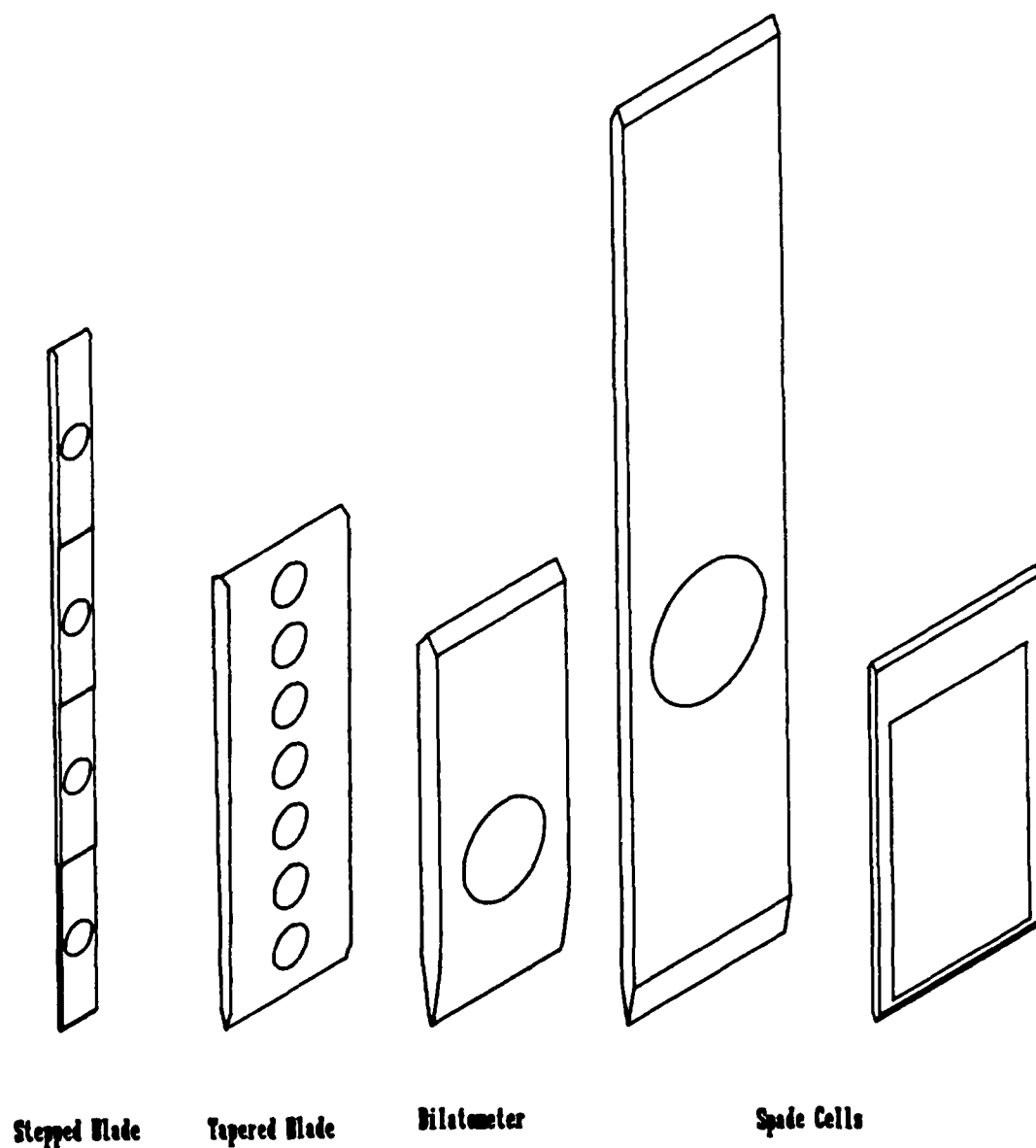
Figure 1.1: Some of the commonly used flat-plate penetrometers (Handy et al. 1982; Marchetti, 1980; Handy and Lutenegger, 1985; Ladd et al. 1979; and Fukuoka and Imamura, 1983)

2

1980; Handy et al., 1982);

3. A sharp and relatively thin flat-plate penetrometer causes less soil disturbance (as opposed to a 60 degree cone penetrometer) and therefore requires less extrapolation in predicting the undisturbed soil parameters (Marchetti, 1980);

4. The tests are relatively simple to perform, cost effective and results are potentially useful (Schmertmann, 1981).

One might also add that it is mechanically easier to install pressure sensors on the face of a flat-plate as evidenced by the designs of the Dilatometer and the K_o-Stepped Blade.

In a very general sense, the flat-plate penetration can be considered a special class of soil failure problems, i. e. , the soil is failed during insertion to give room for the penetrometer. Scott (1987) has suggested that there are three components of a failure and for it to be understood in the most general sense, information is necessary on all three components. They are mechanism, properties, and analysis. A common approach in interpreting flat-plate penetration tests is to assume the mechanisms (e. g. , plane strain or cylindrical cavity expansion), perform the analysis based on the test data (e. g. , tip resistance or membrane expansion pressure) and back calculate the soil properties (e. g. , shear strength or modulus). The validity of this approach is directly related to that of the assumed mechanisms which are, in general, the least known.

1.2 Lateral Compression in An Elastic Half Space

Handy et al. , (1982) admitted the lack of knowledge regarding the soil disturbance during penetration and stated that "... Although disturbance cannot be directly evaluated, it should relate to thickness of a penetrating blade ...". The K_o-Stepped Blade

3

was actually conceived based on this premise. Similar conjectures were used to form the basis for many other types of flat-plate penetrometers. The situation is understandable because of the large strain and three-dimensional nature of flat-plate penetrations. Essentially, all the currently available interpretation methods (Marchetti, 1980; Handy et al. ,1982; Tedd and Charles, 1983) for flat- plate penetration tests are based on elastic theories. They deal with a boundary value problem of a rigid plate translating laterally in an elastic half space (Figure 1.2). Liam Finn (1963) solved the problem considering the plate as infinitely long. The stress at the center of the rigid plate is related to displacement as:

$$P_y = \frac{d}{B\pi} \frac{E}{(1 - \nu^2)} \tag{1.1}$$

This is the basis for the interpretation of spade cell tests as suggested by Tedd and Charles (1983). Marchetti (1980) used a solution essentially for the same boundary conditions except the plate is circular and

$$P_y = \frac{\pi d}{2D} \frac{E}{(1 - \nu^2)} \tag{1.2}$$

For the DMT, D = 60 mm, d = 1 mm, Eq. 1.2 becomes:

$$\frac{E}{(1 - \nu^2)} = 38.2(P_1^{DMT} - P_0^{DMT}) \tag{1.3}$$

The left hand term of Eq. 1.3 is commonly referred to as the dilatometer modulus, E_D.

Handy et al. (1982) adopted a suggestion by Janbu (1967) that the soil compressive modulus is proportional to stress. An exponential relationship between P_y and d (= t/2) was derived as:

$$P_y = P_0 a e^{bt} \tag{1.4}$$

Eq. 1.4 provides the basis of extrapolating the insitu lateral earth pressure from K_0-Stepped Blade tests.

4
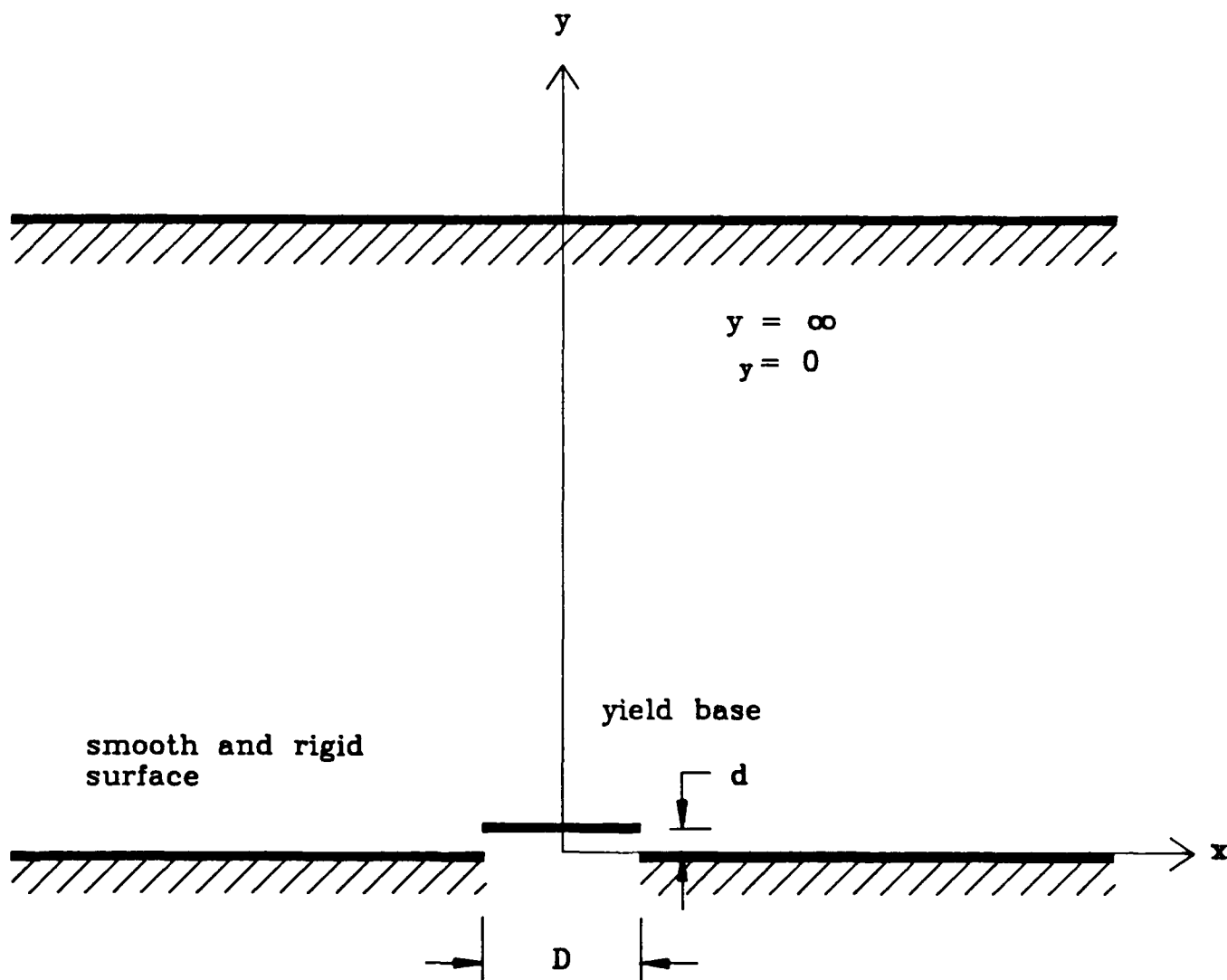
Figure 1.2: Lateral compression in elastic half space (Liam Finn, 1963)

Although never clearly stated before, the use of lateral compression approach in analyzing the flat-plate penetration problems is obviously influenced by the cylindrical cavity expansion theory (Vesic, 1972). It considers the penetration mechanisms as such that strains in the horizontal direction are the predominant component during a vertical penetration. For cylindrical penetrometers, i.e. , piles or cones, Baligh (1985) had shown that the lateral strains do represent the predominant component. However, there has been little evidence to prove that the same is true for flat-plate penetrations. Had this not been the case, then the lateral compression approach is not even relevant to the problem it intends to solve except for the case of DMT expansion.

A fundamental understanding of how soils respond to the insertion of a flat-plate penetrometer is paramount to the success of interpreting the results produced by such instruments and the continued application to Geotechnical problems. Without a rational basis, the interpretation of results will remain strictly empirical and will be limited by local experience with local soils.

1.3 Objectives of The Research

The objectives of this research were to :

1. Estimate the soil strain field during a steady penetration of a flat-plate insertion in saturated cohesive soils and study its relationship with the geometry of a penetrometer;

2. Evaluate the strain components and unique features of the strain field in the soil during the flat-plate penetration;

3. Perform a general study of the total stress and pore pressure distribution in the soil as a result of a flat-plate penetration;

4. Validate the results of the above studies by performing laboratory flat-plate penetration tests in a calibration chamber;

5. Conduct laboratory experiments on the same soil used in the chamber testing to provide reference soil properties. Detailed studies regarding the soil response to flat-plate induced strain paths will then follow;

6. Evaluate available field test data in light of the analytical and experimental studies.

To achieve the objectives, the research was divided into three tasks. The first task concentrated on analytical studies. A numerical technique which is capable of performing strain path analyses for arbitrary three- dimensional penetrometers was developed. The corresponding stress field was determined using a Modified Cam Clay Model. The pore pressure distribution was estimated by considering the stress equilibrium.

A series of reference laboratory experiments and penetration tests of a model flat Dilatometer were performed in the second task. A calibration chamber system along with other testing equipment associated with the research were fabricated. The calibration chamber was used to perform model flat Dilatometer penetration tests under a controlled environment.

A series of field flat-plate penetration test data along with other in situ and laboratory test results from a research test site in Massena, New York were compiled and studied in the third task. The report describes the details of the research, presents the results and discusses the merits of flat-plate penetration tests as a result of the research.

Chapter 2

Three-Dimensional Strain Path Analyses

2.1 Background

The strain path method (SPM) was developed by M.M. Baligh (1985) as a result of his research in deep foundations. The method was inspired by the observations of soil deformations caused by the undrained penetration of rigid objects in saturated clays. Baligh (1985) hypothesized that, "...due to the severe kinematic constraints that exist in "deep" penetration problems, soil deformations and strains are, by and large, independent of the shearing resistance of the soil. This means that these problems are essentially strain-controlled and implies that, even if relatively "simple" soil properties (e. g. , isotropy) are utilized to estimate deformations and strains caused by penetration, the errors introduced are expected to be small. ...". Based on these premises and further assumptions that a saturated clay is inviscid and incompressible, the strains are decoupled from stresses; a result that simplifies the strain path analysis to a potential flow problem. Valuable contributions have been made

by Baligh and his coworkers using SPM in the understanding of the soil response due to penetration of solid as well as hollow, cylindrical penetrometers in saturated clays (Baligh, 1985; 1986; 1986a; and Baligh, et al. , 1987). A similar technique was also developed by Tumay, et al. (1985) using conformal mapping. The SPM is superior to the conventional cavity expansion theories (Vesic, 1972) in many ways as indicated by Baligh's work. The current SPM is, however, applicable only to axisymmetric penetrometers such as a cone or a tube sampler. Calculations of potential flow about an axisymmetric or essentially any two-dimensional bodies are well established in fluid dynamics and solutions are readily available (Chow, 1982). To apply the SPM concept to flat-plate penetrations, however, the above mentioned techniques have to be extended to three-dimensional cases. A literature review indicated that such a challenge was not unique to Geotechnical Engineers. The need to calculate fluid flows about bodies of complicated configurations such as an airplane with wings, tail, and engine appendages stimulated some aeronautical engineers and developed a numerical technique commonly known as the "panel method" for handling bodies of arbitrary shape (Chow, 1982; Hess and Smith, 1962; 1964; and Hess, 1974). A numerical technique was developed based on this method in the three-dimensional strain path analyses for flat-plate penetrations. The following is a description of the theoretical background and development of this technique.

2.2 Mathematical Statement of Potential Flow Problem

The problem considered is that of the steady flow of an ideal fluid (inviscid and incompressible) about a three-dimensional body. Consider the surface of this body,

S be described as

$$F(x_i) = 0 \qquad (2.1)$$

where x_i are Cartesian coordinates. The onset flow, i. e. , the flow in the fluid before disturbance by the body, is taken as a uniform stream of unit magnitude, and is represented as V_i and

$$| V_i^\infty | \qquad (2.2)$$

The condition of a steady, onset flow and the intrusion of a three-dimensional body is shown in Figure 2.1. In the case of SPM, the onset flow velocity is equivalent to the steady penetration rate of a penetrometer. The fluid velocity V_i at a point may be expressed as the negative gradient of a potential function Φ, which has two components

$$V_i = \partial_i \Phi = -\partial_i(\rho^\infty + \rho) \qquad (2.3)$$

where

$$\rho^\infty = -\int V_i^\infty dx_i \qquad (2.4)$$

is the uniform stream potential associated with the onset flow.

$$\rho = -\int V_i^\infty dx_i$$

or

$$v_i = -\partial_i \rho \qquad (2.5)$$

ρ is the disturbance potential and V_i is the induced flow velocity due to the body. The Φ satisfies the Laplace's equation in the region R that is exterior to S, has a zero normal derivative on S (Figure 2.1), and approaches the uniform stream potential at infinity. Symbolically

$$\partial_i \partial_i \Phi = \partial_i \partial_i(\rho^\infty + \rho) = 0 \qquad (2.6)$$

Since the onset flow is uniform

$$\partial_i \partial_i \rho^\infty = 0$$

10
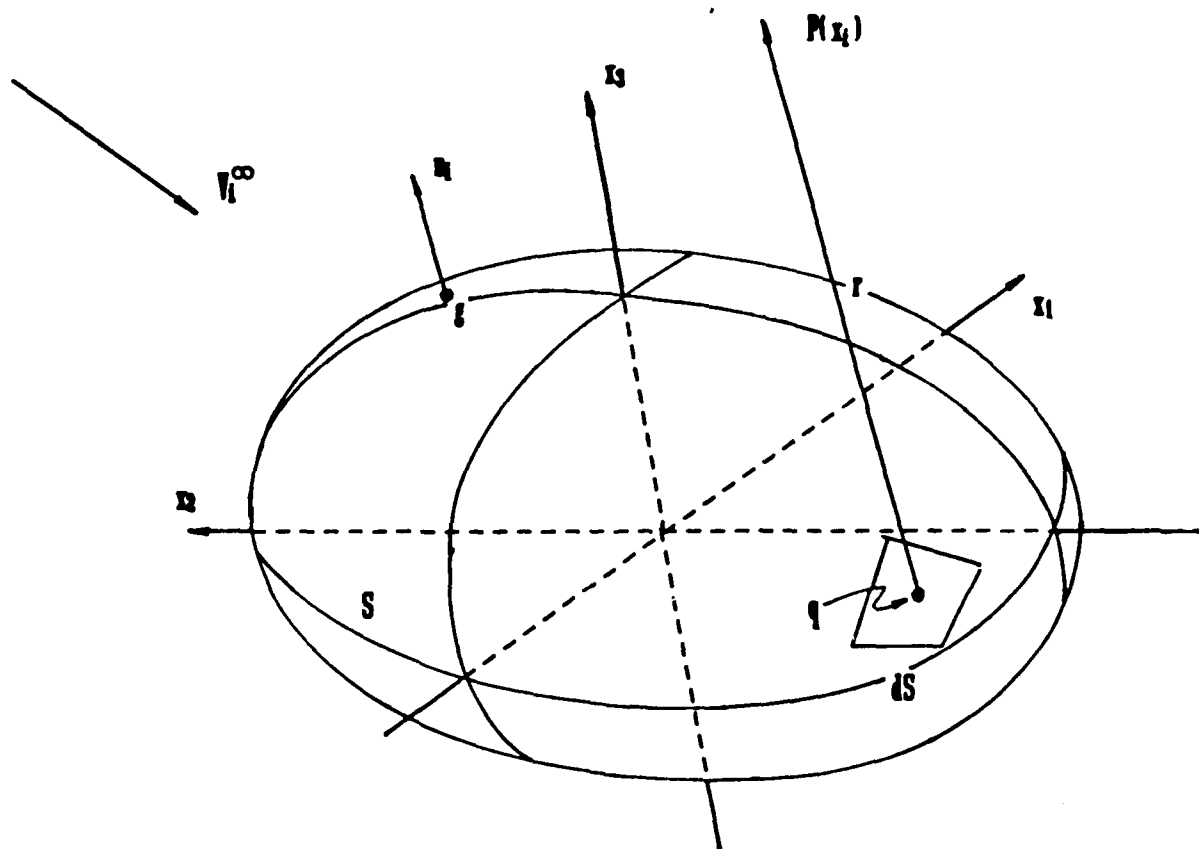
Figure 2.1: Three-dimensional body surface.

so from Eq. 2.6

$$\partial_i \partial_i \rho = 0 \qquad (2.7)$$

The fact that the body surface is impervious requires that

$$n_i \partial_i \Phi \mid_{F=0} = 0 \qquad on \ \ S \qquad (2.8)$$

or

$$n_i \partial_i \rho \mid_{F=0} = -n_i V_i^\infty$$

$$\lim_{x_i x_i \to \infty} \Phi = \rho^\infty \qquad (2.9)$$

or

$$\lim_{x_i x_i \to \infty} \rho = 0$$

since n_i is the unit outward normal vector at a point on S (Figure 2.1)

$$n_i = \left[\frac{\partial_i F}{\mid \partial_i F \mid} \right]_{F=0} \qquad (2.10)$$

If the body surface is represented by a series of sources q (Figure 2.1), each having a density $\Phi(q)$, then the induced potential ρ at a point $P(x_i)$ is (Kellog, 1929)

$$\rho(x_i) = \int \int_S \frac{\sigma(q)}{r(P,q)} dS \qquad (2.11)$$

where r(P,q) is the distance between points P and q. The ρ as given in EQ. 2.11 satisfies EQ. 2.6 and EQ. 2.9. The condition of equation EQ. 2.8 is used to solve for $\sigma(q)$.

$$- n_i \partial i \Phi \mid_{F=0} = 2\pi \sigma(q) - \int \int_S n_i \partial_i \frac{\sigma(q)}{r(g,q)} dS + n_i V_i^\infty = 0 \qquad (2.12)$$

or

$$2\pi \sigma(q) - \int \int_S n_i \partial_i \frac{\sigma(q)}{r(g,q)} dS = -n_i V_i^\infty \qquad (2.13)$$

In EQ. 2.12, g represents a point on the body surface S. The second term on the left hand side of EQ. 2.13 reaches infinity as $r(g,q) \to 0$ or as g approaches q. The

12

numerical solution as described later ensures that as g approaches q, EQ. 2.13 reduces to

$$2\pi\sigma(q) + n_i V_i^\infty = 0 \qquad (2.14)$$

EQ. 2.13 is a two-dimensional Fredholm integral equation of the second kind. Once $\sigma(q)$ are solved from EQ. 2.13, the potential function ρ can be derived from EQ. 2.11 and hence the induced velocities are determined following EQ. 2.5.

2.3   The Panel Method

The panel method is essentially a numerical technique to obtain an approximate solution of EQ. 2.13. The following sections provide a brief description of this method. Readers are referred to Hess and Smith (1962 and 1964) for further details.

2.3.1   Approximation of the body surface

The body surface is represented by a large number of plane quadrilateral elements ("panels") as shown in Figure 2.2 , within each of which the source density σ is assumed constant. The purpose is to eventually replace the integral EQ. 2.13 by a set of linear algebraic equations. The accuracy of the calculation depends on the number of elements and the manner in which these elements are distributed over the body surface. Generally speaking, elements should be concentrated in regions of high curvature of the body surface.
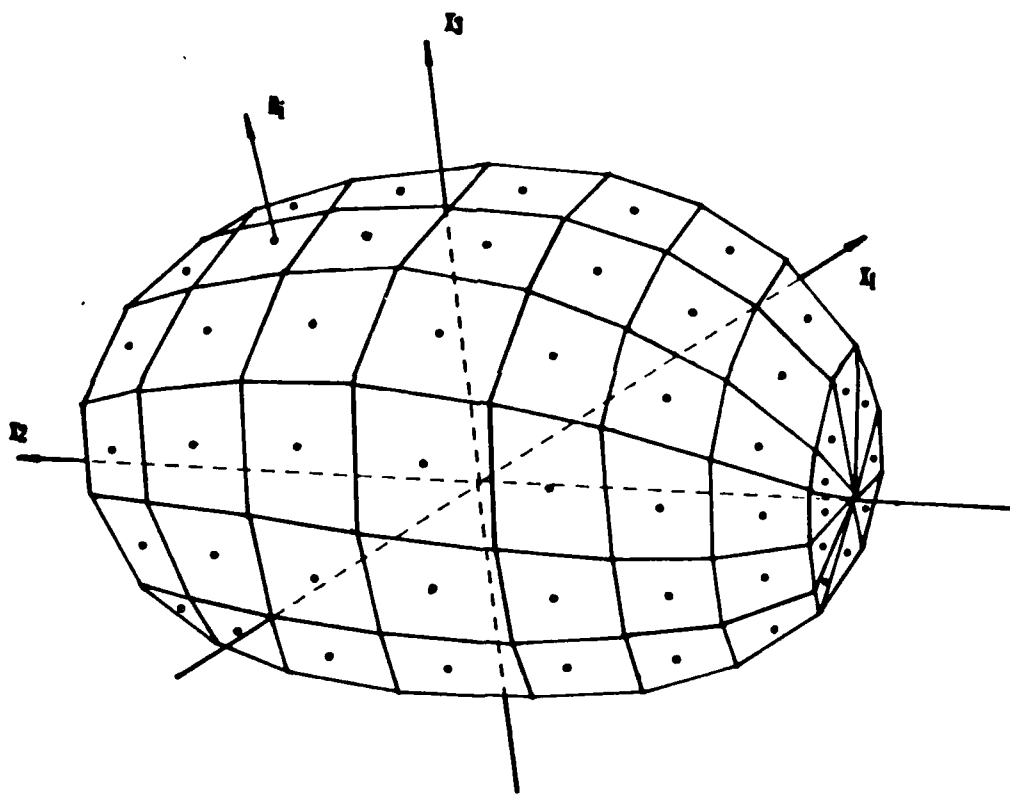
Figure 2.2: Approximation of body surface.

14

2.3.2 Induced flow velocity due to a plane element

Following equation EQ. 2.11 the induced potential at a point $P(x_j)$ due to a single plane quadrilateral element with a uniform source density is

$$\rho(x_i) = \sigma \int \int_A \frac{dA}{r(P,q)} \tag{2.15}$$

and the induced velocity

$$V_i(x_i) = -\partial_i \rho(x_j) = \sigma \int \int_A \frac{(x_j - \xi_j)dA}{r^3(P,q)} \tag{2.16}$$

where ξ_j = coordinates of point q on the plane quadrilateral.

To facilitate numerical computation of EQ. 2.16, a local coordinate system is used so that the quadrilateral lies in the x_1,x_2-coordinate plane as shown in Figure 2.3. Let the local coordinates at the four corners of the quadrilateral be $c_i(k)$ (k = 1,2,3,4). The corners are numbered in increasing order as the perimeter of the quadrilateral is traversed in the clockwise direction as seen from the unit normal vector to the plane of quadrilateral. Considering a unit source density ($\sigma = 1$), at any point $P(x_i)$ in the local coordinate system, the following induced velocity components I_i are derived (Hess and Smith, 1964)

$$I_1 = \sum_{i=1}^{4} \left[\frac{c_2(j) - c_2(i)}{d(i,j)} \right] \ln \left[\frac{r(i) + r(j) - d(i,j)}{r(i) + r(j) + d(i,j)} \right] \tag{2.17}$$

$$I_2 = \sum_{i=1}^{4} \left[\frac{c_1(i) - c_1(j)}{d(i,j)} \right] \ln \left[\frac{r(i) + r(j) - d(i,j)}{r(i) + r(j) + d(i,j)} \right] \tag{2.18}$$

$$I_3 = \sum_{i=1}^{4} \left[tan^{-1} \left(\frac{mn(i,j)e(i) - h(i)}{x_3 r(i)} \right) - tan^{-1} \left(\frac{mn(i,j)e(j) - h(j)}{x_3 r(j)} \right) \right] \tag{2.19}$$

where

$$d(i,j) = \left[(c_1(j) - c_1(i))^2 + (c_2(j) - c_2(i))^2 \right]^{1/2} \tag{2.20}$$

15
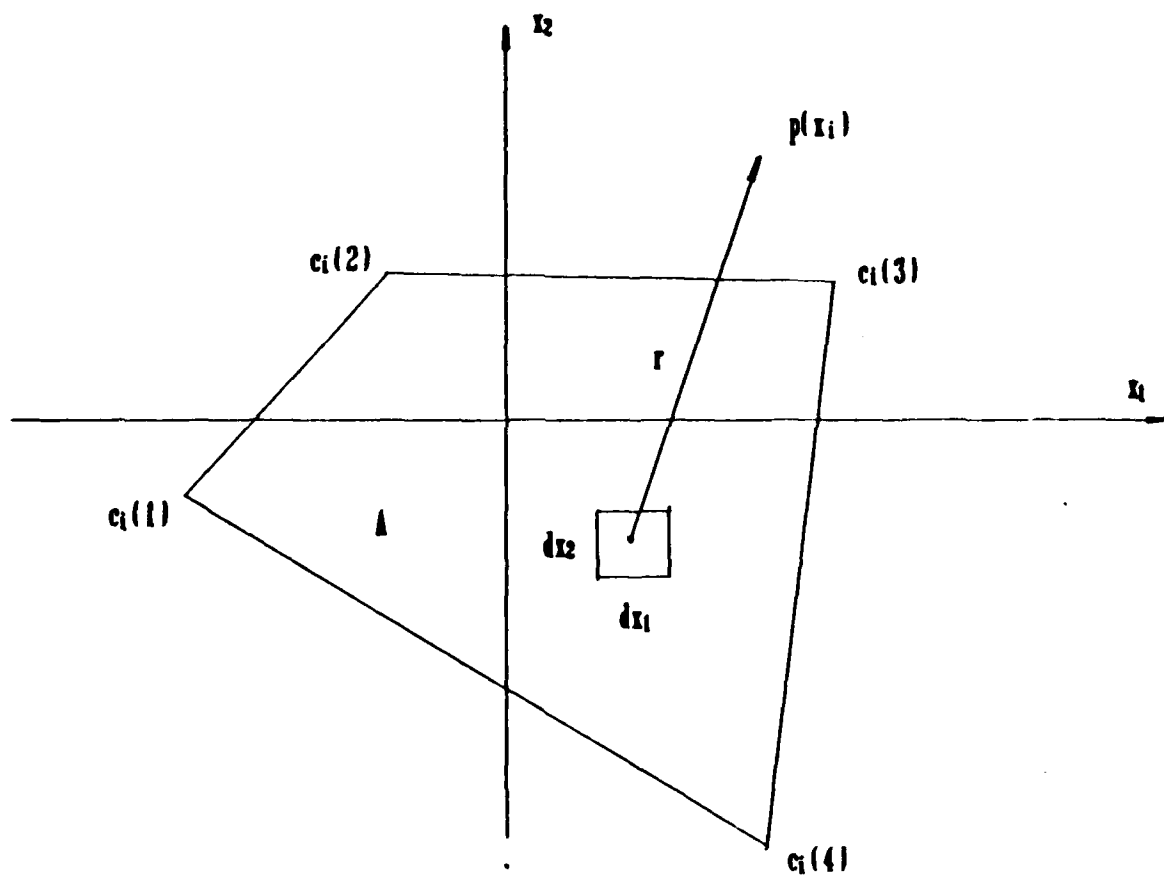
Figure 2.3: A plane quadrilateral lying in x_1,x_2-plane.

$$mn(i,j) = \frac{c_2(j) - c_2(i)}{c_1(j) - c_1(i)} \qquad (2.21)$$

$$r(i) = \left[(x_1 - c_1(i))^2 + (x_2 - c_2(i))^2 + x_3\right]^{1/2} \qquad (2.22)$$

$$e(i) = x_3^2 + (x_1 - c_1(i))^2 \qquad (2.23)$$

$$h(i) = (x_2 - c_2(i))(x_1 - c_1(i)) \qquad (2.24)$$

$$(2.25)$$

and j = i + 1, if i = 4 then j = 1.

EQ. 2.17 to EQ. 2.19 are valid essentially for any polygon plane elements (Hess and Smith, 1964) such as triangles.

2.3.3 The null point

On each quadrilateral element a point is selected where the flow velocity normal to the element is required to vanish and where the source density is eventually calculated. The point, designated as the null point, is taken where the element gives to no velocity in its own plane. Analytically, it means that if the condition of EQ. 2.8 is applied at a null point, no singularity will occur to the second term of EQ. 2.13. In the local coordinate system, $x_3 = 0$ and hence $I_3 = 0$ (EQ. 2.19) for the null point since it lies on the element plane. The determination of the null point is essentially to select a local coordinate $(x_1, x_2, 0)$ so that $I_1 = I_2 = 0$ or to solve the nonlinear simultaneous equations of EQ. 2.17 and EQ. 2.18.

2.3.4 Formulation of linear equations

Selection of null points enables the evaluation of EQ. 2.13 at a finite number of locations on the approximated body surface. Before establishing the linear equations, a global coordinate system is needed where all the induced velocity components are eventually summed and evaluated. Let $V_i(j, k)$ be the velocity vector, in the global

17

coordinate, at the null point of jth element due to a unit source density on the kth element. This is done by first converting the jth null point to the local coordinate of kth element. The induced velocities I_i are calculated according to EQ. 2.17 to EQ. 2.19. A coordinate transformation is then performed to convert the induced velocity into the global coordinate.

$$V_i = \ell_{i,j} I_j \tag{2.26}$$

where $\ell_{i,j}$ is the direction cosines of the local coordinates.

The normal velocity component A(j,k) at the null point of jth element by a unit source density on the kth element is the dot product of $V_i(j,k)$ with the unit normal vector to the jth element in global coordinates, i. e. ,

$$A(i,j) = n_i(j)V_i(j,k) \tag{2.27}$$

The normal velocity at the jth null point due to the entire approximated body surface must equal the negative of the normal component of the onset flow; that is

$$\sum_{k=1}^{NQ} A(j,k)\sigma(k) = -n_i(j)V_i^\infty \tag{2.28}$$

where NQ is the number of elements used to approximate the body surface. EQ. 2.28 must be satisfied at each null point. Repeating EQ. 2.28 for each element results in the set of linear algebraic equations that replaces the integral EQ. 2.13 as

$$[A]\{\sigma\} = \{-n_i V_i^\infty\} \tag{2.29}$$

The selection of null points ensures that $A(j,k) = 2\pi$ as j = k (all the diagonal terms of matrix A). The solution of EQ. 2.29 gives the source density values r for each quadrilateral. Once these source densities are obtained, the induced velocities at any point away from the body surface are given by

$$V_i = \sum_{j=1}^{NQ} V_i(j)\sigma(j) \tag{2.30}$$

18

The calculation of induced velocity $V_i(j)$ due to each element follows EQ. 2.17 to EQ. 2.19 and transformed to the global coordinates as was done for the null points.

2.4 Potential Flow and Strain Paths

For penetration problems, it is convenient to use a Eulerian coordinate system where a point on the penetrometer is chosen as the origin. The advantage of this system is that all the field variables are fixed in space with reference to this origin. Results of solving the potential flow problem as in EQ. 2.30 generate the induced flow velocity at a point in space. Considering a short time period dt, the amount of displacement at that point is

$$\dot{U}_i = \int V_i dt \simeq V_i dt \tag{2.31}$$

during this time period. EQ. 2.31 implies that the induced velocities remain constant during each time increment dt. In order for this assumption to be valid, it is necessary to use a sufficiently small dt for each increment which results in very small displacements. Therefore, even the final accumulated strains could be large, the small strain-displacement relationship is sufficiently accurate for each increment where

$$\dot{\varepsilon}_{ij} = \frac{1}{2}(\dot{U}_{i,j} + \dot{U}_{j,i}) \tag{2.32}$$

Or according to EQ. 2.31

$$\dot{\varepsilon}_{ij} = \frac{1}{2}(V_{i,j} dt + V_{j,i} dt) \tag{2.33}$$

where

$$\dot{U}_{i,j} = \frac{\partial \dot{U}_i}{\partial x_j}$$

$$V_{i,j} = \frac{\partial V_i}{\partial x_j}$$

19

In local coordinates, the induced strain tensor due to each quadrilateral is

$$\dot{\varepsilon}_{ij} = \frac{1}{2}(I_{i,j}dt + I_{j,i}dt) \qquad (2.34)$$

where

$$I_{i,j} = \frac{\partial I_i}{\partial x_j}$$

The derivatives are determined analytically from EQ. 2.17 to EQ. 2.19. Transforming to global coordinates

$$\dot{\varepsilon}_{ij} = \varepsilon_{kl}\ell_{ik}\ell_{jl} \qquad (2.35)$$

Summing the components from all the elements, the induced strain tensor increment becomes

$$\dot{\varepsilon}_{ij} = \sum_{k=1}^{NQ} \dot{\varepsilon}_{ij}(k) \qquad (2.36)$$

Integration of EQ. 2.31 is analytically intractable. This is basically because the potential flow analysis computes flow velocities only. To keep track of the displacements and strains in soil elements, at a given time t, they are integrated numerically by following a stream line from a starting point far ahead of the penetrometer (Levadoux and Baligh, 1980).

$$D_i = \sum_{m=1}^{NT} \dot{U}(m) = \sum_{m=1}^{NT} V_i(m)dt(m) \qquad (2.37)$$

$$\varepsilon_{ij} = \sum_{m=1}^{NT} \dot{\varepsilon}_{ij}(m) \qquad (2.38)$$

where

NT = number of time increments

dt = duration of each time increment

D_i = displacement components

ε_{ij} = accumulated strain tensor

The accumulated strain from EQ. 2.38 could be very large as will be demonstrated later. However, it should not be considered the same as that resulted from computations using large strain theories (Chen and Saleeb, 1982).

2.5 Two-Dimensional Panel Methods

The implementation of the above three-dimensional panel method is very time consuming and demands large computer memories. This is especially true when a large number of panels are involved. The computation time can be reduced by one order of magnitude, if the problem is simplified into 2-D. For example, if a flat-plate penetrometer is infinitely wide in x_3 direction, then all velocity and strain components related to x_3 coordinate are zero. The 2-D simplification is accomplished by treating the panels as infinitely long x_3. In cases of axisymmetric bodies, two-dimensionalpanels are a series of frustums of cones. The induced velocities are derived by modifying the integral EQ. 2.16. These procedures are well established in aeronautical engineering (Hess and Smith, 1962) and can be easily formulated to compute strain paths. The two-dimensionalSPM programs have also developed in this research which are capable of analyzing strain paths for infinitely wide and axisymmetric penetrometers.

2.6 Evaluation of the panel method

A series of preliminary strain path analyses were performed for a cone and a flat dilatometer to validate the new SPM technique. Figure 2.4 shows the distribution of panels on the cone and dilatometer tips. The simulated cone was 820 mm long, had a 60 degree apex and a diameter of 35.6 mm. The flat dilatometer (DMT) was simulated as 14 mm thick, 94 mm wide and 235 mm long. The penetration rate was 20 mm/sec in both cases. A reference radius R is used in presenting the

data. The radius of cone (17.8 mm) and half thickness (7 mm) of the DMT was used as the R value for the respective penetrometer. For the cases to be presented, the integration of displacements and strains started at an initial coordinate of (0,-200R,R) which was 200 R ahead of the penetrometer tip (see Figure 2.4) for the coordinate system). The initial integration interval was 5R and reduced as the to penetrometer distance shortened. A minimum integration interval of 0.02R was used and maintained when a distance of 10R was reached. These parameters are similar to those used by Levadoux and Baligh (1980). Further reduction of these integration intervals showed no significant change in results.

In presenting the strain paths, the E_i-space (Prevost, 1978) is used, where

$$e_1 = \varepsilon_{22} \tag{2.39}$$

$$E_2 = \frac{1}{\sqrt{3}}(\varepsilon_{11} - \varepsilon_{33}) \tag{2.40}$$

$$E_3 = \frac{2}{\sqrt{3}}\varepsilon_{23} \tag{2.41}$$

$$E_4 = \frac{2}{\sqrt{3}}\varepsilon_{12} \tag{2.42}$$

$$E_5 = \frac{2}{\sqrt{3}}\varepsilon_{13} \tag{2.43}$$

Compressive strain is negative. The E_i space provides a simple method to present a six component strain tensor in a three-dimensional space. The components are directly related to some major shearing modes. The E_1-strain is produced by a shearing mode of triaxial tests, the E_2-strain is caused by lateral expansion and E_3, E_4 and E_5-strain is produced by direct simple shear tests.

A total of 576 panels were used to cover the flat DMT which has a rather simple geometry. The adequacy of this panel configuration was first evaluated in two-dimensional. The DMT was considered infinitely long in x_1 direction shown in Figure 2.4 . Panels behind the DMT tip are parallel to the direction of penetration and their effects to strain paths are insignificant. Figure 2.5 shows the strain paths in terms of E_2 versus

22
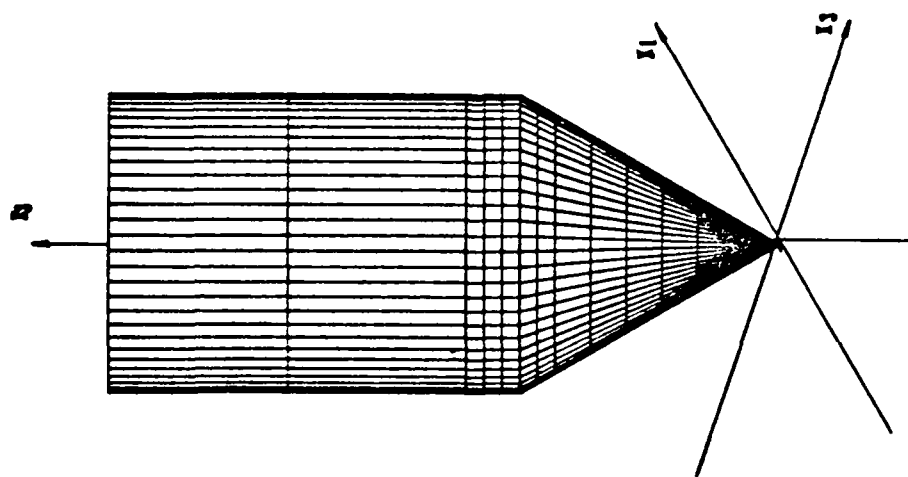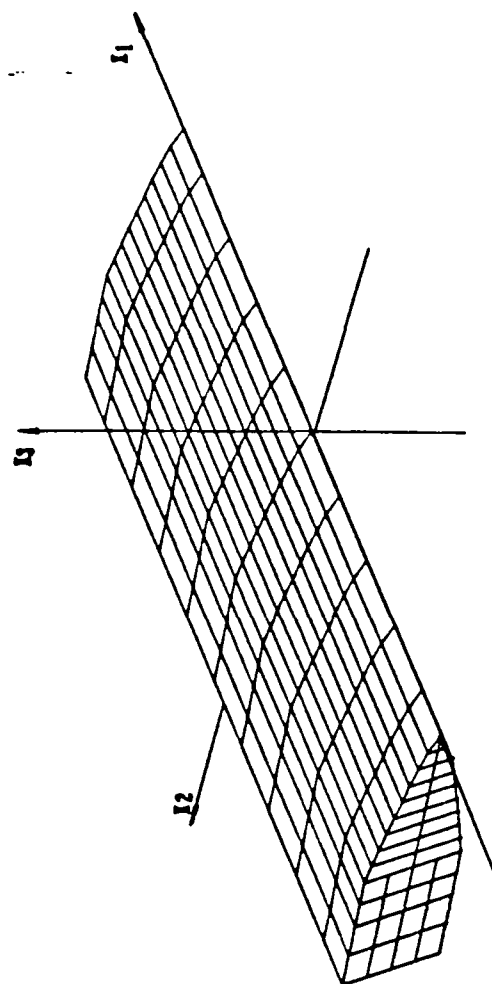
(b) Flat dilatometer

(a) Cone

Figure 2.4: Distribution of elements on the penetrometer tips.

23
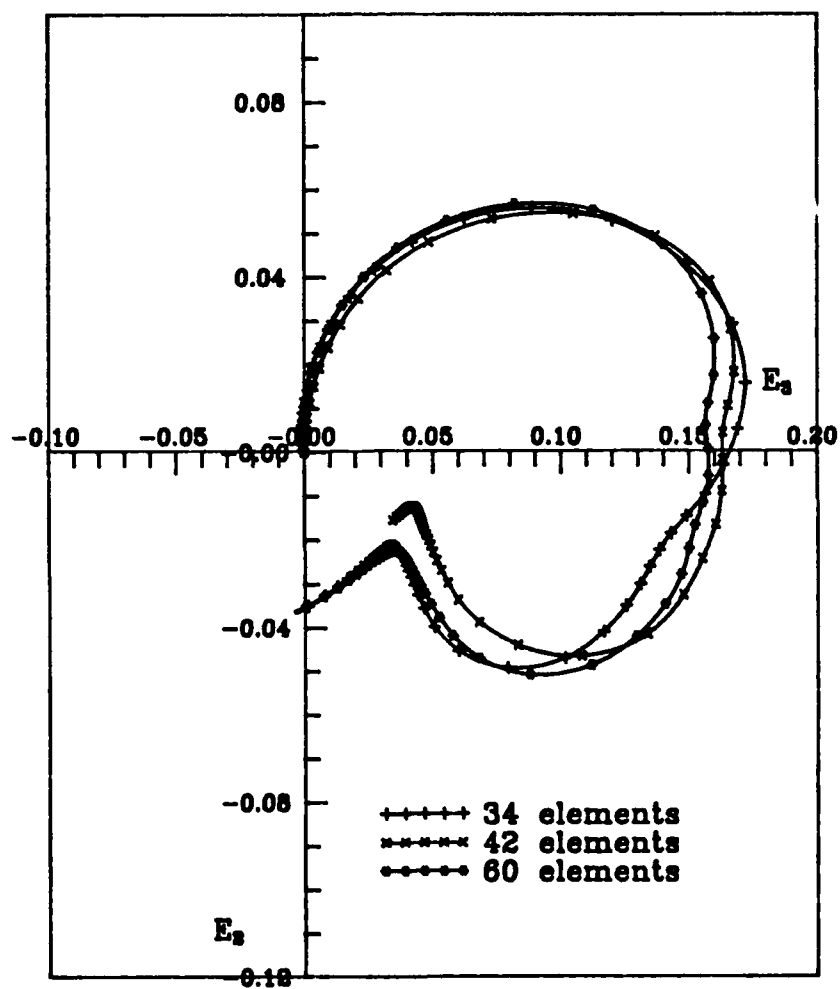
Figure 2.5: Effects of resolution on strain paths.
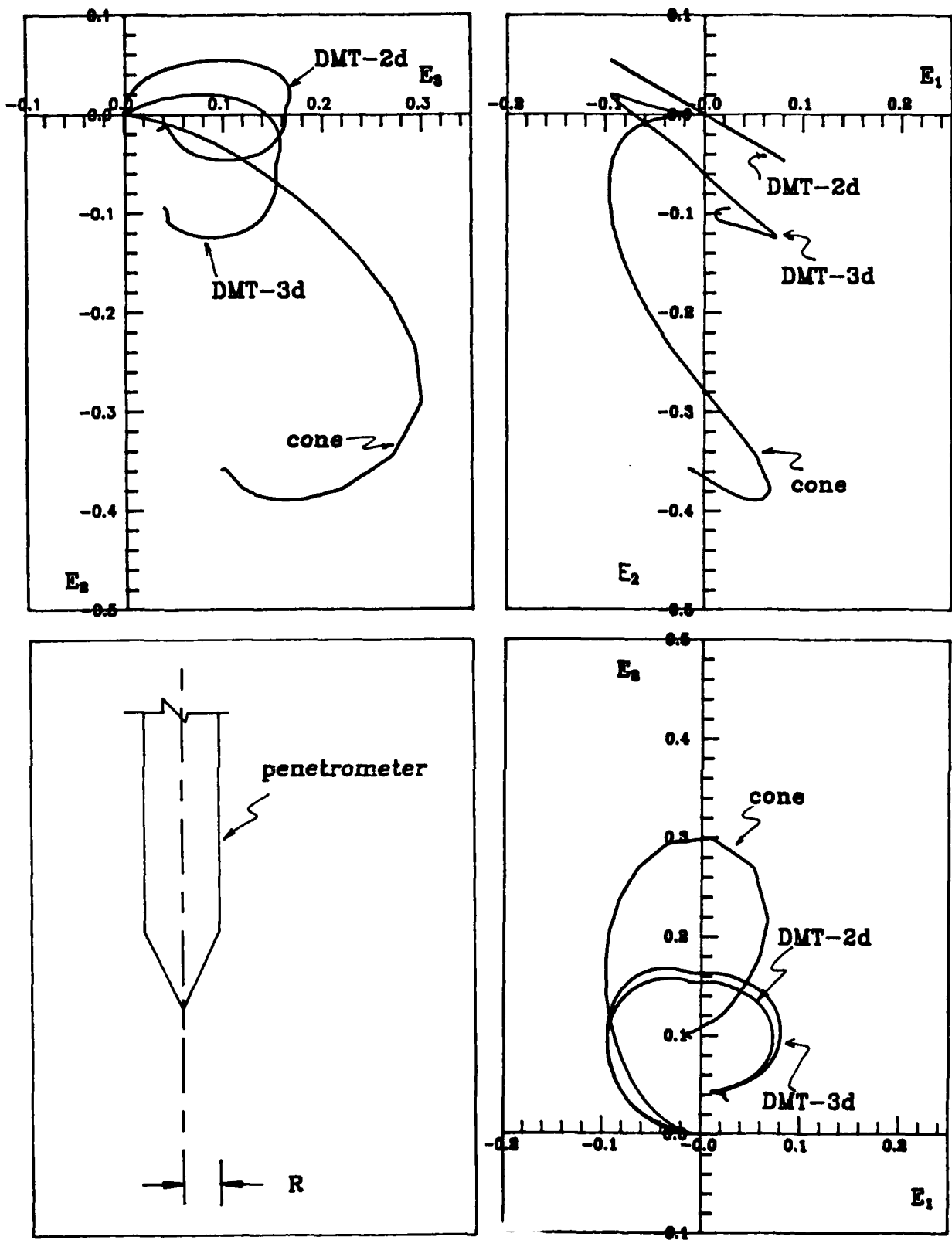
Figure 2.6: Induced strain paths.
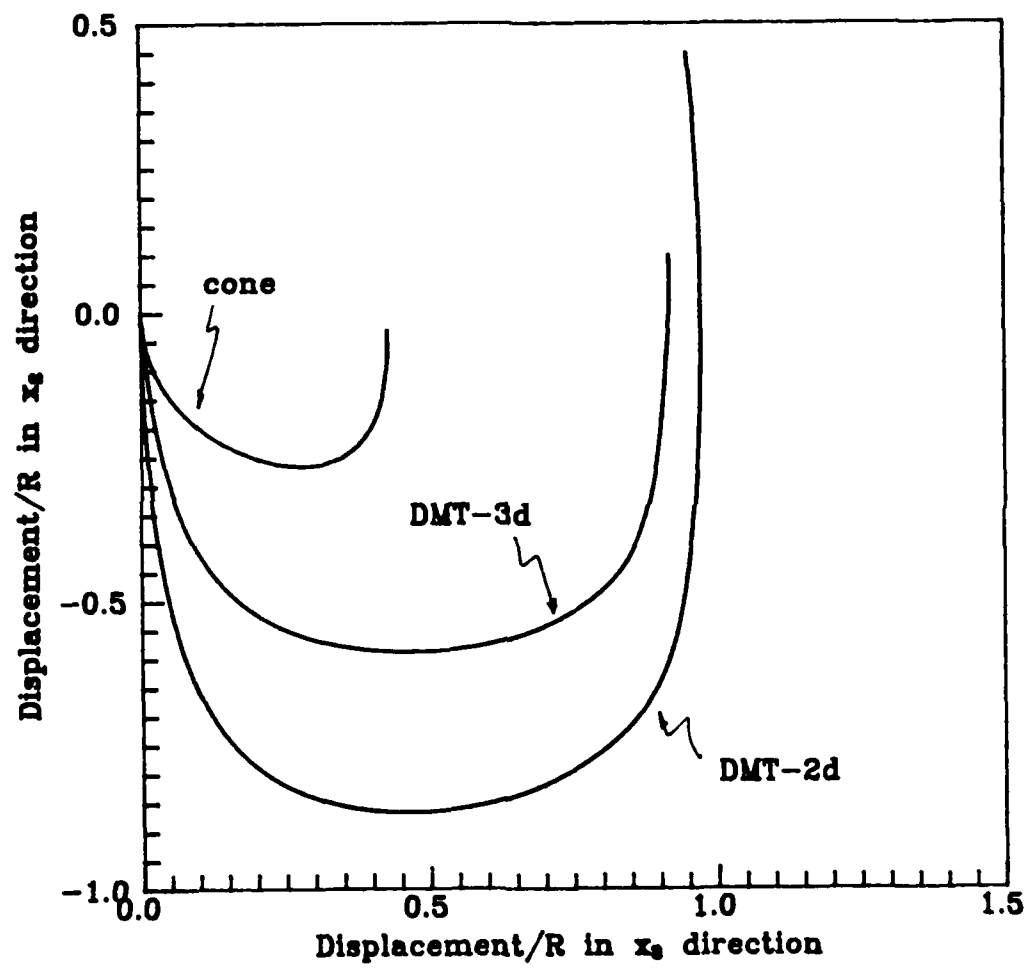
Figure 2.7: Induced displacements.

26

E_3 resulted from three analyses using different number of elements. The first curve (32 elements) had half the number of panels as that of 42 elements on the DMT tip. The last curve (60 elements) had double the number of panels on the tip. We can say that these three curves are identical, considering the qualitative nature of the strain path method, even as the resolution of panels changed by four fold. Further increase of the panel number resulted in no significant differences in strain paths. Because the DMT has a uniform shape in the x_1 direction, the number of panels in this dimension has little effect to the results. The configuration shown in Figure 2.4 was selected basically to give a reasonable length to width ratio for each panel. A total of 2880 elements were used to simulate the cone (Figure 2.4) in a three-dimensional SPM computation. This is far more than necessary to give reasonable results. The higher element number was used primarily to demonstrate that the round surface of a cone can be realistically represented by a large number of such plane quadrilaterals. It should also be noticed that there was no need to avoid the sharp corner at the base of the cone tip as in other methods (Baligh, 1985) of strain path computations. The analysis was also performed using a technique based on axisymmetric, two-dimensionalpanel method where the cone surface was represented by 25 line elements. The displacement and strain components (Figure 2.6 and Figure 2.7) of the cone from both the two-dimensionaland three-dimensional analyses are essentially identical to those reported by Levadoux and Baligh (1980).

Chapter 3

The Strain Field

The new numerical technique enabled strain path analyses be performed for flat-plates which were not possible before. Analyses were conducted for the DMT, K_o-Stepped Blade and continuously tapered blade for the first time, using the new three-dimensional strain path technique. Dimensions of these penetrometers used in the computations are shown in Figure 3.1. This chapter describes the characteristics of the strain field during a flat-plate penetration.

A slightly different coordinate system was adopted herein after. Figure 3.2 shows the coordinate system used and its relation to the flat-plate. All linear dimensions are normalized with respect to a reference radius R. For axisymmetric penetrometers R is the actual radius, whereas R equals the half thickness of the blade for flat-plates Figure 3.1. Computations of soil displacements and strains follow a stream line started far ahead of the penetrometer, typically at $y = -200R$ as described previously. In presenting the strains, the starting coordinates (x,z) of the associated stream line are given and the E_i space (Prevost, 1978) as mentioned before is used. A strain ratio SR_i is used to indicate the relative importance for each strain component during

t = 14 mm

250 mm

DMT

R = 7 mm
w = 84 mm

t = 2.3 mm   t = 3.5 mm   t = 4.6 mm   t = 5.8 mm

4 x 100 mm

stepped blade

R = 1.15 mm
w = 12 mm

t = 6.6 mm   t = 12 mm

285 mm

tapered blade

R = 3.3 mm
w = 88 mm
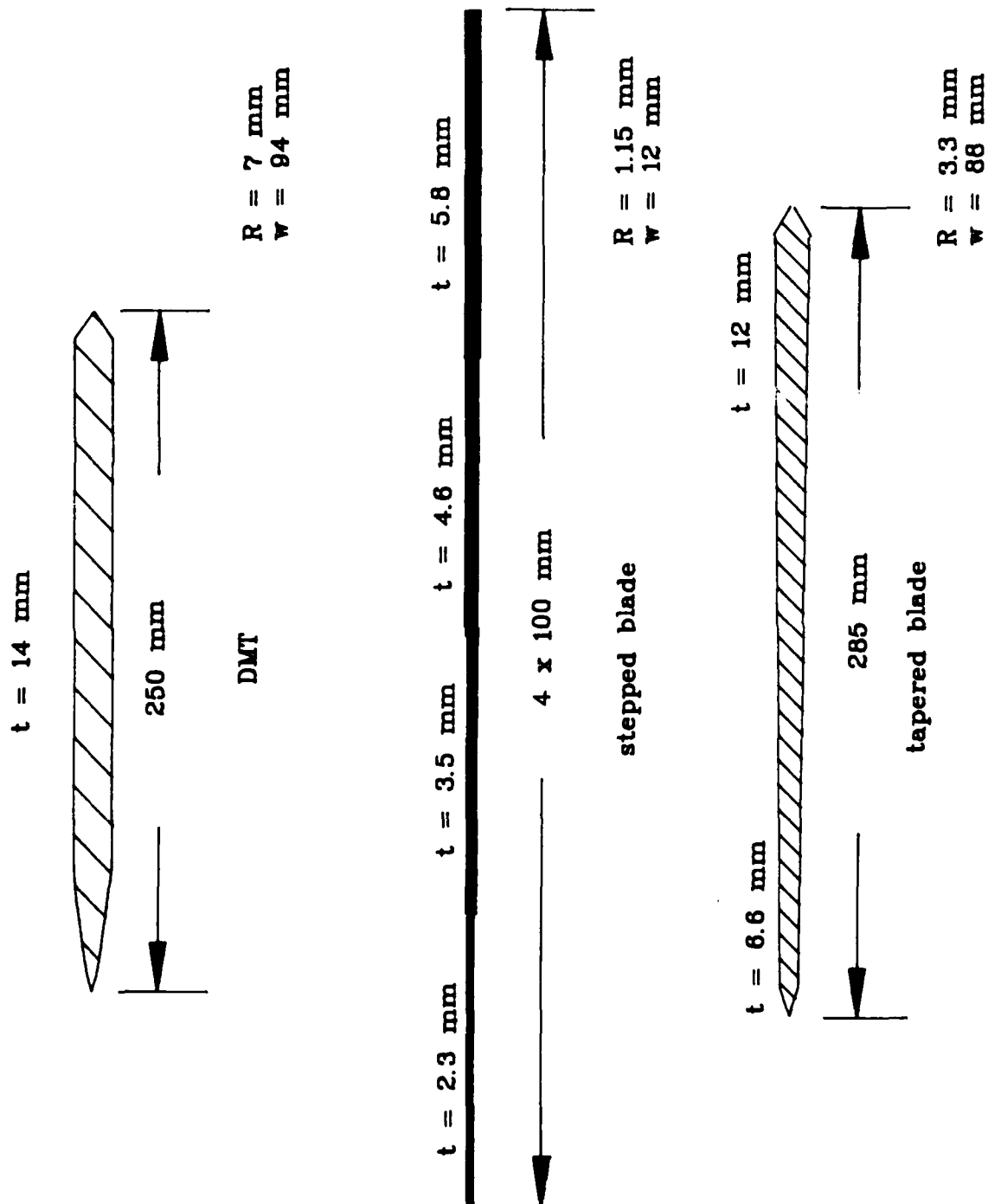
Figure 3.1: Dimensions of the flat-plates analyzed.

penetration.

$$SR_i = \frac{E_i^2}{\sum_{i=1}^3 E_i^2} \qquad (3.1)$$

Plots of E_i and SR_i versus y/R describe how they vary as the soil moves relative to the penetrometer.

Strain paths (E_2 versus E_3) and soil displacements following streamlines started at $z = 1R$, 3R, 5R and 10R, and $x = 0R$ are shown in Figure 3.3. The results indicate that the magnitudes of strains and displacements decrease with distance to the plate. However, the pattern of strain paths as shown in Figure 3.3a remains similar. As a reference, the strain path during a cone penetration (CPT), along a stream line started at $z = 1R$ and $x = 0R$ is also included in Figure 3.3. Both penetrometers cause significant strain reversals as demonstrated in Figure 3.3a. However, an important difference between the CPT and the DMT is the much higher magnitude of E_2-strain which occurs during the CPT penetration. This is the result of a very large tensile circumferential strain which develops during the CPT penetration. Plots of strain ratios following stream lines at $z = 1R$ and $x = 0R$ (Figures 3.4 and 3.5) show that in both cases, E_1 is the predominant strain component before the soil particle reaches the tip of penetrometers ($y = 0R$). For the DMT, E_3 and E_2 exchange their role as the predominant strain component after passing the tip with E_2 becoming the predominant component when approaching the flexible membrane ($13R < y < 17R$). Beyond the tip (as $y > 0R$), E_2 becomes the major strain component in the case of CPT penetration, which provides some justification to use cylindrical cavity expansion theory in the interpretation of CPT results.

3.1 Three Dimensional Effects

To demonstrate the three-dimensional nature of the DMT penetration, Figures 3.6 and 3.7 show a quadrant of the contours of displacements, ds and shear octahedral

strains, γ_{oct} at $y = 13R$. This is approximately the same level at the center of the DMT flexible membrane. The displacement is computed as:

$$ds = \frac{(dx^2 + dz^2)^{1/2}}{R} \tag{3.2}$$

and the shear octahedral strain

$$\gamma_{oct} = \frac{2}{3} \left[(\varepsilon_{xx} - \varepsilon_{yy})^2 + (\varepsilon_{xx} - \varepsilon_{zz})^2 + (\varepsilon_{yy} - \varepsilon_{zz})^2 + 6(\varepsilon_{xy}^2 + \varepsilon_{yz}^2 + \varepsilon_{zx}^2) \right]^{\frac{1}{2}} \tag{3.3}$$

The magnitudes of shear octahedral strains are much higher towards the corner of the plate (Figures 3.6 and 3.7). The limited plate width affects not only the magnitude but also the characteristics of the strains. Figure 3.8 shows E_2 versus E_3 following stream lines at $x = 0R$, $3.4R$ and $6.7R$ ($z = 1R$ for all). At $x = 6.7R$, the stream line passes the corner of the DMT. Along the center of the DMT (i.e. at $x = 0R$) ε_{xx} is compressive while ε_{zz} is tensile. The E_2-strain increases towards the corner of the DMT and approaches the magnitude which occurs during CPT penetration or a cylindrical cavity expansion Figure 3.3a). Immediately adjacent to the DMT corner, there is a reversal of signs for both ε_{xx} and ε_{zz}. This results in a positive E_2-strain along the corner of the blade as shown in Figure 3.8.

To further demonstrate the three-dimensional nature of the DMT penetration, the corresponding shear octahedral strain and displacement values from 2-D ($w/t = \infty$) analyses are included in Figures 3.6 and 3.7. The results clearly indicate that the 2-D simplification would significantly underestimate the shear octahedral strains. Also, the strain and displacement components attenuate much slower with distance in 2-D analyses.

A series of strain path analyses were performed using different widths for the blade to investigate the significance of three-dimensional effects. Figure 3.9 shows the strain

31

paths in terms of E_2 and E_3-strains following stream lines at $x = 0R$ and $z = 1R$. In these analyses, the width over thickness ratios, w/t varied from 2 to infinity. For a blade with infinite width, the analysis actually produces a 2-D solution. The results presented in Figure 3.9 show that with $w/t = 2$, the E_2-strain approaches the corresponding values obtained during CPT (Figure 3.3a). As w/t increases, the strain paths approach the 2-D solution. Above a w/t of approximately 20, the computed strain paths resemble that from 2-D analysis where the plate width was considered infinite. Further increase of w/t ratios beyond 20 did not result in any significant differences in strain paths. The results of Figure 3.9 suggest that the strain paths immediately adjacent to the center ($x = 0R$) of a penetrating, thin flat-plate would approximate the 2-D case.

3.2 Effects of Tip Apex Angles

Using the 2-D analyses, it was possible to evaluate the effects of the DMT apex angles without the complication caused by the limited plate width. Figure 3.10 shows the predicted soil distortions around the penetrometer with four different tip apex angles ranging from 10 to 60 degrees. The DMT has an equivalent apex angle of approximately 20 degrees. The strain paths along stream lines at $z = 1R$ show that E_3-strain is very sensitive to the apex angle Figure 3.11. At an apex angle of 60 degrees, E_3 is much larger than E_2 which is not the case during a comparable CPT penetration (see Figure 3.3a). The predominant strain component during a flat-plate penetration is therefore, affected by the tip apex angle. Further results to be shown later would demonstrate that the same is true from actual three-dimensional strain path analyses.

The contrast in soil distortions between the 60 degree plate and the DMT are comparable to that presented by Levadoux and Baligh (1980) for cones with 60 and 18

degree apex angles. One might conclude that if the DMT penetration does induce less soil disturbance than the CPT as stated by Marchetti (1981), it is most likely due to the sharper apex angle of the DMT and not necessarily because of the geometry (i. e. , flat versus cylindrical).

3.3   Effects of Geometry

From the context of the interpretation theories, Handy, et al. (1982) actually assumed that E_2 is the predominant strain component during penetration and E_2 is proportional to the blade thickness. The Stepped-Blade was made thin enough so that the penetration can be considered plane strain, which is a requirement for Eq. ?? to be valid. In an attempt to increase the number of stress measurements and improve the reliability of stress extrapolation a continuously tapered blade was conceived as a taxadjunct to the Stepped Blade (Handy and Lutenegger, 1985). The development of this device by the second author has yielded a blade which has a continuous taper of 3 degrees and is instrumented with seven stress sensors along one face. Currently, the interpretation of results from the tapered blade has followed the extrapolation procedure proposed by Handy, et al. (1982).

Figures 3.12 through 3.16 show the results of the three-dimensional analyses for the K_o-Stepped and tapered blade penetrometer in terms of displacements, E_i strains and strain ratios SR_i. All computations follow stream lines started at $x = 0R$, $y = -200R$ and $z = 1R$. These strain paths are considered representative in the area adjacent to the pressure sensors (diameter less than 25.4 mm) on the blades.

For the K_o-Stepped Blade, the results show that displacements in the z direction are approximately proportional to the blade thickness (Figure 3.12). However, the

strain components are far from those assumed by Handy, et al. during a stepped-blade penetration. According to Figures 3.12 and 3.13, E_3-strain is the predominant strain component and increases with the blade thickness. The E_2-strain remains approximately constant and appears independent of blade thickness. Also, all strain components undergo significant strain reversals between successive steps. The strain paths imply that the stresses measured on the face of a stepped-blade are equivalent to the normal stress response during a cyclic simple shear test where E_3-strain is the major component. Since the width is constant, the K_o-Stepped Blade has a w/t ratio which starts at about 22 at the first step and decreases to 8.7 at the fourth step (Figure 3.1). In view of the aforementioned w/t studies for the DMT (Figure 3.9), the stepped-blade penetration is not likely to be plane strain, at least for the thicker part of the blade due to the less favorable w/t ratios. This was in part recognized by Handy, et al. (1982) who hypothesized that thicker blades would result in a transition to cylindrical cavity behavior and thus produce a "limit" pressure.

The soil disturbance induced by the tapered blade penetration (Figures 3.12, 3.15 and 3.16) is less erratic compared with that of the stepped-blade. As in stepped-blade, the E_3-strain is the predominant component. After passing the tip, all three strain components remain relatively constant as the blade thickness increased from 6.6 mm to 12 mm. There are no strain reversals as there are no "steps" and thus the soil does not undergo an unloading sequence.
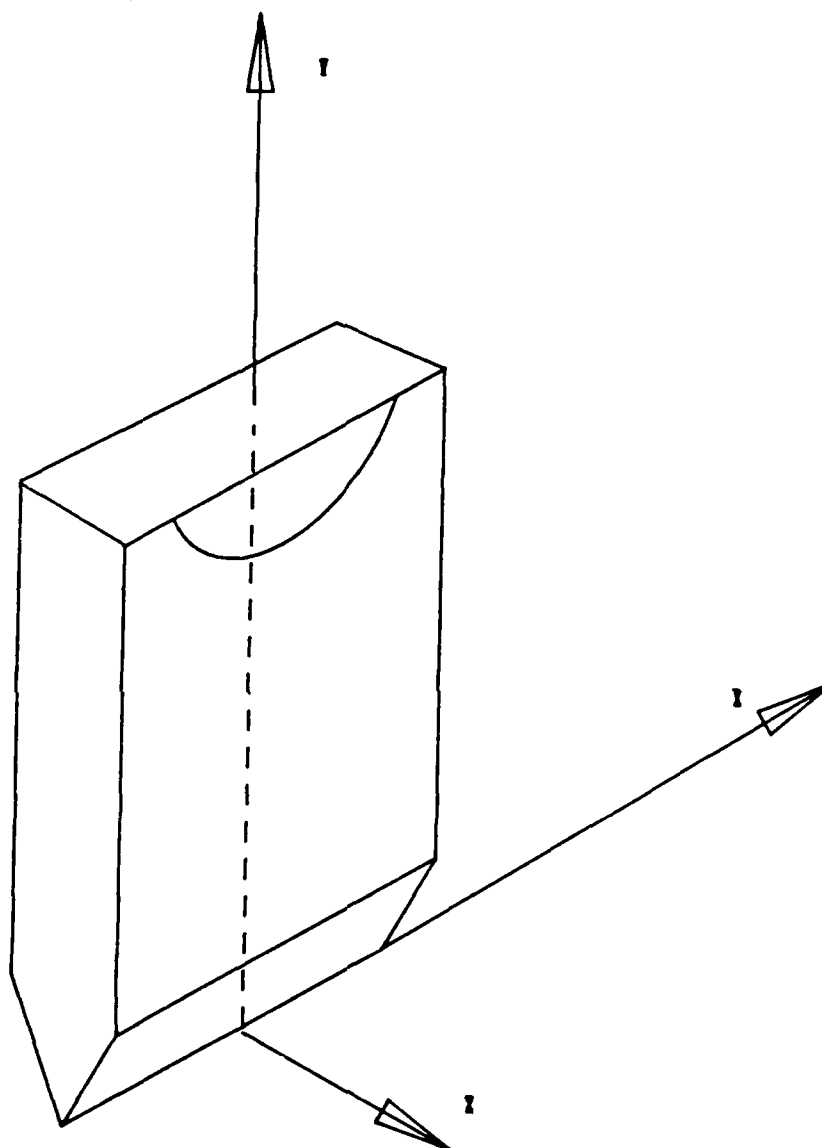
Figure 3.2: The coordinate system.
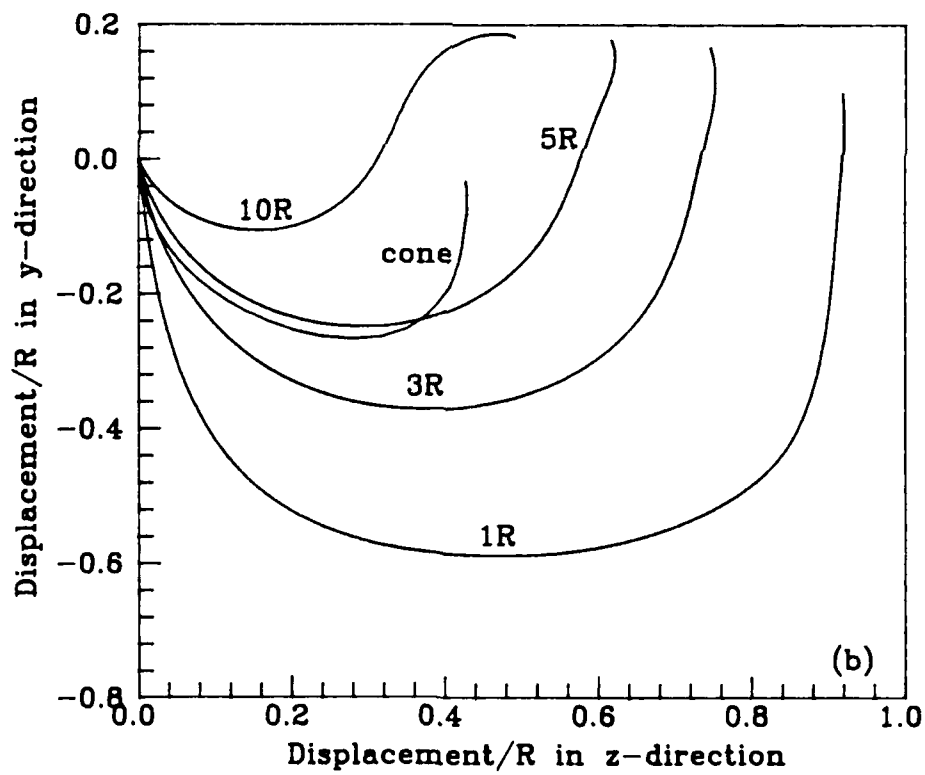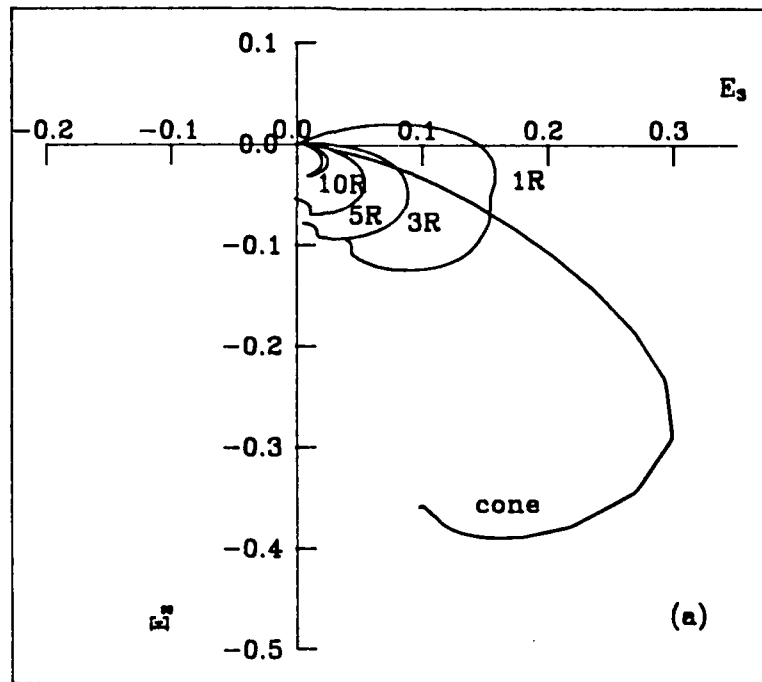
Figure 3.3: Strain paths and displacements during DMT penetration.
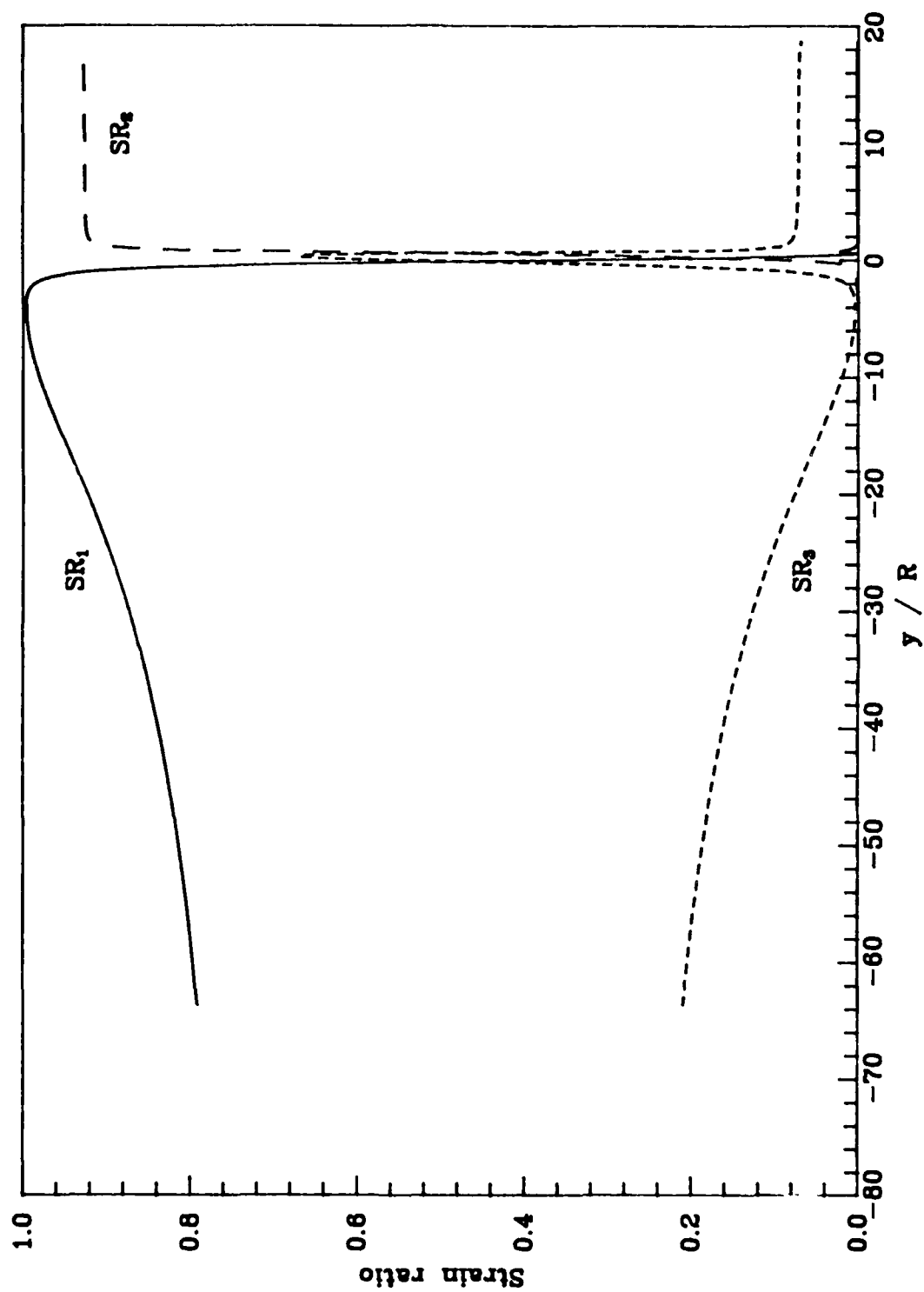
Figure 3.4: Strain ratios during CPT penetrations.
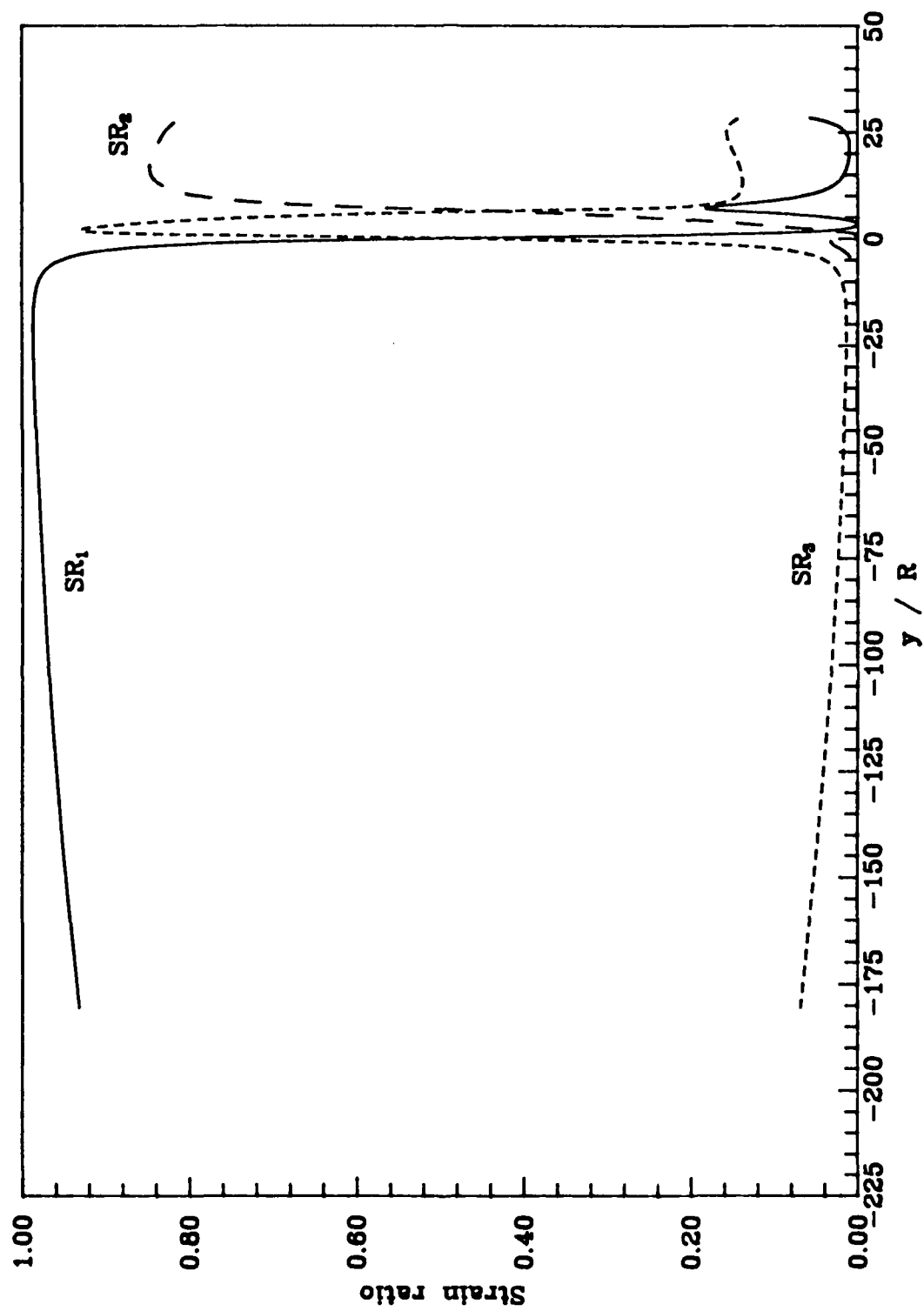
Figure 3.5: Strain ratios during DMT penetration.
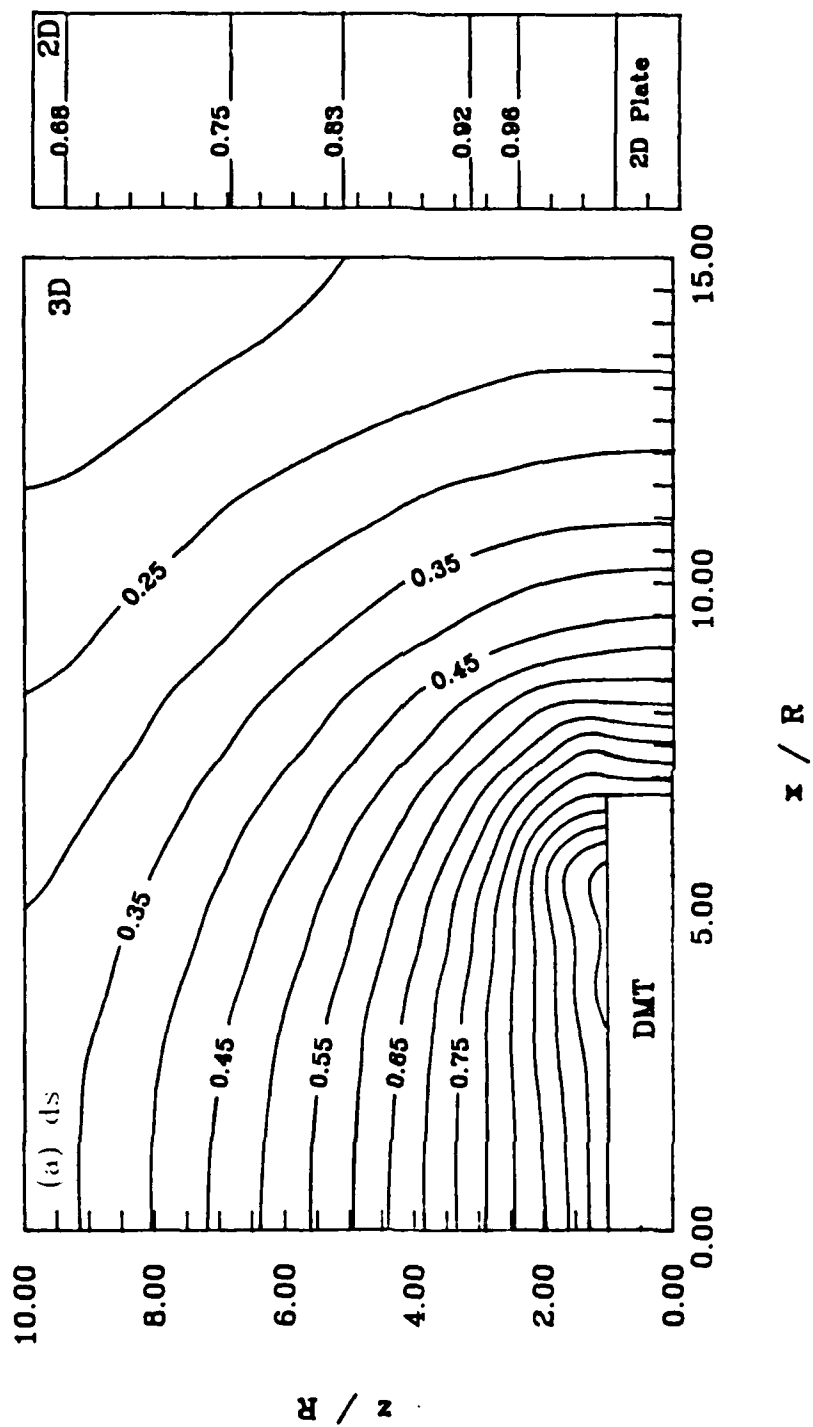
Figure 3.6: Contours of displacements.

39
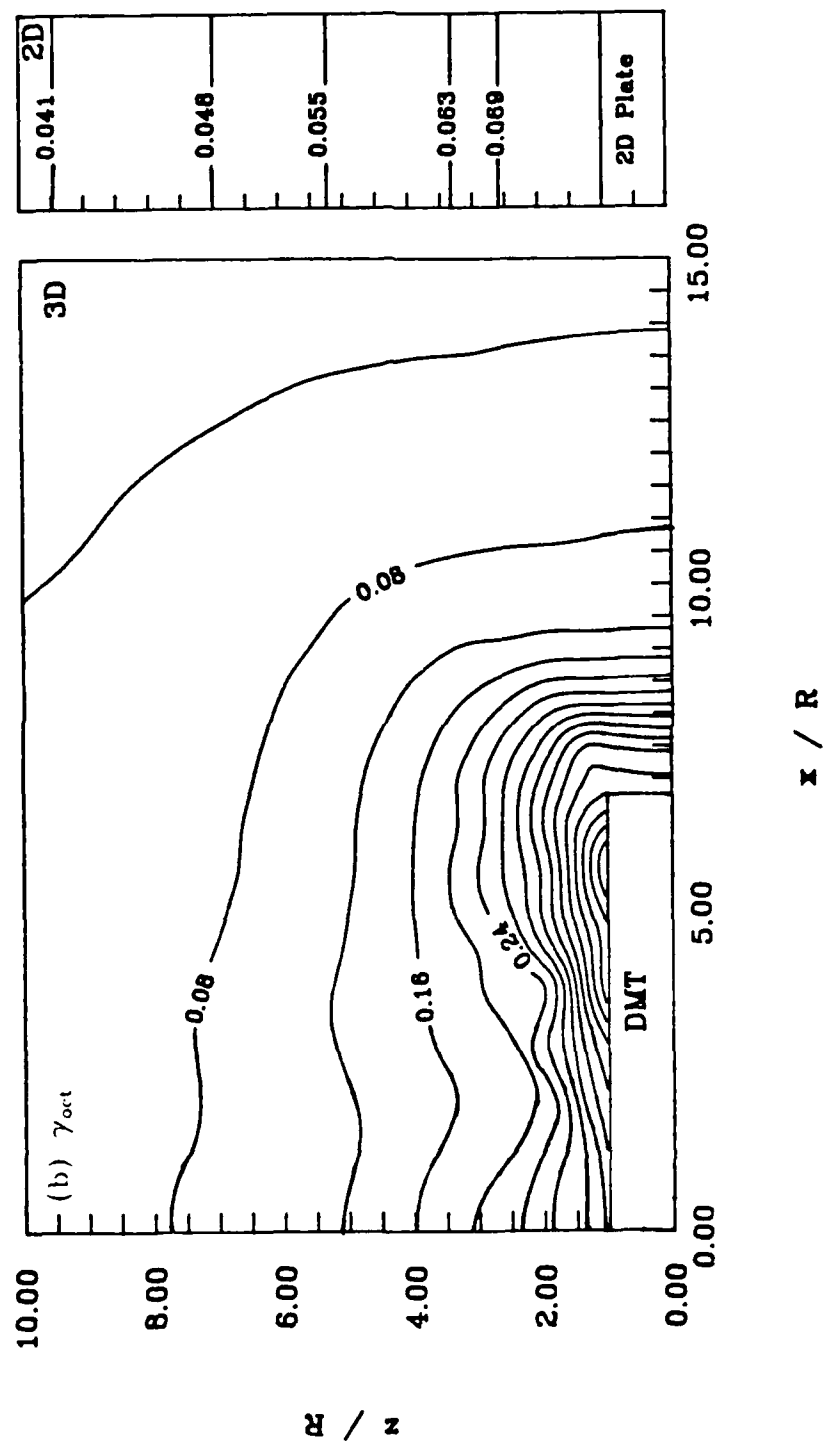
Figure 3.7: Contours of shear octahedral strains.
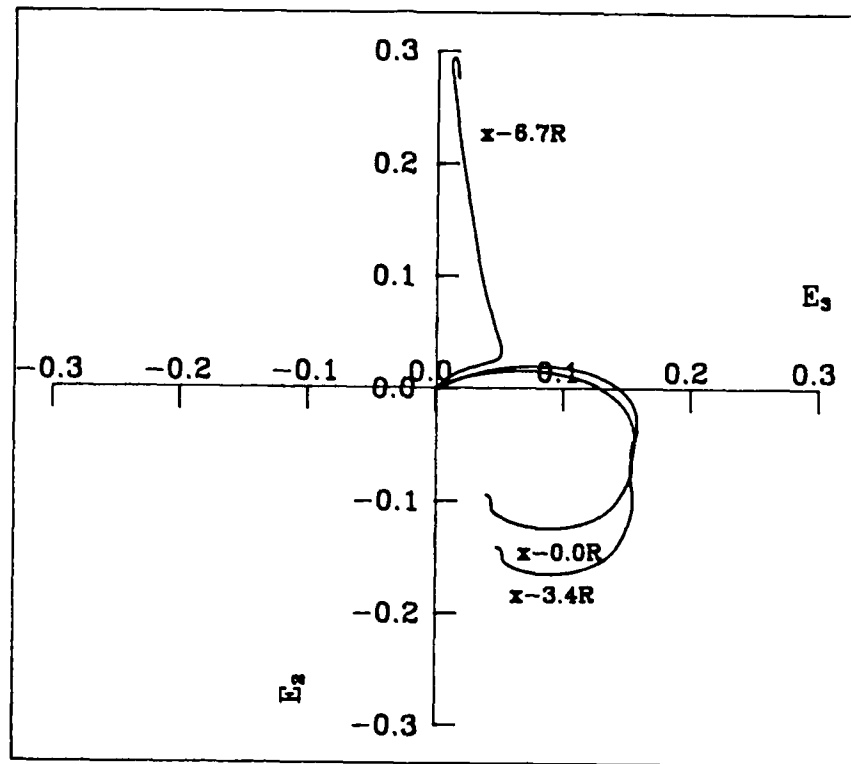
Figure 3.8: Strain paths approaching the corner of DMT.
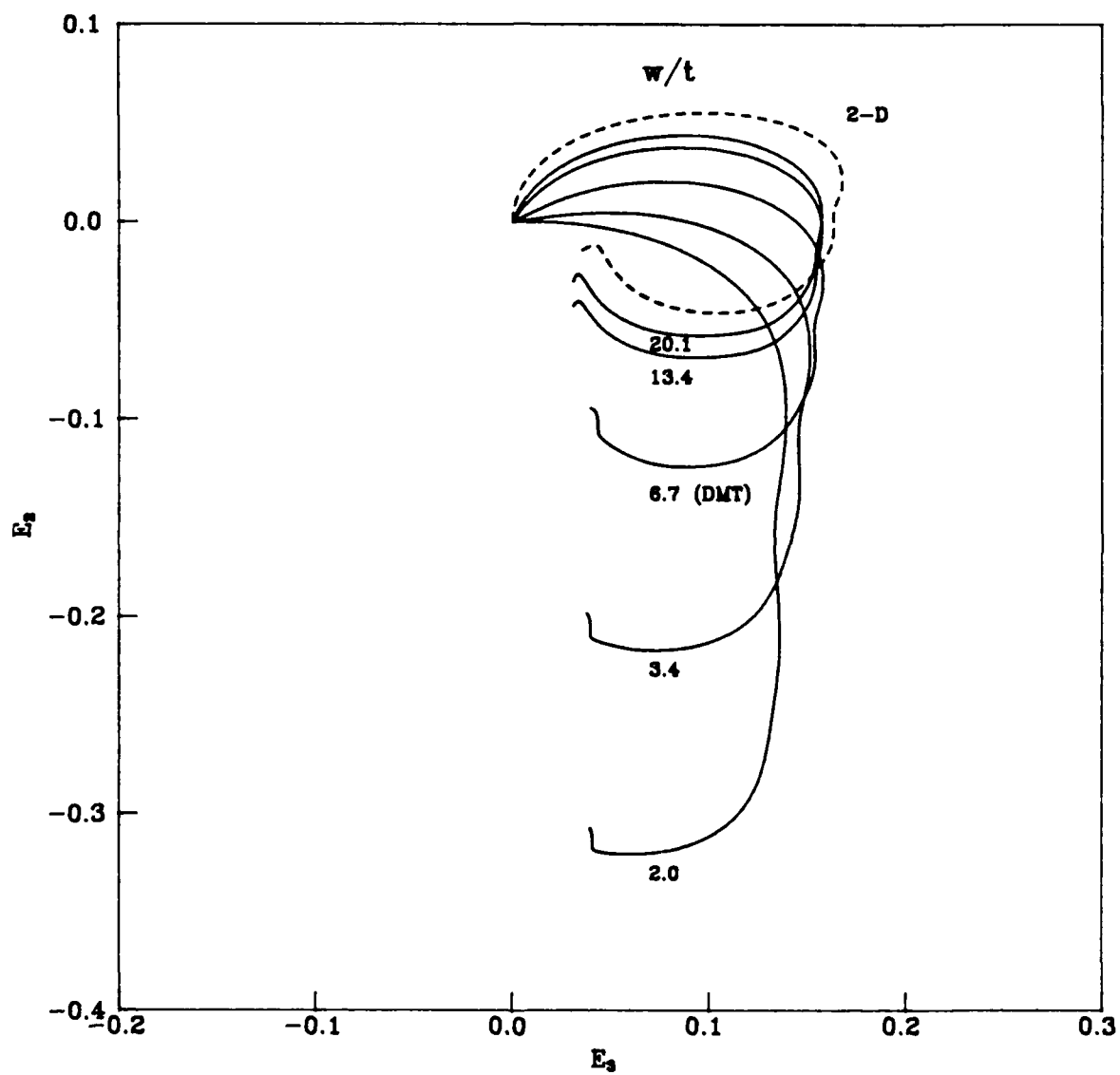
Figure 3.9: Effects of w/t on strain paths.
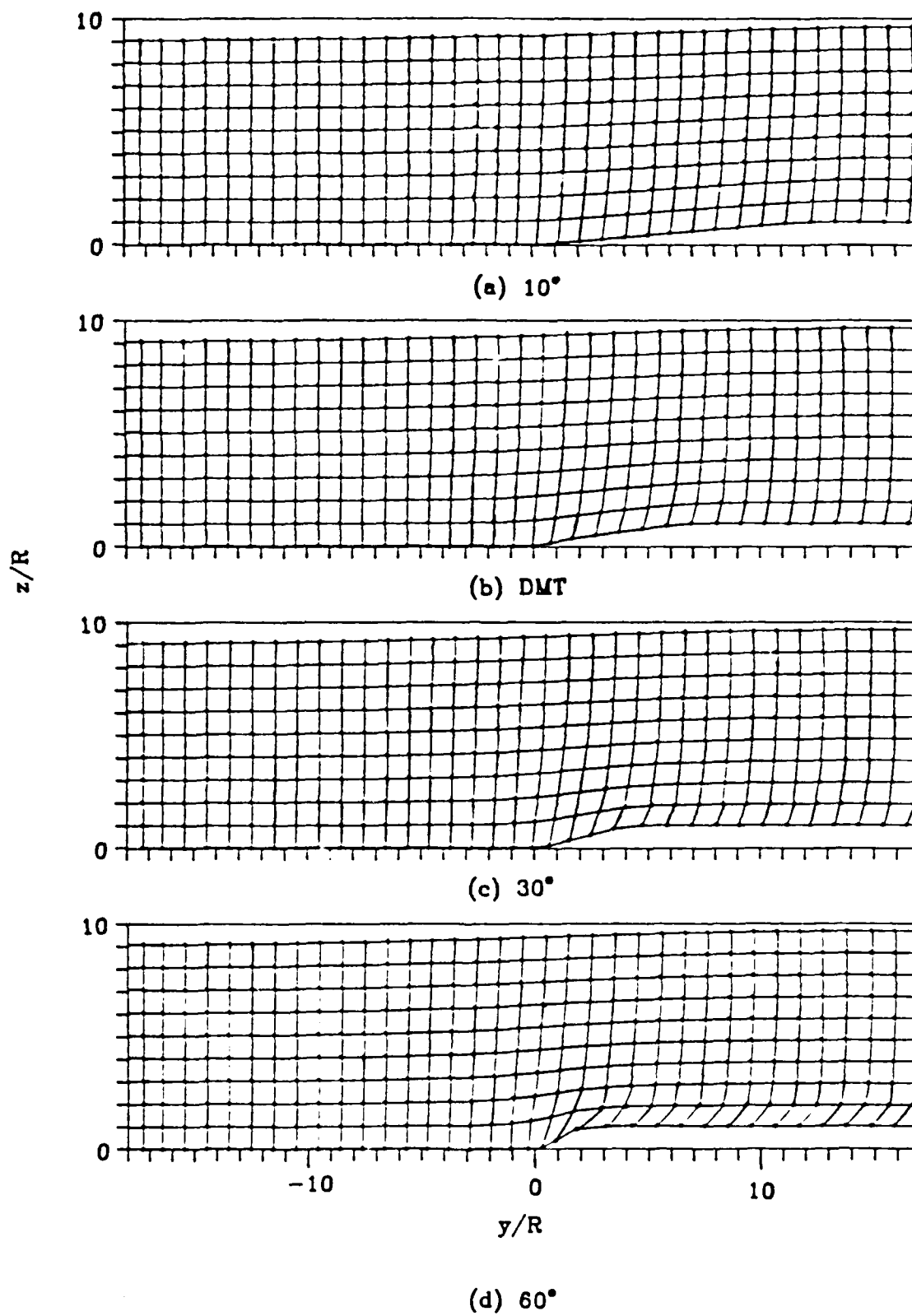
Figure 3.10: Effects of tip apex angle on soil disturbance.

43
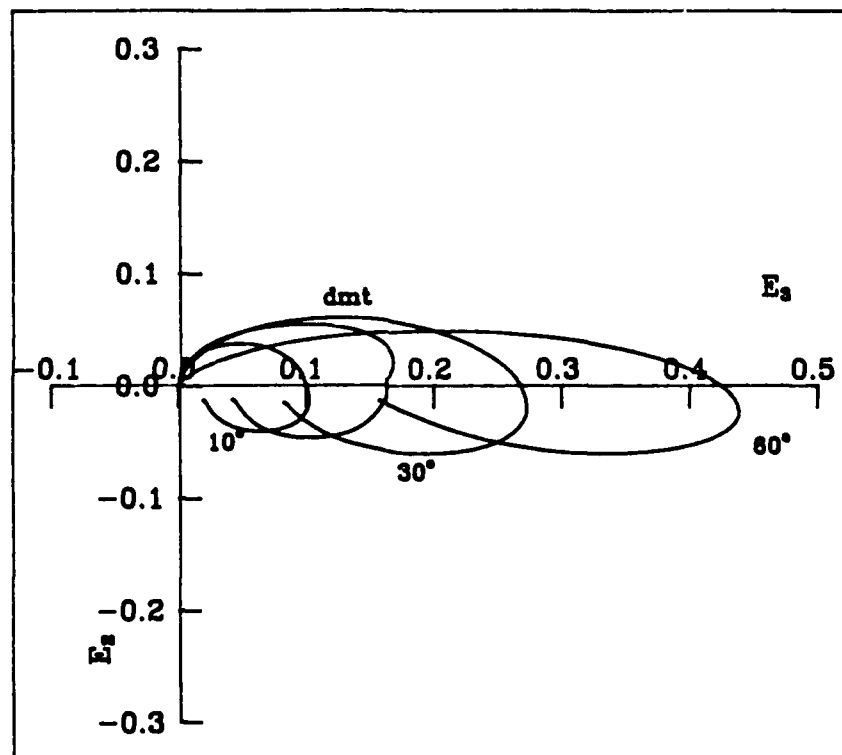
Figure 3.11: Effects of tip apex angle on strain paths

44
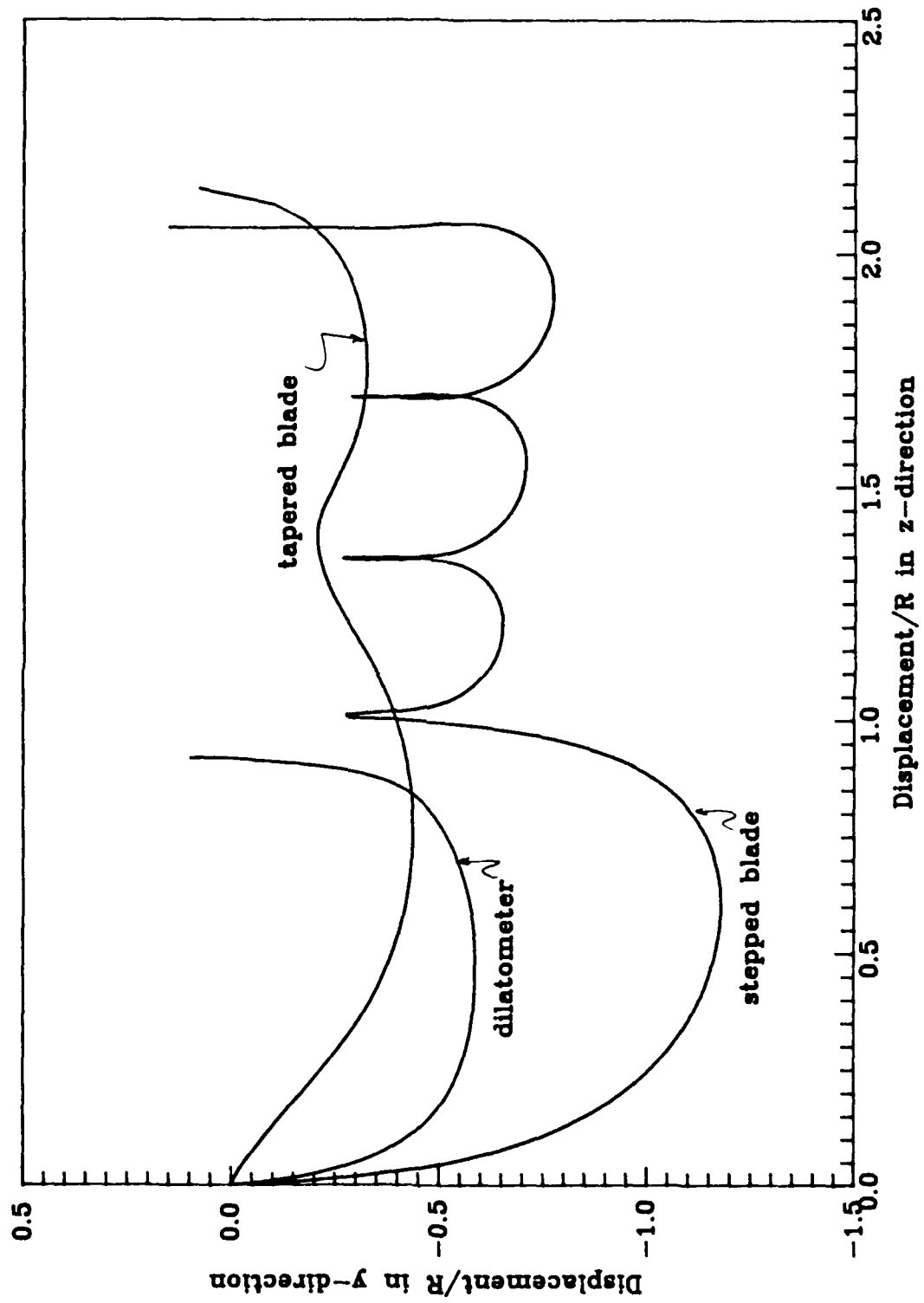
Figure 3.12: Displacements during the stepped and tapered blade penetration.
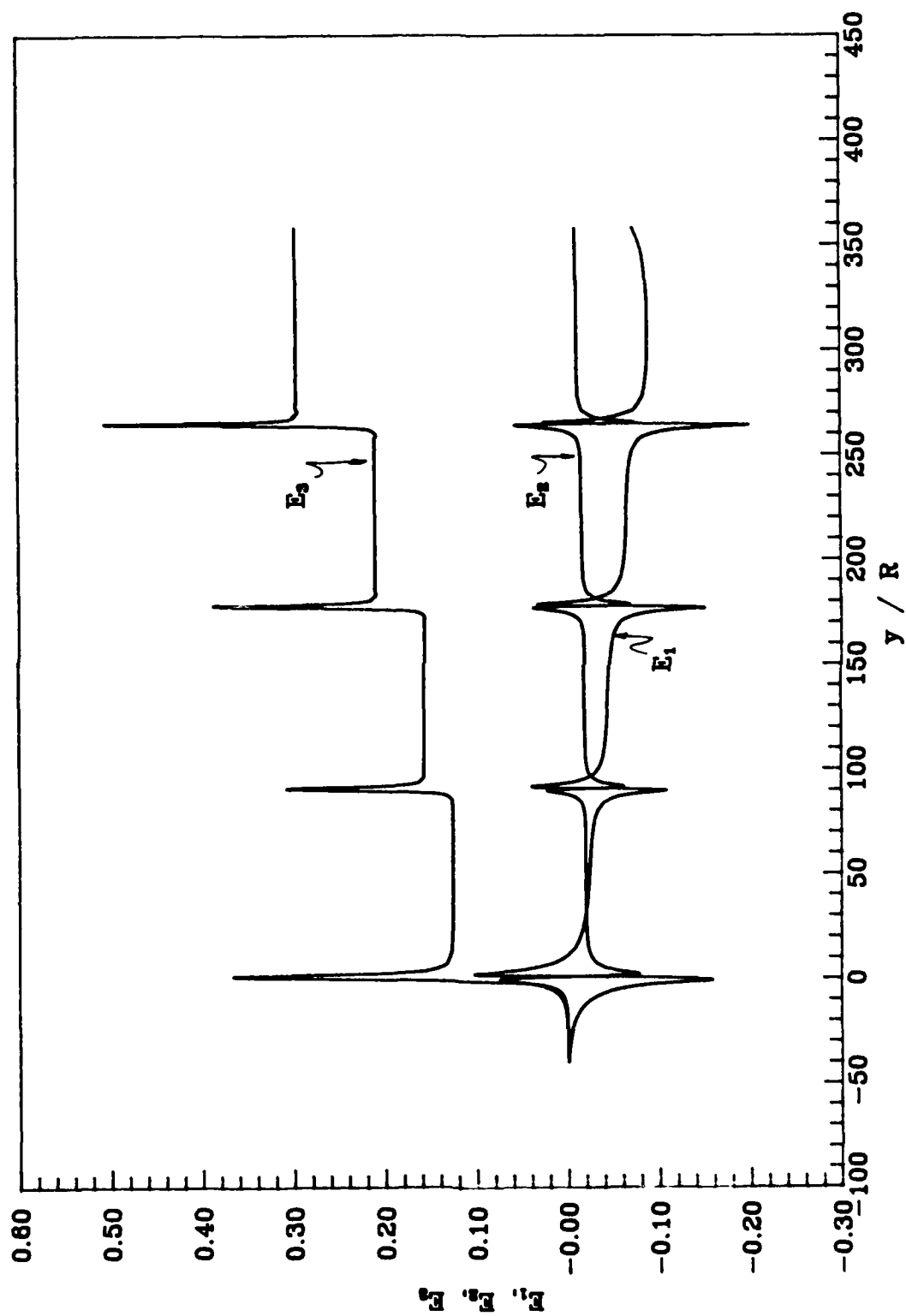
Figure 3.13: Strain components during the stepped blade penetration.

46
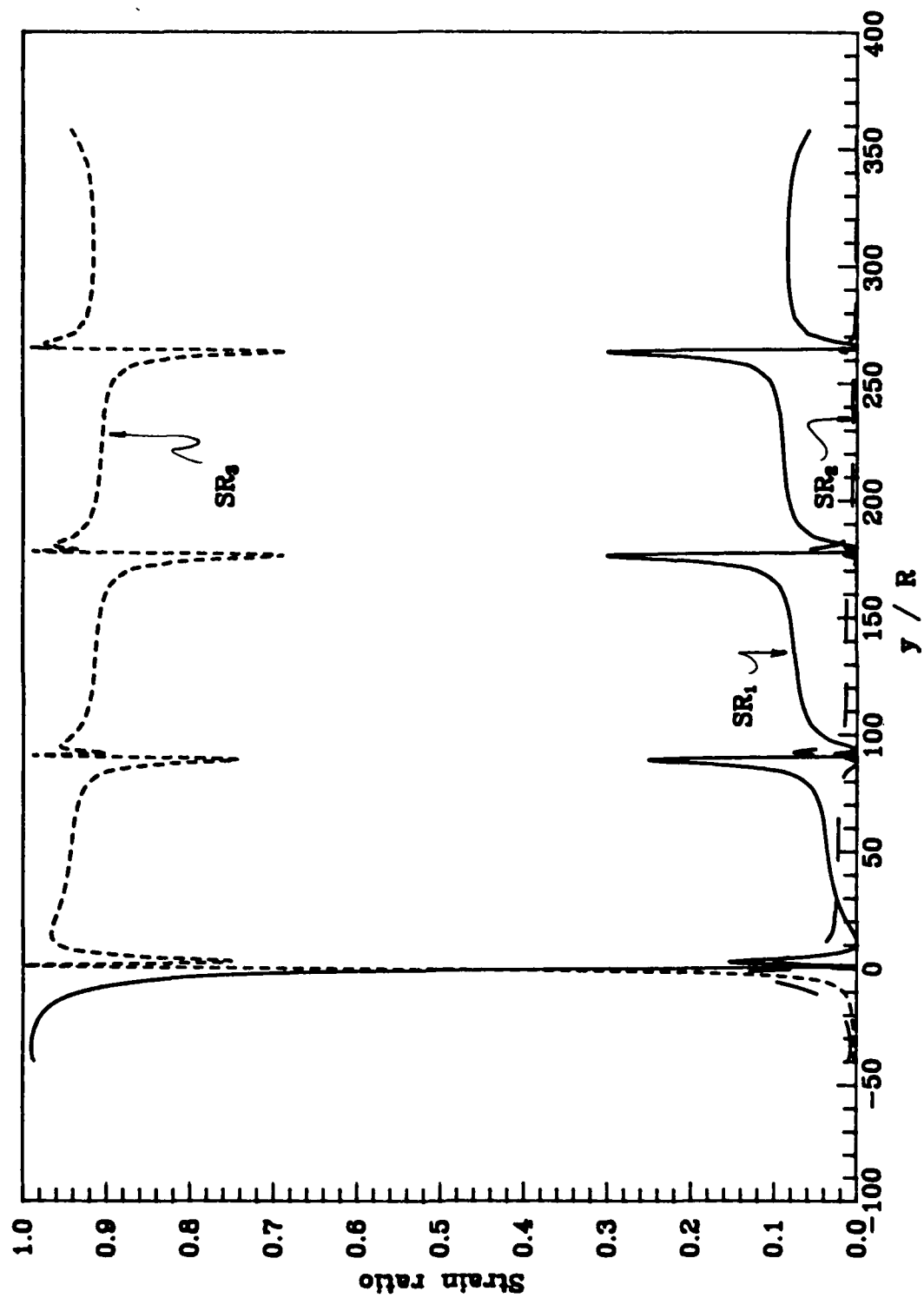
Figure 3.14: Strain ratios during the stepped blade penetration.

47
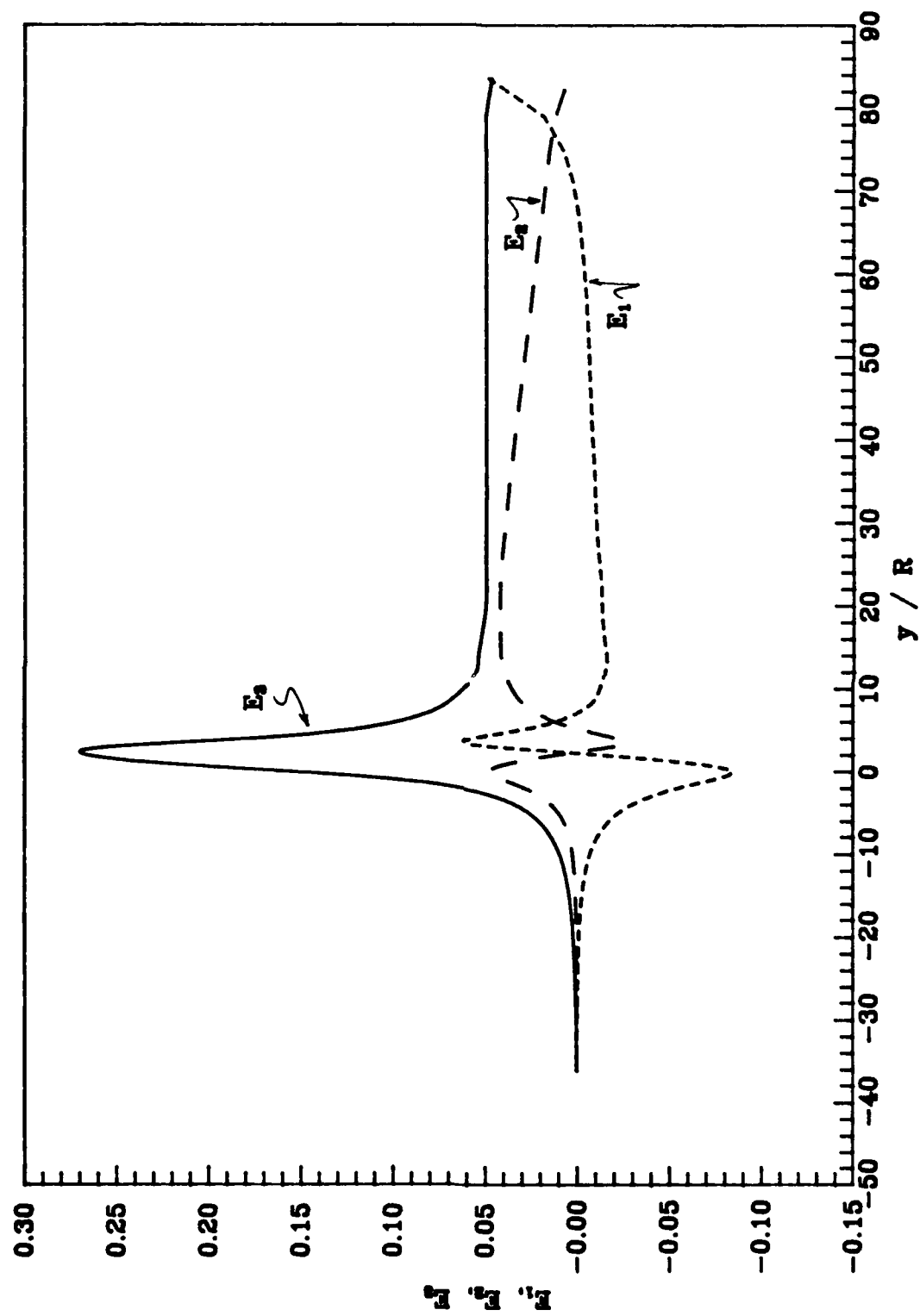
Figure 3.15: Strain components during the tapered blade penetration.
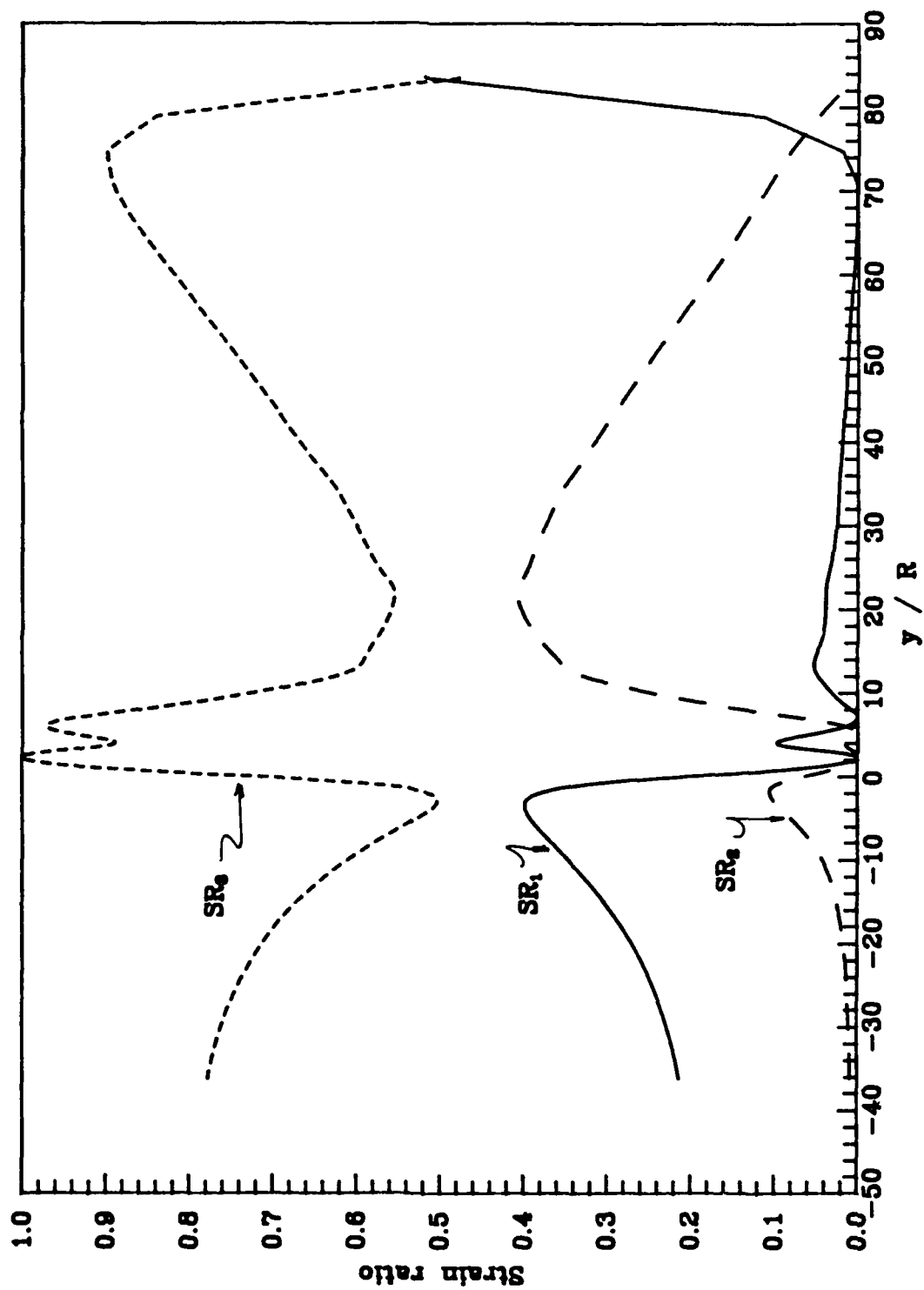
Figure 3.16: Strain ratios during the tapered blade penetration.

49

Chapter 4

Deviatoric Stress Model

The strains are completely decoupled from stresses in the strain path computations. Therefore, the strain path analysis itself does not yield any information about stresses. In an attempt to improve the situation, Baligh (1985) proposed to relate stresses to strains through an inverted stress-strain model. Most of the conventional stress-strain models are so called "stress-space" models where stresses are the independent variables. When inverted, there is no direct mechanism to relate deviatoric strains (volumetric strains $\equiv 0$ during undrained penetration) to normal stresses. Thus, only the deviator stresses, s_{ij} can be estimated as

$$s_{ij} = f(\varepsilon_{ij}) \tag{4.1}$$

Ideally, the soil model used in estimating the stress field should be able to consider a) complicated strain paths including strain reversals and large plastic strains: b) initial and stress induced anisotropy; c) post peak behavior; and d) time dependent deformations (e.g., undrained crep relaxation). Such a comprehe: sive model is not available at the present time. Many existing models can deal with complicated strian paths and anisotropy. Few models, however, fares well in handling post peak behavior and time dependent deformation. A strain based Modefied Cam Clay (MCC) Model was selected to estimate the corresponding stresses from the strains generated in the SPM analyses. This selection was based on the following reasons:

1. MCC is an isotropic model capable of handling the complicated strain paths as demonstrated by Kavvadas(1982). Because of the large strains involved, a sophisticated model is likely to mask out important characteristics predicted by SPM. In addition, the SPM generated strain field should be considered as qualitative because of the way it is computed. It is hardly justifiable to consider issues such as anisotropy and time dependent deformations;

2. MCC model is simple in establishing the input parameters and it has been used extensively;

3. Contrast to cone penetrations, it is not known if shear stress induced pore water pressure is significant in comparison wi h the mean normal stress related pore water pressure. Because MCC is an effective stress model, the shear stress induced pore water pressure is computed directly.

The model was calibrated according to a series of controlled gradient consolidation and consolidated undrained triaxial (CIU) tests. This chapter describes the implementation of the MCC model using strains as the independedent variables following the development by Kavvadas (1982).

4.1   General Concepts of Plasticity

It is common in conventional plasticity to divide the total strain increment, corresponding to an infinitesimal stress increment, into two parts:

1. the reversible portion called the *elastic* strain increment, $\dot{\varepsilon}_{ij}^{e}$, and;

2. the reversible *plastic* strain increment, $\dot{\varepsilon}_{ij}^{p}$

Thus,

$$\dot{\varepsilon}_{ij} = \dot{\varepsilon}_{ij}^{e} + \dot{\varepsilon}_{ij}^{p} \tag{4.2}$$

The conventional definition of deviatoric and volumetric parts of the strain increment are accepted. They can be stated as:

$$\dot{\varepsilon} = \dot{\varepsilon}_{ij} I_{ij} \tag{4.3}$$

51

and,

$$\dot{e}_{ij} = \dot{\varepsilon}_{ij} - \frac{1}{3}\dot{\varepsilon}_{ij}I_{ij} \tag{4.4}$$

where, $\dot{\varepsilon}_{ij}$ and $\dot{e}_{ij}$ are, respectively, the volumetric and deviatoric part of the strain increment. I_{ij} is the second order identity tensor. Such division into volumetric and deviatoric components, can be extended to the elastic and plastic components of both volumetric and deviatoric strain increments separately. Therefore:

$$\dot{\varepsilon}^e = \dot{\varepsilon}_{ij}^e I_{ij}$$
$$\dot{\varepsilon}^p = \dot{\varepsilon}_{ij}^p I_{ij} \tag{4.5}$$

and

$$\dot{e}_{ij}^\epsilon = \dot{\varepsilon}_{ij}^\epsilon - \frac{1}{3}\dot{\varepsilon}_{ij}^\epsilon I_{ij}$$
$$\dot{e}_{ij}^p = \dot{\varepsilon}_{ij}^p - \frac{1}{3}\dot{\varepsilon}_{ij}^p I_{ij} \tag{4.6}$$

Similarly, for the effective stress tensor we can define the *mean effective stress* as:

$$\overline{\sigma} = \frac{1}{3}(\overline{\sigma}_{ij}I_{ij}) \tag{4.7}$$

and *deviatoric stress* tensor as:

$$s_{ij} = \overline{\sigma}_{ij} - \overline{\sigma}I_{ij} \tag{4.8}$$

Increments in mean effective stress and deviatoric stress are expressed as:

$$\dot{\overline{\sigma}} = \frac{1}{3}(\dot{\overline{\sigma}}_{ij}I_{ij})$$
$$\dot{s}_{ij} = \dot{\overline{\sigma}}_{ij} - \dot{\overline{\sigma}}I_{ij} \tag{4.9}$$

4.1.1 Elastic Part of Elastoplastic Deformation

For most loading sequences the elastic part of soil deformation is much smaller than the plastic part. Thus, simple isotropic (linear or nonlinear) models are justified and

are commonly used (e.g., Roscoe and Burland, 1968; Davis and Mullenger, 1978). The following isotropic relationship with two independent parameters is used.

$$\dot{\bar{\sigma}} = K \dot{\varepsilon}^e$$

$$\dot{s}_{ij} = 2G\dot{e}^e_{ij} \tag{4.10}$$

where, K is the elastic bulk modulus and G is the elastic shear modulus.

For normally consolidated clays that not sensitive:

$$K = \frac{1 + e_0}{\kappa}\bar{\sigma} \tag{4.11}$$

where e_0 is the initial void ratio and κ is a material constant and equals the slope of *swelling line* in the Cam-clay model.

The elastic shear modulus G affects the initial stiffness and also the stiffness of the unloading part of the shear stress strain curve. The Modified Cam-Clay model neglects elastic shear strain which means G is infinitely large. Such an assumption is not realistic and leads to numerical problems. Therefore, Kavvadas (1982), proposed that the ratio $\frac{G}{K}$ be a constant. The value of this constant is dictated by elastic Poisson's ratio, $\bar{\nu}$.

$$\frac{2G}{K} = 3\frac{1 - 2\bar{\nu}}{1 + \bar{\nu}} \tag{4.12}$$

Thus K and G are both functions of the current level of $\bar{\sigma}$. This means that the elastic portion of soil deformation is non-linear (and isotropic).

4.1.2 Plastic Part of Elastoplastic Deformation of Soil

The relationship between the plastic part of strain increment and effective stress increment can be stated in a general form as:

$$\dot{\varepsilon}^p_{ij} = \dot{\Lambda}P_{ij} \tag{4.13}$$

where, $\dot{\Lambda}$ is a scalar controlling the the magnitude of strain increment and P_{ij} is a second order tensor that determines the direction of strain increment. Further, P_{ij}

is independent of $\dot{\bar{\sigma}}$. $\dot{\Lambda}$ can be written as a linear combination of the components of effective stress increment.

$$\dot{\Lambda} = \frac{1}{H}(Q_{ij}\dot{\bar{\sigma}}_{ij}) \tag{4.14}$$

where, H is the elastoplastic modulus and Q_{ij} is a second order tensor that determines the magnitude of incremental strain through $\dot{\Lambda}$. The second order tensors P_{ij} and Q_{ij}, like the strain tensor can be divided into their volumetric components (P, Q) and deviatoric components (P'_{ij}, Q'_{ij}).

Equation 4.13 can be expressed separately for volumetric and deviatoric components in the form:

$$\dot{\varepsilon}^p = \dot{\Lambda}P$$
$$\dot{e}^p_{ij} = \dot{\Lambda}P'_{ij} \tag{4.15}$$

combining equations 4.14 and 4.15 we get:

$$\dot{\Lambda} = \frac{1}{H}(Q'_{ij}\dot{s}_{ij} + Q\dot{\bar{\sigma}}) \tag{4.16}$$

Finally equations 4.13 and 4.14 lead to:

$$\dot{\varepsilon}^p_{ij} = \frac{1}{H}(Q_{kl}\sigma_{kl})P_{ij} \tag{4.17}$$

Soil penetration problems such as cone penetration and Dilatometer penetration are, inherently, strain controlled. The strains induced around the penetrometer are a result of kinematic constraints. Thus, the problem is posed inversely: *Given the applied strain increment $\dot{\varepsilon}_{ij}$ it is required to establish the corresponding stress field around the penetrometer.* The stress field comprises of the effective stress increment $\dot{\bar{\sigma}}_{ij}$ or its component $\dot{\bar{\sigma}}$ and $\dot{s}_{ij}$.

Combining equations 4.2 and 4.10 we get:

$$\dot{\bar{\sigma}} = K\dot{\varepsilon}^e = K(\dot{\varepsilon} - \dot{\varepsilon}^p)$$
$$\dot{s}_{ij} = 2G\dot{e}^e_{ij} = 2G(\dot{e}_{ij} - \dot{e}^p_{ij}) \tag{4.18}$$

51

using equations 4.10 and 4.15

$$\dot{\overline{\sigma}} = K(\dot{\varepsilon} - \dot{\Lambda}P)$$

$$\dot{s}_{ij} = 2G(\dot{e}_{ij} - \dot{\Lambda}P'_{ij}) \qquad (4.19)$$

Now, using equations 4.15 and 4.19

$$H\dot{\Lambda} = Q'_{ij}\dot{s}_{ij} + Q_{ij}\dot{\overline{\sigma}} = 2GQ'_{ij}(\dot{e}_{ij} - \dot{\Lambda}P'_{ij}) + KQ(\dot{\varepsilon} - \dot{\Lambda}P) \qquad (4.20)$$

Solving for $\dot{\Lambda}$;

$$\dot{\Lambda} = \frac{2G(Q'_{ij}\dot{e}_{ij}) + KQ\dot{\varepsilon}}{H + 2G(Q'_{ij}P'_{ij}) + KQP} \qquad (4.21)$$

Equation 4.18 gives the increment of mean effective stress and also the deviatoric stress increment in terms of volumetric and deviatoric strain increments. Equation 4.21 is linear in stress and strain increments. $\dot{\Lambda}$ is a linear function of strain increments, therefore if K, G, P, P'_{ij}, Q, Q'_{ij} and H are known the above equation can be implemented in a numerical scheme.

4.2 The Yield Function and Flow Rule

The MCC model assumes an ellipsoidal yield surface, in the effective stress space, symmetric about its hydrostatic axis (Figure 4.1a). The effective stress space is comprised of the deviatoric stress subspace s_{ij} and the mean effective stress $\overline{\sigma}$. The yield function for such a yield surface is written as;

$$f(\overline{\sigma}, \overline{\alpha}, s_{ij}) = s_{ij}s_{ij} - c^2\overline{\sigma}(2\overline{\alpha} - \overline{\sigma})$$

or,

$$\hat{f}(\overline{\sigma}, \overline{\alpha}, s_{ij}) = r^2 - c^2\overline{\sigma}(2\overline{\alpha} - \overline{\sigma}) \qquad (4.22)$$

where,

- $r = (s_{ij}s_{ij})^{\frac{1}{2}} = \sqrt{2}J_2$

55

(a)

$\underset{\sim}{s}$
(or, $r \equiv \{\underset{\sim}{s} : \underset{\sim}{s}\}^{1/2}$)

critical state line

L

undrained effective stress path

F

R

current stress state

current yield surface

$c\bar{a}$

O

$\bar{\sigma}$

A

E

$\bar{a}$

$\bar{a}$

F'

(b)

void ratio

virgin isotropic consolidation curve

critical state line

isotropic
rebound curve

F

R

E

e

L

A

$\bar{\sigma}$

$\bar{\sigma}$

$\bar{\sigma}_e$

$\bar{\sigma}_o$
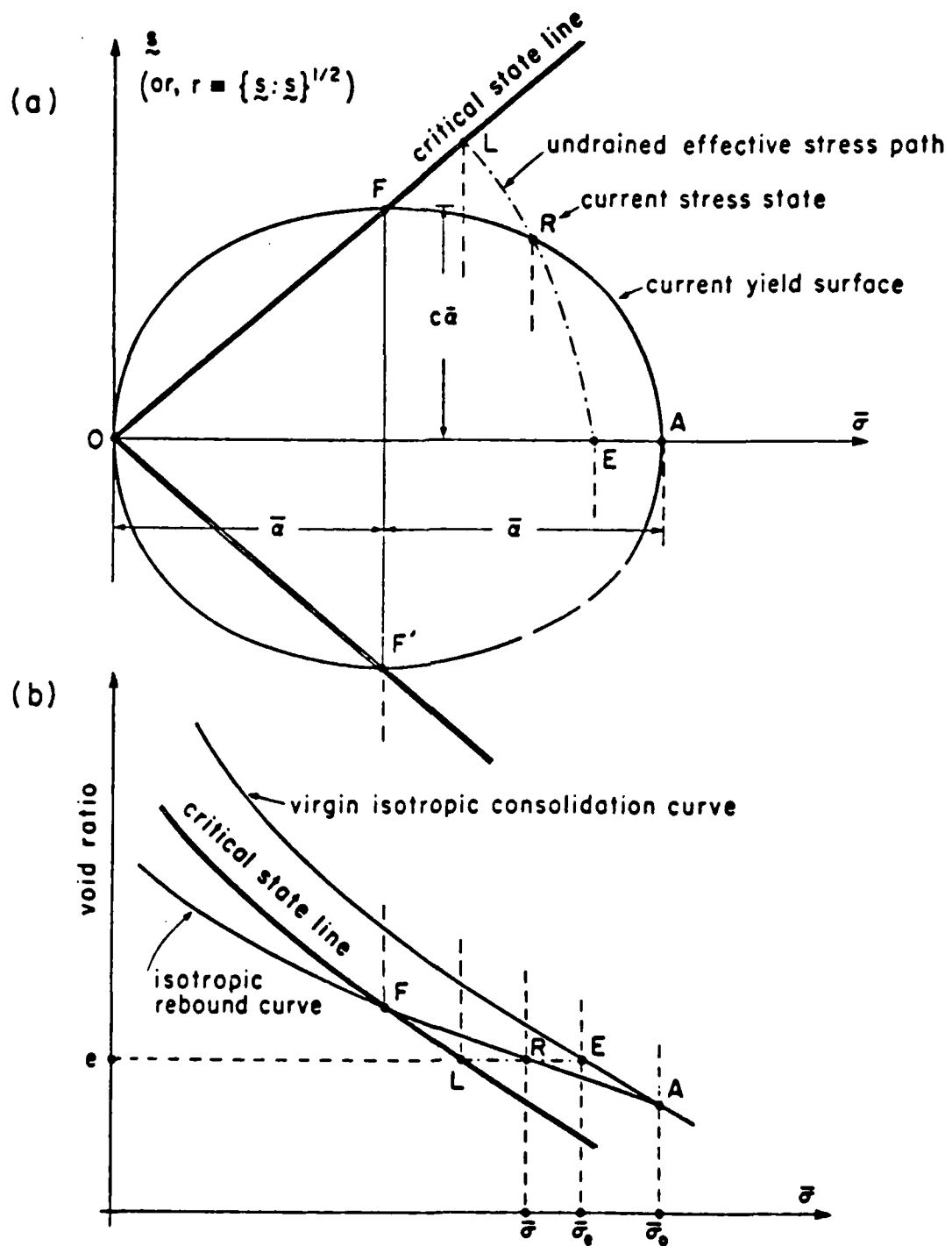
Figure 4.1: Yield surface of MCC model in $s_{ij} - \bar{\sigma}$ space.

56

- J_2 is the second invariant of deviatoric stress tensor

- c is the material constant and is equal to the ratio of the axes of the yield surface

$$c = \sqrt{\frac{2}{3}} M$$

- $M = q/p$ and, $q = (\sigma_I - \sigma_{II})$, $p = \overline{\sigma}$ at critical state.

- $\overline{\alpha}$ is a state variable called the *hardening parameter*. It controls the size of the yield surface. Changes of $\overline{\alpha}$ during deformation allow the strength to increase with consolidation.

4.2.1 Plastic Loading and Elastic Unloading from Elastoplastic States

The flat-plate penetration mechanism involves complex deformation in the soil element under consideration. Certain stress components decrease while other stress components increase, therefore the definitions of *loading* and *unloading* have to be unambiguous. The MCC model satates that:

the application of an infinitesimal effective stress increment represents <u>plastic</u> *loading if both plastic and elastic strains occur, and represents* <u>elastic</u> *unloading if only elastic strains occur.*

Therefore starting from a stress state on the yield surface i.e. normally consolidated state, elastic unloading implies a retreat of the stress point from the yield surface causing zero plastic strain. Whereas, plastic loading implies an effective stress increment directed outside the yield surface thus leading to a new elastoplastic state. A smooth transition between the elastic unloading and plastic loading at the boundary is effected, in MCC model, by the limiting case assumption that; an effective stress increment at a tangent to the yield surface causes no plastic strains. This requirement is satisfied if the second order tensor Q_{ij} is defined as the gradient of the yield surface at the stress point representing the current state of stress.

$$Q_{ij} = \frac{\partial f}{\partial \overline{\sigma}_{ij}} \qquad (4.23)$$

Decomposing Q_{ij} into its volumetric and deviatoric parts we get:

$$Q = \frac{\partial f}{\partial \overline{\sigma}} \qquad (4.24)$$

$$Q'_{ij} = \frac{\partial f}{\partial s_{ij}} - \frac{1}{3}(\frac{\partial f}{\partial s_{kl}} I_{kl}) I_{ij} \qquad (4.25)$$

Having defined Q_{ij} as the gradient of the yield surface at the stress point representing the current state of stress, the MCC model proposes a quantitative relation to distinguish between the plastic loading and elastic unloading from elastoplastic states. For the case of elastic unloading the plastic strain increment is defined to be zero and the stress point retreats from the yield surface. Since Q_{ij} is directed towards the outer normal to the yield surface it follows that for elastic loading:

$$Q_{ij}\dot{\overline{\sigma}}_{ij} < 0 \qquad (4.26)$$

using the decomposition of the effective stress increment and Q_{ij} into its volumetric and deviatoric parts we can show that:

$$Q'_{ij}\dot{s}_{ij} + Q\dot{\overline{\sigma}} < 0 \qquad (4.27)$$

Using equations 4.10 and 4.27 the following criterion for elastic unloading is obtained:

$$2G(Q'_{ij}\dot{e}_{ij}) + KQ\dot{\varepsilon} < 0 \qquad (4.28)$$

and the conjugate criterion for plastic loading:

$$2G(Q'_{ij}\dot{e}_{ij}) + KQ\dot{\varepsilon} \geq 0 \qquad (4.29)$$

Having defined the plastic loading and elastic unloading criteria the components of Q_{ij} can be specified further using equations 4.23, 4.24 and 4.25 for the specific yield function of the MCC model:

$$Q = 2c^2(\overline{\sigma} - \overline{\alpha}) \qquad (4.30)$$

$$Q'_{ij} = 2s_{ij} \qquad (4.31)$$

Furthermore the model employs an associated flow rule, so that:

$$P = Q$$

$$P'_{ij} = Q'_{ij} \qquad (4.32)$$

This means that the direction of the plastic strain increment (given by P_{ij}) coincides with the normal to the yield surface (given by Q_{ij}).

4.3 Hardening Characteristics

In general, the hardening characteristics of a model describe the evolution of model parameters specifying the shape, size and orientation of the yield surface during plastic deformation. The MCC model utilized herein adopts an isotropic hardening rule and $\overline{\alpha}$ is the only parameter describing the yield surface of the MCC model. The hardening rule determines the evolution of $\overline{\alpha}$ during plastic deformation of soil. This allows the yield surface to expand in the stress space without changing its shape.

The MCC model assumes that for one-dimensional consolidation or isotropic consolidation of normally consolidated clay the stress path gives a linear relationship between the void ratio e and the natural logarithm of mean effective stress $\overline{\sigma}$, with slope λ:

$$\lambda = -\frac{de}{d(ln\overline{\sigma})} \qquad (4.33)$$

A stress path for the above mentioned one-dimensional consolidation or isotropic consolidation of normally consolidated clay is also called *radial stress path*. The MCC model assumes that for plastic loading along a radial stress path (in effective stress space) the hardening parameter $\overline{\alpha}$ is proportional to to the mean effective stress $\overline{\sigma}$ and thus,

$$de^p = de - de^e = -\lambda.d(ln\overline{\sigma}) + \kappa d(ln\overline{\sigma})$$

$$de^p = -(\lambda - \kappa)d(ln\overline{\sigma}) = -(\lambda - \kappa)d(ln\overline{\alpha}) \qquad (4.34)$$

59

or:

$$\dot{e}^p = -(\lambda - \kappa)\frac{\dot{\overline{\alpha}}}{\overline{\alpha}} \tag{4.35}$$

where, $\dot{e}^p$ is the plastic increment of void ratio and $\dot{\overline{\alpha}}$ is the increment of the size parameter $\overline{\alpha}$. However, from the definition of void ratio:

$$\dot{e}^p = -(1 + e_0)\dot{\varepsilon}^p \tag{4.36}$$

where, e_0 is the initial void ratio and $\dot{\varepsilon}^p$ is the volumetric component of the plastic strain increment. Combining equations 4.35 and 4.36 we get:

$$\dot{\overline{\alpha}} = \frac{1 + e_0}{\lambda - \kappa}\overline{\alpha}\dot{\varepsilon}^p \tag{4.37}$$

or, combining equation 4.15 with the above result we get:

$$\dot{\overline{\alpha}} = \frac{1 + e_0}{\lambda - \kappa}\overline{\alpha}\dot{\Lambda}P \tag{4.38}$$

4.4   The Elastoplastic Modulus H

During plastic loading the stress point remains on the yield surface. Thus the effective stress increment $\dot{\overline{\sigma}}_{ij}$ and the change in the size of the yield surface must, continuously, satisfy the condition $f = 0$. This is the well known Prager's Consistency condition which specifies that:

$$\dot{f}(\overline{\alpha}, \overline{\sigma}_{ij}) = 0 \tag{4.39}$$

using the chain rule

$$Q_{ij}\dot{\overline{\sigma}}_{ij} + \frac{\partial f}{\partial \overline{\alpha}}\dot{\overline{\alpha}} = 0 \tag{4.40}$$

using equations 4.15, 4.37, 4.38 and solving for H

$$H = \frac{1 + e_0}{\lambda - \kappa}.(-\frac{\partial f}{\partial \overline{\alpha}}).\overline{\alpha}P \tag{4.41}$$

using the definition of the yield surface we can obtain:

$$\frac{\partial f}{\partial \overline{\alpha}} = -2c^2\overline{\sigma} \tag{4.42}$$

and using equation 4.30 and associated flow rule:

$$P = 2c^2(\overline{\sigma} - \overline{\alpha}) \tag{4.43}$$

60

4.5 Effective Stress Path for Undrained Deformation of Clay

Figure 4.1a is a geometrical representation of the ellipsoidal yield surface in the effective stress space $(s_{ij}, \overline{\sigma})$. The point R on the yield surface represents an elastoplastic state of stress. Figure 4.1B represents the same yield surface in the $e - \overline{\sigma}$ space, e being the void ratio. The model assumes, that, for a given elastoplastic stress state the point A at the tip of the yield surface (Figure 4.1a) is represented by the intersection of the virgin isotropic consolidation curve and the isotropic rebound curve (Figure 4.1b). It is evident from Figure 4.1a that:

$$\overline{\sigma}_0 = 2\overline{\alpha} \tag{4.44}$$

where $\overline{\sigma}$ is the value of effective stress at the tip of the yield surface.

Let us define η as the ratio of r to the mean effective stress $\overline{\sigma}$:

$$\eta = \frac{r}{\overline{\sigma}} \tag{4.45}$$

The equation of the yield surface (EQ. 3.22) can be expressed as:

$$\frac{\overline{\sigma}}{\overline{\sigma}_0} = \frac{c^2}{c^2 + \eta^2} \tag{4.46}$$

This is identical to the equation of the yield surface given by Roscoe & Burland (1968), i.e. it describes an *ellipsoid*.

Undrained deformation is given by a straight line parallel to the $\overline{\sigma}$ axis in the $e - \overline{\sigma}$ space. Furthermore, assuming that the virgin isotropic consolidation curve and the critical state curve are straight lines in the $e - \overline{\sigma}$ space, with slopes λ and κ respectively, we have:

$$\lambda ln(\frac{\overline{\sigma}_e}{\overline{\sigma}_0}) = \kappa ln(\frac{\overline{\sigma}}{\overline{\sigma}_0}) \tag{4.47}$$

or:

$$\frac{\overline{\sigma}}{\overline{\sigma}_e} = \frac{\overline{\sigma}}{\overline{\sigma}_0}^{1-\frac{\kappa}{\lambda}} \tag{4.48}$$

61

combining equations 3.34 and 3.35 we get:

$$\frac{\overline{\sigma}}{\overline{\sigma}_e} = \left(\frac{c^2}{c^2 + \eta^2}\right)^{1-\frac{\kappa}{\lambda}} \tag{4.49}$$

where, $\overline{\sigma}_e$ and $\overline{\sigma}_0$ are the mean effective stresses associated with points E and A respectively in Figure 4.1A and 4.1B. The above equation gives the effective stress path during undrained shear of clay with a void ratio e associated wit a specific value of the mean effective stress, $\overline{\sigma}_e$.

4.6 Implementation of the MCC Model

The MCC model was used to study a variety of flat-plate penetrometers and their two dimensional approximations. Table 4.1 summarizes the relations needed to employ the MCC Model. The model was implemented in the following sequence:

1. Examine the value of a pre-defined 'flag' to check whether the current state of stress of the soil element is *elastic* or *elastoplastic*. If the state is elastic go to (5), else continue;

2. Equations 4.28 and 4.29 is the criterion used to distinguish between plastic loading and elastic unloading. If the strain increment causes elastic unloading go to (5), else continue;

3. Compute P_{ij}, H, $\dot{\Lambda}$. Use the elastoplastic stress strain increment relation 4.18 to calculate the effective stress increment corresponding to the applied strain increment;

4. The effective stress state is updated. Then, the hardening rules are employed to update the remaining state variables are updated. Exit the algorithm;

5. This step in reached if the state of the soil element is elastic or if elastic unloading takes place. The elastic incremental stress-strain relations are used in order

Incremental stress-strain relations for the MCC model	
$\kappa = 0.434C_s$, $\lambda = 0.434C_c$	$c = \sqrt{2/3}M$ $K = \frac{1+e_0}{\kappa}$
$\dot{\varepsilon} = \dot{\varepsilon}_{ij}I_{ij}$	$\dot{e}_{ij} = \dot{\varepsilon}_{ij} - \frac{1}{3}\dot{\varepsilon}Iij$
$Q = P = 2c^2(\overline{\sigma} - \overline{\alpha})$	$Q'_{ij} = P'_{ij} = 2s_{ij}$
$H = 2c^2\overline{\sigma}\overline{\alpha}(\frac{1+e_0}{\lambda - \kappa})P$	
$\Lambda = \frac{2G(Q_{ij}\dot{e}_{ij})+KQ\dot{\varepsilon}}{H+2G(Q'_{ij}P'_{ij})+KQP}$	
$\dot{\overline{\sigma}} = K(\dot{\varepsilon} - \Lambda P)$	$\dot{s}_{ij} = 2G(\dot{\varepsilon}_{ij} - \Lambda P'_{ij})$
$\dot{\overline{\alpha}} = (\frac{1+e_0}{\lambda - \kappa})\overline{\alpha}\Lambda P$	
$\overline{\sigma} = \overline{\sigma} + \dot{\overline{\sigma}}$ $s_{ij} = s_{ij} + \dot{s}_{ij}$	$\overline{\alpha} = \overline{\alpha} + \dot{\overline{\alpha}}$

Table 4.1: Incremental stress-strain relations for MCC model

63

to compute the effective stress increment correspⁱⁿ⁾ding to the applied strain increment;

6. The new effective stress state $\overline{\sigma}_{ij}$ is then examined to see if it is still inside the yield surface or on the yield surface, or if it has crossed the yield surface. The ᶜʳst two cases require the appropriate setting of the 'flag' variable. However, if the stress state has crossed the yield surface then it means that the strain increment is too large and the following step must be followed;

7. The point of intersection is then calculated and the fraction of the strain increment responsible for this stress state is computed;

8. The stress state is then updated using the point of intersection of the with the yield surface as the new stress state. The remaining strain increment is then evaluated subtracting the strain increment required to reach yield surface from the applied strain increment. The flag is appropriately set and algorithm control is transferred to (3).

4.7 Input Parameters

4.7.1 Soil Properties

The soil used for modelling the flat plate-penetration using the MCC model is 50-50 blend of kaolinite and Edgar sand. Figure 4.2 presents the grain size distribution of both soils. It is apparent from the distribution that the soil borders between clay and silt. The results of Atterberg Limit tests (performed separately on Kaolinite and sand and also on their mixture yielded the following results:

A series of controlled gradient consolidation (CGC) tests and isotropically consolidated triaxial (CIU) tests were performed to provide the input parameters for MCC model. In the CGC tests, a small pore pressure difference was maintained between the two end of the specimen by varying the axial load. The soil sample was satuɪated under a 413kPa back pressure. An excessive 20.68kPa pore presure difference was

Gravel	Coarse to Medium Sand	Fine Sand	Silt	Clay
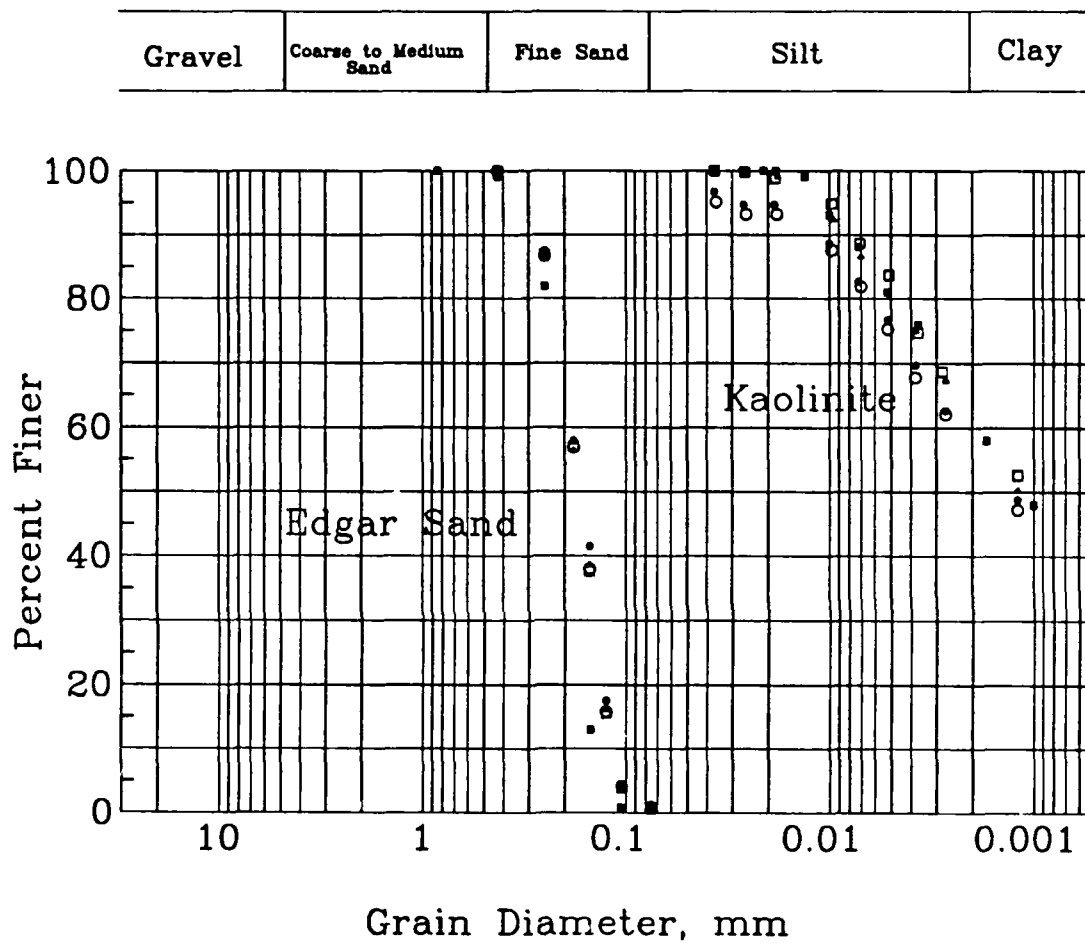
Figure 4.2: Grain size distribution curves

Soil	liquid limit L.L.	plastic limit P.L.	plasticity index P.I.	specific gravity G_s
Kaolinite	51.5 - 56.0	25.2 - 30.0	23.4 - 26.3	2.62 - 2.68
Kaolinite and Sand (blend)	29.2 - 30.9	16.3 - 16.8	12.5 - 14.1	-
Sand	-	-	-	2.63-2.71

Table 4.2: Properties of kaolinite and Edgar sand

maintained at the lower face of the specimen.

The CIU triaxial tests were perfomed on soil specimens normally consolidated under confining stresses of 218 kPa, 360 kPa and 505 kPa. The specimens were saturated under a back pressure of 414 kPa. Details of the test procedures and results of the consolidation and triaxial tests !x !xare presented in the Chapter on "Reference Soil Properties".

4.7.2   MCC Model Parameters

The MCC model requires two consolidation parameters, namely λ and κ that are related to the conventional parameters C_c and C_s as:

$$\kappa = 0.434 C_s \tag{4.50}$$

$$\lambda = 0.434 C_c \tag{4.51}$$

The model also uses a strength parameter, M, the shear elastic modulus, G, and the initial void ratio e_0.

The strength parameter, M, was evaluated from the stress path obtained from an undrained triaxial test, Figure 4.3. The slope of the tangent to this curve, starting

Input parameters for the Modified Cam-Clay model		
PARAMETER	USED FOR	HOW TO OBTAIN
M or c $(M = 0.93)$ $(c = 0.759)$	Shape of Yield Surface	M equals the common tangent to the stress paths of undrained triaxial tests with different preconsolidation stresses $c = \sqrt{2/3}M$
C_c or λ $(\lambda = 0.13)$ $(C_c = .299)$	Changes of the size of the Yield Surface	From the virgin isotropic consolidation curve $\lambda = (0.434).C_c = de/d(ln\overline{\sigma})$
C_s or κ $(\kappa = 0.026)$ $(C_s = 0.0599)$	Changes of the size of the Yield Surface	From the isotropic rebound curve: $\kappa = (0.434).C_s = de/d(ln\overline{\sigma})$
G $(= 130Kpa)$	Elastic Shear Modulus	From the small strain region of shear stress-strain curve of undrained triaxial test
$e_0(= 0.6889)$	Initial void ratio	Laboratory Measurement

Table 4.3: Input parameters for the MCC model

from the origin is equal to M.

The consolidation parameters, λ and κ were obtained from a series of controlled gradient consolidation tests. Results of these tests will be presented in Chapter 7. The slope of the virgin compression curve equals λ and the average slope of the unload-reload curve equals κ.

The Elastic shear modulus was obtained from the shear stress-strain curve Figure 4.4. G equals the slope of this curve in the small strain region. The parameters used in the MCC model and their values, as obtained from laboratory tests are presented in table 4.3. The calibrated model was used to generate the shear stress-strain curve of a undrained triaxial(CIU) test on the soil (Figure 4.4). The MCC Model overestimates the peak shear stress $(\sigma_1' - \sigma_3')$ by 16%. This discrepancy is not entirely unexpected since the test soil consists of 50% sand whereas the MCC Model is more suitable for soils with higher clay content. Sand was used for speeding up the drainage during consolidation of a soil sample in the calibration chamber. Thus, using the model parameters described above, the effective stress increment $\dot{\overline{\sigma}}_{ij}$ (or its components $\dot{\overline{\sigma}}$ and $\dot{s}_{ij}$) caused by a given strain increment $\dot{\varepsilon}_{ij}$ can be evaluated.
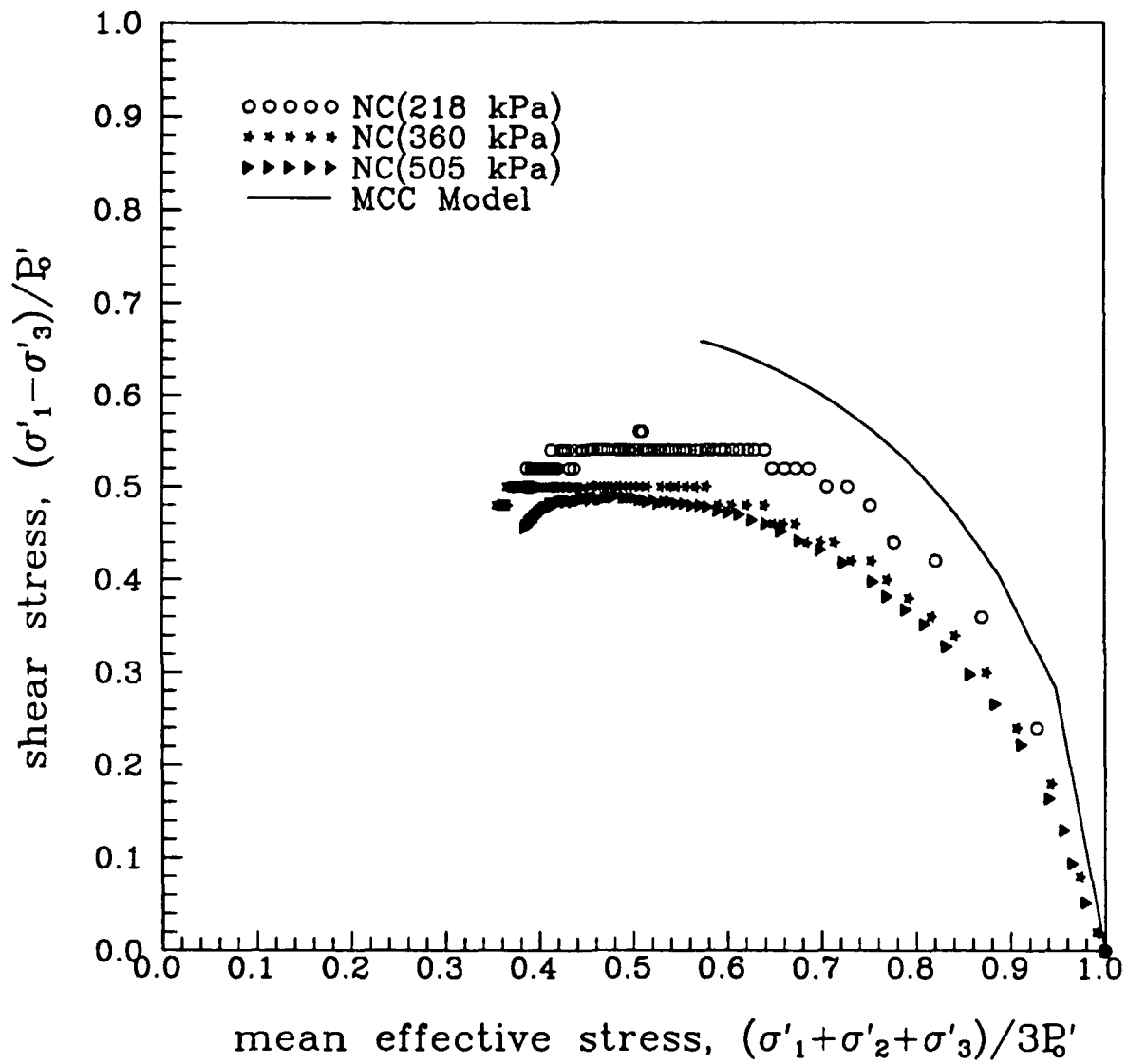
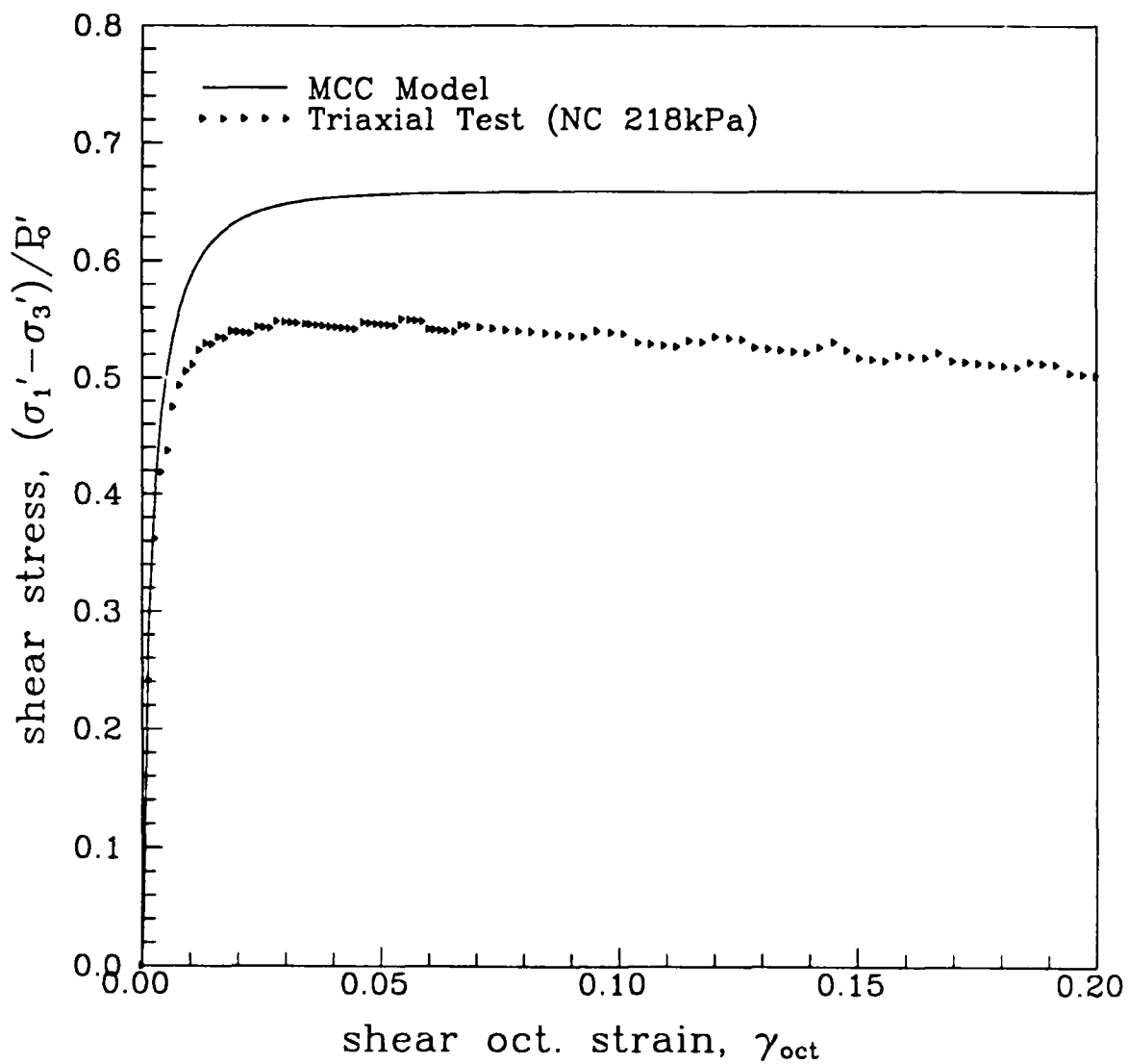Figure 4.3: Stress paths for MCC model and triaxial tests.

Figure 4.4: Shear stress versus shear strain for MCC model and triaxial test.

Chapter 5

Deviatoric Stress Field

The strain path along a streamline forms the input to the MCC model. Computations resulted in the corresponding change of deviatoric stress (s_{ij}) and mean effective stress ($\bar{\sigma}$). In demonstrating the stress field, the same reference radius R described in Chapter 2 is used to denote the relative position of the soil element. R is defined as half the minimum dimension of the penetrometer. The following R values were used for different penetrometers:

$R_{DMT} = 7mm$

$R_{CONE} = 17.8mm$

$R_{Stepped\,Blade} = 1.15mm$

$R_{Tapered\,Blade} = 3.3mm$

The same coordinate system chown in Figure 3.2 is used to ptresent the results.

5.0.1 S_i Stress Space

In three dimensional problems, a stress state is described by six independent components. Since the flat-plate penetration deformation is posed as an undrained shearing problem, the sum of normal stress components vanishes ($\sigma_{ii} = 0$). The soil deformation mechanism can not be simulated by any one simple soil test. It is, however, possible to view the soil deformation as a combination of shearing modes in Triaxial Compression test (TC), Direct Simple Shear (DSS) and Pressuremeter Test (PMT)

71

(Prevost, 1978). To relate the soil deformation mechanism to the above mentioned soil tests an S_i subspace similar to the one suggested by Kavvadas (1982) is adopted. The components of 5-dimensional S_i stress space are related to components of deviatoric stress tensor as follows:

$$
\begin{aligned}
S_1 &= (2s_{yy} - s_{xx} - s_{zz})/\sqrt{6} \\
S_2 &= (s_{zz} - s_{xx})/\sqrt{2} \\
S_3 &= s_{yz}/\sqrt{2} \\
S_4 &= s_{xy}/\sqrt{2} \\
S_5 &= s_{zx}/\sqrt{2}
\end{aligned}
\tag{5.1}
$$

S_1 denotes the, shearing mode in triaxial compression, S_2 signifies the cylindrical cavity expansion mode (the cavity being infinitely long in the x direction) and S_3 implies the shearing mode in direct simple shear. S_4 and S_5 are similar to the S_3 but in the xy and zx directions respectively.

5.0.2 Stress Distribution

The stress distributions due to different steady penetrating penetrometes were analyzed and will be presented in the following text in terms of:

1. *stress profiles:* plots showing stress components versus y/R;

2. *stress paths:* plots of S_i versus S_j, $i \neq j$;

3. *stress contours:* plots showing distribution of different stress components in a plane.

5.1 Axisymmetric versus Three-dimensional Penetration

To evaluate the effect of geometry on strain rates, shear strain rate ($\dot{\gamma}_{oct}$) profiles corresponding to $z/R = 1$ were compared for the cone and DMT (Figures 5.1 and

72

5.2). In the case of the DMT, profiles were plotted for x/R values of 0, 4, 5 and 6. The x/R value of 6 corresponds to approximately the corner of the DMT.

For both penetrometers strain rates are very high (maximum strain rate $\approx 20\%$ /sec.) in the tip region ($0R - 5.67R$). However there is no further similarity between the cone and the DMT. Shear strain rate shows a positive peak at the base of cone tip ($y/R = 5.67$), whereas $\dot{\gamma}_{oct}$ profiles for the DMT are characterized by a positive peak at the tip ($y/R = 0$) and a negative peak at the base. Such a reduction in strain rates to the extent of forming a negative peak is unique to flat plate geometry. It is caused presumably due to the presence of a limited blade thickness which allows strain dissipation or relaxation at the corners of the blade. The influence of DMT corners resulting in strain rate relaxation around the edges will hereafter be referred to as the *end effect*. Shear strain rates for streamlines further from the center of the blade show less reduction in the tip region. Such a compensation in strain rate occurs because soil deformation in x direction, on account of the end effect, is more significant towards the sides of the blade (Figure 5.1).

The ensuing text deals with differences in the stress fields due to axisymmetric and flat plate penetration. The axisymmetric character of the cone makes it sufficient to present stress in any one vertical plane passing through its vertical axis. However there is no such representative plane for the DMT. Therefore the stresses due to DMT penetration were examined in three xz planes and one yz plane.

1. $y/R = 0$: horizontal plane at the tip;

2. $y/R = 5.67$: horizontal plane at the base of the tip;

3. $y/R = 13$: horizontal plane at the center of the DMT membrane;

4. $x/R = 0$: vertical plane through the center of the DMT.

In the MCC approach the DMT and cone penetration mechanism are both associated with symmetric deviatoric stress tensors with four *significant* components, namely;

73

s_{xx}, s_{yy}, s_{zz} and s_{yz}. Figure 5.3 shows the location of the data labels (relative to the penetrometer) used in marking stress path plots for the cone and DMT.

In addition to the deviatoric stress components, shear octahedral stress (τ_{oct}) and mean effective stress $\bar{\sigma}$ were also used to study the stress field due to both penetrometers. Plots are presented to compare stress fields around a cone and a DMT. The apex angle for both penetrometers being 20°, the tapered region or the tip extends from $0R - 5.67R$. Stress components of both the S_i space and the deviatoric stress tensor were plotted in the tip region of the cone and the DMT (Figures 5.4, 5.5, 5.6 and 5.7). The following observations were made:

- s_{xx}, the least significant of the stress components for DMT, is the predominant tensile stress component for the cone i.e. it reaches the maximum magnitude in tension. The smaller dimension of the DMT allows relaxation of s_{xx} at the corners.

- s_{yy} for both penetrometers is in compression just before the tip. s_{yy} of DMT undergoes a complete unload-reload cycle in the tip region. s_{yy} of cone shows similar cyclic characteristics but the reloading is only partial. The vertical stress components s_{yy} is pronounced for both penetrometers but picks up magnitude earlier for DMT.

- s_{zz} shows an loading-unloading cycle for both penetrometers but unloading is partial for the cone.

- s_{yz} of cone and s_{yz} of DMT are comparable in both magnitude and direction.

The above stress characteristics can also be observed and explained using the S_i components in terms of stress states typical to conventional laboratory tests. S_1, representing the triaxial state of stress follows the same trend as s_{yy} for both penetrometers. The pressuremeter mode of stress represented by S_2 is more prominent for the cone than the DMT (Figure 5.6). The S_2 versus S_3 plot shows that the part of the curve representing the tip region is almost flat for the DMT. S_3, which is essentially similar to s_{yz} does not show marked differences between the cone and the DMT.

5.2 Effects of Flat Plate Geometry

s_{zz} and τ_{oct} contours for DMT penetration (Figures 5.10 and 5.11) show that towards the end of the blade (in x direction), a sharp stress relaxation occurs. This phenomena is obviously not accounted for by plane strain approximation (i.e. $w/t = \infty$). Such a redistribution of stress around corners is expected for all flat plates and is due to the end effect. The extent and influence of end effect and its dependence on shape geometry of the penetrometer was examined. Analyses were carried out for the following variations:

1. Different w/t ratios, where w is the width and t is the thickness of the flat plate. In all cases t was equal to 14mm and the angle of taper was 20° which are the same as DMT. These flat plates will be referred to as the simple flat plates herein after;

2. Other flat-penetrometers, namely a) Tapered Blade and b) Stepped Blade.

To illustrate the effect of lateral distance (z/R) on a stress element, stress paths are plotted for elements at $1R$ and $5R$. A comparison of stress paths for these two elements shows that points further away experience a smaller range of stress states. Figures 5.12 shows that differences between a three dimensional simple flat plate and its two-dimensional (plane strain or $w/t = \infty$) approximation can be reduced by increasing w/t ratio. $w/t = 20$ was found to have stress paths very similar to two-dimensional stress paths. Increasing the w/t ratio makes the center relatively closer to the side of the blade thereby increasing the influence of end effect on the stress path. Stress paths for lower w/t ratios compare closer with those caused by cone penetration as opposed to the plane strain approximation.

To further demonstrate the three-dimensional nature of the flat plate penetration, stress paths and stress profiles of three different penetrometers (DMT, Tapered Blade and Stepped Blade) were plotted (Figures 5.14 - 5.21). The stress paths for tapered blade are essentially similar to those for the DMT because of the inherent similarity in shape. Stress paths and stress profiles for stepped blade show a cyclic character

because of the loading-unloading of stresses caused by steps. The penetration mechanism of the stepped blade can be thought of as a continuous penetration of a series of flat plates (of the DMT geometry) with decreasing w/t ratios. The Tapered Blade, according to design by Handy and Lutenegger (1985) has a range of w/t ratios from 13.33 at the tip to 7.33 at the end. The Stepped Blade (Handy et al., 1992), has four steps with w/t ratios of 10.8, 7.14, 5.4 and 4.31 respectively. Both Stepped Blade and Tapered Blade have high initial w/t ratios which explains the similarity between the initial parts of 2D and three dimensional stress paths.
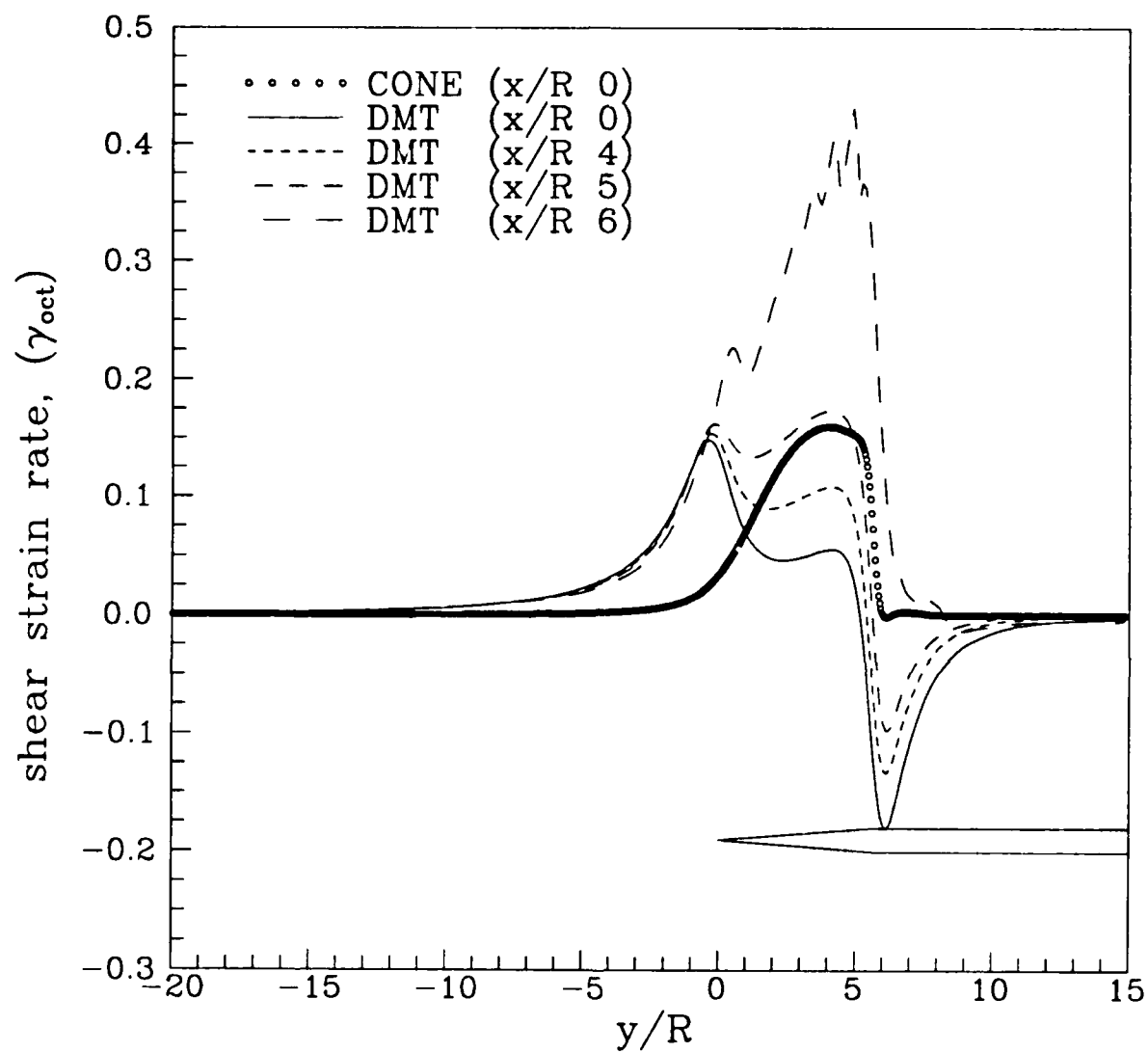
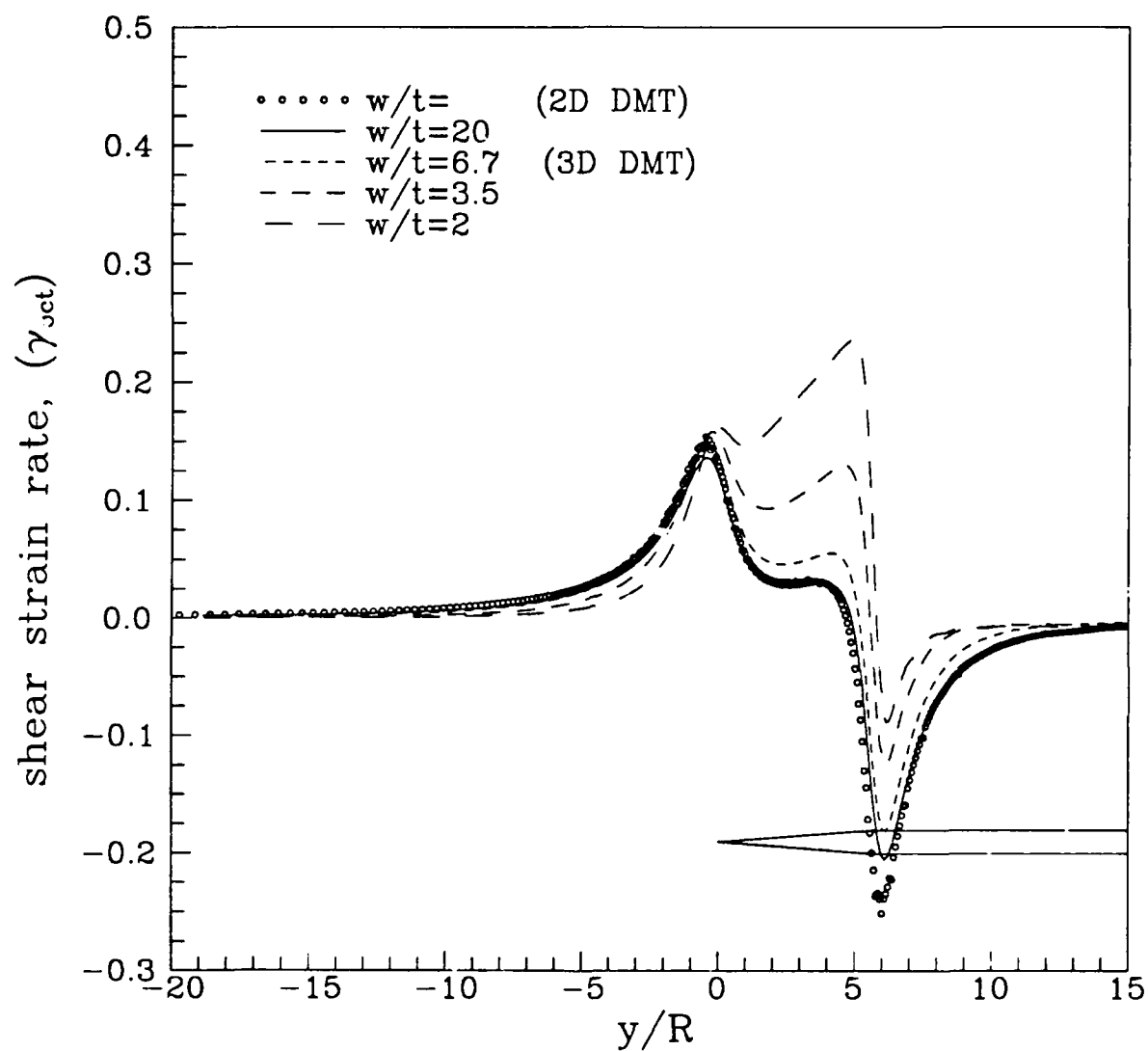Figure 5.1: Shear strain rate ($\dot{\gamma}_{oct}$/sec) profiles for cone and DMT.

77

Figure 5.2: Shear strain rate ($\dot{\gamma}_{oct}$/sec) profiles for DMT with different w/t ratios.
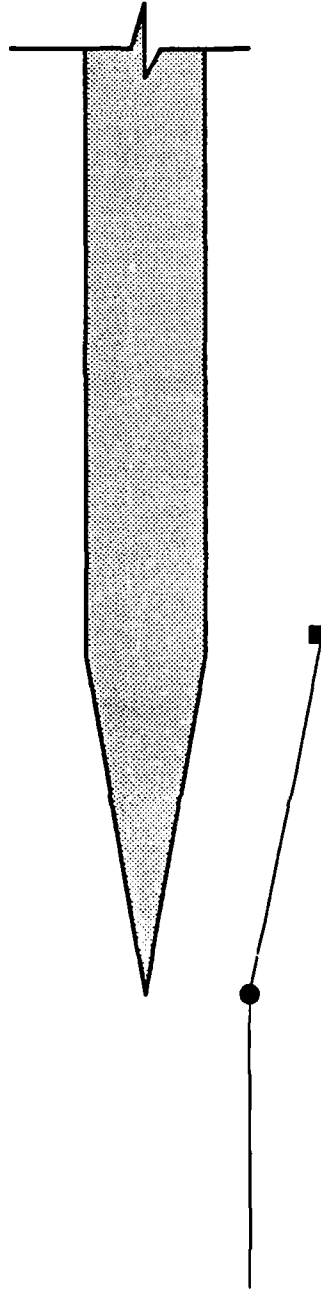
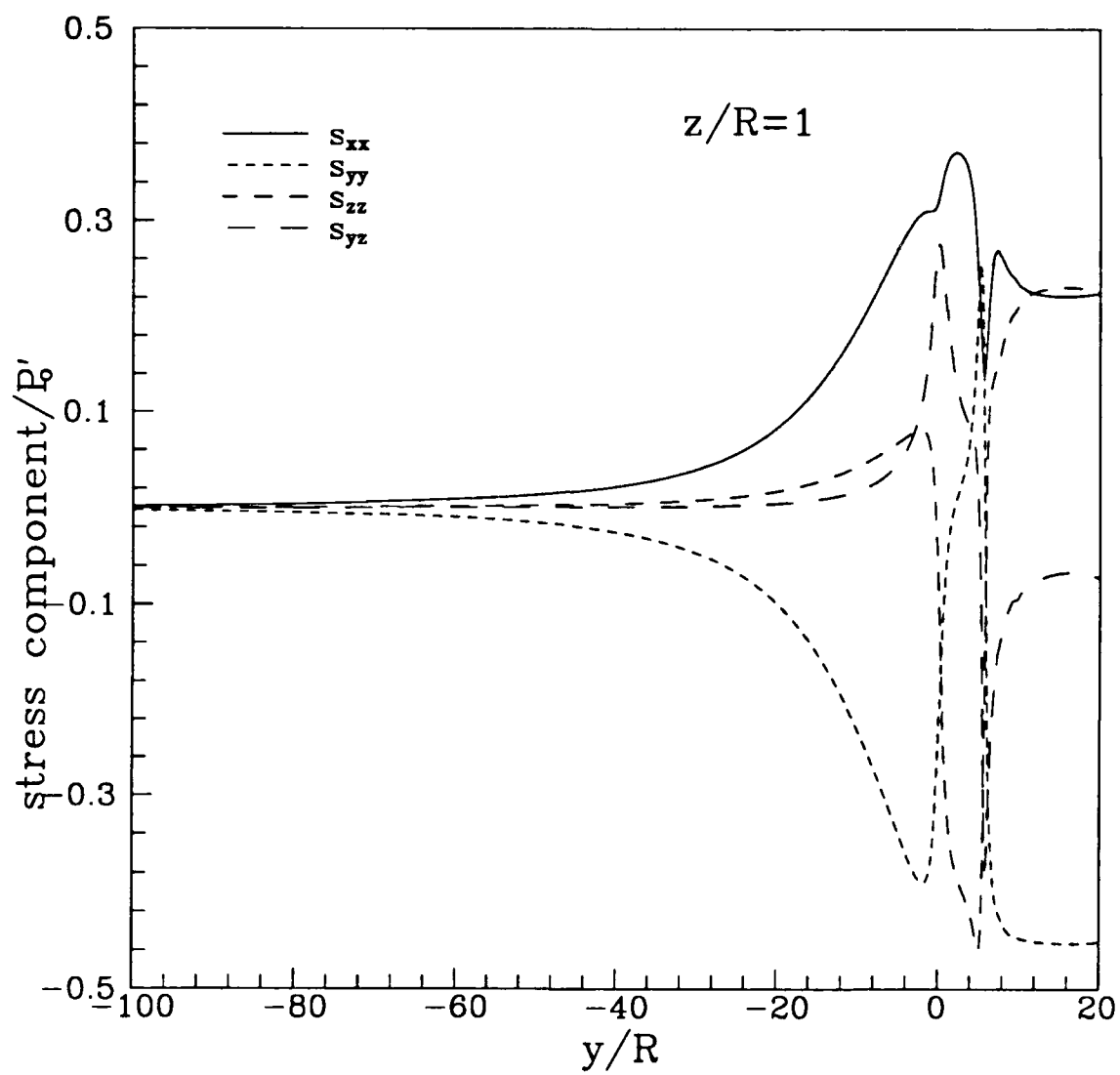Figure 5.3: y/R locations for data labels indicated in stress paths for cone and DMT.

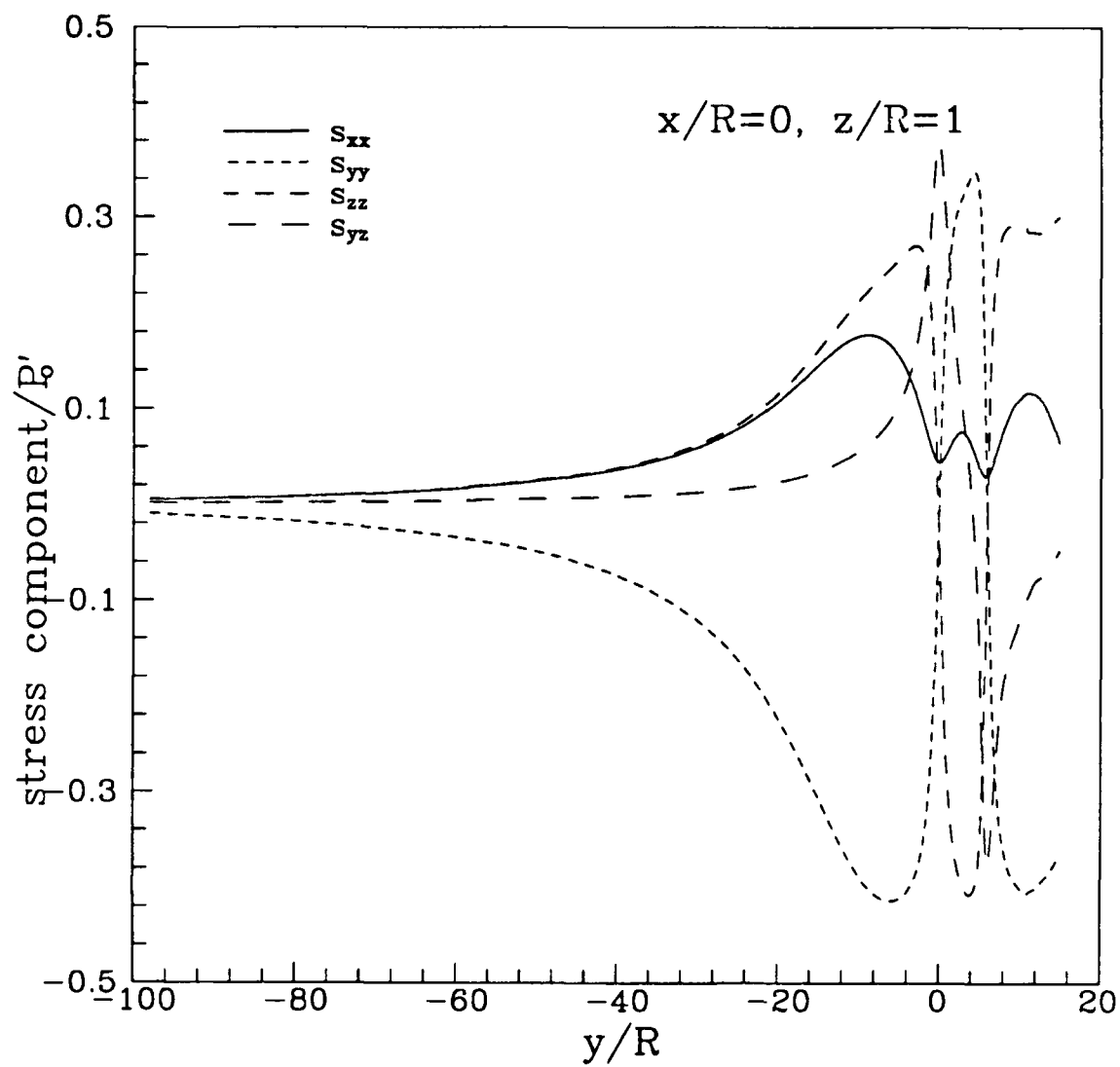Figure 5.4: Profiles of normalized stress components for cone penetration.
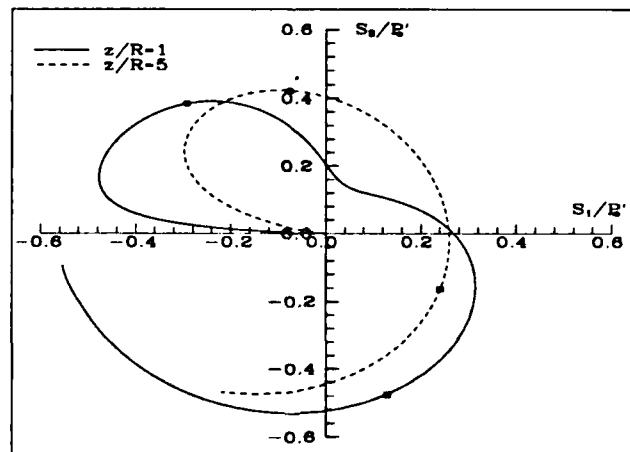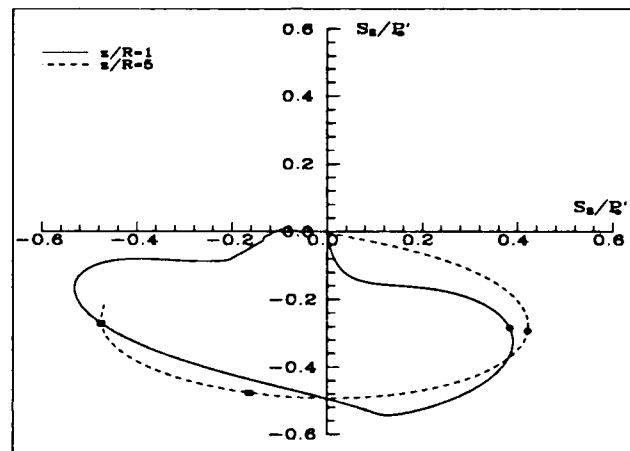
Figure 5.5: Profiles of normalized stress components for DMT penetration.
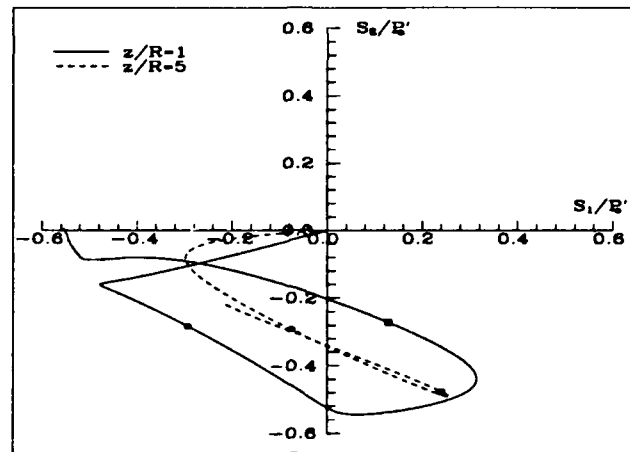
Figure 5.6: Normalized stress paths for 20° cone.
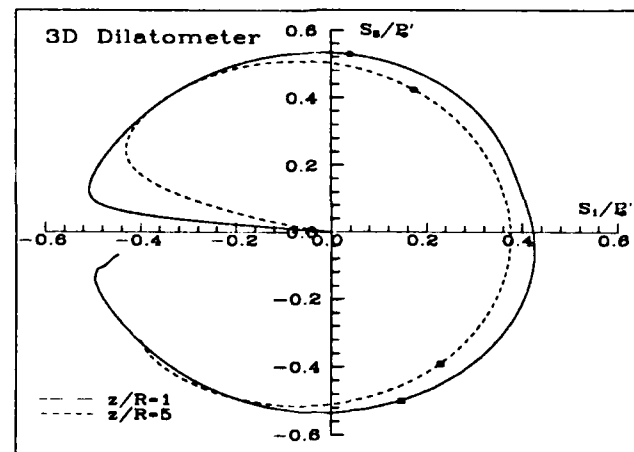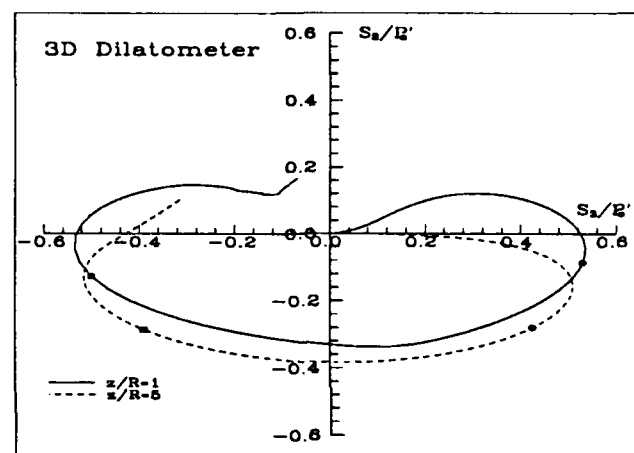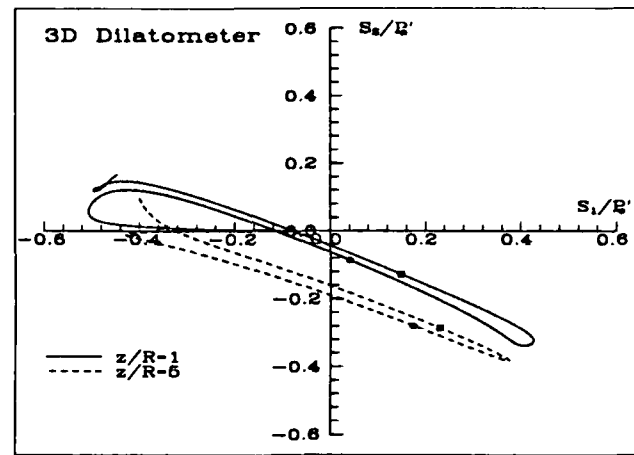
Figure 5.7: Normalized stress paths for DMT.
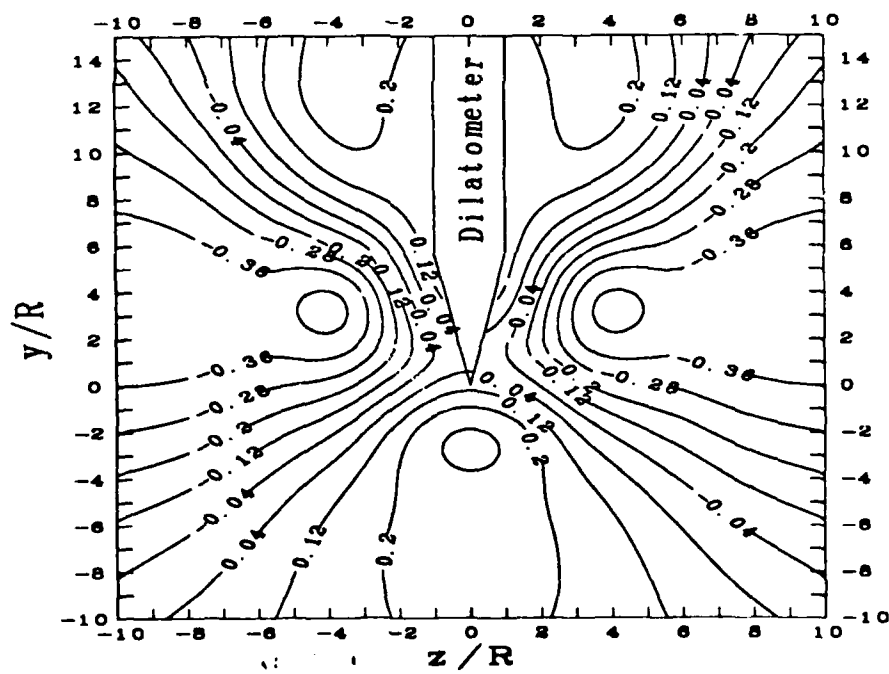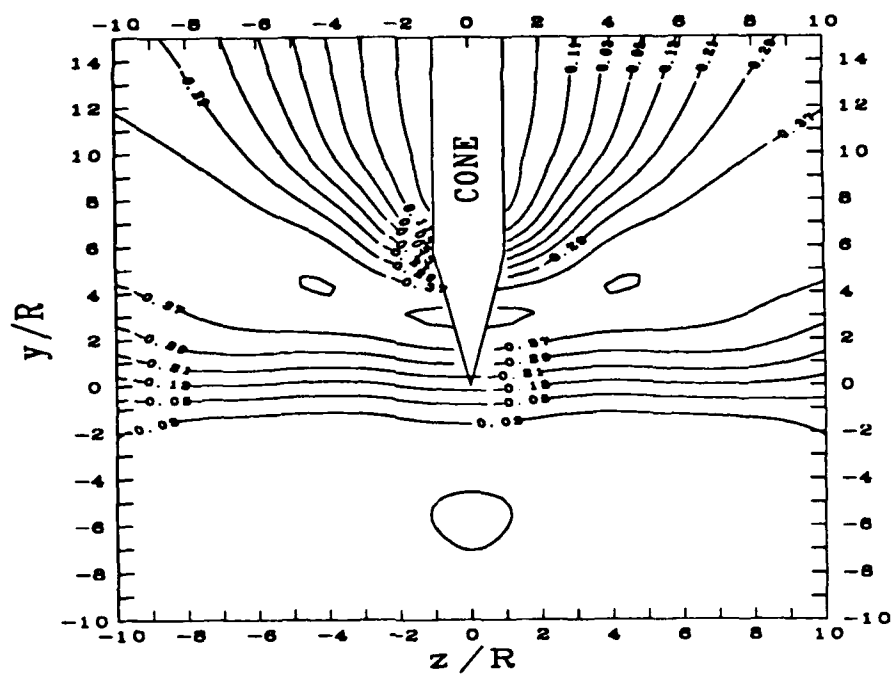
Figure 5.8: s_{zz} contours for cone and DMT.

Figure 5.9: τ_{oct} contours for cone and DMT.
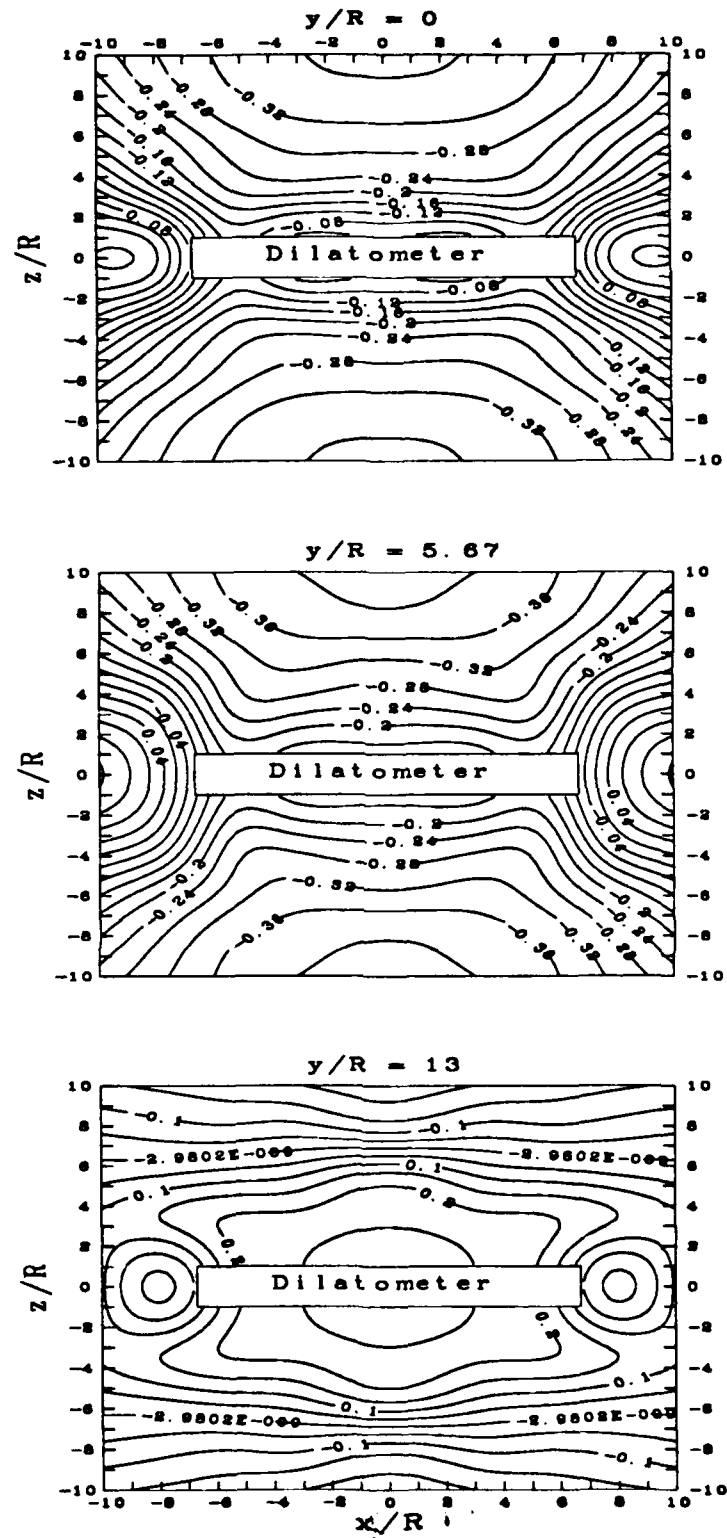
Figure 5.10: s_{zz} contours for DMT in different horizontal planes.
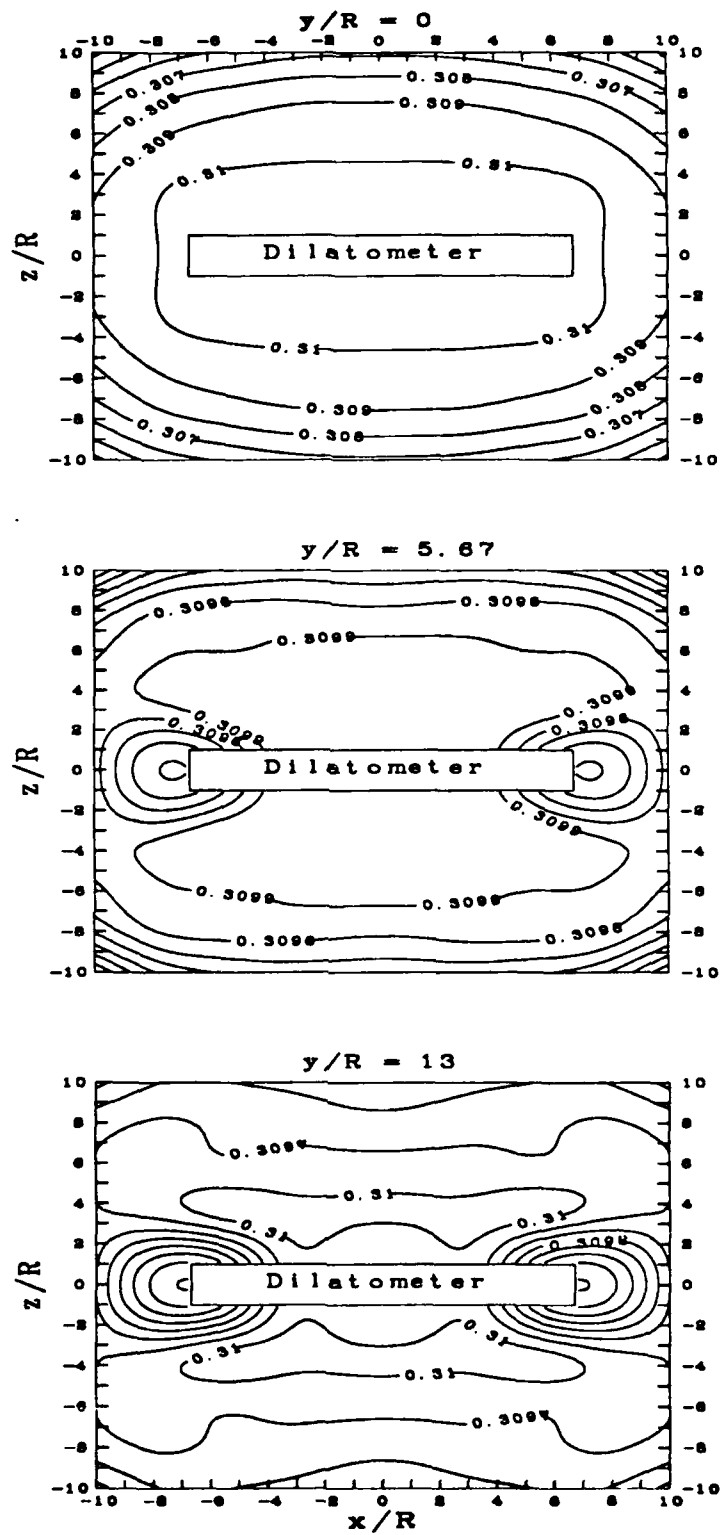
Figure 5.11: τ_{oct} contours for DMT in different horizontal planes.

87
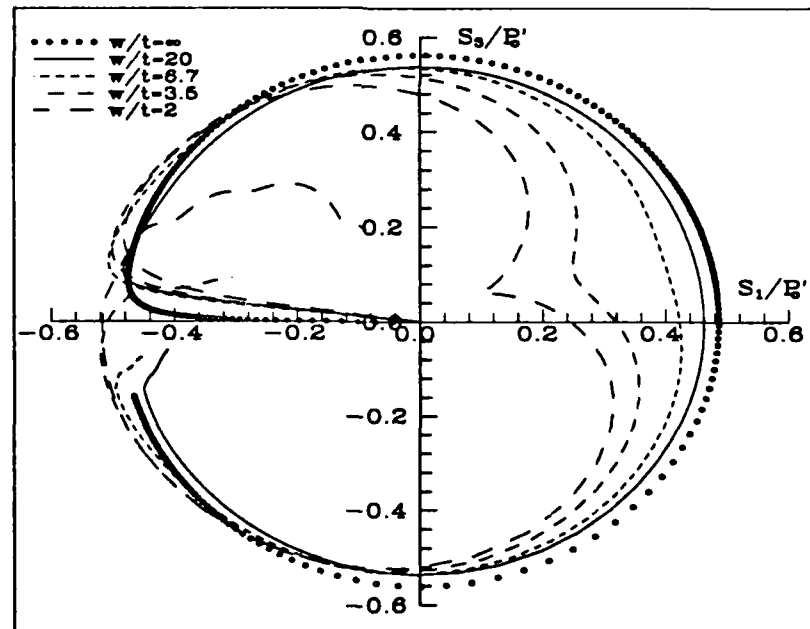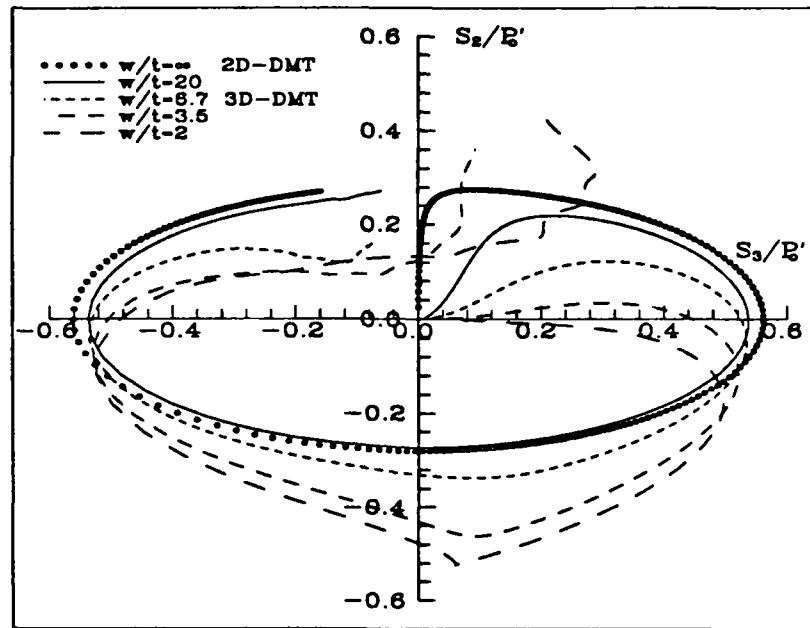
Figure 5.12: Stress paths showing effect of w/t ratio.
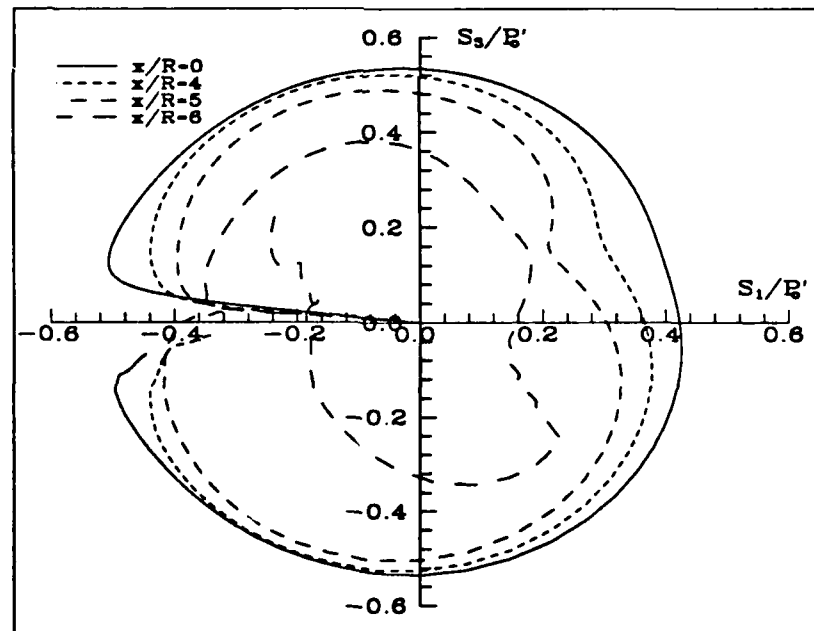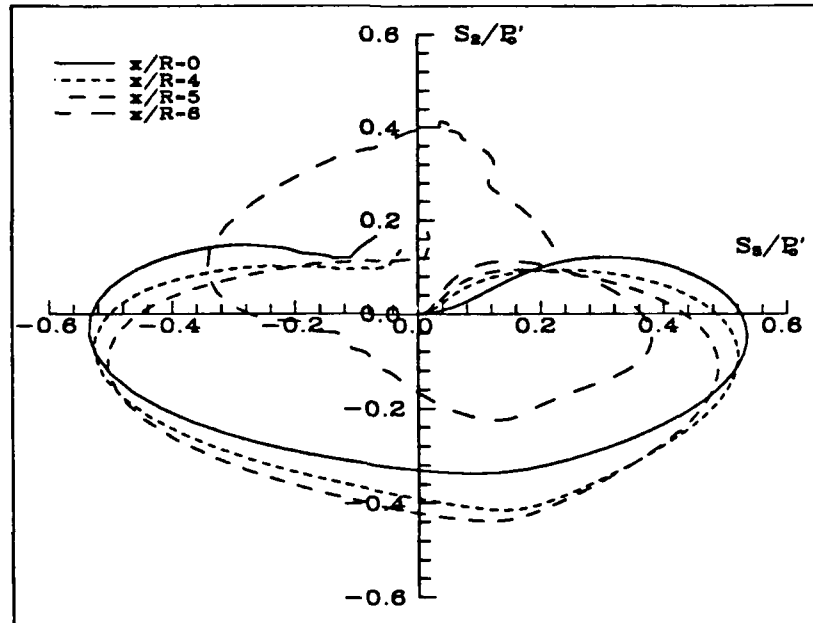
Figure 5.13: Stress paths for different x/R values.
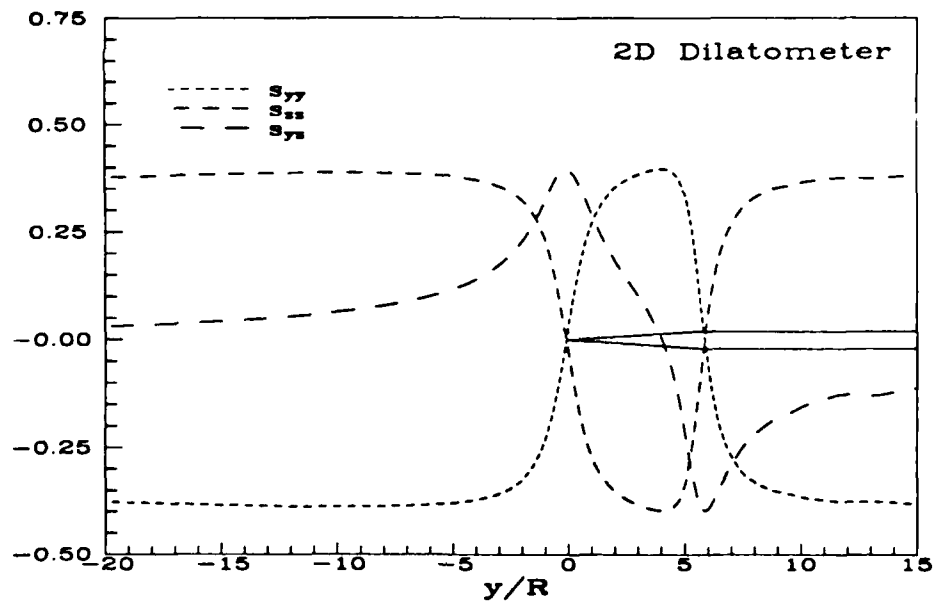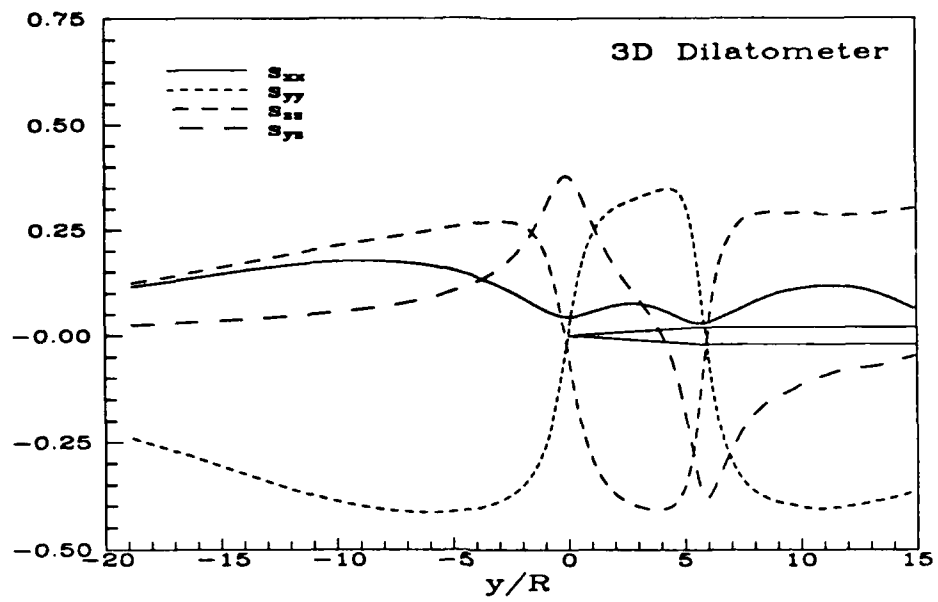
Figure 5.14: Stress profiles during a DMT penetration.

90
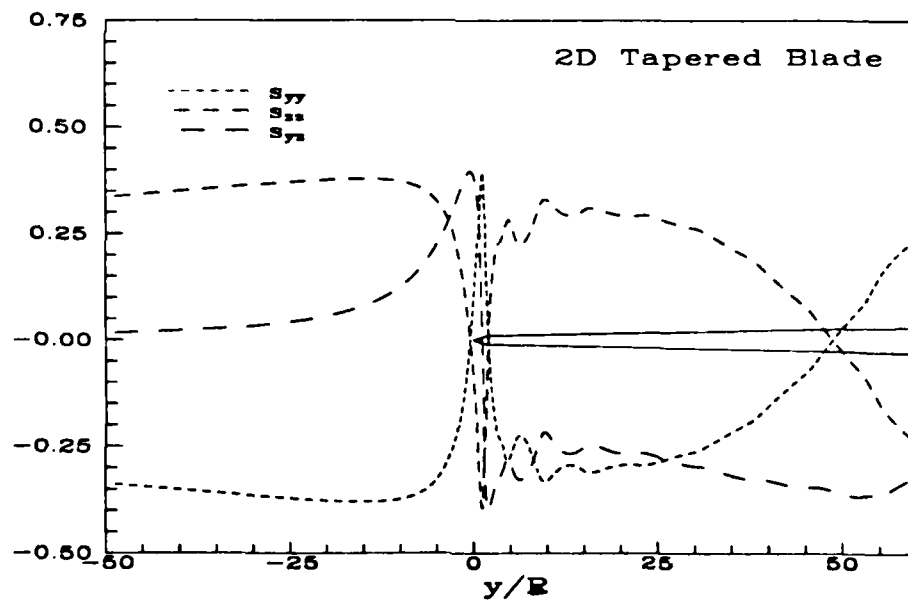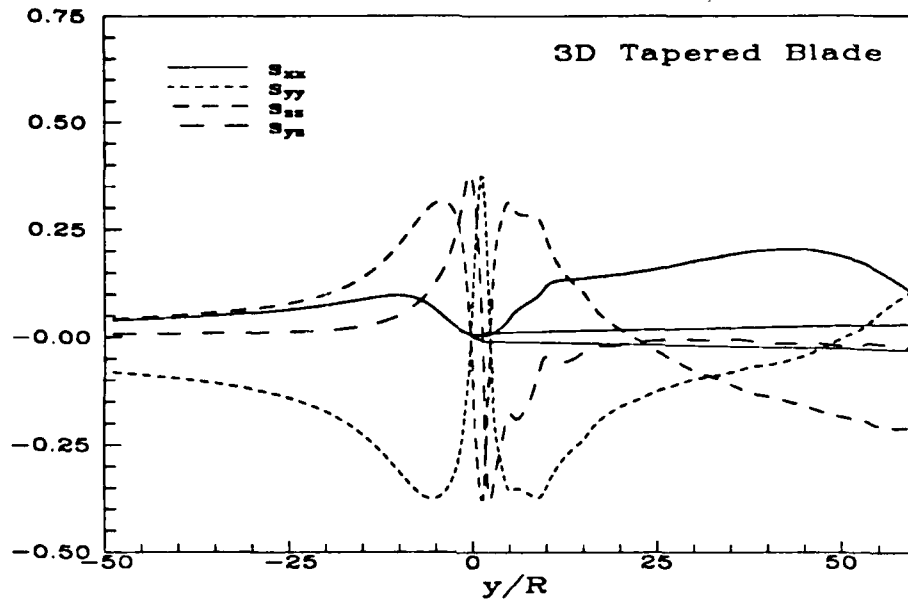
Figure 5.15: Stress profiles during a tapered blade penetration.
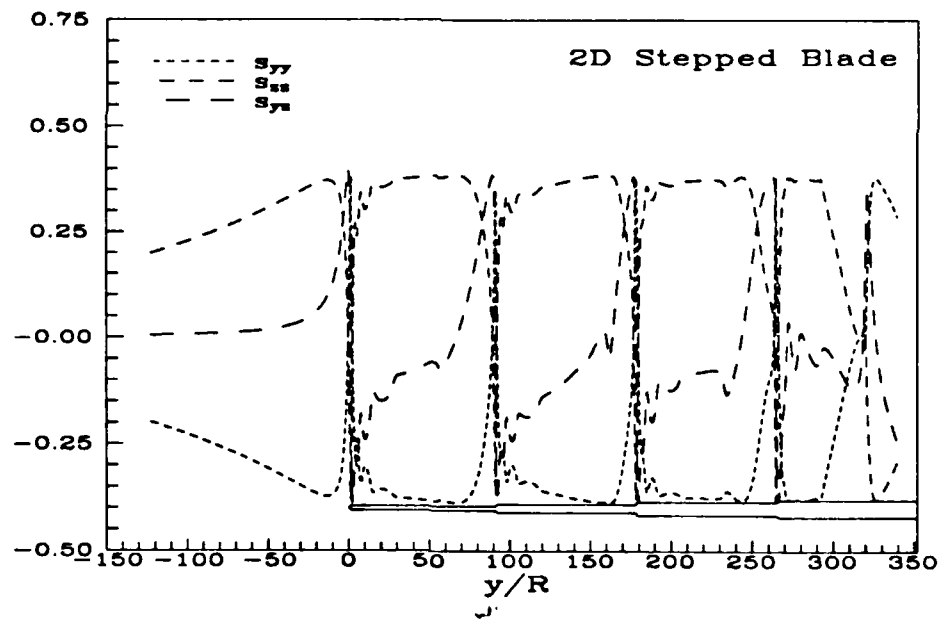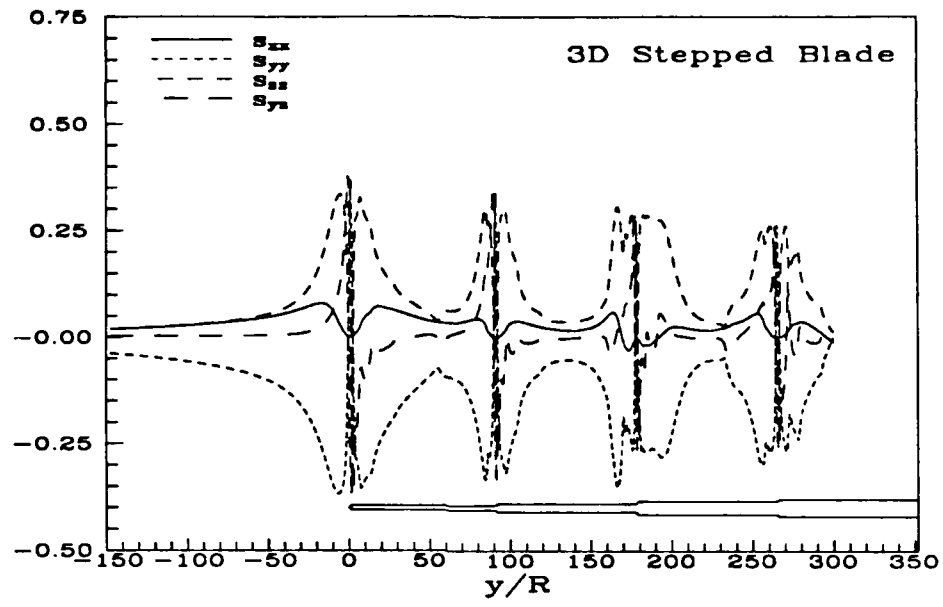
Figure 5.16: Stress profiles during a stepped blade penetration.
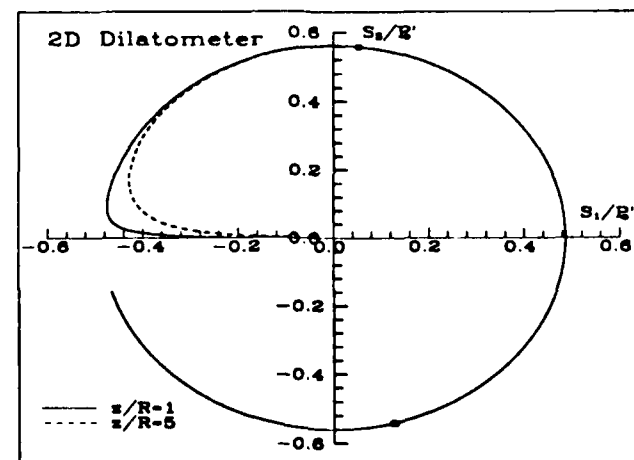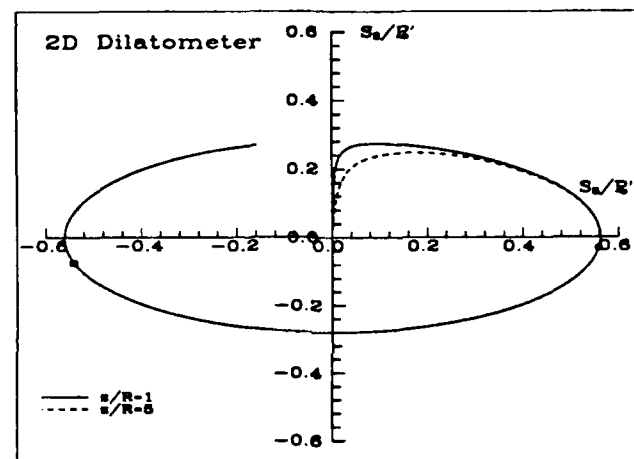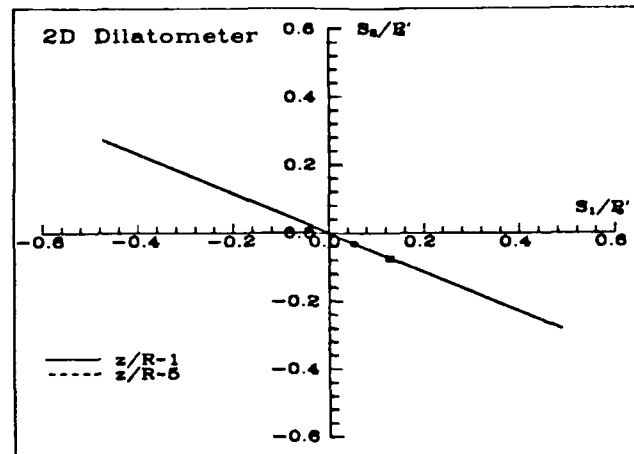
Figure 5.17: Stress paths for two-dimensional DMT

93
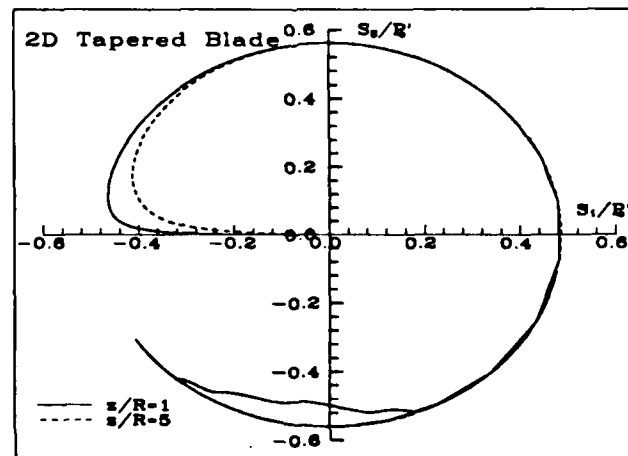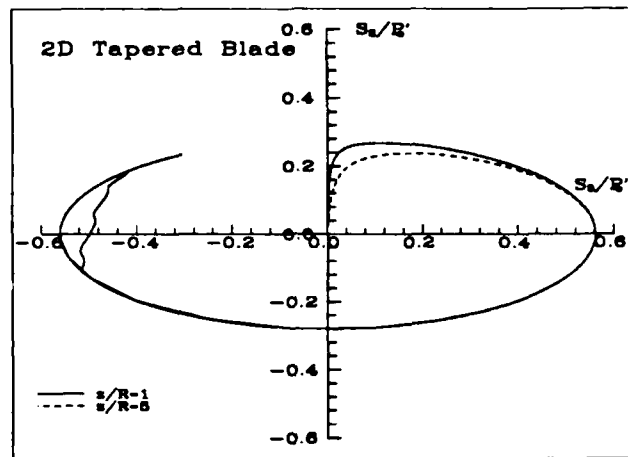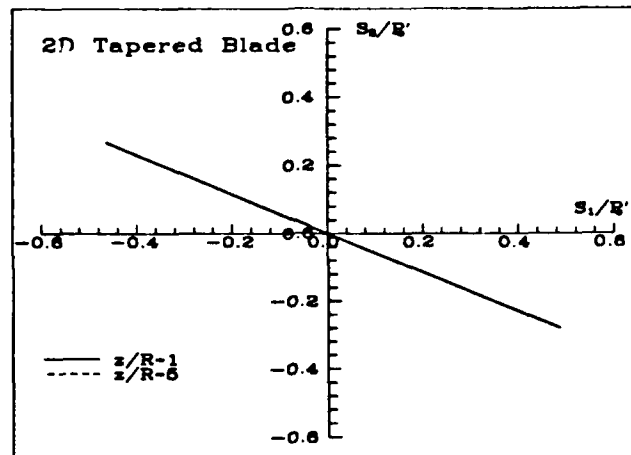
Figure 5.18: Stress paths for two-dimensional tapered blade

94
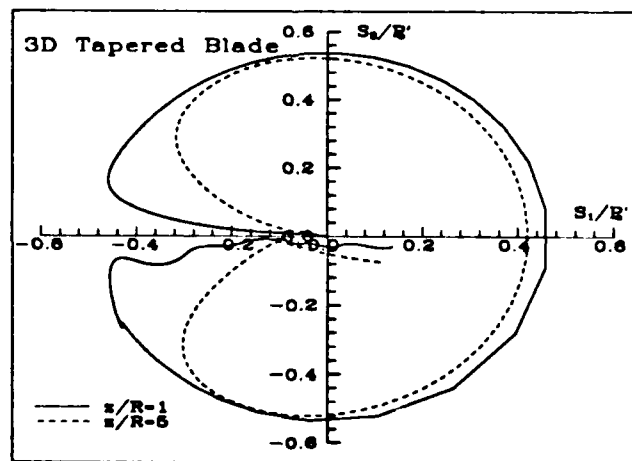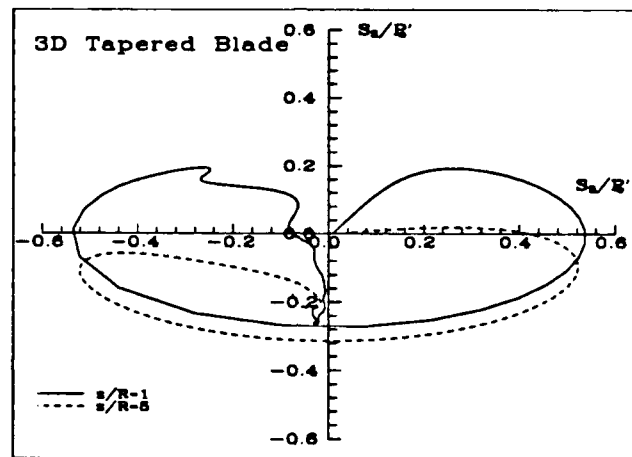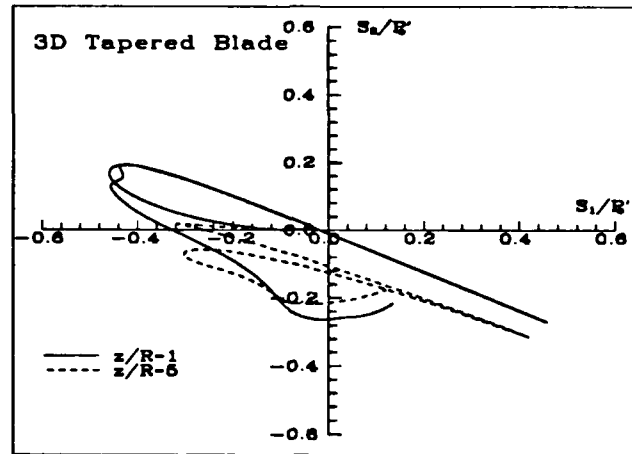
Figure 5.19: Stress paths for three-dimensional tapered blade.
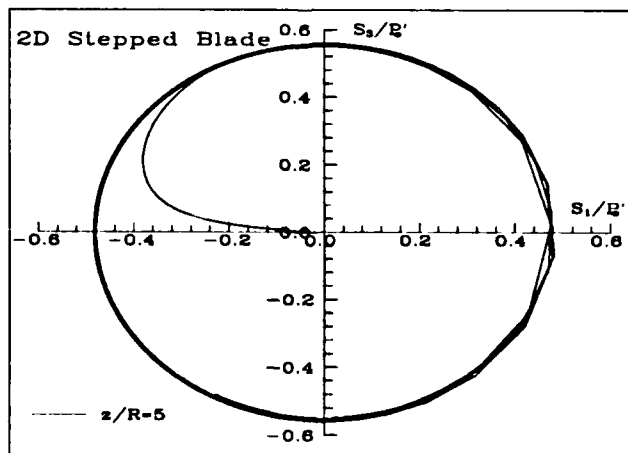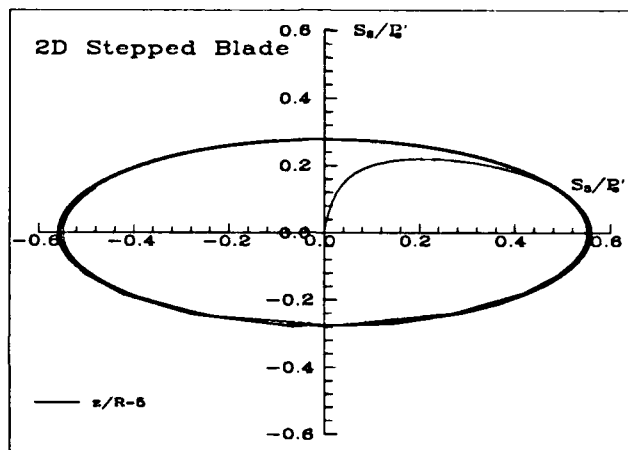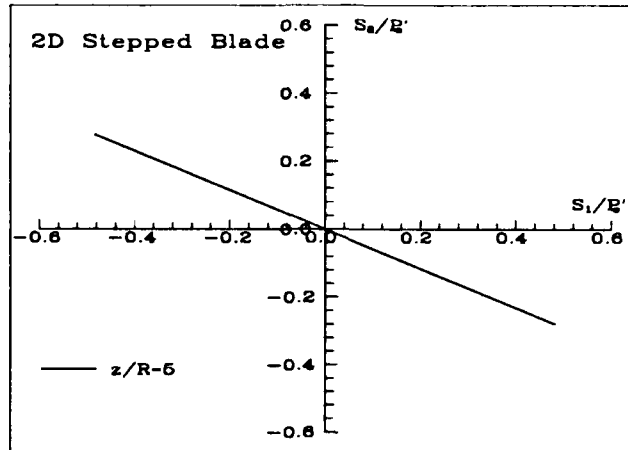
Figure 5.20: Stress paths for two-dimensional stepped blade.
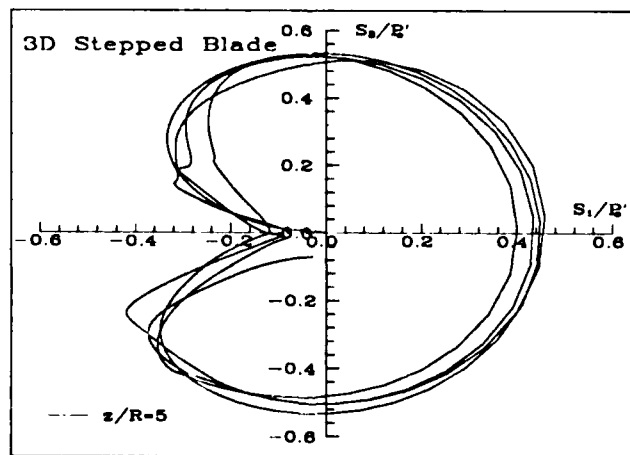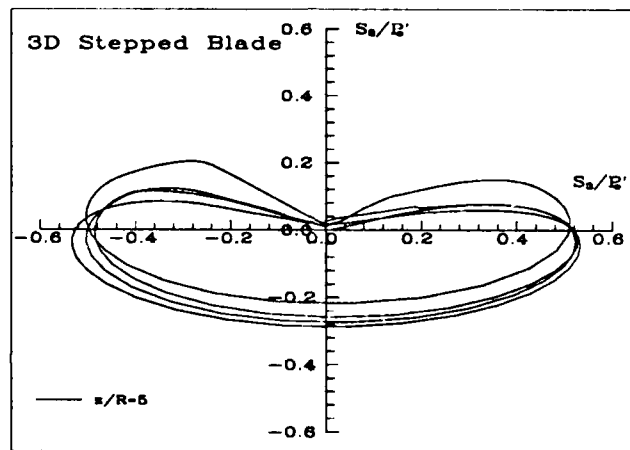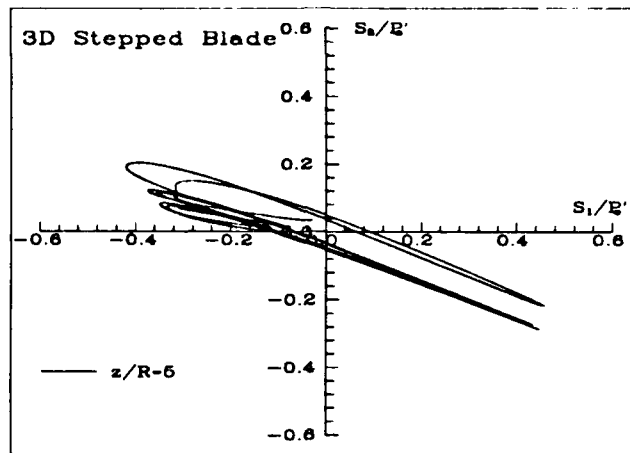
Figure 5.21: Stress Paths for three-dimensional tepped blade.

97

Chapter 6

Total Stress and Pore Pressure

Since the soil was treated as incompressible, normal octahedral stress σ_{oct} can not be estimated from MCC model and therefore must be determined from equilibrium considerations. Asuming the clay as fully saturated, the mean normal stress related pore pressure varations can be estimated from σ_{oct}. Along with the deviatoric stresses, estimates of σ_{oct} and pore pressure comprise of a complete solution to the penetration problem.

6.1   Equilibrium Considerations

For a general three-dimensional penetration problem the equilibrium in x, y and z directions can be written as:

$$\frac{\partial \sigma_{oct}}{\partial x} = -\frac{\partial s_{xx}}{\partial x} - \frac{\partial s_{xy}}{\partial y} - \frac{\partial s_{xz}}{\partial z}$$

$$\frac{\partial \sigma_{oct}}{\partial y} = -\frac{\partial s_{yx}}{\partial x} - \frac{\partial s_{yy}}{\partial y} - \frac{\partial s_{yz}}{\partial z}$$

$$\frac{\partial \sigma_{oct}}{\partial z} = -\frac{\partial s_{zx}}{\partial x} - \frac{\partial s_{zy}}{\partial y} - \frac{\partial s_{zz}}{\partial z} \tag{6.1}$$

For the axisymmetric penetration problem the above set equations can be reduced in the cylindrical coordinate system as:

$$\frac{\partial \sigma_{oct}}{\partial r} = -\frac{\partial s_{rr}}{\partial r} - \frac{\partial s_{rz}}{\partial z} - \frac{s_{rr} - s_{\theta\theta}}{r}$$

$$\frac{\partial \sigma_{oct}}{\partial z} = -\frac{\partial s_{rz}}{\partial r} - \frac{\partial s_{zz}}{\partial z} - \frac{s_{rz}}{r} \tag{6.2}$$

where the r in cylindrical coordinates corresponds to z direction in cartesian system. θ in cylindrical coordinates corresponds to x direction in cartesian system and z in cylindrical coordinates corresponds to y direction in cartesian system.

Levadoux and Baligh (1980) showed that integration of any one of the set of equations 6.2 yields the value of σ_{oct}. The value of σ_{oct} thus determined is path dependent i.e. it is different for integration in r and z direction, unless the following condition is satisfied.

$$\frac{\partial}{\partial r}(\frac{\partial \sigma_{oct}}{\partial z}) = \frac{\partial}{\partial z}(\frac{\partial \sigma_{oct}}{\partial r}) \tag{6.3}$$

The above condition can be satisfied only if the strains are compatible with the deviatoric stress model. Furthermore, strains should be determined as an exact solution to the penetration problem rather than approximate solutions corresponding to an ideal fluid.

The simplistic extension of the concept used by Baligh (1985), to the general three-dimensional case of DMT penetration proved to be less desirable. The error in integration is multiplied, presumably because of three directions in which integration can be performed to calculate σ_{oct}. To correctly analyze this problem it is necessary to solve a poisson equation in three-dimension. Such computation is beyond the scope of this research. The following evaluation of pore pressure and total stresses are therefore restricted to plane strain cases. Since the equilibrium considerations have been successfully employed to determine σ_{oct} for axisymmetric cone penetration (Teh, 1987; Baligh, 1985), it is therefore expected that two-dimensional plane strain approximations of the flat penetrometers will generate reasonable estimates of σ_{oct} and pore pressure. In plane strain simplification, the width of the penetrometer is assumed to be infinite in x direction (Figure 3.2). The equilibrium equations for plane strain simplification can be written as:

$$\frac{\partial \sigma_{oct}}{\partial y} = -\frac{\partial s_{yy}}{\partial y} - \frac{\partial s_{yz}}{\partial z}$$

$$\frac{\partial \sigma_{oct}}{\partial z} = -\frac{\partial s_{zy}}{\partial y} - \frac{\partial s_{zz}}{\partial z} \tag{6.4}$$

where integration can be performed in the y and z direction (Figure 3.2). A central difference iterative integration scheme was used to evaluate σ_{oct}. The scheme utilized isoparametric elements (Levadoux and Baligh, 1980) for evaluating derivatives. The fluid flow idealization of soil behavior during deep steady penetration is believed generally to overestimate the shear strains ε_{yz} (or ε_{rz} in cylindrical coordinates). This is because of the lack of shearing resistance in a perfect fluid. Furthermore, in the deviatoric stress model the predicted shear stress s_{yz} (or s_{rz} in cylindrical coordinates) is controlled by shear strain ε_{yz} (or ε_{rz} in cylindrical coordinates) which can therefore be unrealistic. It was shown by Baligh (1985) and Teh (1987) that for integration in z direction, the effect of s_{yz} is minimized and hence more reliable estimates of σ_{oct} are obtained. Therefore, prediction of pore pressure and total stresses presented subsequently are determined by means of integration along the z direction.

6.2   Results

Pore pressure and total stress computations were performed for the various penetrometers discussed so far. In addition, a flat-plate geometry similar to a two-dimensional DMT but with a $60°$ tip was also analyzed in order to study the effect of varying the tip angle.

Figures 6.1 and 6.2 show the pore pressure and total stress profiles for a $20°$ DMT and a cone respectively. It is evident from these figures that for the same apex angle the total stress state just ahead of the tip is different for axisymmetric (cone) and plane strain (two-dimensional DMT) penetration. Pore pressure and total stress is generally higher for cone penetration. Furthermore, the rate of change of total stress and pore pressure is higher for axisymmetric penetration. Since the *end effect* in the case of three-dimensional DMT causes stress relaxation around corners of the flat-plate, peak pore pressure and total stresses can be expected to be lower than the plane strain approximation. The pore pressure due to axisymmetric and flat-plate

penetration being different the initial conditions for the subsequent consolidation are also expected to be dissimilar.

The effect of shape and geometry was studied by analyzing flat-plate geometries with:

1. a 60° tip;

2. a 3° taper (Tapered Blade); and

3. steps (Stepped Blade)

Pore pressure and total stress computations for the above mentioned flat plate geometries were carried out. The results have been presented at the end of this chapter in form of profiles an contours of pore pressure and total stresses. Characteristics of pore pressure and total stress distribution can be summarized as follows:

- Pore pressure and total stress profiles (Figures 6.1 - 6.5) show a positive peak in the tip region for all penetrometer geometries.

- The peak magnitude for pore pressure and total stress is comparable for the DMT and the cone.

- Increasing the tip angle to 60° for the DMT makes the total stresses more concentrated in the tip region, however there is no significant increase in the peak magnitude. Furthermore, the total stresses and pore preessure fall quicker (after the tip) and to a lower value when the tip angle was increased to 60°.

- As observed in the case of deviatoric stress distribution, pore pressure and total stresses for tapered blade and stepped blade do not exibit an exponential increase with the thickness of the blade. The total stress and pore pressure profile for the tapered blade shows a sharp peak of magnitudes significantly higher than those observed for the DMT and cone. Profiles for the stepped blade show peaks corresponding to the loading unloading cycles caused due to each step of increasing w/t ratio. Pore pressure and the different components of total stress show almost identical trends for both, stepped blade and tapered blade.
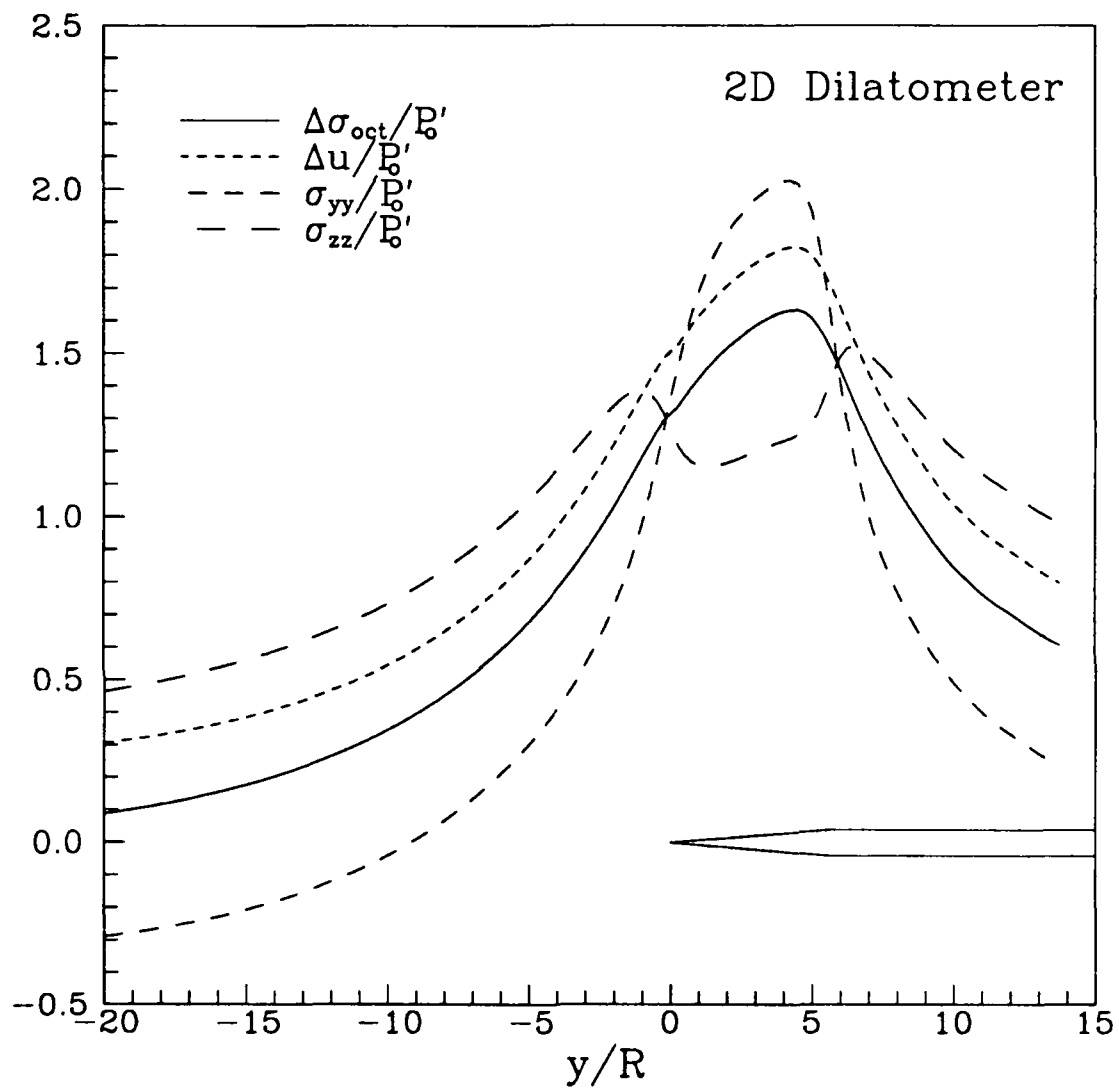
Figure 6.1: Normalized total stress and pore pressure profiles for 20° DMT .

102
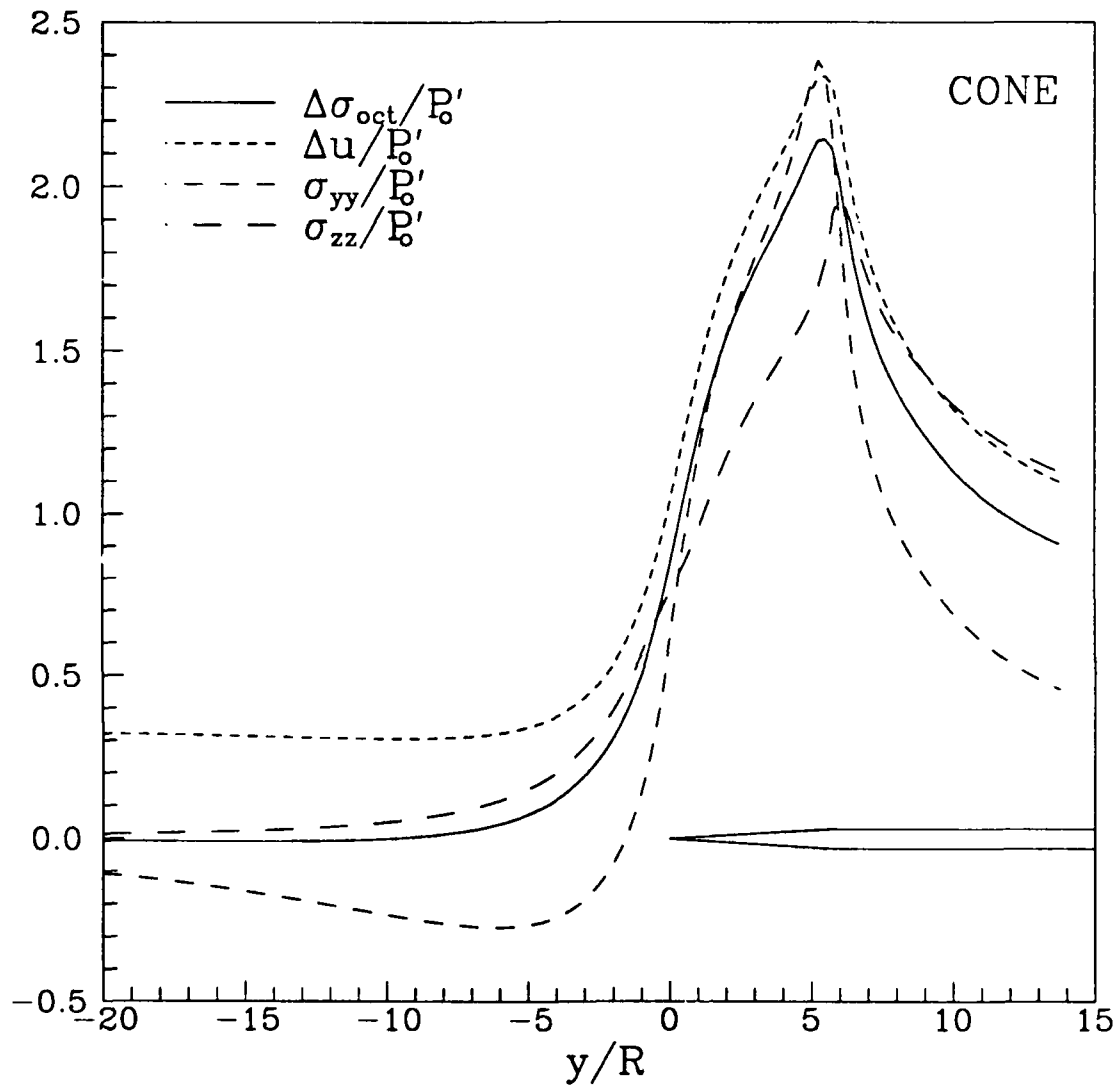
Figure 6.2: Normalized total stress and pore pressure profiles for 20° cone .

103
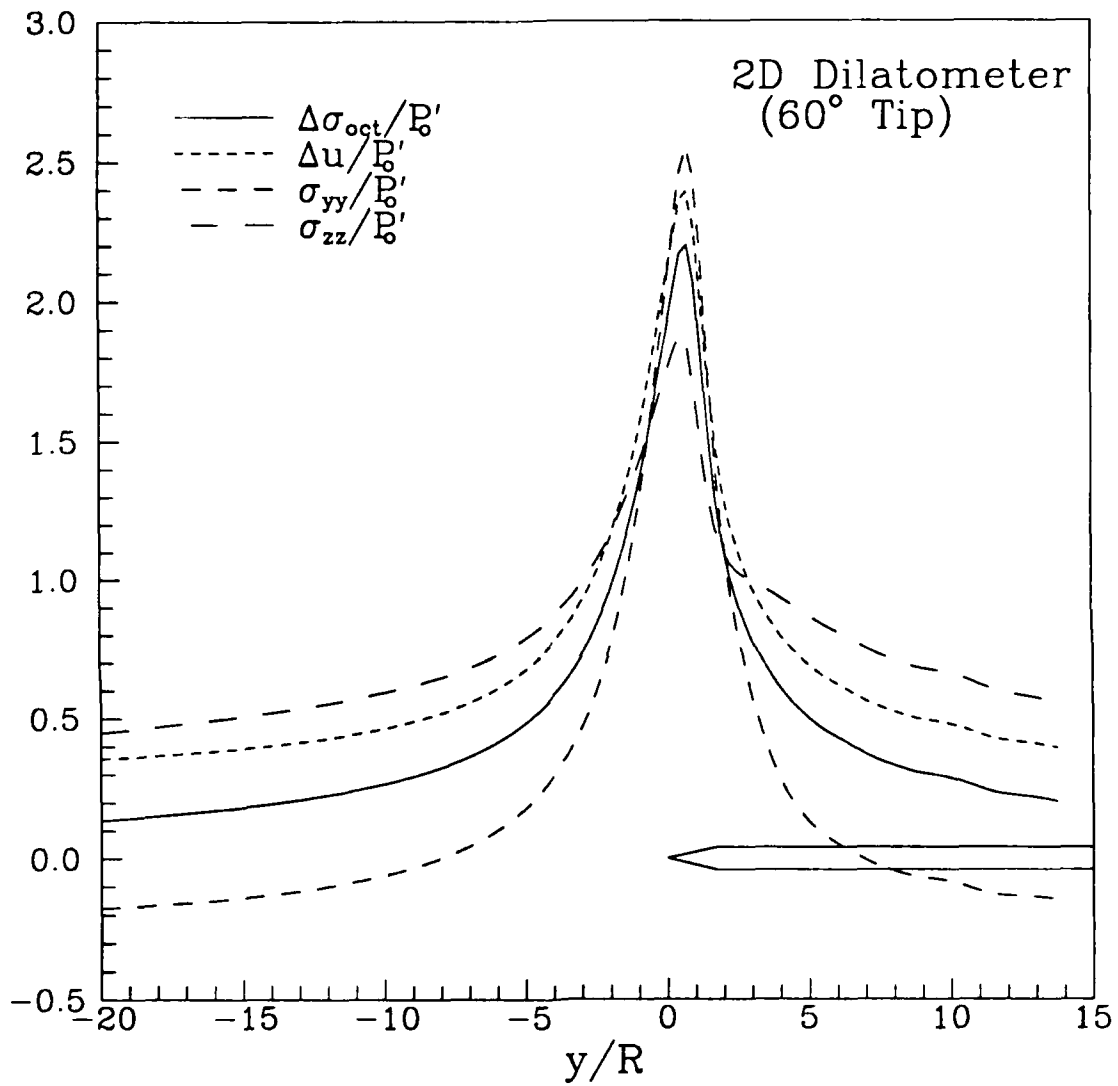
Figure 6.3: Normalized total stress and pore pressure profiles for $60°$ DMT .
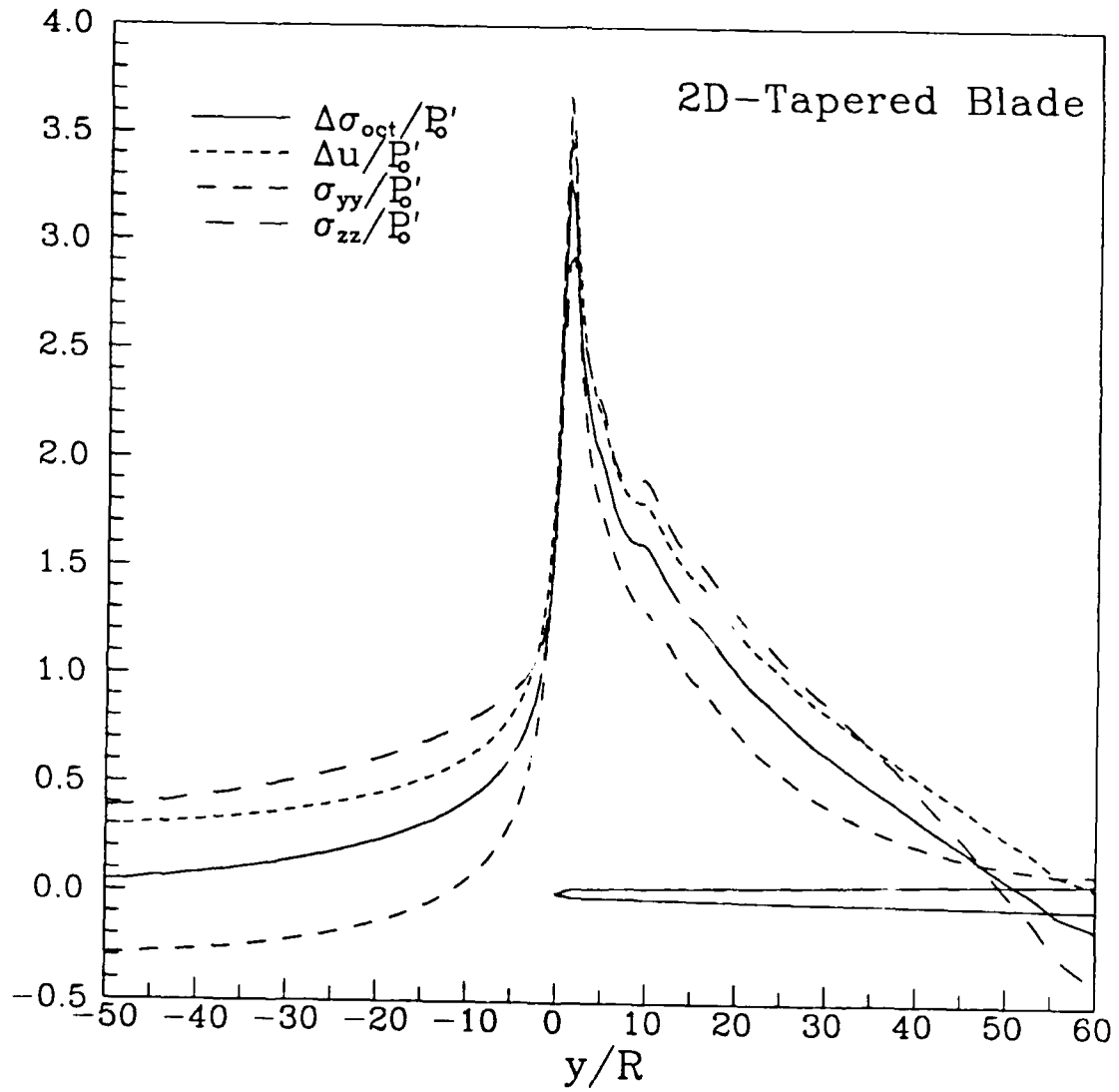
Figure 6.4: Normalized total stress and pore pressure profiles for tapered blade.
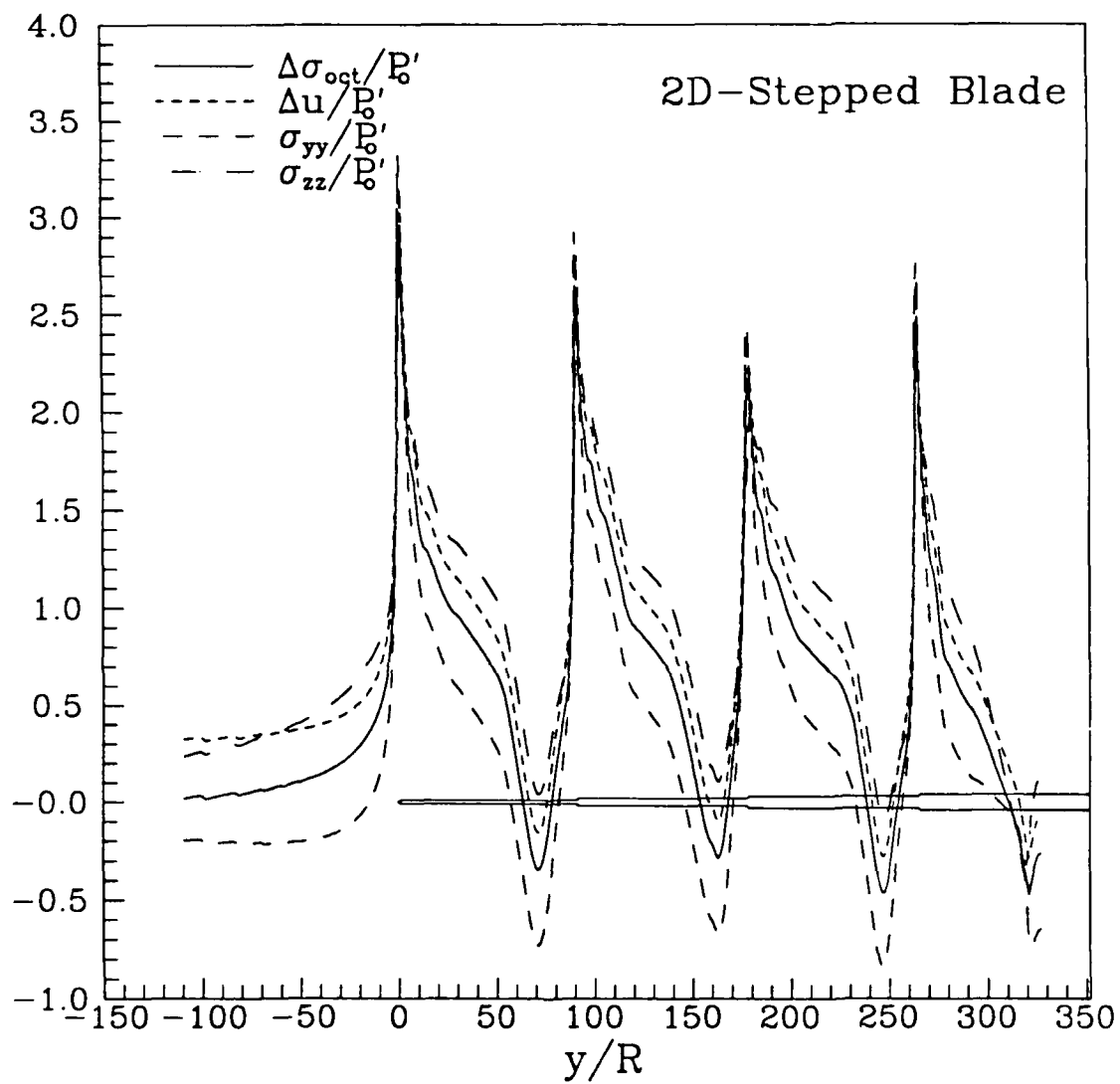
Figure 6.5: Normalized total stress and pore pressure profiles for stepped blade

106
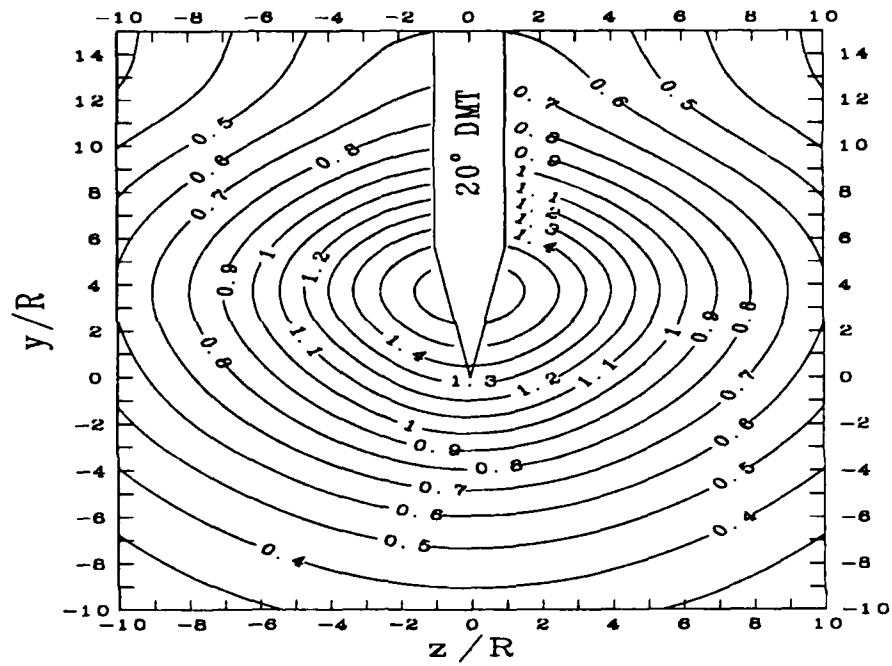
Figure 6.6: $\Delta\sigma_{oct}/P'_o$ contours for $20°$ DMT.
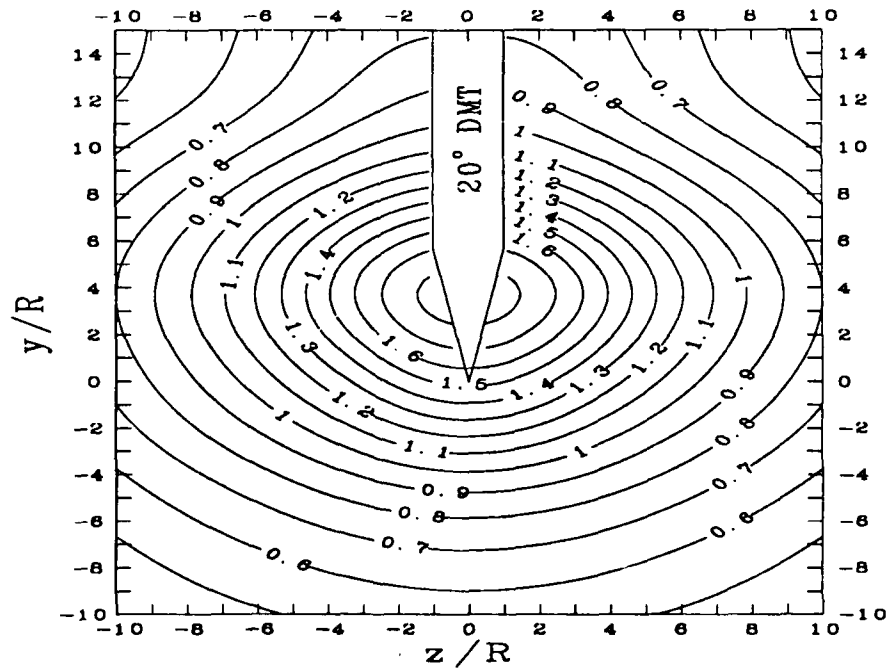
Figure 6.7: $\Delta u/P'_o$ contours for $20°$ DMT.
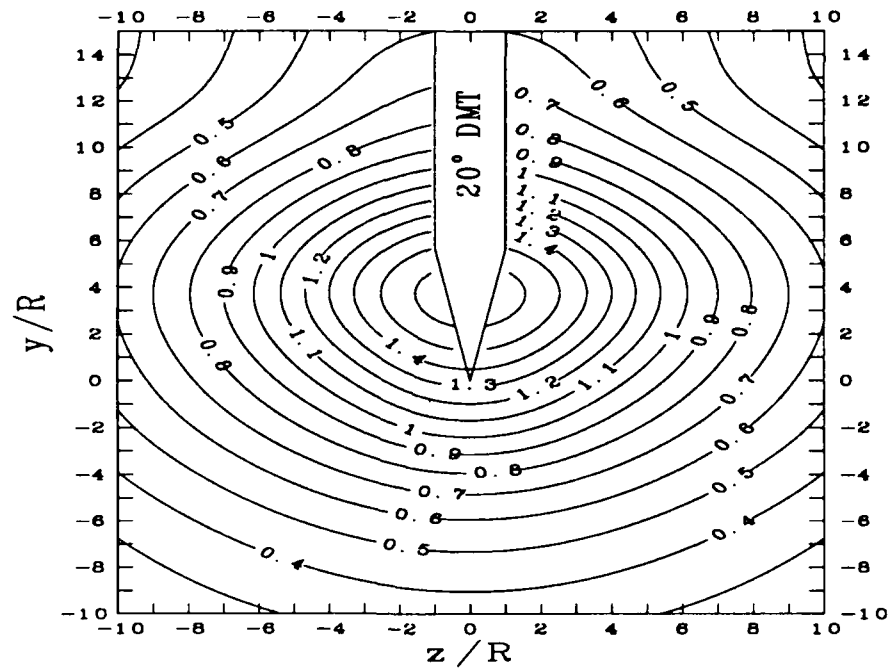
107

Figure 6.8: σ_{yy}/P_o' contours for $20°$ DMT.

Figure 6.9: σ_{zz}/P_o' contours for $20°$ DMT.

Figure 6.10: $\Delta\sigma_{oct}/P_o'$ contours for 20° cone.

Figure 6.11: $\Delta u/P_o'$ contours for 20° cone.

109
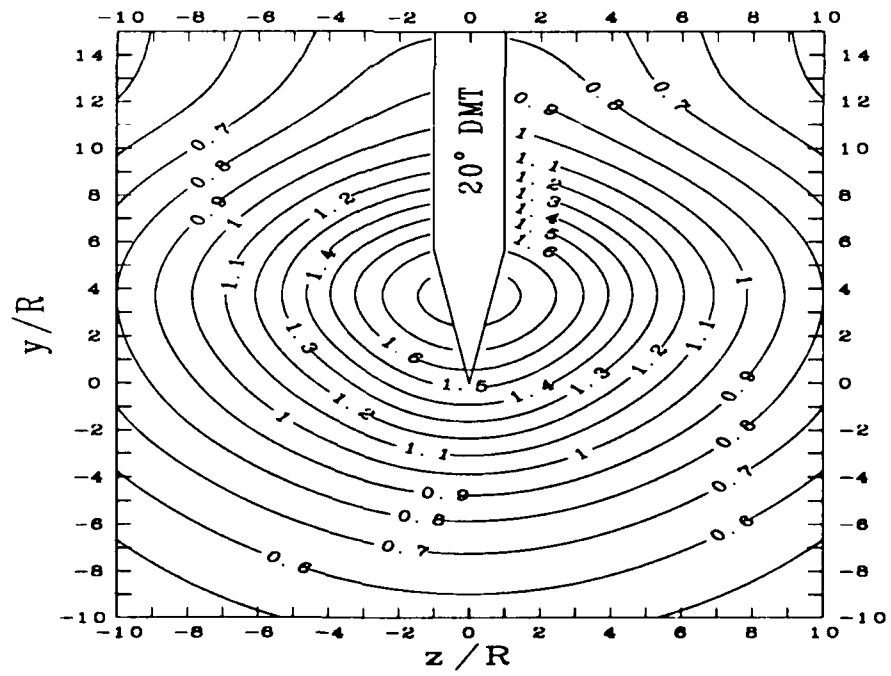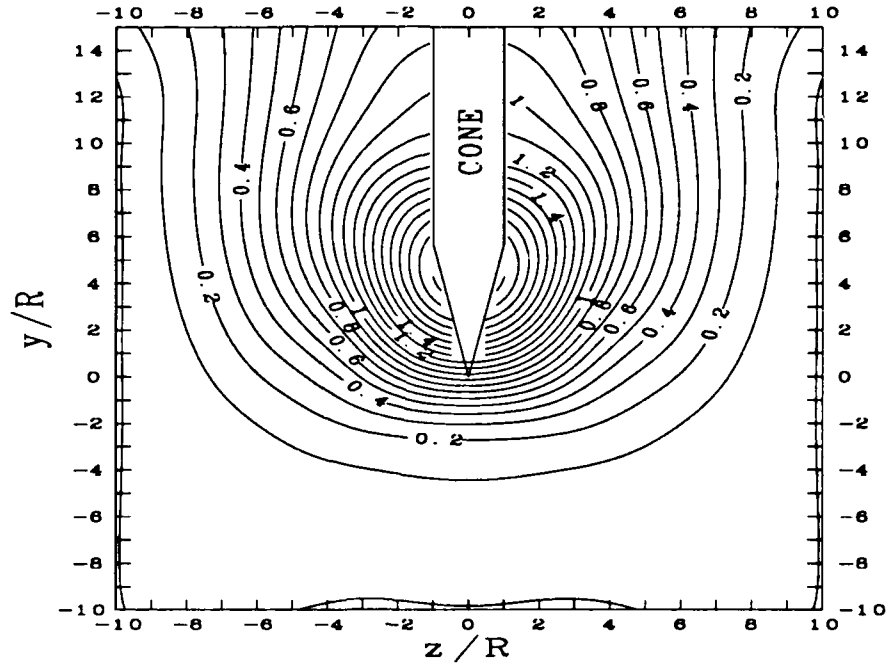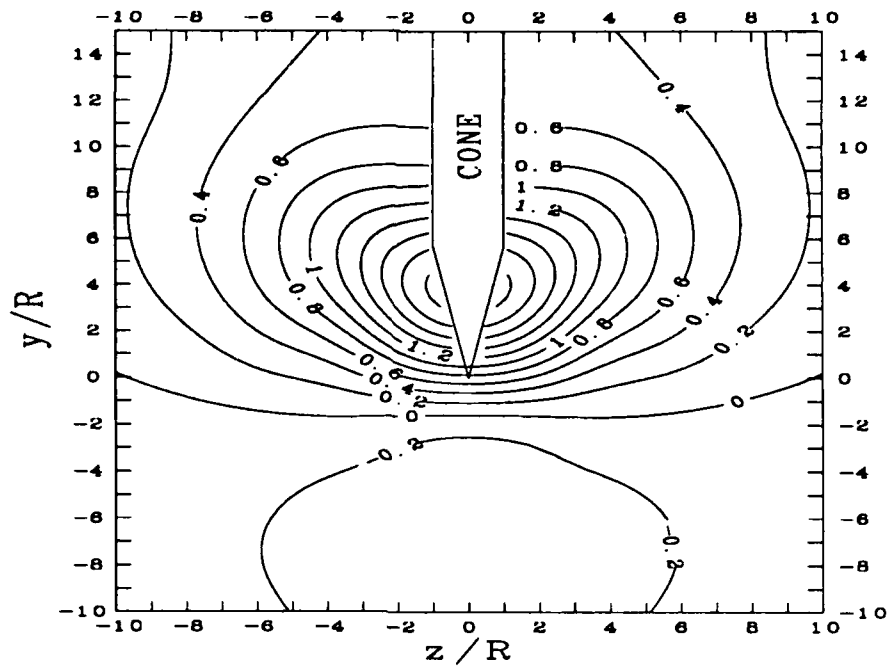
Figure 6.12: σ_{yy}/P'_o contours for $20°$ DMT.

Figure 6.13: σ_{zz}/P'_o contours for $20°$ DMT.

110
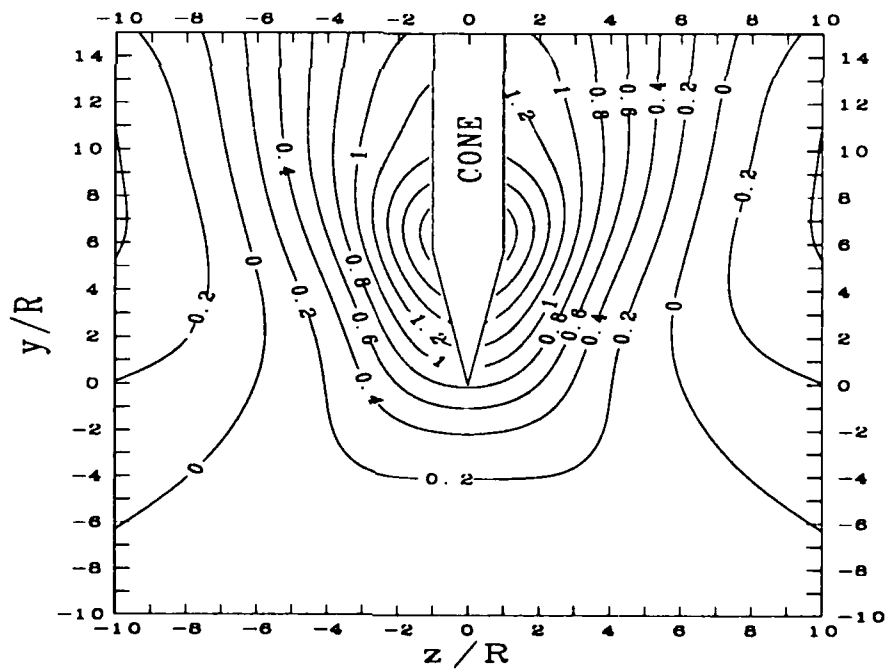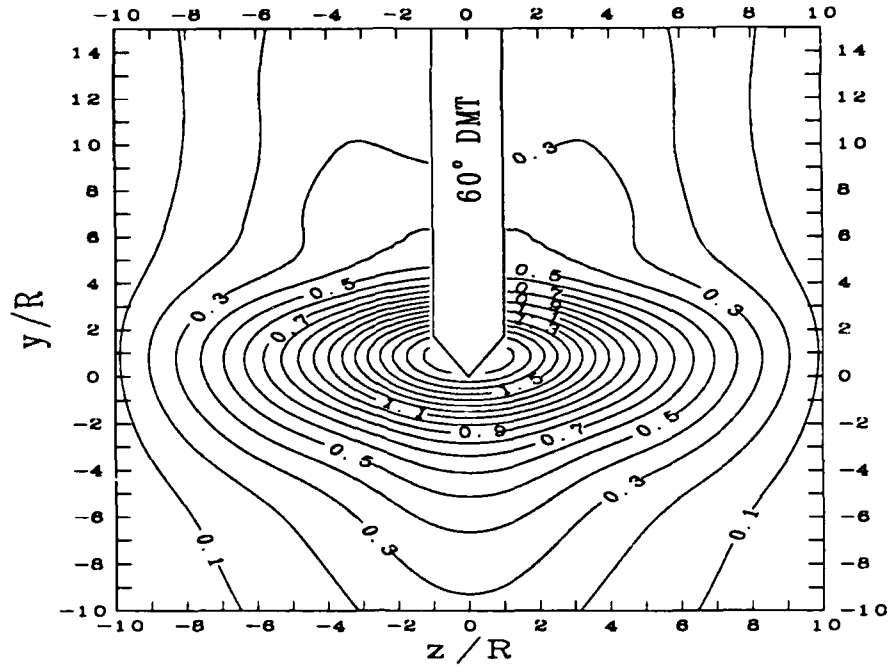
Figure 6.14: $\Delta\sigma_{oct}/P_o'$ contours for 60° DMT.
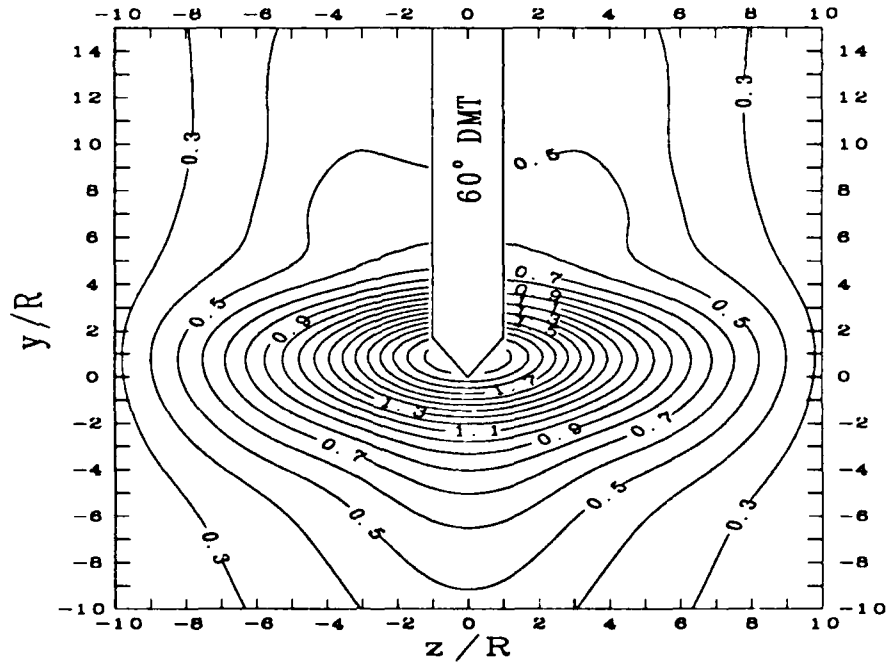
Figure 6.15: $\Delta u/P_o'$ contours for 60° DMT.

Figure 6.16: σ_{yy}/P_o' contours for $60°$ DMT.

Figure 6.17: σ_{zz}/P_o' contours for $60°$ DMT.

112

Figure 6.18: $\Delta\sigma_{oct}/P'_o$ contours for tapered blade.

Figure 6.19: $\Delta u/P'_o$ contours for tapered blade.

113
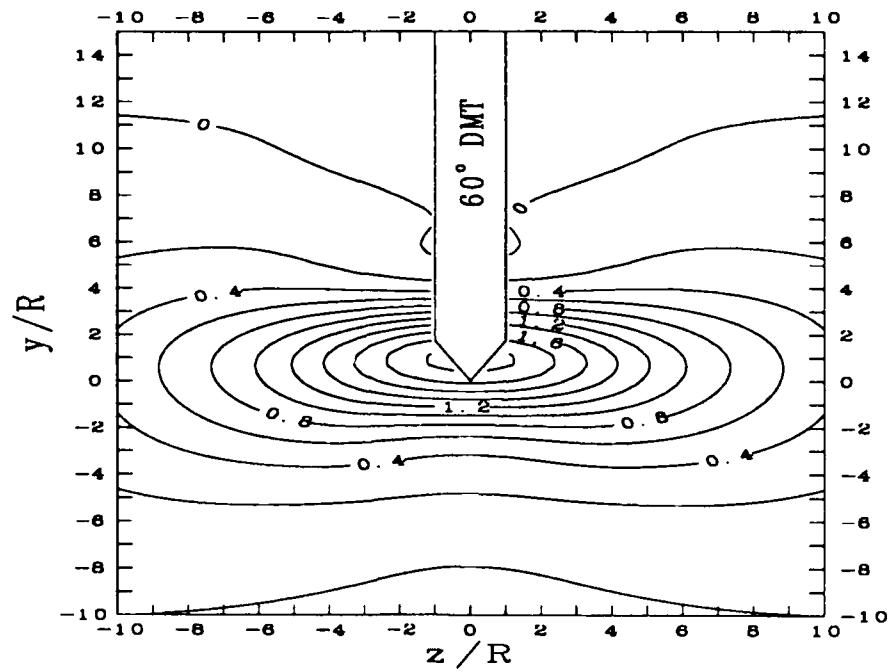
Figure 6.20: σ_{yy}/P'_o contours for tapered blade.
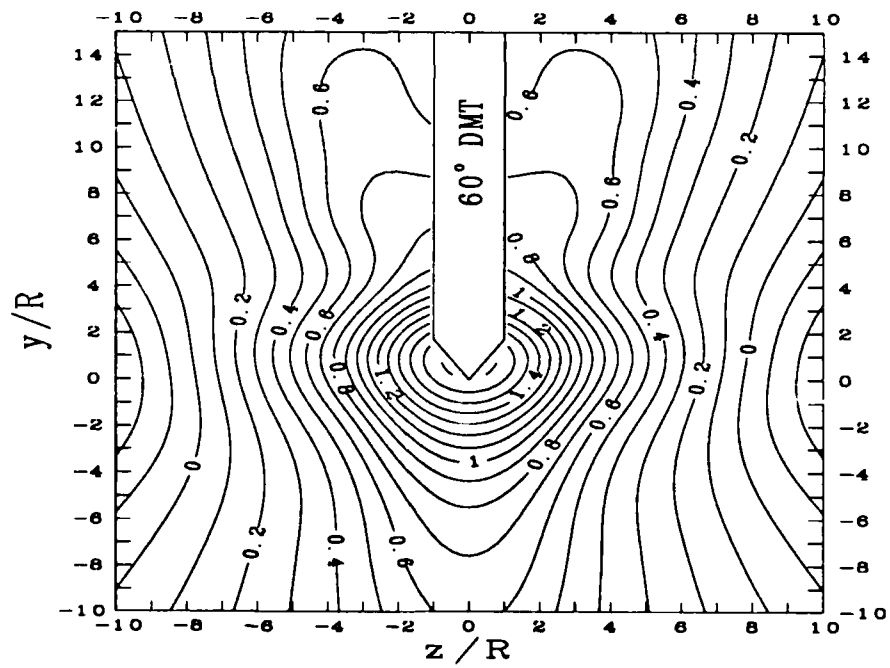
Figure 6.21: σ_{zz}/P'_o contours for tapered blade.
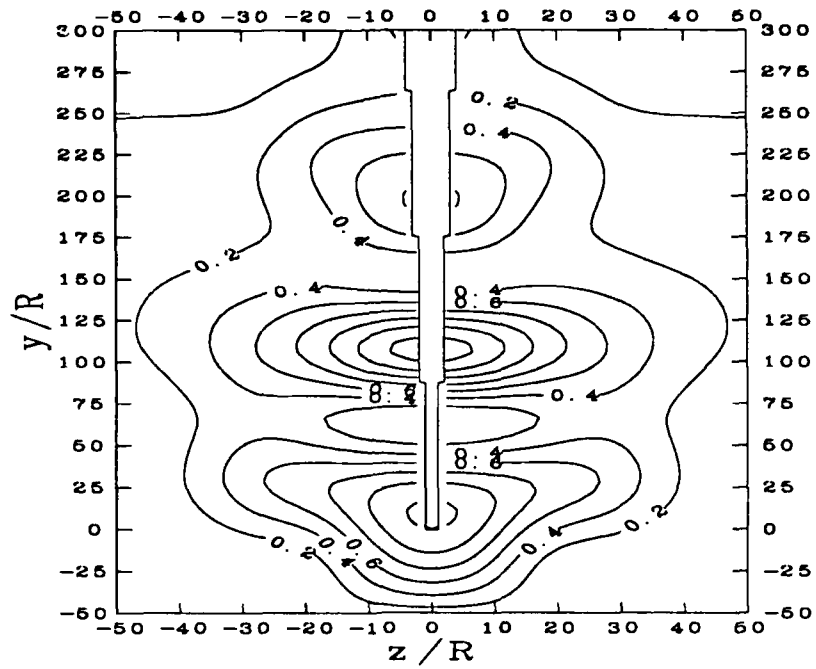
Figure 6.22: $\Delta\sigma_{oct}/P_o'$ contours for stepped blade.
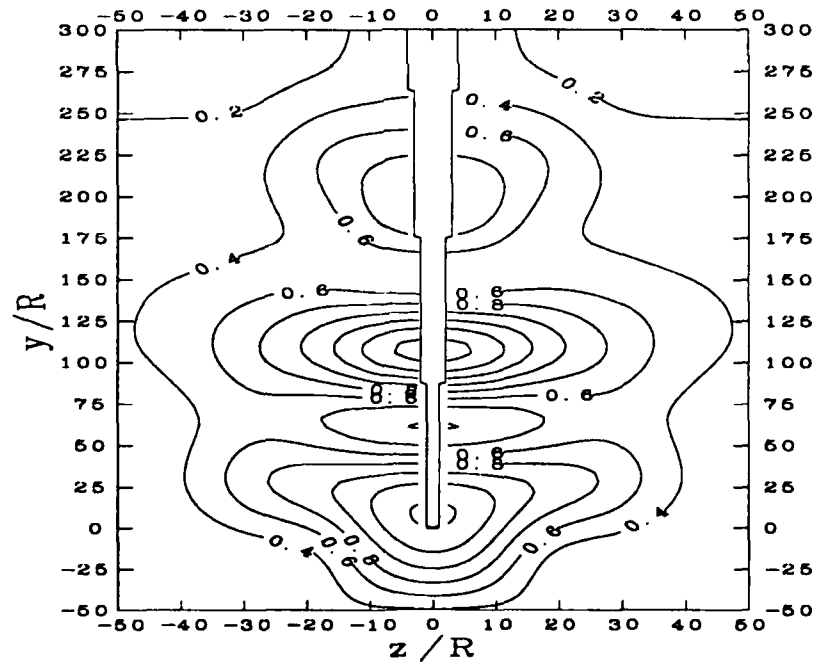
Figure 6.23: $\Delta u/P_o'$ contours for stepped blade.
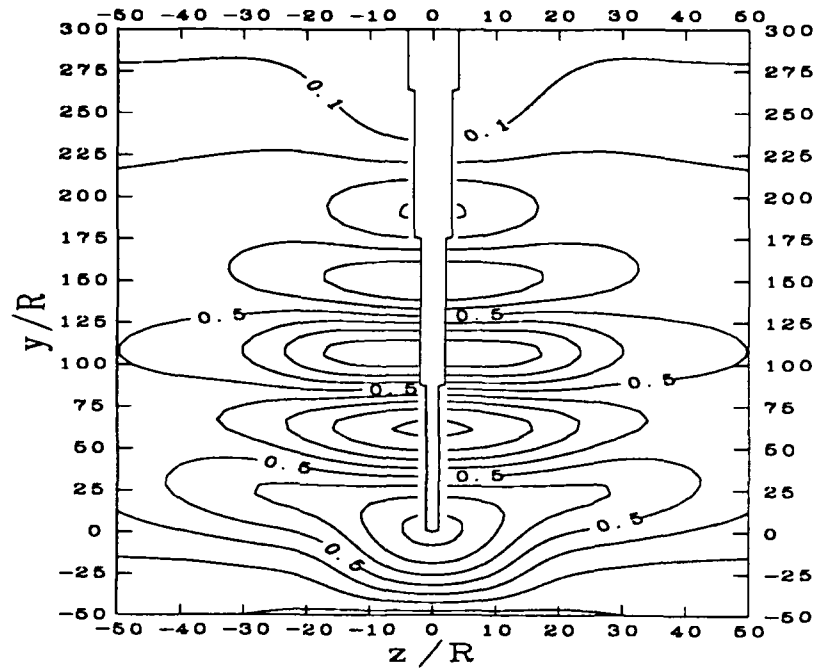
Figure 6.24: σ_{yy}/P_o' contours for stepped blade.

Figure 6.25: σ_{zz}/P_o' contours for stepped blade.

116
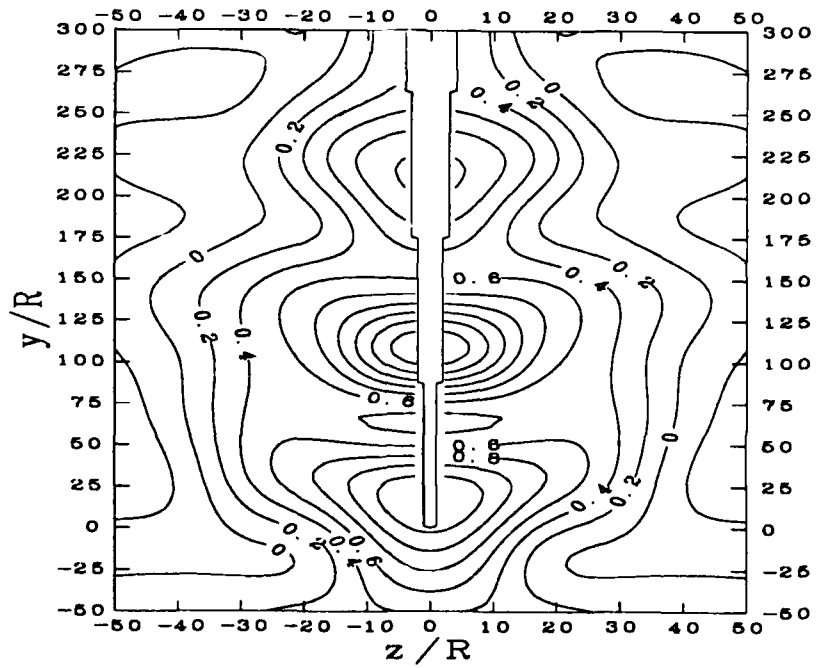
Chapter 7

Reference Soil Engineering Properties

A mixture of 50% kaolinite and 50% Edgar sand was used to create the clay specimens in the calibration chamber tests. To establish the geotechnical engineering properties of the clay, a series of laboratory experiments were performed. In addition to the determination of basic engineering properties, the experiments included consolidation and triaxial tests. This chapter describes the details of those experiments and their results.

7.1 Soil Classification

Figure 7.1 shows the grain size distributions of the kaolinite and Edgar sand. Atterberg limit tests (ASTM D4318) were conducted on the 100% kaolinite and the kaolinite/Edgar sand mixture with the results listed in Table 7.1. In this table the specific gravity (ASTM D850) of kaolinite and Edgar sand is also shown. The 100% kaolinite will be referred to as K100 and the 50/50 mixture will be referred to as K50 hereinafter.

Based on USCS the kaolinite can be classified as MH-CH which is typical for kaoli-

117

Gravel	Coarse to Medium Sand	Fine Sand	Silt	Clay
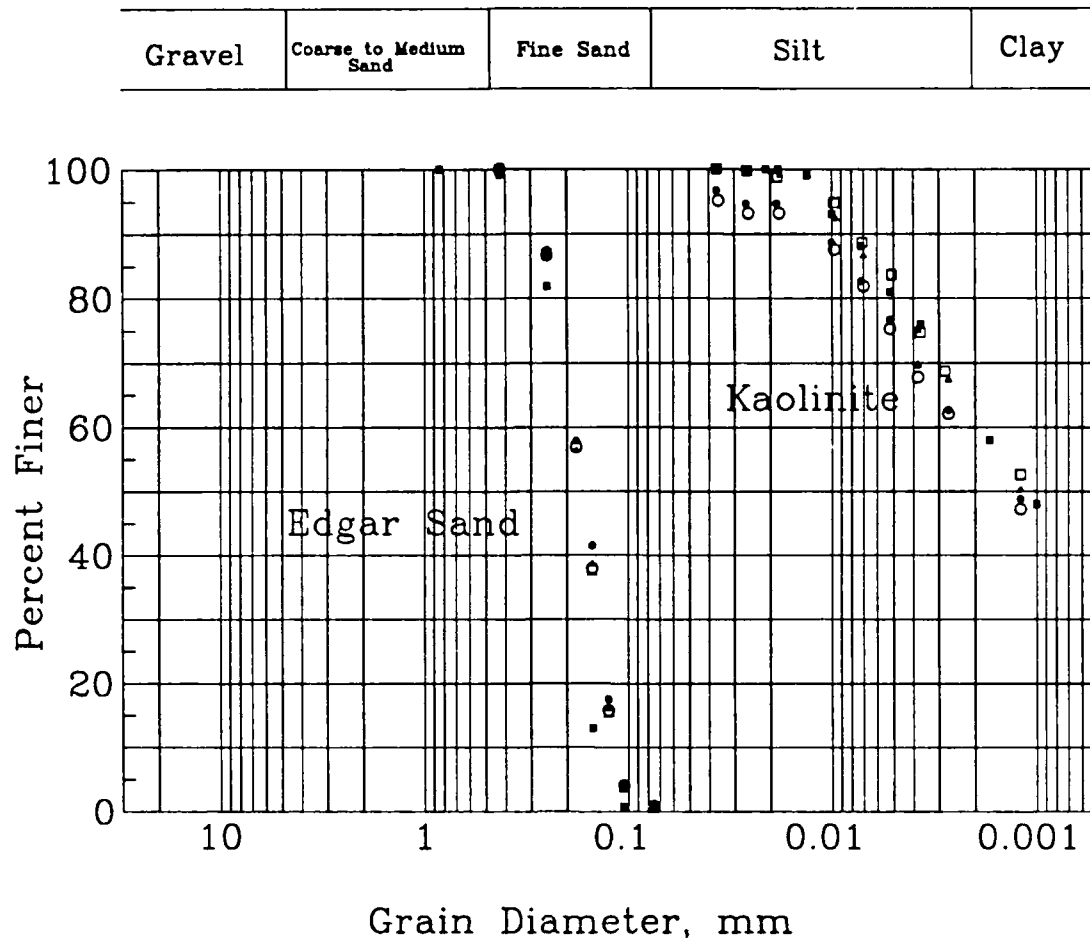
Figure 7.1: Grain size distribution of kaolinite and Edgar sand.

Soil Type	Liquid Limit (%)	Plastic Limit (%)	Plastic Index (%)	Specific Gravity
Kaolinite	51.5 to 56.0	25.2 to 30.1	23.4 to 26.3	2.62 to 2.69
Kaolinite and Sand (50/50 Mix)	29.2 to 30.9	16.3 to 16.8	12.5 to 14.1	N/A
Sand	N/A	N/A	N/A	2.63 to 2.71

Table 7.1: Engineering properties of K50 soil.

118

nite (Mitchell, 1976). The Edgar sand was classified as SP or poorly graded fine sand.

7.2 Consolidation Characteristics

To provide the consolidation characteristics of the clay specimens used in the research, a series of controlled gradient consolidation (CGC) tests were conducted. The advantages of CGC method are well recognized (Lowe et al., 1969). This method is especially attractive since it can be servo-controlled by a computer and therefore eliminates the need to take readings and to adjuste the consolidation pressure manually.

7.2.1 The Controlled Gradient Consolidation Test Procedures

The clay specimens were prepared in the laboratory from slurry following the techniques developed by Huang et al. (1988). The slurry was mixed with an initial water content of twice the liquid limit. Deionized and deaired water was used in the preparation of the slurry. Upon mixture, the slurry was consolidated under a vertical pressure of 138 kPa. At the end of slurry consolidation, a clay specimen with sufficient consistancy to support its own weight was created.

The controlled gradient consolidation testing device fabricated as part of the research is shown in Figure 7.2. The specimen is completely contained to enable a back pressure to be applied to the specimen. In all the CGC tests, a back pressure of 414 kPa was applied. A *Bellofram*/linear ball bearing piston configuration was used to minimize shaft friction. The soil specimen was obtained by pushing a tapered ring (angle of taper = 3°) into the clay. The ring has an inside diameter of 61 mm and a height of 17.8 mm.
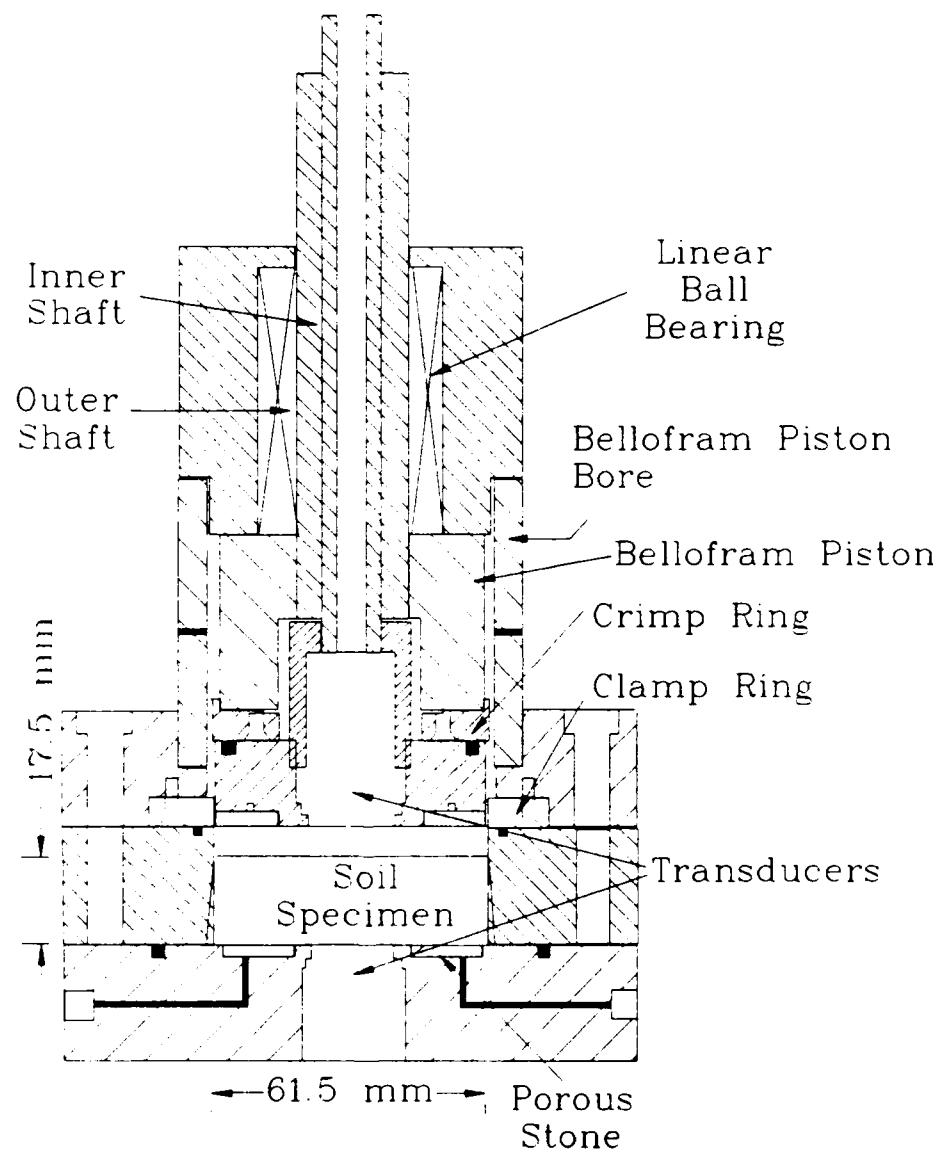
Figure 7.2: Cross sectional view of the controlled gradient consolidation device.

120

The consolidation pressure was monitored by pressure tranducers located at the top and bottom of the specimen. This arrangement enables any significant friction on the side of the specimen to be detected. Drainage was allowed only through the top of the specimen against the back pressure. A differential pressure transducer was used to measure the pore pressure difference between the top and bottom of the specimen. The vertical consolidation pressure was servo-controlled by a computer to maintain a positive excess pore pressure of 20.7 kPa at the bottom of the specimen. A *Fairchild* T5221 I/P and E/P transducer regulator was used to control the consolidation pressure.

7.2.2   Consolidation Test Results

Plots of the test data are shown in Figures 7.3 to 7.10. In tests K50-2 and K100-2 the consolidation pressure was increased to 276 kPa and then unloaded prior to the controlled gradient consolidation tests. The preconsolidation pressures depicted in either the time-displacement (Figures 7.3 and 7.7) or the e-log p curves (Figures 7.6 and 7.10) are essentially the same as the known values listed in Table 7.2. This is an indication of the good quality of the tests. Table 7.2 reveals key parameters found in the CGC tests. The C_v values are obtained by taking derivatives of laboratory data. The somewhat erratic results are therefore expected and numbers given in Table 7.2 represent a range of C_v values for the indiviual tests. The K50 has a C_v typically at 2 to 5 times that of K100. This is clearly due to the presence of sand in the K50 specimens.

Test No.	Preconsolid. stress, kPa	$C_v, 10^{-3} cm^2/sec$		
		Virgin Loading	Unload	Reload
K100-1	138	1.5 to 3.5	2.0 to 28.0	5.0 to 15.0
K100-2	276	1.5 to 3.5	2.0 to 28.0	5.0 to 15.0
K50-1	138	2.0 to 7.0	10.0 to 50.0	5.0 to 40.0
K50-2	276	2.0 to 7.0	10.0 to 50.0	5.0 to 40.0

Table 7.2: Summary of the controlled gradient consolidation tests.
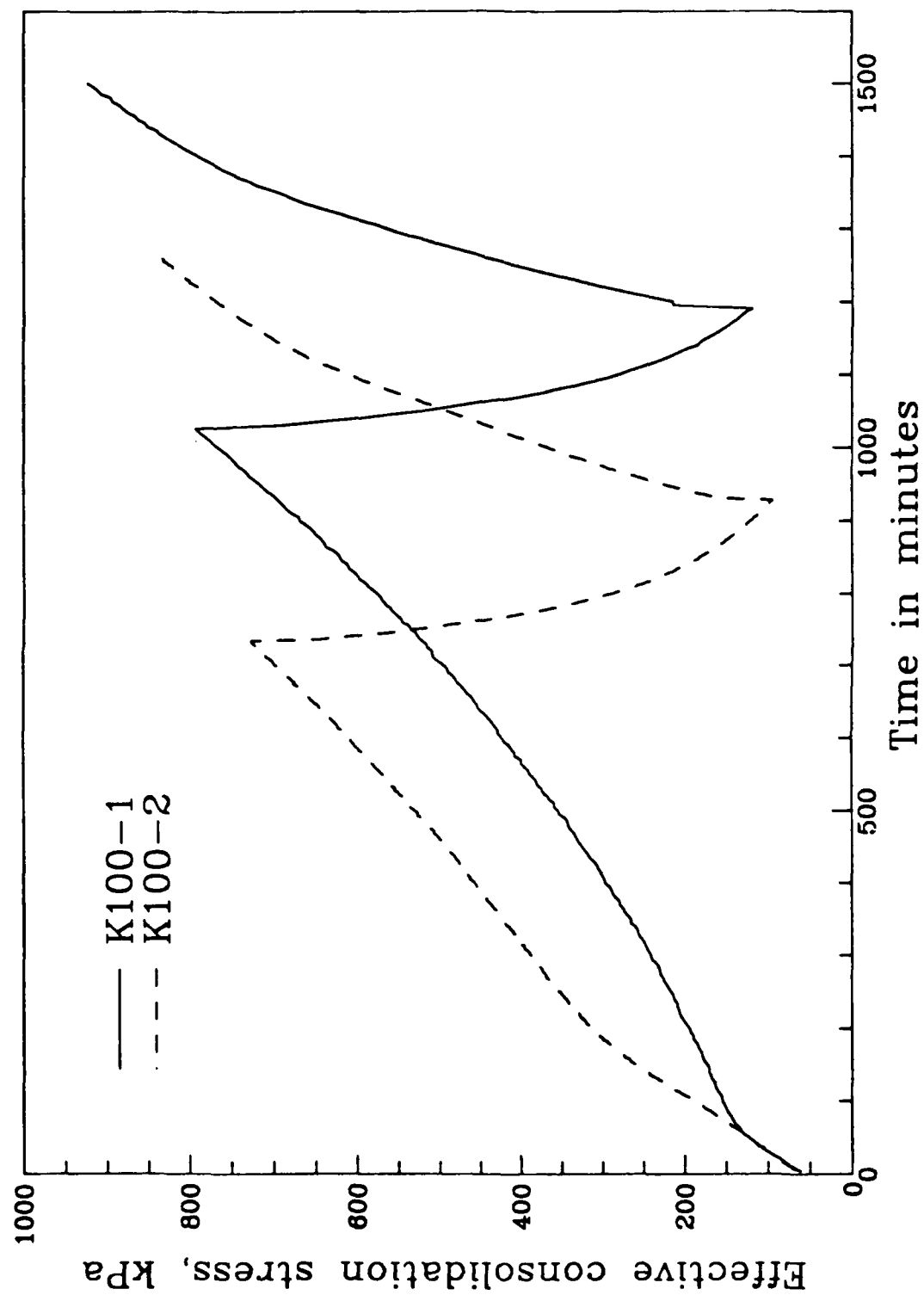
Figure 7.3: Time displacement curves of tests K100-1 and K100-2.

123
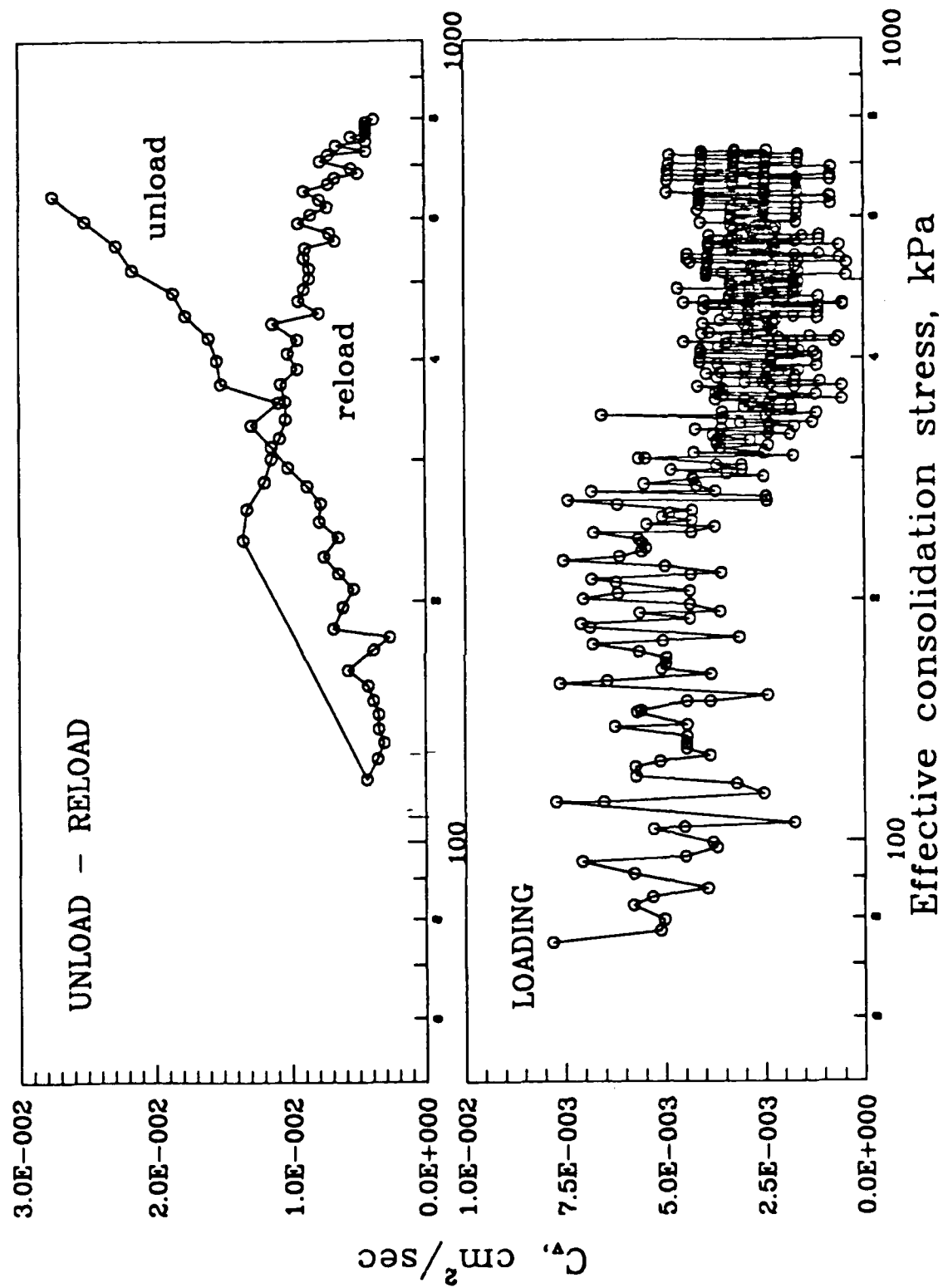
Figure 7.4: C_v versus effective consolidation stress for K100-1.
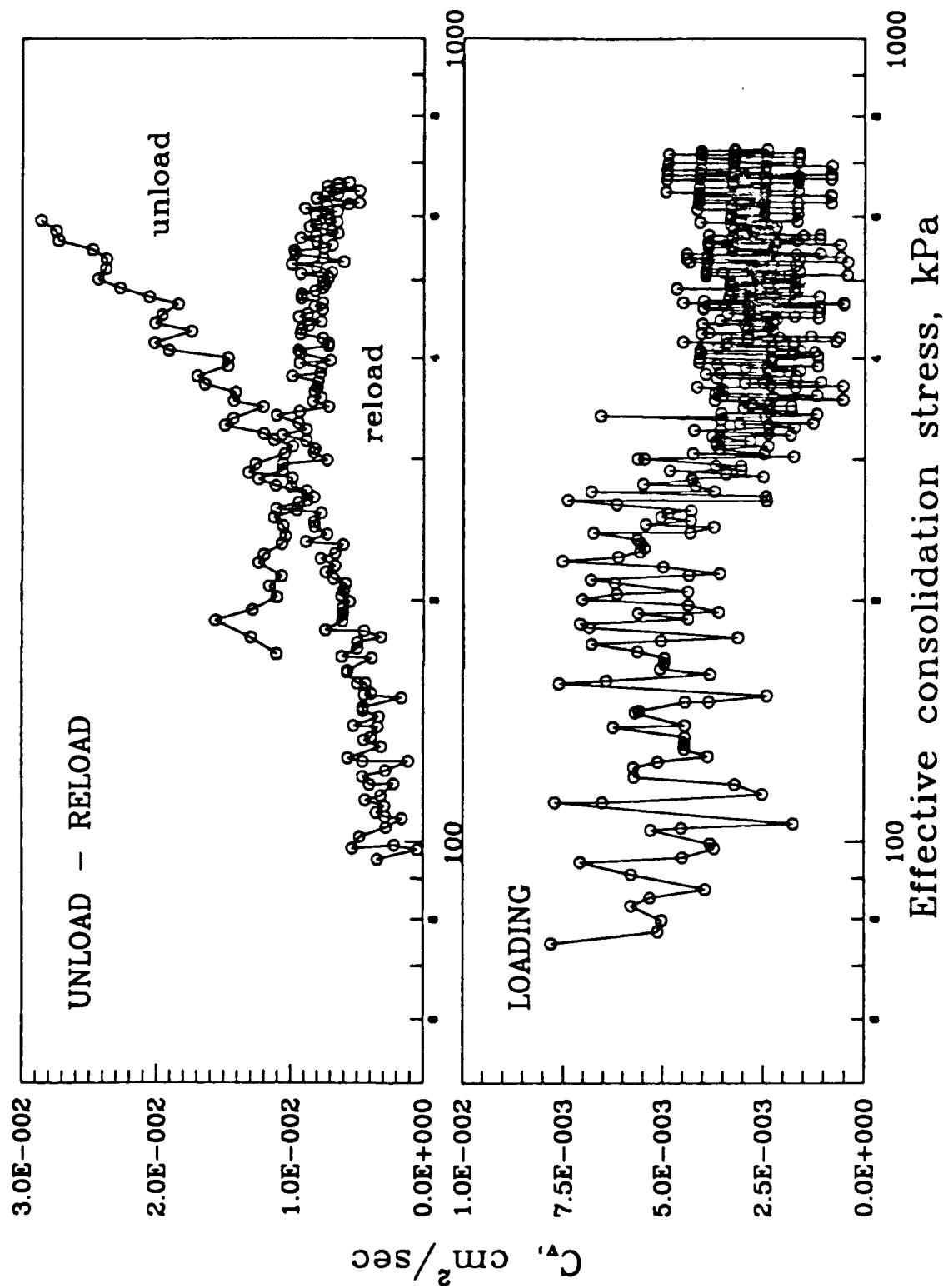
Figure 7.5: C_v versus effective consolidation stress for K100-2.

125
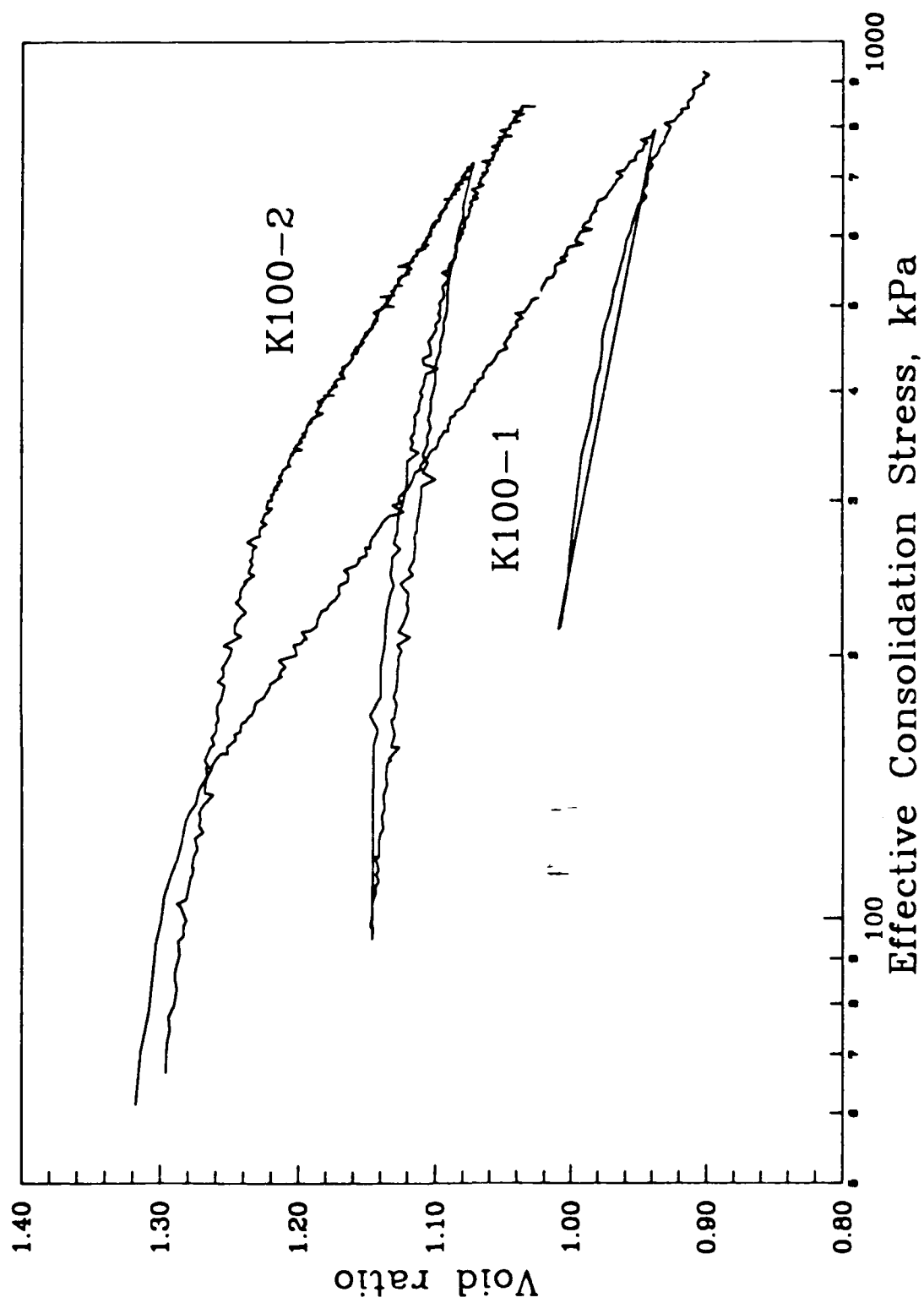
Figure 7.6: Void ratio versus effective consolidation stress of tests K100-1 and K100-2.
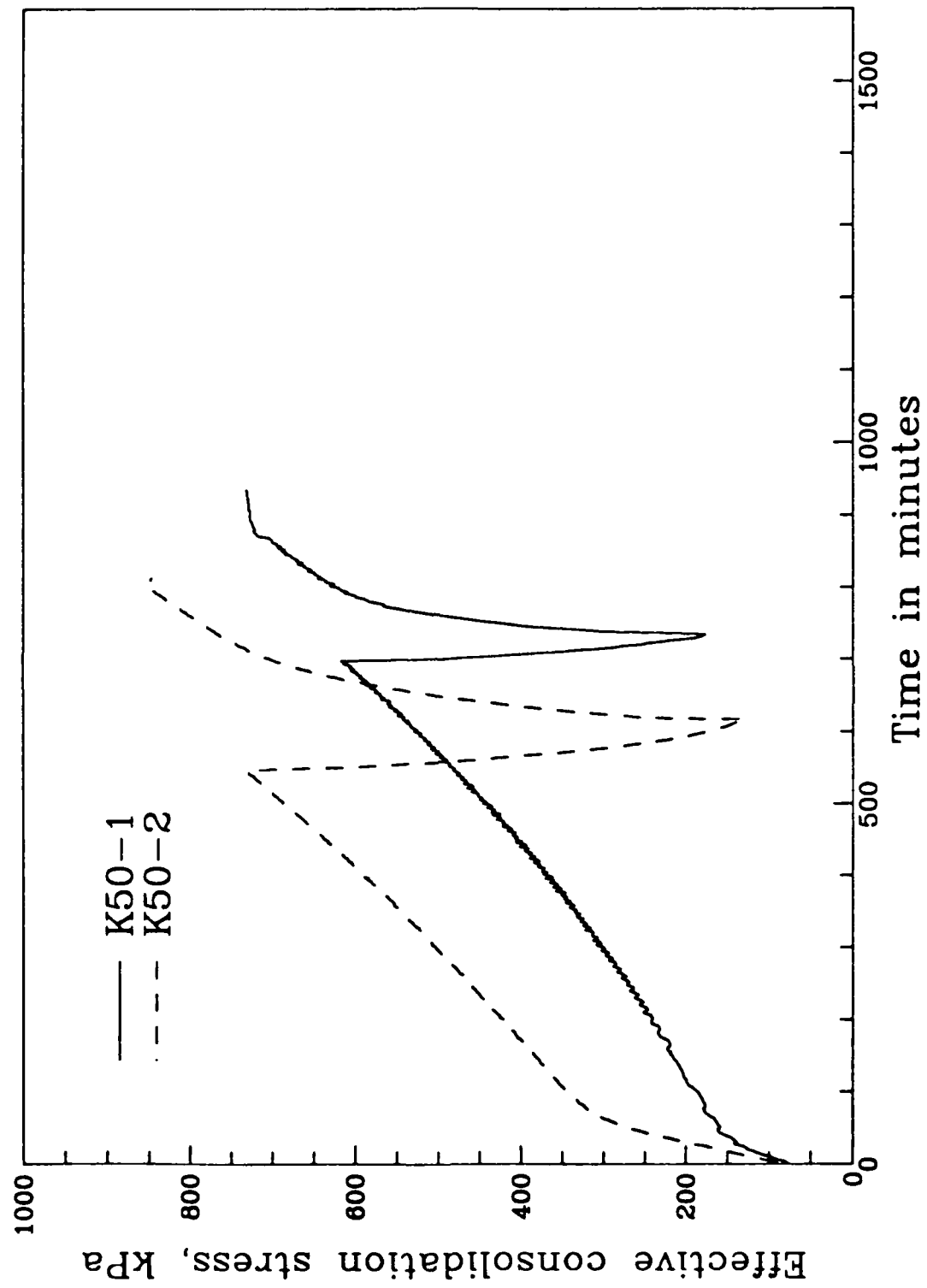
Figure 7.7: Time displacement curves of tests K50-1 and K50-2.

127
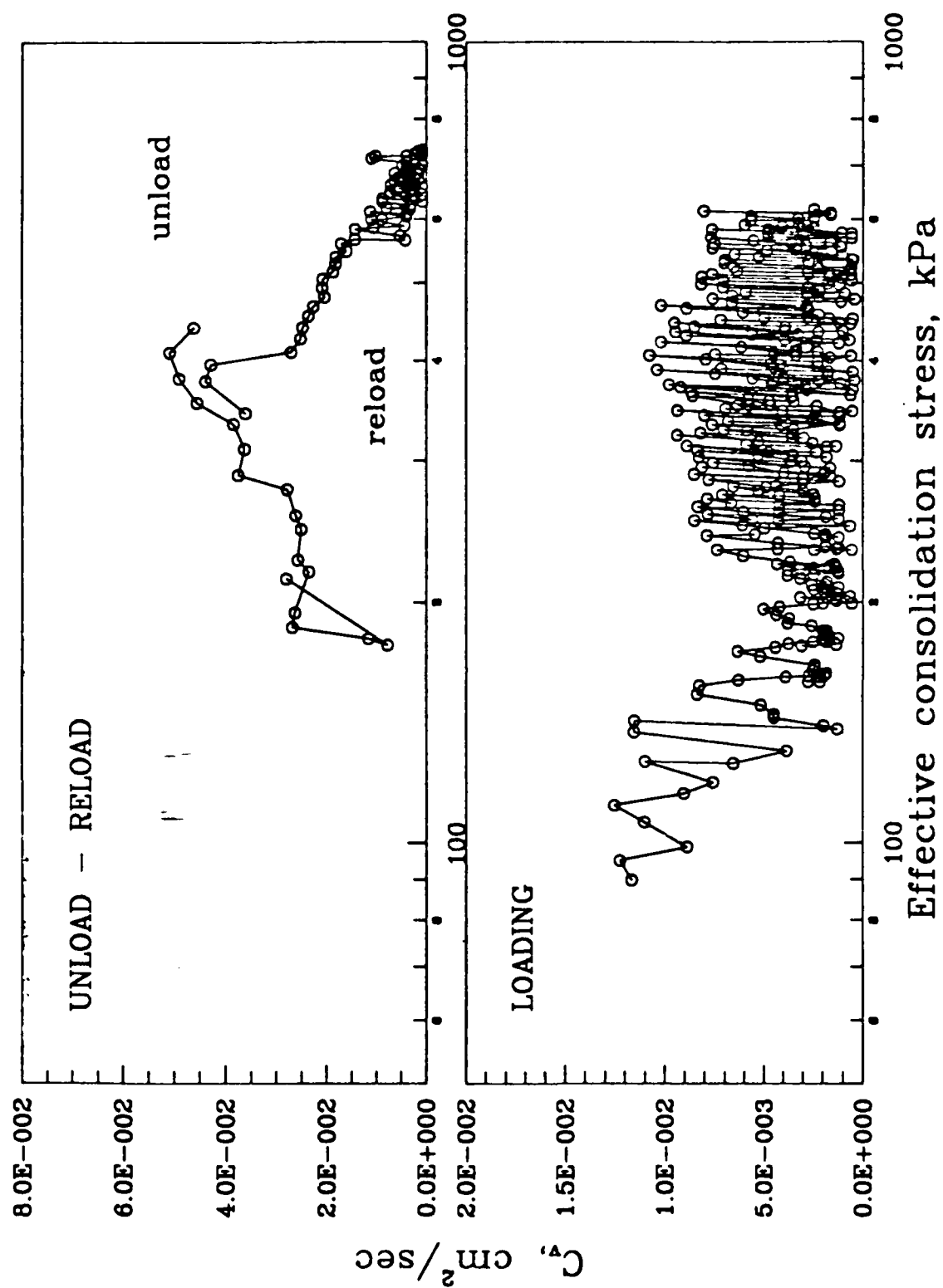
Figure 7.8: C_v versus effective consolidation stress for K50-1.

128
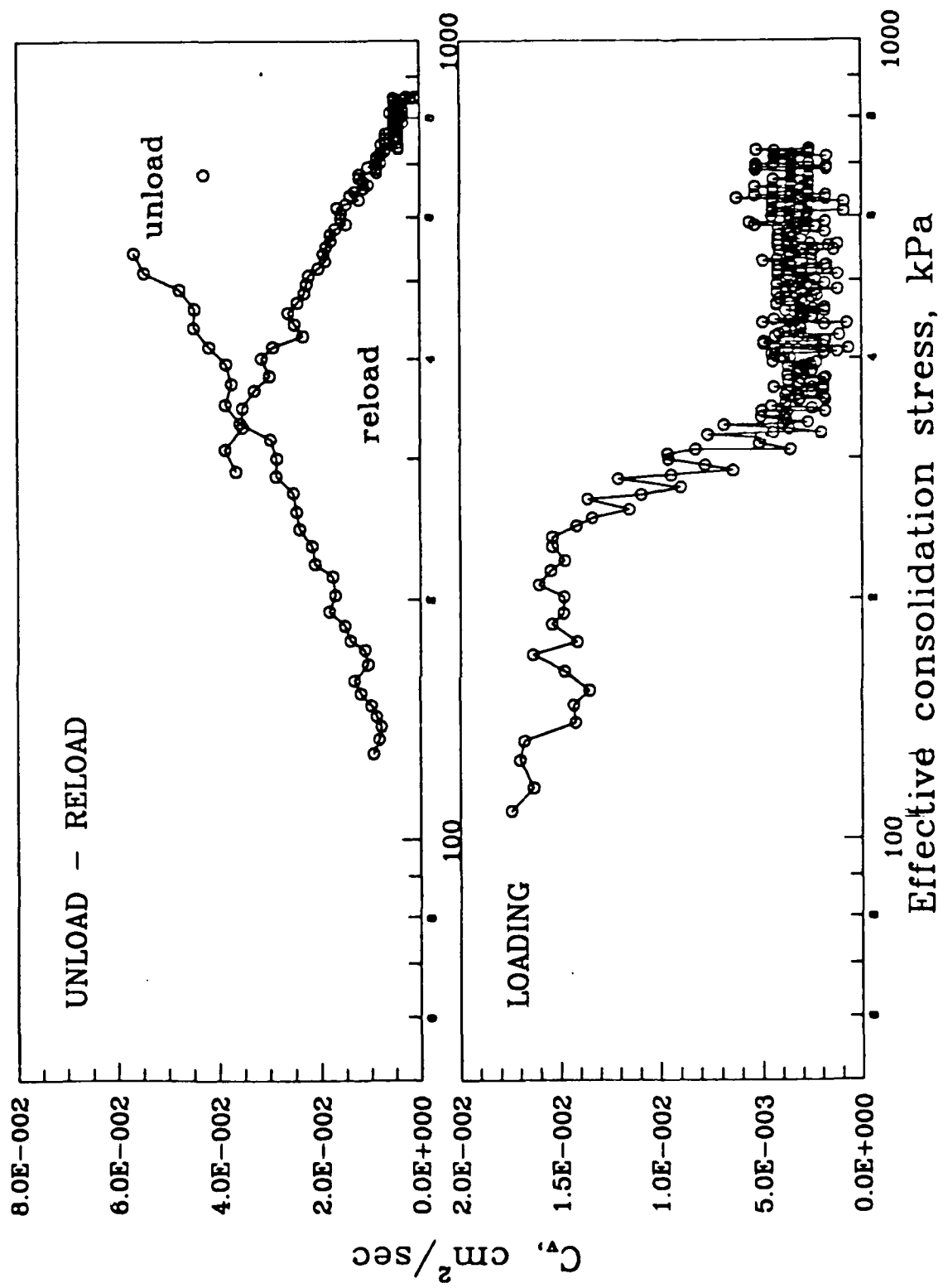
Figure 7.9: C_v versus effective consolidation stress for K50-2.

129

7.3 Undrained stress-strain and Strength Relationships

A series of isotropically and anisotropically consolidated undrained triaxial tests (CIU and CAU) were conducted to establish the stress-strain and strength relationships of the K50 clay. Triaxial tests were limited to K50 specimens since this was the only soil used in the calibration chamber tests.

The same slurry preparation and consolidation process as in the consolidation tests were used to create triaxial test specimens. The slurry consolidometer was made of a plexiglass tube with an inside diameter of 62 mm and a total height of 380 mm (see Figure 7.11). Consolidation pressure was applied through the top piston. Drainage was allowed at both the top and bottom of the specimen. The height of the specimens were approximately 150 mm and the water content was at 27-28% at the end of slurry consolidation. Upon extrusion, the specimen was inserted directly into a rubber membrane. Trimming was necessary only at the ends of the specimen to a final required height for the triaxial test of 140 mm. All specimens were consolidated and sheared under a back pressure of 550 kPa.

7.3.1 CIU Triaxial Test Results

The CIU tests included axial compression and extension tests on specimens normally consolidated (σ'_{vo} = 218, 360, 505 kPa) and overconsolidated (OCR = 5 and 10). To evaluate the strain rate effects, a series of tests were performed on normally consolidated specimens with strain rates of 0.013, 0.127, and 0.508 cm/min. Tests with unload reload cycles were performed on NC and OC specimens. These cycles were applied after the peak stress difference was reached. The SPM studies indicated that soil elements around a penetrometer typically experience a process of unloading (cone and flat-plate) and reloading (flat-plate) only after a large strain or soil failure has occurred. Previous laboratory experimental studies have been limited to unload-reload

130
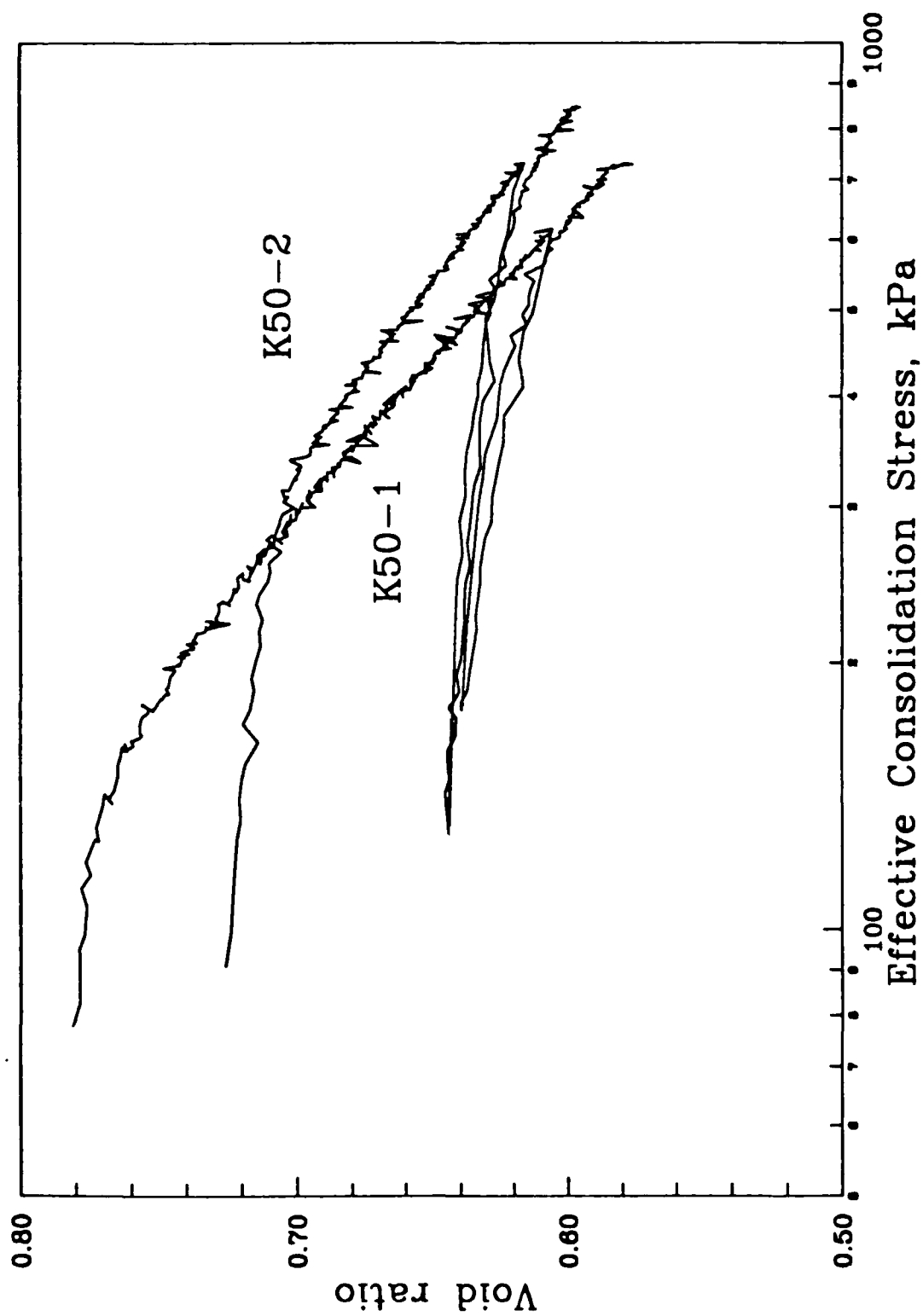
Figure 7.10: Void ratio versus effective consolidation stress of tests K50-1 and K50-2.
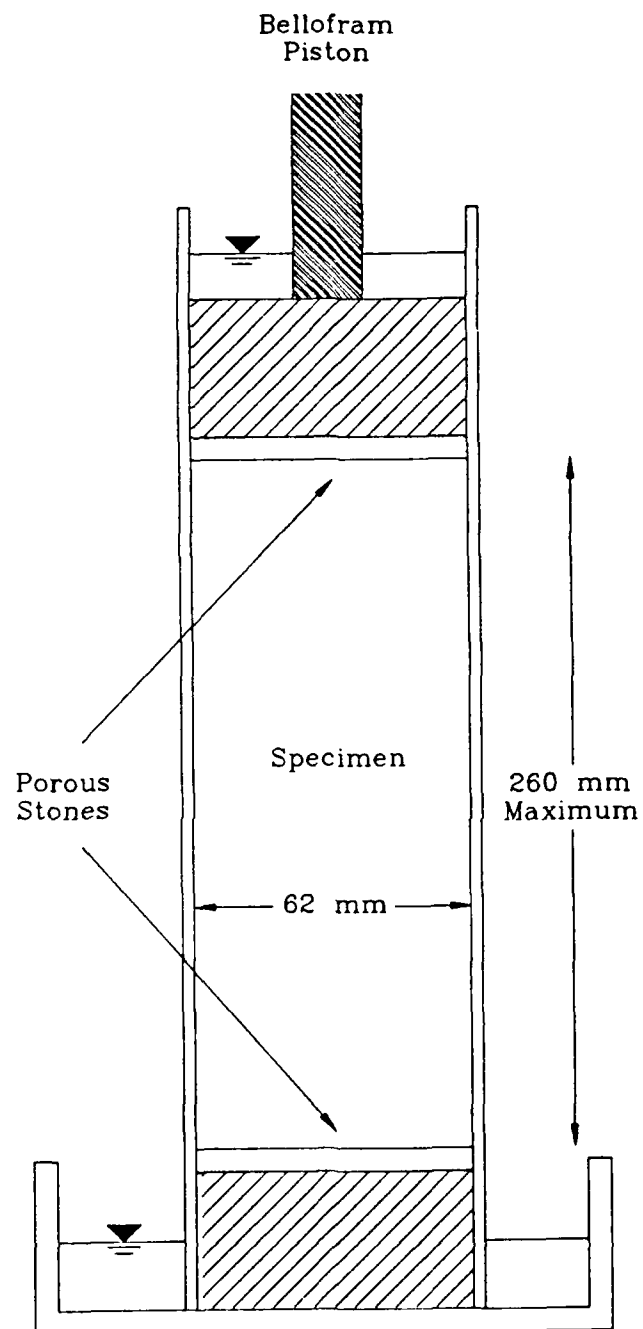
Figure 7.11: Cross sectional view of the slurry consolidometer for triaxial specimens.

132

cycles prior to soil failure. Therefore, these cyclic tests have important implications for the interpretation of penetration tests.

A number of key parameters were determined for each triaxial test. They included Skempton's pore pressure parameter at failure (A_f) (Skempton, 1954), and the undrained Young's modulus at 50 % of the maximum deviator stress (E_{50}). Other key parameters included s_u, the undrained shear strength, ϕ', the friction angle and M, the slope of the critical state line. These parameters are defined as follows.

$$A_f = \frac{\Delta u}{\Delta(\sigma_1 - \sigma_3)} \tag{7.1}$$

$$E_{50} = \frac{(\sigma_1 - \sigma_3)_{max}/2}{\epsilon_f/2} \tag{7.2}$$

$$s_u = \frac{(\sigma_1 - \sigma_3)_{max.}}{2} \tag{7.3}$$

$$\phi' = sin^{-1}(tan(\psi)) \tag{7.4}$$

$$M = \frac{3(\frac{1+sin\phi'}{1-sin\phi'}) + 3}{2(\frac{1+sin\phi'}{1-sin\phi'}) + 4} = \frac{(\sigma_1' - \sigma_3')_{critical}}{(\sigma_1' + 2\sigma_3')/3} \tag{7.5}$$

Figure 7.12 shows the effective stress paths for the tests on NC and OC specimens. The stress-strain curves normalized with respect to the preconsolidation stress for all the tests on NC specimens are shown in Figure 7.13. The closeness of these normalized stress-strain curves indicates that the tests are reasonably repeatable and that K50 has a fairly normalized behavior. Tables 7.3 and 7.4 present a summary of the key parameters found in compression and extension triaxial tests respectively. The (A_f) values would indicate that the K50 may behave like a sensitive clay. This is most likely due to the substantial amount of sand in the clay mixture. However, the stress-strain curves show only slight strain softening in the axial compression tests on NC specimens (see Figure 7.13).

Figures 7.14 and 7.15 show the effective stress path of the tests with load-unload cycles on NC and OC specimens respectively. The data show that regardless of the

stress history, the excess pore pressure experiences an increase and then decrease during the reloading process (Figures 7.16 and 7.17). The stress path during reloading is similar to that of an OC clay even when the soil is normally consolidated as shown in Figure 7.14. As a result, the stress path crosses the critical state line which violates one of the fundamental concepts in critical state soil mechanics. It should be emphasized at this point that the triaxial test is known for its unreliability while performing tests with unload-reload cycles. This is mainly due to the inevitable delay during the change of loading direction. These tests may therefore not be repeatable. However, the evidence is sufficient to indicate that a post failure unload-reload process does involve significant variation of pore pressure. Furthermore, this variation may not follow the conventional pattern as indicated by previous studies which are limited to unload-reload cycles applied before failure. Since excess pore pressure is an important part of the interpretation and essentially all penetration tests involve post failure unloading and/or reloading. It is therefore imperative to establish, experimentally, the behavior of soils under these conditions before the theories can be refined.

Figure 7.18 shows the normalized stres-strain curves of tests on NC specimens with varying strain rates. The results show an approximate increase of peak deviator stress of 17.5% for every ten fold increase of the strain rate.

7.3.2 CAU Triaxial Test Results

The CAU tests included an axial compression and extension test on specimens normally consolidated at 218 kPa. Anisotropic consolidation was performed while maintaining a K value of 0.52 (σ'_h/σ'_v). The K value was determined from the isotropically consolidated triaxial tests by using the ϕ' value and the equation, $K = 1 - sin\phi'$. Drainage was allowed against the back pressure at the top of the specimen only. The cell and axial pressure were servo-controlled to maitain an excess pore pressure of 34 kPa at the bottom of the specimen while keeping the K value at 0.52. Undrained shearing was performed at a strain rate of 0.01% per minute. Key parameters deter-

mined from the tests are summarized in Table 7.5. Plots of deviator stress and pore pressure versus the axial strain are shown in Figures 7.19 and 7.20. The strain paths for both tests are shown in 7.21.

Test	A_f	E_{50}, kPa	s_u, kPa	E_{50}/s_u	s_u/P_o'
NC(218 kPa)	1.25	48,000	60	800	0.28
NC(360 kPa)	1.44	91,000	91	1000	0.25
NC(505 kPa)	1.36	87,900	123	700	0.24
OC(OCR = 5)	0.12	480,000	96	500	0.89
OC(OCR = 10)	-0.19	6,600	64	100	1.35
$\phi' = 29.2°, M = 1.194$					

Table 7.3: Summary of the CIU triaxial tests sheared in axial compression.

Test	A_f	E_{50}, kPa	s_u, kPa	E_{50}/s_u	s_u/P_o'
NC(218 kPa)	0.41	65,700	46	1400	0.21
NC(360 kPa)	0.50	118,600	83	1400	0.24
NC(505 kPa)	0.53	151,200	108	1400	0.21
OC(OCR = 5)	-0.10	106,000	53	2000	0.65
OC(OCR = 10)	0.40	73,000	73	1000	1.04
$\phi' = 28.5°, M = 1.189$					

Table 7.4: Summary of the CIU triaxial tests sheared in axial extension.

Test	A_f	E_{50}, kPa	s_u, kPa	E_{50}/s_u	s_u/P_o'
compression	0.59	110,500	65	1700	0.30
extension	1.11	15,000	20	750	0.09
$\phi' = 27.2°, M = 1.180$					

Table 7.5: Summary of the CAU triaxial tests (NC 218 kPa).

136
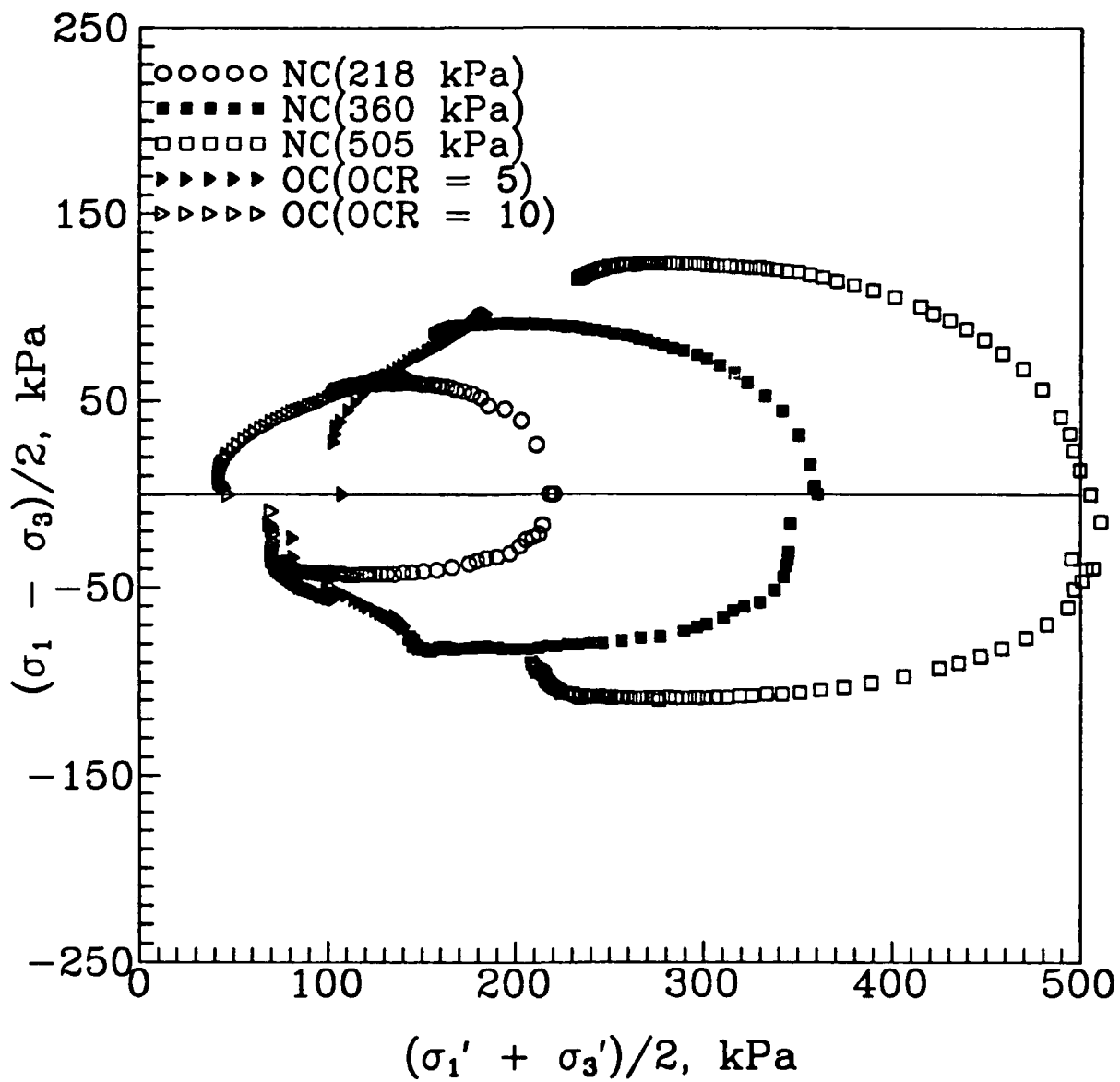
Figure 7.12: Effective stress path of the CIU triaxial tests.
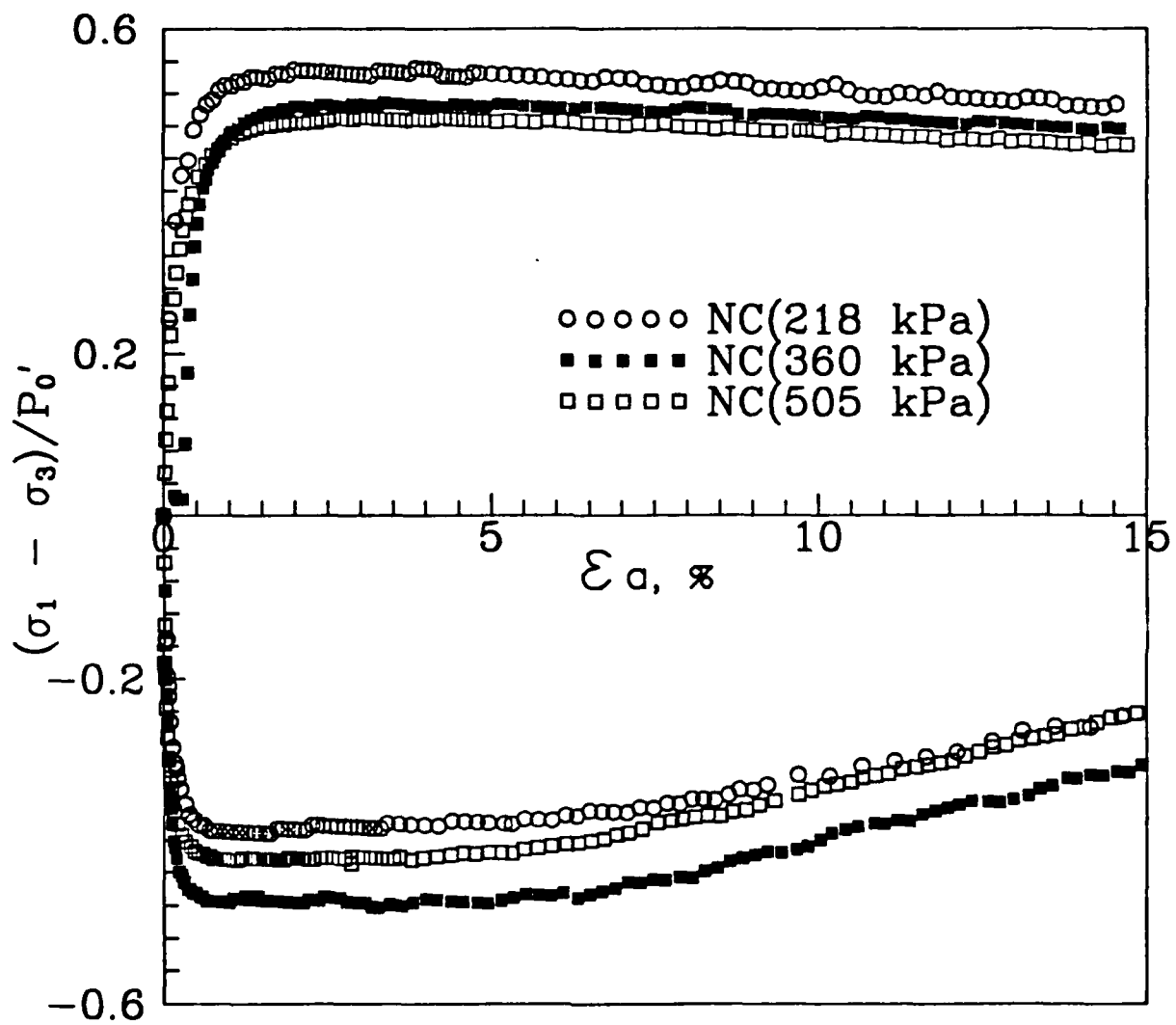
Figure 7.13: Normalized deviator stress versus strain for the NC CIU triaxial tests.
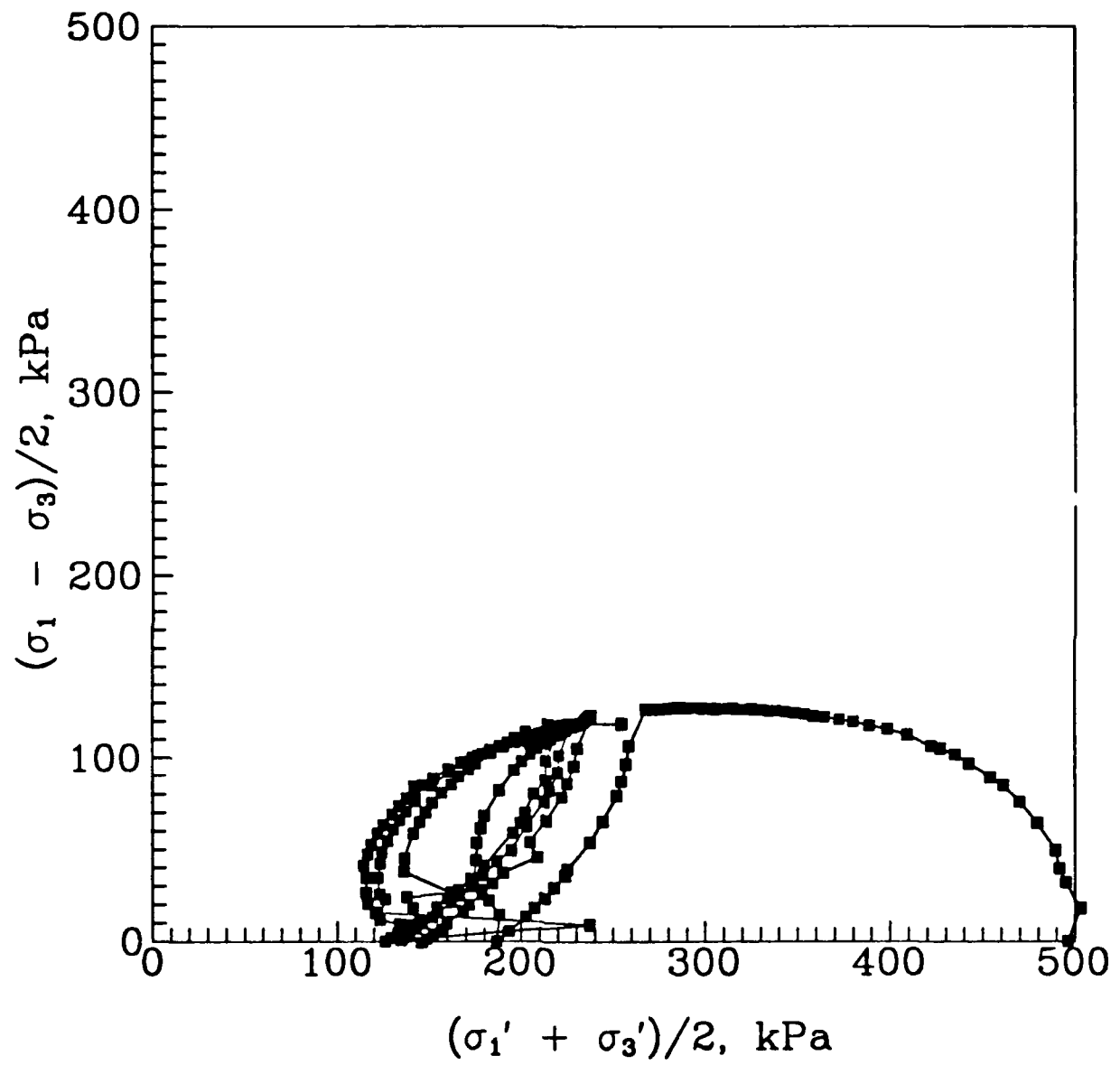
Figure 7.14: Effective stress path of the NC load - unload triaxial test.

139
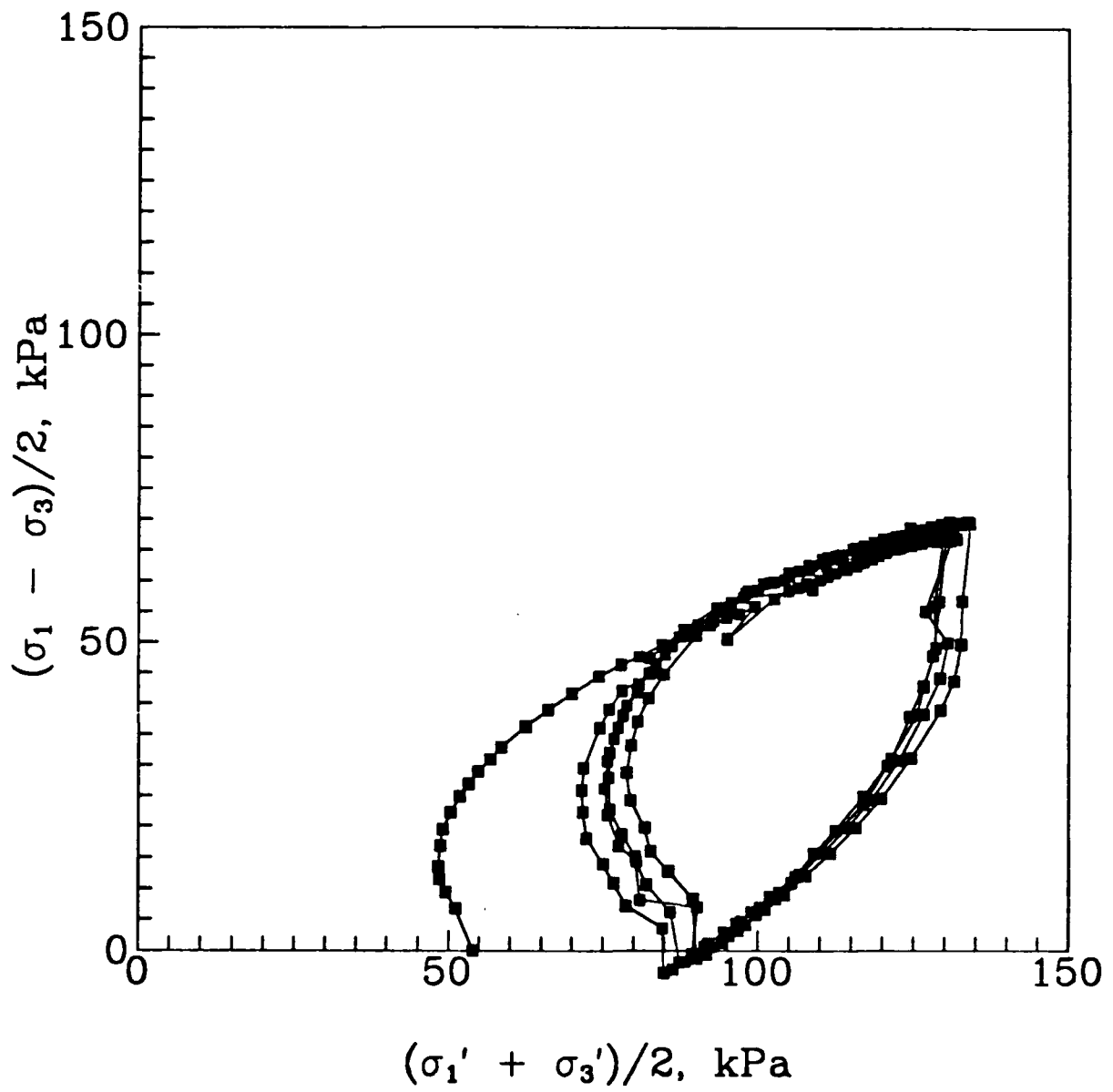
Figure 7.15: Effective stress path of the OC load - unload triaxial test.
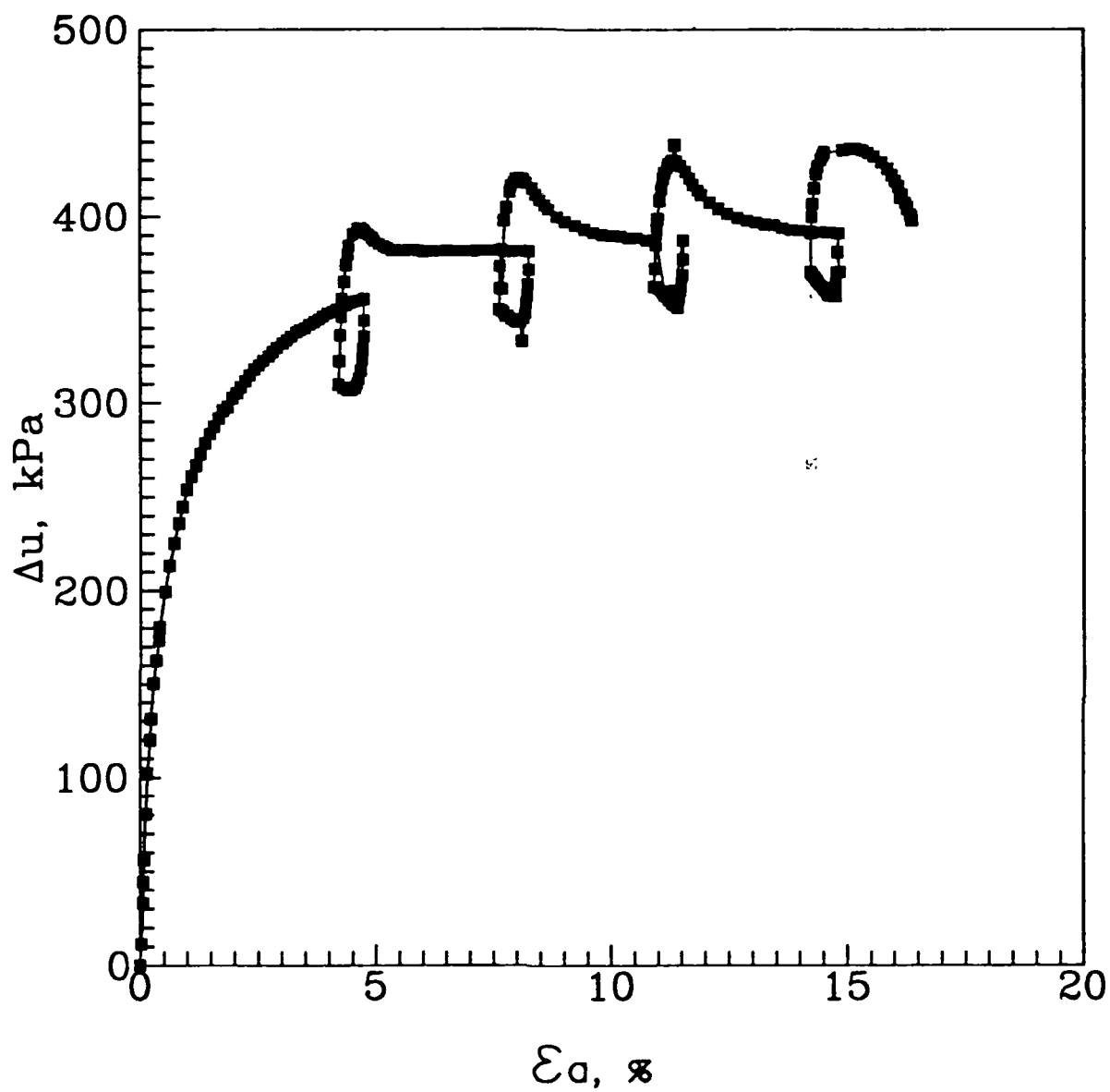
Figure 7.16: Change of pore pressure versus strain for the NC load-unload triaxial test.
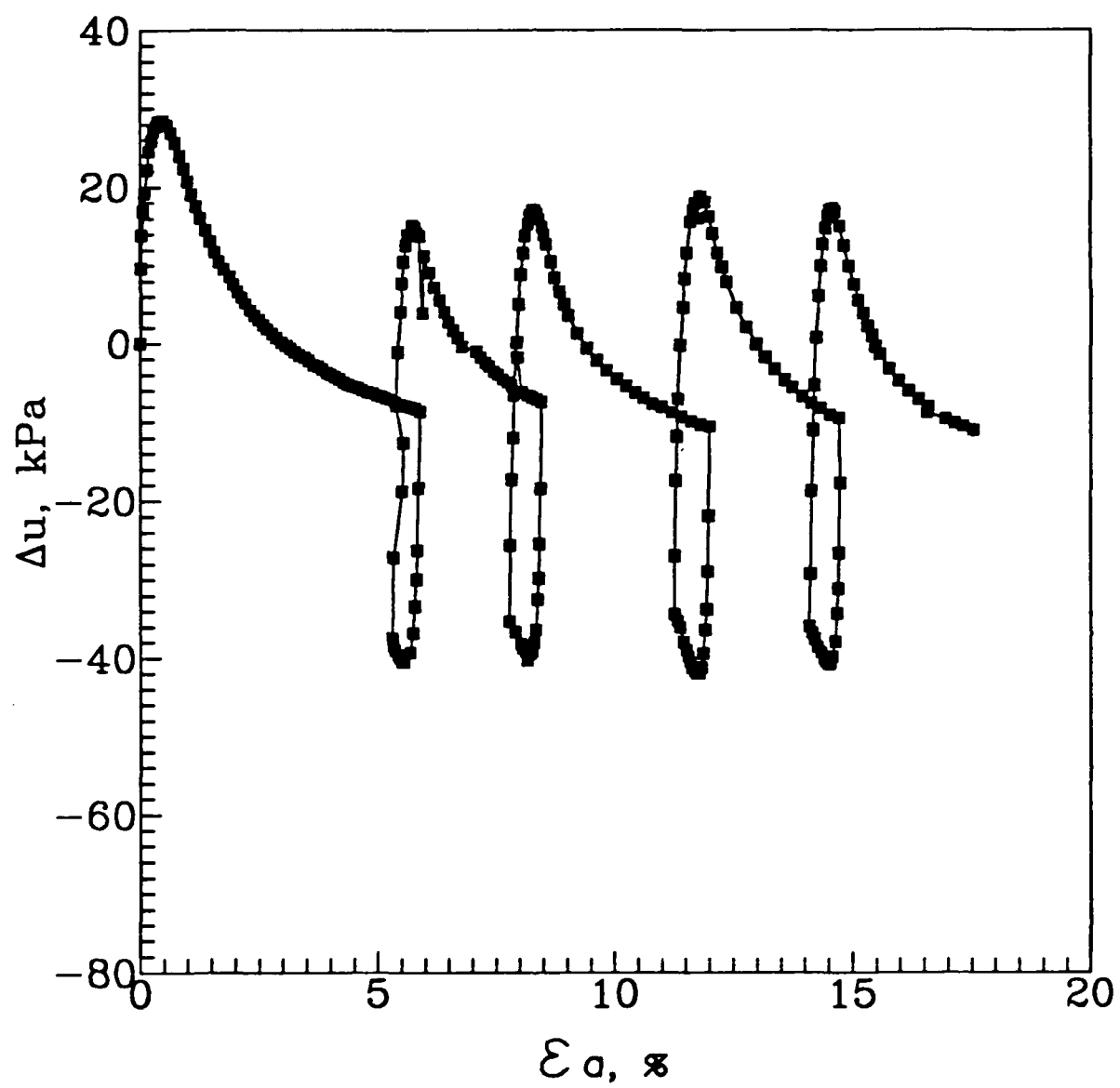
Figure 7.17: Change of pore pressure versus strain for OC load-unload triaxial test.
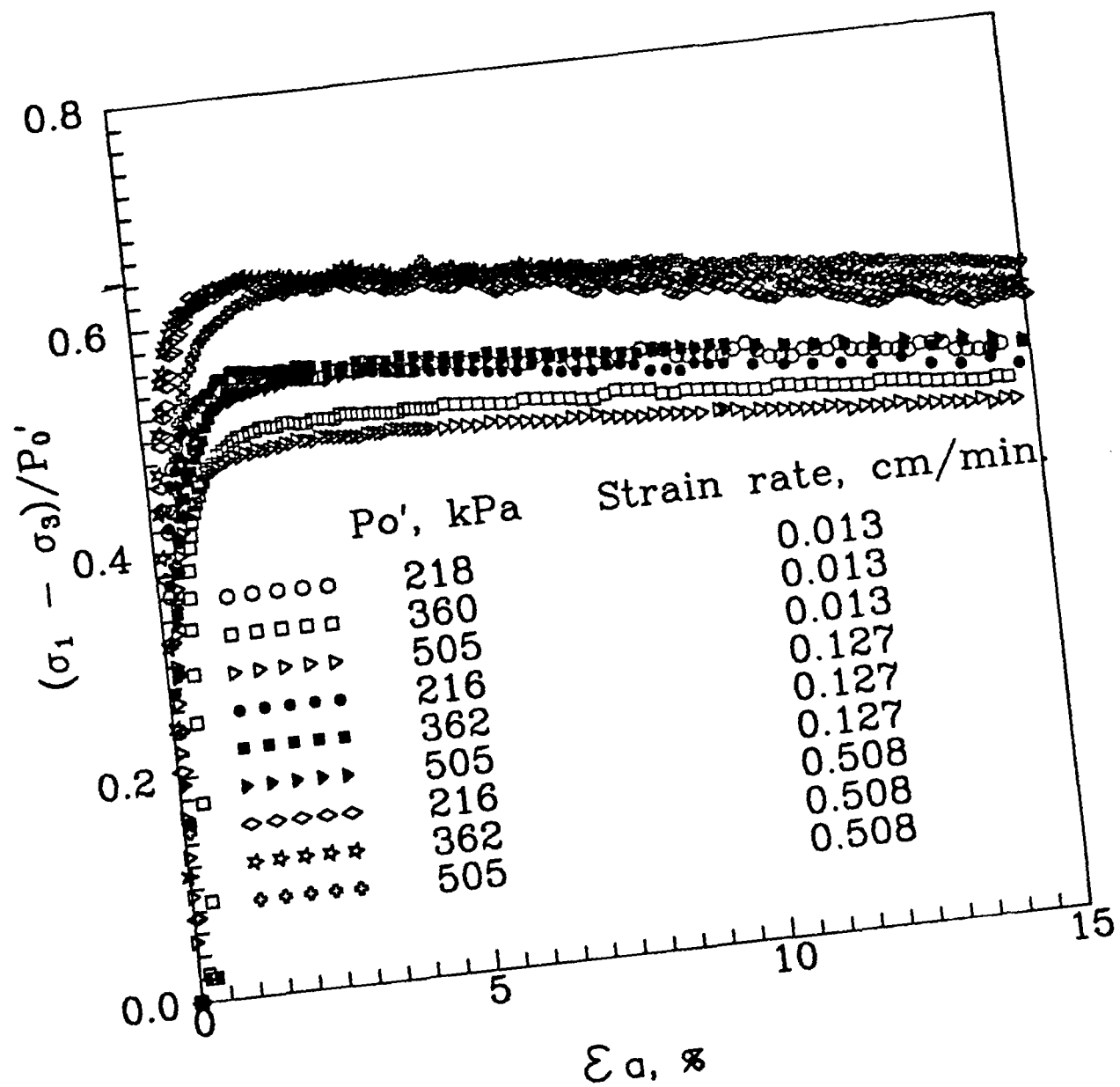
Figure 7.18: Normalized deviator stress versus strain for different shearing strain rates.

143
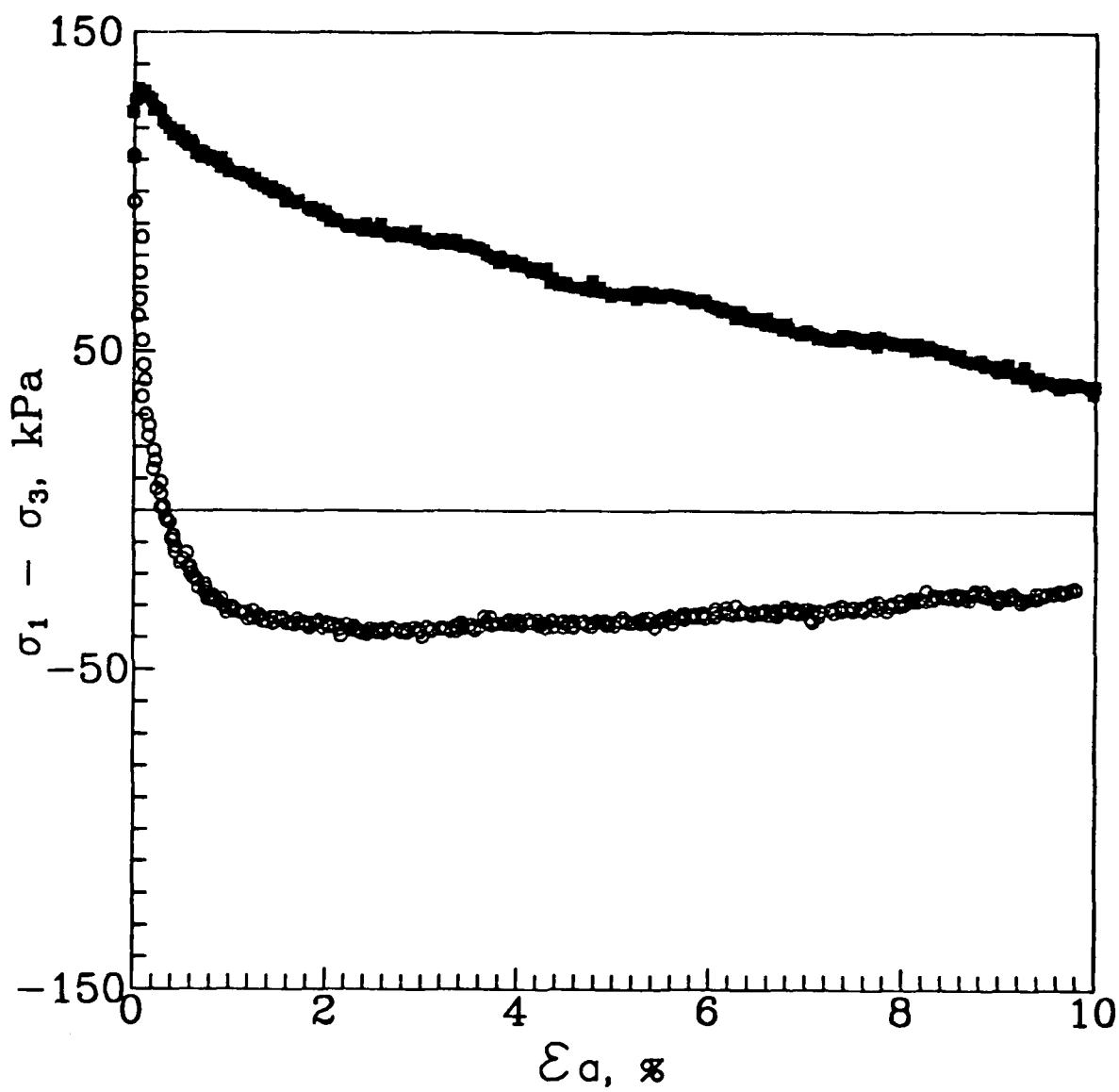
Figure 7.19: Deviator stress versus strain for anisotropically consolidated specimens.
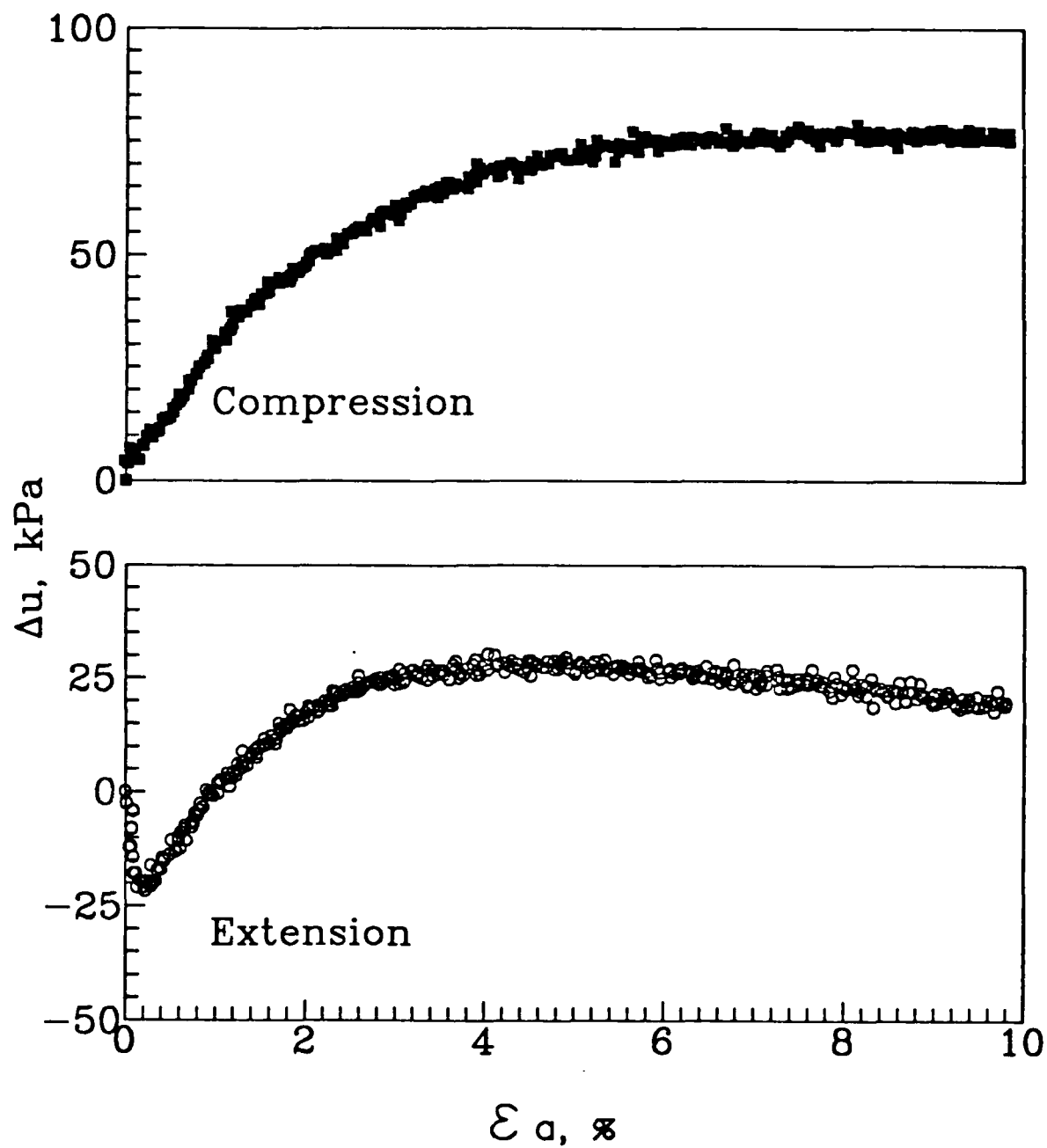
Figure 7.20: Change of pore pressure versus strain for anisotropically consolidated specimens.
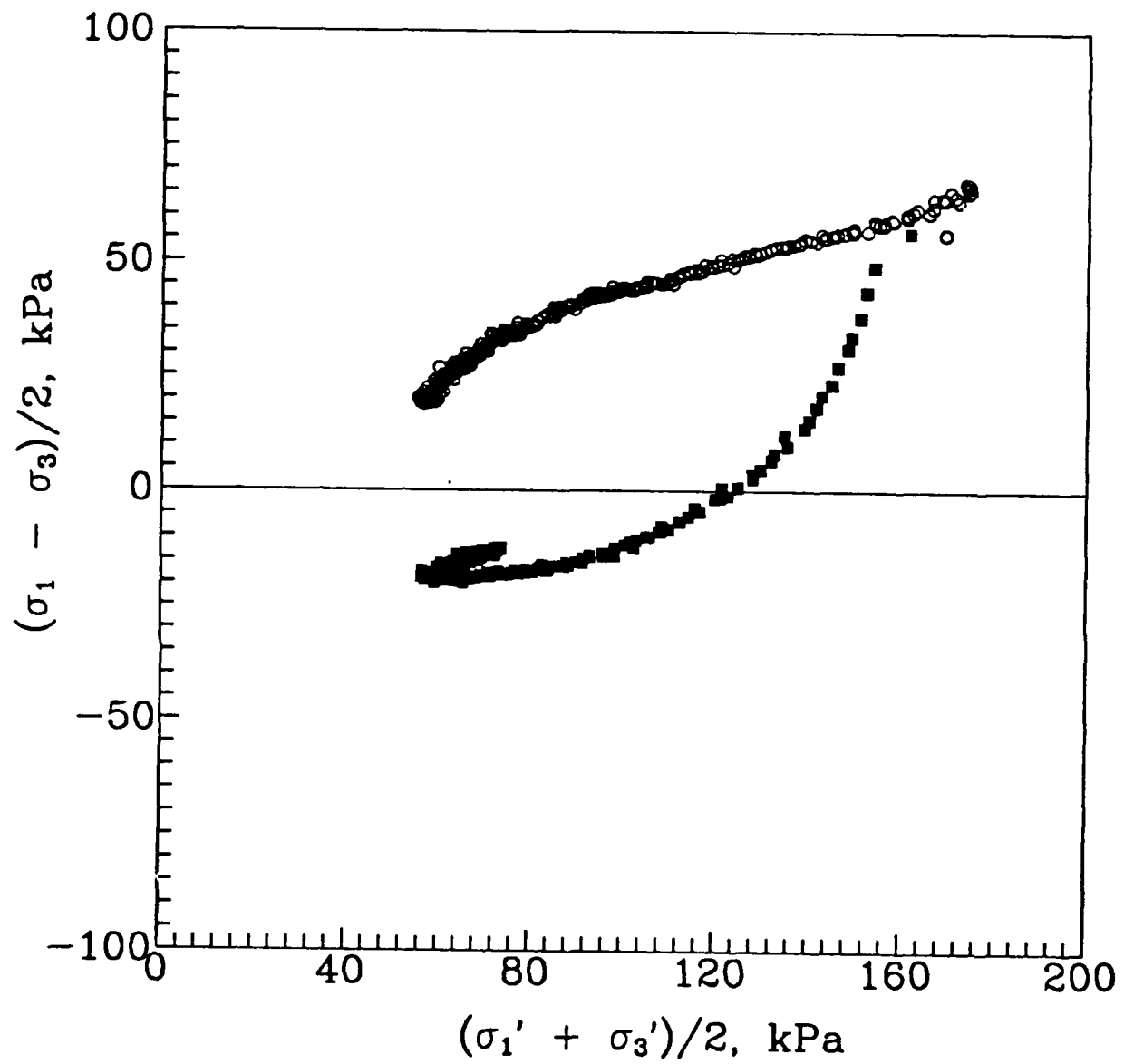
Figure 7.21: Effective stress path of the anisotropically consolidated specimens.

Chapter 8

The Calibration Chamber System, Testing Procedure and Program

A slurry consolidation and a calibration chamber system were fabricated for the research. The system enables a clay specimen to be consolidated from slurry and then transported to the chamber for the second stage consolidation and the calibration test. Designs of the testing devices and set up followed the techniques developed by Huang (1986). The system included a slurry consolidometer, a computer servo controlled calibration chamber system and model flat-plate penetrometers. This chapter provides the details of these apparatuses their applications and the testing program.

8.1   The Slurry Consolidometer

The slurry consolidometer (Figure 8.1) consists of two pieces of PVC tube with an inside diameter of 524 mm which are tighed together by steel rods. The entire unit rests on a frame with casters attached to the bottom to provide mobility.

The uper PVC pipe (see Figure 8.1) houses a piston and provides additional room to hold the slurry during the early stage of slurry consolidation. The bottom compartment was split into two sections longitudinally and a steel frame was mounted
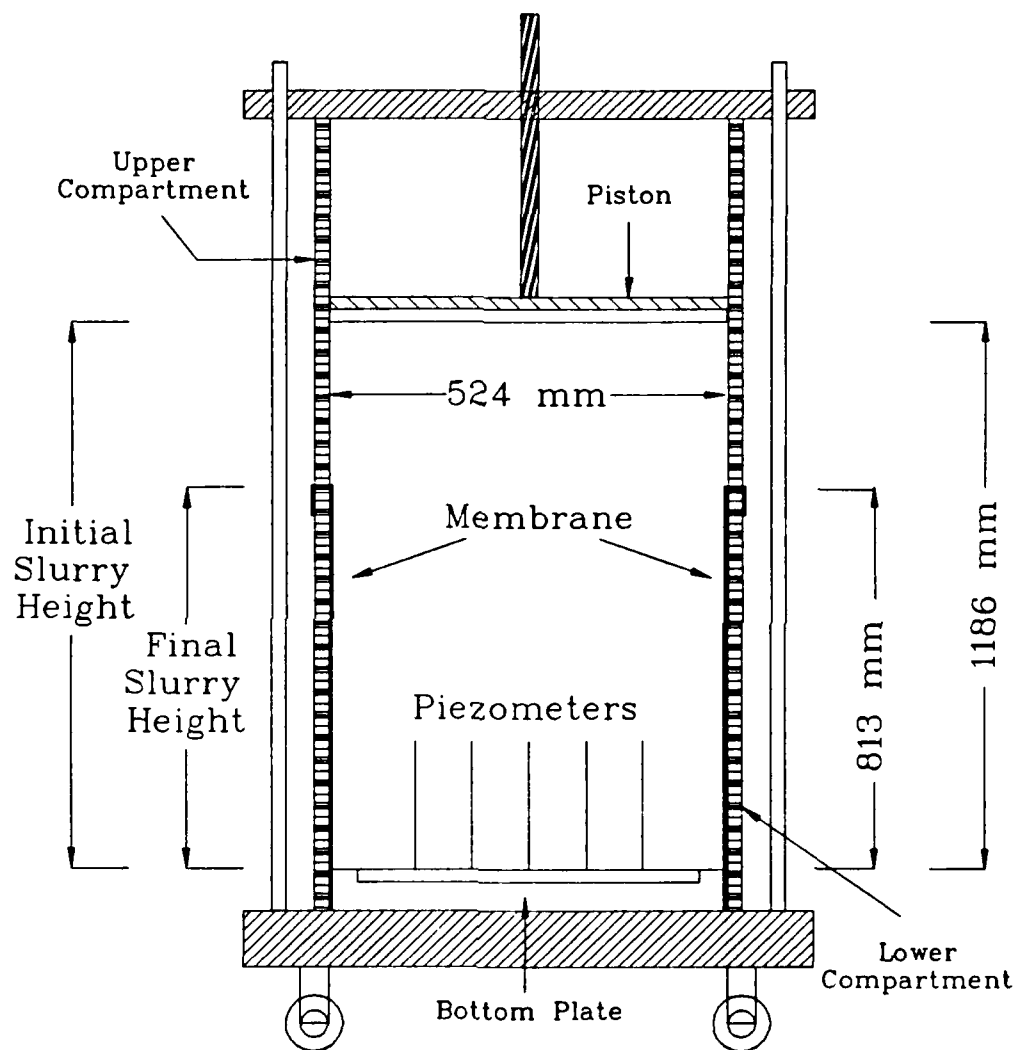
Figure 8.1: Cross sectional view of the slurry consolidometer.

around each piece in order to clamp them together and ultimately take them apart once the soil specimen was ready. A rubber gasket was glued to the cut section of the lower compartment to seal it. Sand paper was attached to the inside of the lower compartment to prevent slippage of the membrane during consolidation. The membrane extended out of the lower compartment and acted as a seal between the two compartments.

The piston consists of an aluminum plate with porous plastic attached to it and an aluminum rod screwed into it to provide some stability. The piston is moved down as air is pumped into a number of rubber truck inner tubes that are joined together with 3.2 mm nylon tubing. The bottom aluminum plate is also the top of the piston for the calibration chamber, and along with the slurry consolidometer piston provides drainage at the top and bottom of the specimen during slurry consolidation. The consolidometer was designed for an initial slurry height of 1186 mm and a final height of 813 mm with a diameter of 524 mm.

8.2 The Calibration Chamber

The entire calibration chamber setup along with the pressure control system and the computerized data logging and control is shown in Figure 8.2. The chamber (Figure 8.3) was desgned to house a 524 mm diameter soil specimen with a miaximum height of 813 mm. A constant stress or zero strain condition can be applied in the vertical and the horizontal direction. The piston applies the vertical pressure and provides bottom drainage. The guide shaft keeps the piston straight as well as provides an opening for the transducer wires and drainage lines. The guide shaft runs through a linear ball bearing that was mounted underneath the base plate. The bottom plate is fitted with porous plastic, drainage lines, 13 piezometers which are attached to pressure transducers, and a pressure transducer mounted flush with the porous plastic that measures σ_v, the vertical stress. The piezometers were placed in such a way as to

measure pore pressure from different radii away from the penetrometer. In Figure 8.4, the piezometer locations are shown with their respective radii away from the center of the penetrometer. The piezometers were made of 1.65 mm diameter, 0.23 mm wall stainless steel tubings. They extended up 250 mm from the bottom plate. The tip was filtered with porous plastic. The stem of the stainless steel tubing was attached to a pressure transducer. All piezometers were installed and flushed with deaired water before the slurry consolidation. Upon insertion of the penetrometer from the top of the specimen, the piezometers will not interfere with the soil response. This is an important advantage of having the piezometers extend up from the bottom plate.

The chamber has two stainless steel drums (910 mm high, 6.5 mm thick) which form the "double wall". This is required if the specimen is to be consolidated under K_o conditions. When the pressure in both the cavities formed by thetwo walls is set equal, the inner wall becomes rigid.

The chamber system was designed to handle 1000 kPa maximum pressure. The pressure was regulated through a control panel by using *Fairchild* model 1000 regulators for manual control and *Fairchild* model T5700 I/P and E/P transducer regulators for computer control. Gages and pressure transducers were used to monitor the pressure.

8.3   Model Piezoblade

The model piezoblade was machined from a single piece of stainless steel and was 117 mm long, 42 mm wide and 7mm thick (Figure 8.5). Four cavities were incorporated to allow pore pressure measurements at different parts of the blade. The four cavities were filled with a porous plastic and were connected to transducer ports outside the chamber by means of stainless steel tubes (1.65 mm OD, 0.23 mm wall thickness). These tubes were laid in grooves cut on the face of the blade and through a 12.7 mm
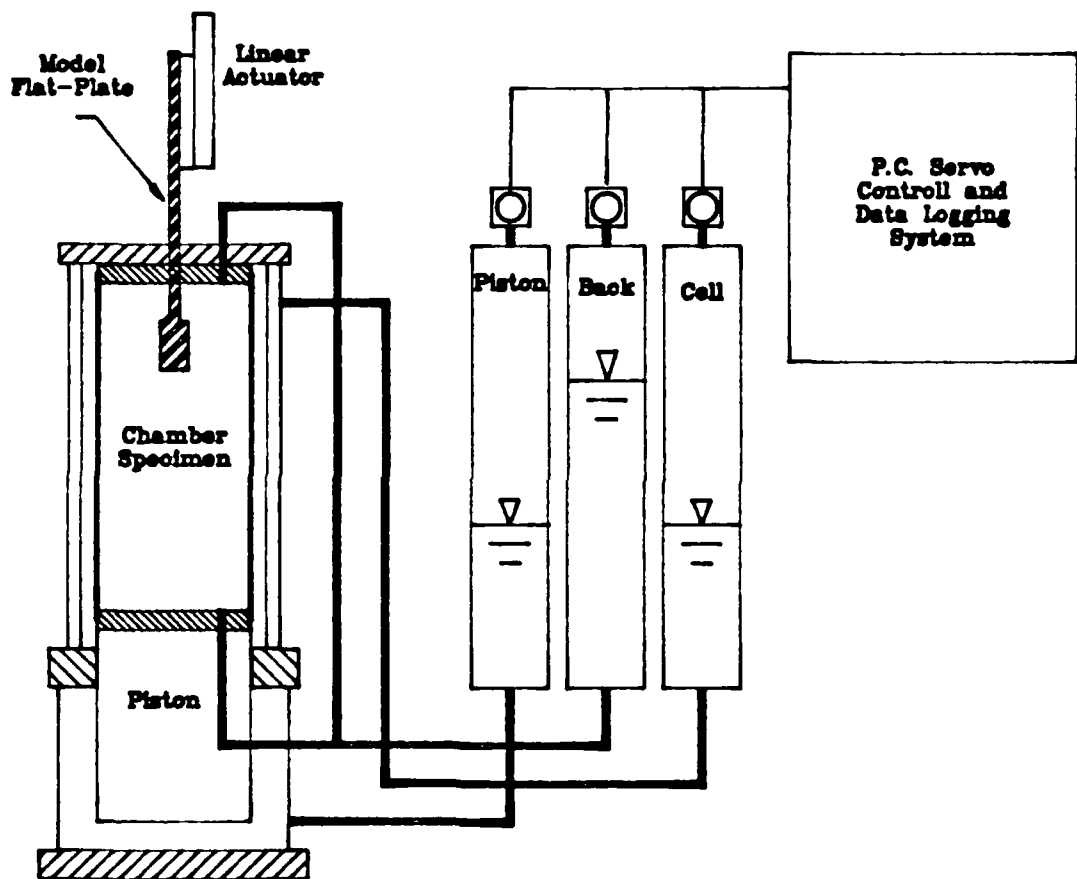
Figure 8.2: Calibration chamber control system.
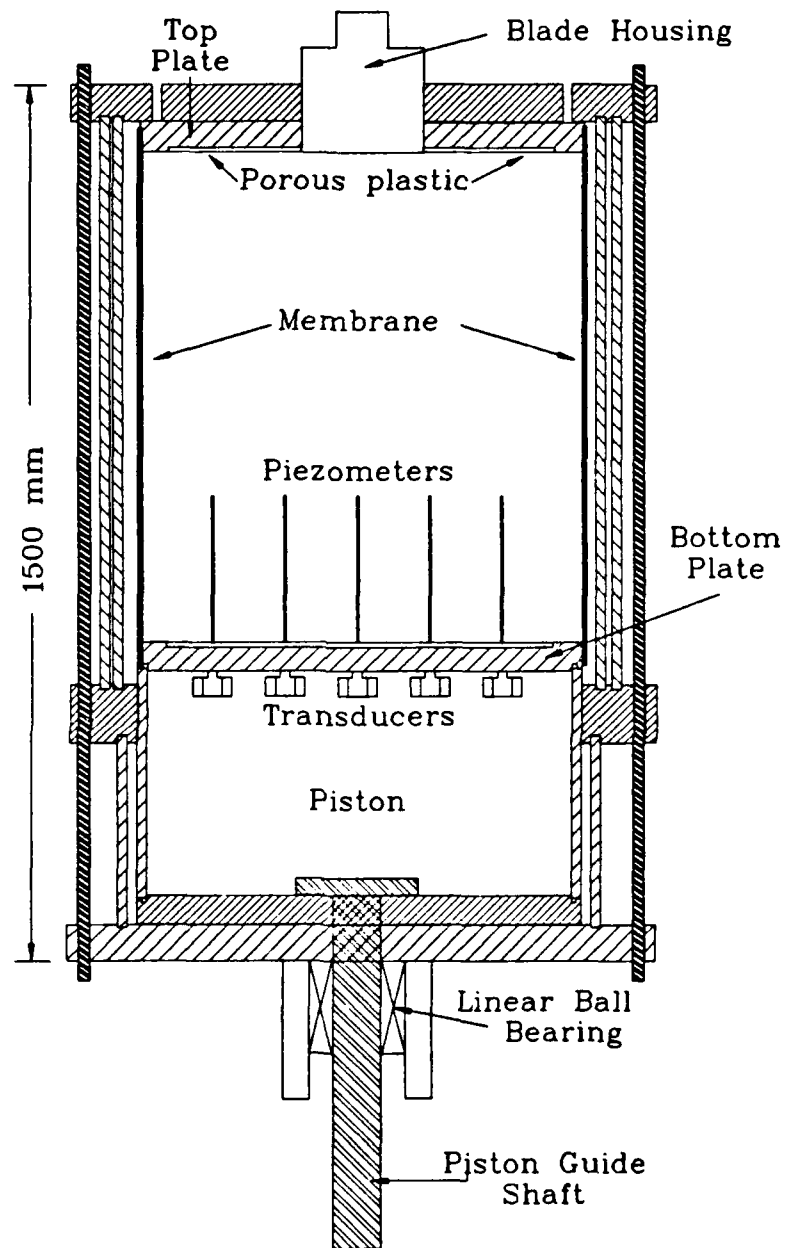
Figure 8.3: Cross sectional view of the calibration chamber.
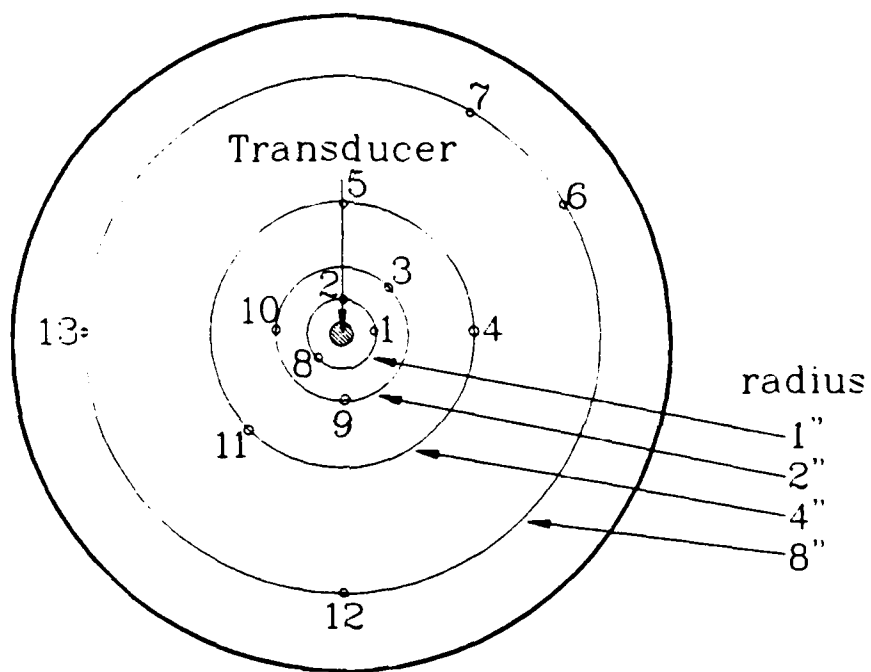
Figure 8.4: Piezometer locations on the top plate of the piston.

OD hollow stainless steel rod 914 mm long. The grooves on the blade were filled with an epoxy to give a smooth finish to the blade. The metal rod, which was used to push the blade, was also attached to the blade with epoxy.

8.4   Model Dilatometer (DMT)

The model Dilatometer (Figure 8.6) has the same dimensions as the model piezoblade. It is exactly 1/2 scale of the Marchetti flat Dilatometer. The tip apex angle is 20° and it has a 30 mm diameter expandable diaphram which was instrumented with a strain gage. The maximum membrane expansion allowed is 0.5 mm. The membrane itself was made of silicone rubber.

The same type of hollow rod used for pushing the piezoblade was attached to the model Dilatometer. A stainless steel tube used for pressure flow into the cavity along with the wires for the strain gage were placed through this rod.

8.5   Blade Housing

It was very important to have the soil contained inside the chamber during the consolidation and consequent blade insertion. In order to keep the back pressure on the soil specimen, a housing had to be developed to hold the blade during the consolidation phase of the procedure. This housing is shown in Figure 8.7.

This unit fit into the top plate of the calibration chamber and into the top drainage plate (Figure 8.3). Drainage ports were provided to flush the unit and to apply the back pressure to the exposed part of the soil. A teflon piece acted as the buffer between the soil and the blade. This teflon piece had a groove cut into it so that the blade and the rod could fit through. This unit also acted as a guide for the rod. A
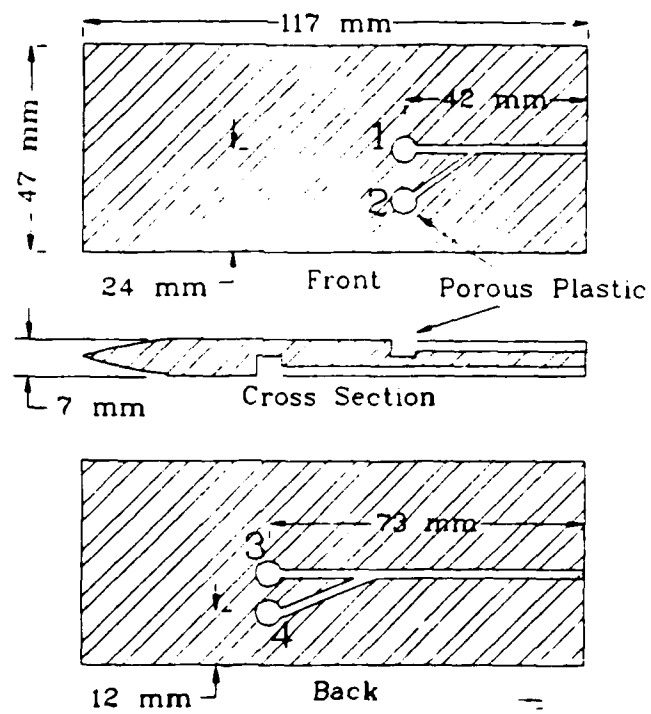
Figure 8.5: Geometry and dimensions of the model piezoblade.

- 7 mm

3 mm

2 mm deep channel

1.5 mm

1 mm

22.5 mm

Cross Section

45 mm

30 mm diam.

45 mm diam.

47 mm

Plane View

117 mm
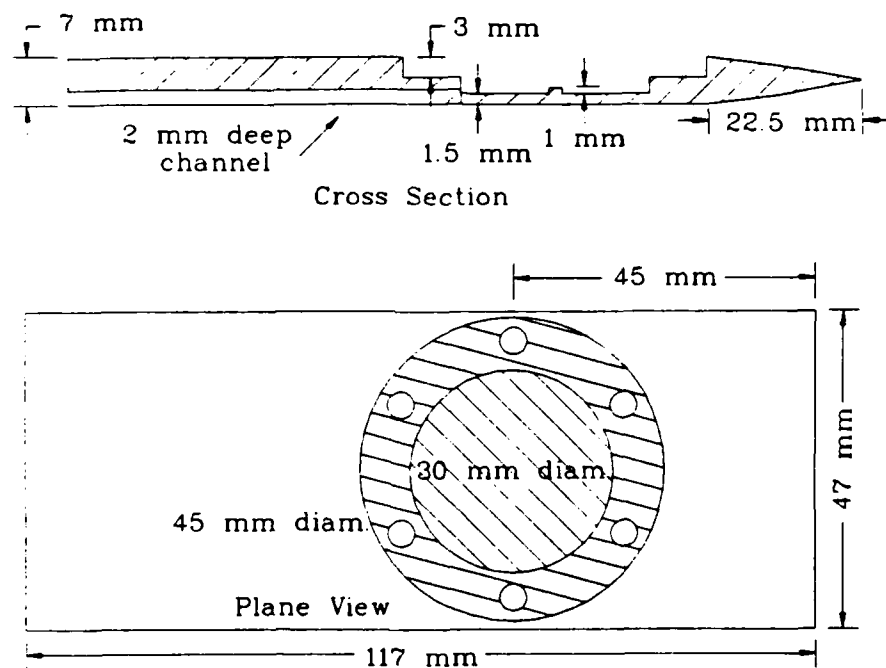
Figure 8.6: Geometry and dimensions of the model dilatometer.
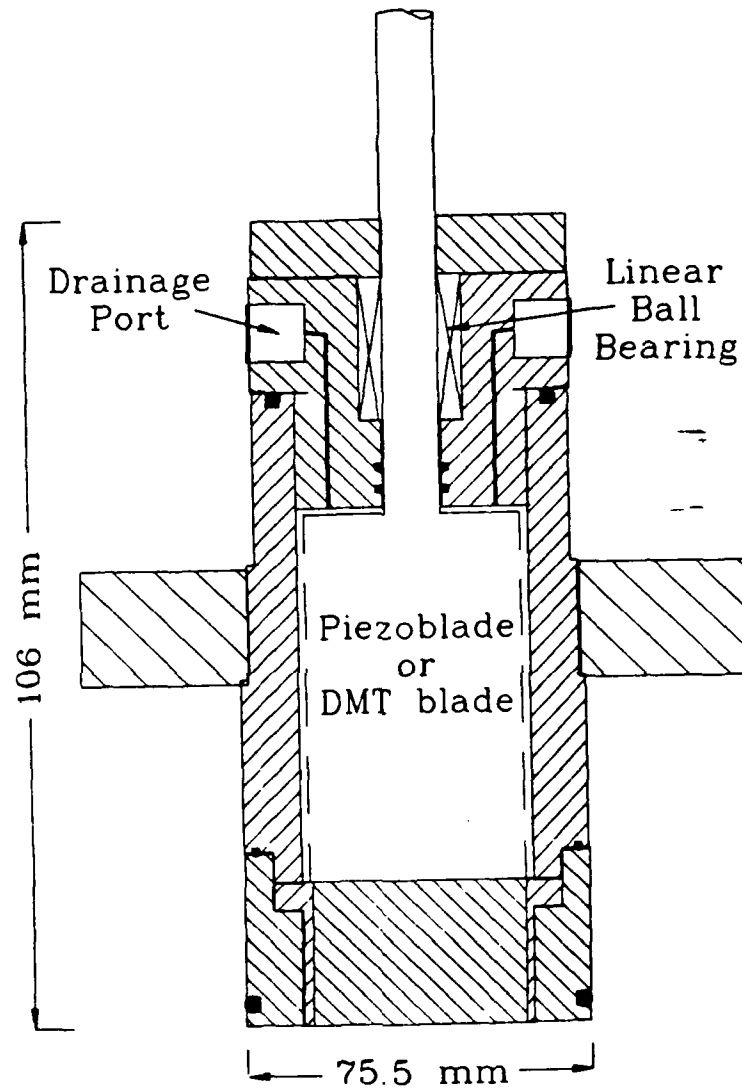
Figure 8.7: Cross sectional view of the blade housing.

linear ball bearing was used to keep the rod straight during the penetration.

8.6 Data Logging and Electrical Control System

A *Zenith* 248 personal computer was used along with a *Metrabyte* DAC-02 board and a *Keithley* Series 500 data logging system to read the pressure transducers and to control the cell and piston pressure during anisotropic consolidation. To control the penetration of the model penetrometers, a stepper motor driven linear actuator was incorporated. By using the stepper motor, the speed and exact position of the blade could be controlled.

Hewlett-Packard DC power supplies were used to supply the excitation voltage to all the transducers and the strain gages in the model Dilatometer. An uninterruptable power supply system was employed in case of a power failure.

8.7 Slurry Preparation and Consolidation

K50 clay was the only soil used in all the calibration chamber tests. The purpose of a slurry consolidometer is to produce uniform and reproducible research specimens of cohesive soils. It is desireable to obtain a high degree of homogeneity both physically and chemically and also to produce a soil specimen with a known stress history.

The water content that was selected for the slurry was chosen by considering a number of factors as revealed by Krizek and Sheeran (1970). A high water content will make the slurry easy to deair and easy to place in the consolidometer. However, a low water content minimizes the segregation of soil particles and makes the consolidation time shorter. They recommended for a kaolinite mixture a water content of 1.5 to 2 times the liquid limit, where the actual amount is found by trial and error.

For the mixture used for this research work, it was found that 2 times the liquid limit was sufficient to satisfy the criteria mentioned above. This corresponds to an initial water content of 60%.

Deionized and deaired water was used for the slurry mixture. The kaolinite and sand were alternately placed in the water a little at a time to provide some mixture in the beginning. The slurry was prepared in a 50 gallon tank, and a mixer was used to make the slurry physically homogeneous. The slurry was scooped out of the mixing tank and poured into the consolidometer. By pouring all the slurry in the same place and letting it flow to the other edges the air was forced out. The air that was added by the mixer or was still in the slurry for other reasons appeared to come out as the slurry was slowly poured into the consolidometer. This method was also used when preparing smaller specimens, which were used for the stepped loading consolidation tests and the triaxial tests.

The slurry was consolidated under a vertical stress of 138 kPa in the slurry consolidometer. It took approximately 30 days to consolidate one specimen. At the end of slurry consolidation, a 524 mm diameter clay specimen with a height of approximately 800 mm, encased in a rubber membrane was created. The specimen was directly transported to the chamber for final specimen preparation without trimming.

8.8 Calibration Chamber Consolidation and Penetration Tests

The specimens had water contents of 27-28% after consolidation in the slurry consolidometer. The Modified Cam Clay model used as part of the strain path analyses assumes isotropic soil behavior. The isotropic consolidation of the chamber specimen therefore provides a more realistic comparison with the strain path studies. However, natural soil deposit is generally consolidated anisotropically by the overburden pres-

159

sure. The idea of performing chamber tests in both isotropically and anisotropically consolidated specimens was to first validate the analytical studies and then evaluate the effects of stress anisotropy. All chamber specimens were normally consolidated.

All the drainage lines were flushed prior to the chamber consolidation. A back pressure was used during consolidation. For isotropic consolidation, an effective consolidation stress of 218 kPa was applied to the cell and piston while maintaining drainage from the top and bottom of the specimen.

For anisotropic consolidation, a K (σ'_h/σ'_v) value of 0.52 was utilized as in the case of CAU triaxial tests. A procedure similar to that of controlled gradient consolidation tests was developed for the anisotropic chamber consolidation. The piezometers installed inside of the specimen had their tips at approximately the same level as the center of the specimen. They were used to monitor the pore pressure at that level of the specimen during consolidation. To maintain a constant gradient, the cell pressure (σ_h) was adjusted to keep the pore pressure readings from these piezometers at 69 kPa above the back pressure. The piston pressure (σ_v) was adjusted accordingly to maintain a K value of 0.52. Drainage against the back pressure was allowed at the top and bottom of the specimen. The double drainage enables the consolidation to be completed within a reasonable period of time while a gradient of 18.5 was maintained between the center and ends of the specimen. This consolidation can only be conducted with a computer servo-controlled system. The consolidation took aproximately one month regardless of the stress anisotropy. The experimental set up allowed one specimen being consolidated in the slurry consolidometer while another one was in the chamber. Overall, a test was conducted every 45 days. The status of consolidation was observed by monitoring the water level in the back pressure tank along with the piezometer or pore pressure readings. Representative results from these measurements are shown in Figures 8.8 and 8.9.

There were a total of three model piezoblade tests performed, the penetration rate
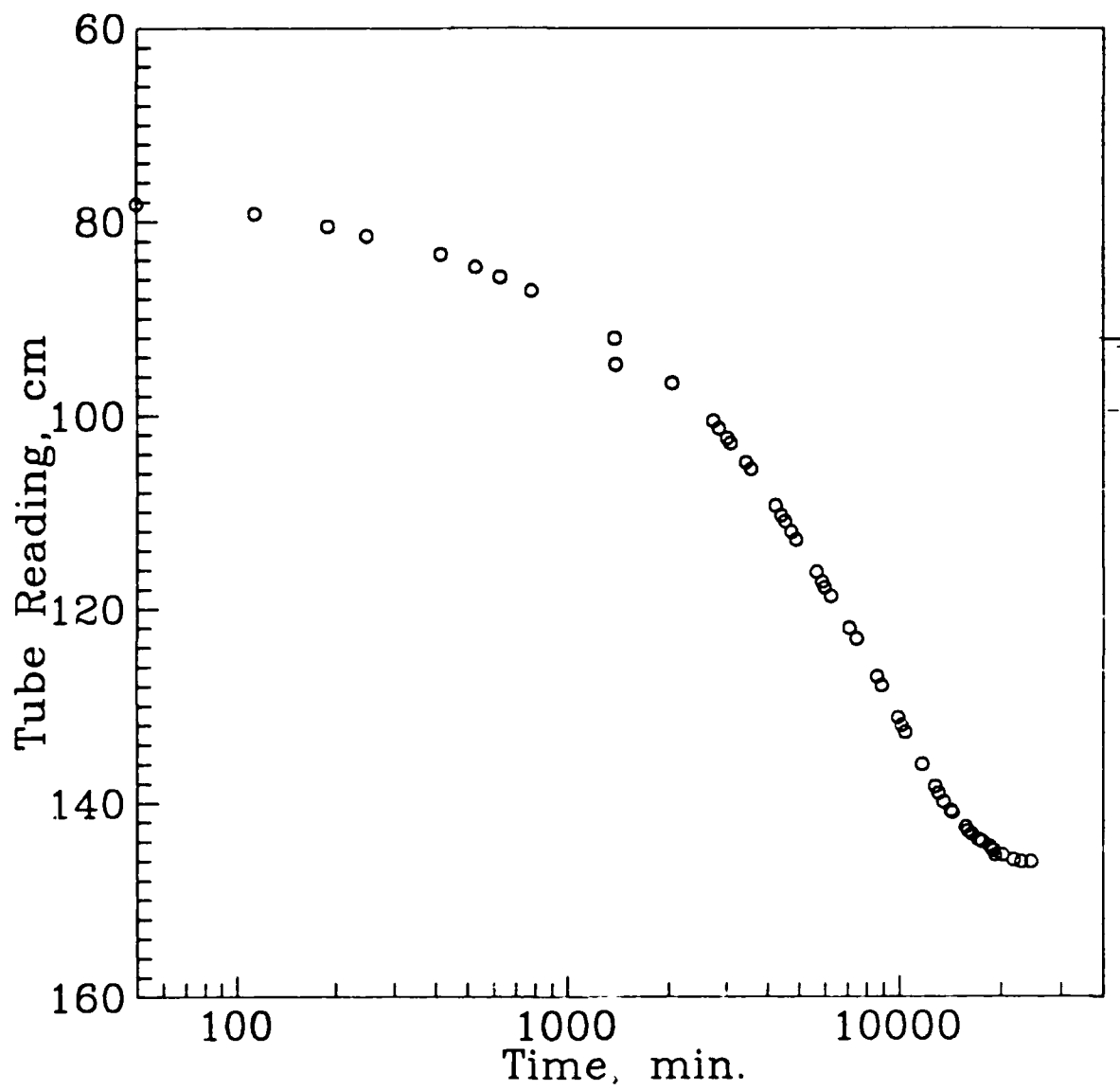
Figure 8.8: Consolidation curve found by tank reading.
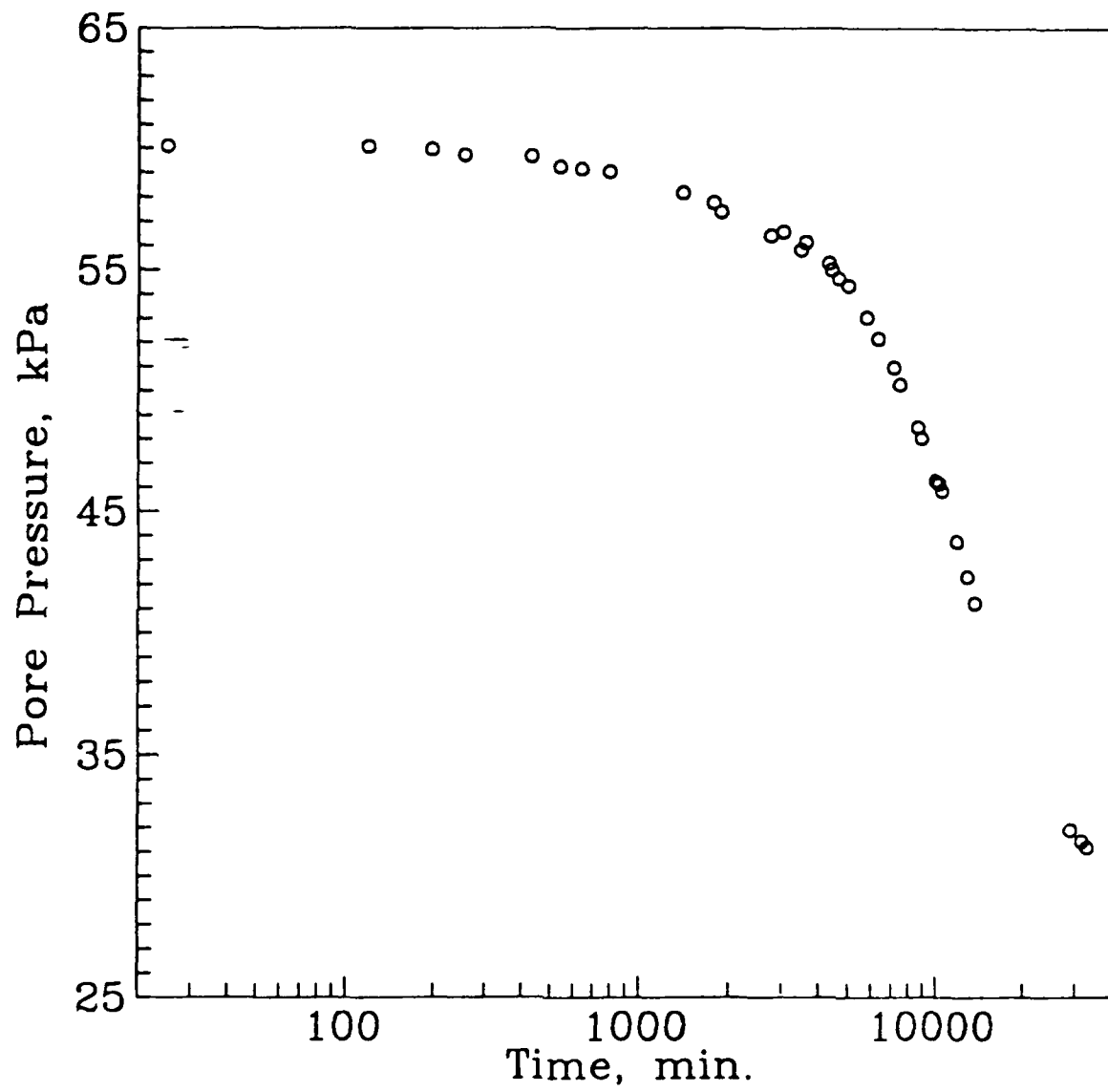
Figure 8.9: Consolidation curve found by piezometer reading.

in the first piezoblade test was faster than for the remaining tests. This provided a comparison between penetration rates. For the remainding tests the blades were pushed at a constant rate of 2 cm/sec.

Three model Dilatometer tests were performed. Prior to the insertion of the model Dilatometer, the diaphram was inflated in the blade housing against the back pressure and then deflated. This procedure provided the measurement of the membrane stiffness needed for the interpretation of the test result.

During the first minute after the DMT was pushed into the specimen, a full Dilatometer inflation test was performed with maximum membrane inflation of 1.0 mm. Following the initial full expansion tests, cycles of inflating the membrane to just pass lift off and back again were performed. The lift-off pressure is generally referred to as the A reading and the pressure where the membrane returns to its deflated position is called the C reading (Lutenegger, 1988). It is important to note here that the full inflation was only performed initially after penetration. Pore pressure was monitored and A and C readings were taken until excess pore pressure induced by the penetration had fully dissipated.

8.9 Experiments After the Penetration Test

8.9.1 Moisture Content Determinations

After the test was completed moisture content samples were taken from the specimen. The samples were taken at different levels through the height of the specimen and at different distances away from the path of the blade. Twenty samples each were taken roughly 25 mm, 150 mm, 305 mm, 457 mm, and 610 mm from the top of the specimen. The samples were taken parallel and perpendicular to the blade path on the horizontal plane starting 25 mm away from the center and 50 mm away from the previous sample after that. In general, more than 100 specimens were taken for water

content tests after each chamber test.

Upon determination of the moisture contents graphs were made to examine the affect of blade penetration on the moisture content. It was expected that as the samples were taken closer to the path of the blade the moisture content would decrease. The results are summarized and discussed in the next chapter.

8.9.2 Controlled Gradient Consolidation Tests

Along with moisture content tests, soil specimens were obtained by pushing stainless steel rings (62 mm ID, 17 mm ht.) into the chamber specimen for controlled gradient consolidation tests. These specimens were taken in the horizontal direction to obtain the corresponding consolidation characteristics. The same controlled gradient consolidation testing procedure as previously described was used.

8.10 Calibration Chamber Testing Program

A total of six flat-plate penetration tests have been conducted in the calibration chamber. Table 8.1 furnishes a summary of the piezoblade (PIEZ1 to PIEZ3) and model dilatometer tests (DMT1 to DMT3). The folowing sections provide a detailed description of the testing procedure.

Test No.	Consolidation	Back Pres., kPa	Vert. Stress, kPa	Horiz. Stress, kPa	Penetration Rate, cm/s
PIEZ1	Iso.	690	896	896	6.0
PIEZ2	Iso.	690	896	896	2.0
PIEZ3	Aniso.	690	896	797	2.0
DMT1	Iso.	207	414	414	2.0
DMT2	Iso.	552	759	759	2.0
DMT3	Aniso.	552	759	659	2.0

Table 8.1: Summary of the calibration chamber tests.

Chapter 9

Calibration Chamber Test Results

Results of the chamber calibration tests are presented in this chapter. These include the penetration induced pore pressure, the pore pressure dissipation after interruption for the piezoblade tests and the expansion curves of the model Dilatometer tests. The same coordinate system as used in presenting the numerical data (see Figure 3.2) is adopted. The half thickness of the blade (R = 3.5 mm) was used to normalize linear dimensions. When appropriate, stresses and pore pressures are normalized with respect to vertical consolidation stress.

9.1 Penetration Induced Pore Pressure

The four piezo elements (sensors) mounted on the piezoblade enabled excess pore pressures to be measured at different locations on the penetrometer during a steady penetration. In test PIEZ1 (see Table 8.1), the rate of penetration was 6 cm/sec. At this penetration rate, large negative pore pressure readings which exceeded the lower limit set up in the data logging system was registered. Such a phenomenum has not been reported for cone penetration tests at a comparable penetration rate. The complete time history of the normalized excess pore pressure, $\Delta u/P_0'$ since the

end of penetration is shown in Figure 9.1. Despite the significant difference in penetration rate and excess pore pressure developed during penetration, the maximum pore pressure recorded in PIEZ1 is very close to that in PIEZ2 where both tests were conducted in an isotropically and normally consolidated specimen. Figure 9.2 shows the profiles of $\Delta u/P_0'$ developed during the penetration in tests PIEZ2 and PIEZ3.

$$\Delta u = u_T - u_o \tag{9.1}$$

where u_T = total recorded pore pressure and u_o = back pressure. A penetration rate of 2 cm/sec was used in these two tests and a relatively stable excess pore pressure was developed at 150 mm after the penetration was initiated. In test PIEZ2 the clay specimen was normally consolidated under an isotropic condition, in test PIEZ3 the consolidation was conducted anisotropically (see Table 8.1). For both tests, the excess pore pressure at the mid height of the blade (sensors 3 and 4) was higher than that recorded torward the end of the blade (sensors 1 and 2). Also, the pore pressure at the center of the blade (sensors 1 and 3) was higher than that recorded close to the edge (sensors 2 and 4) of the blade. Sensor No. 2 of test PIEZ3 was accidentally disconnected during penetration and therefore results are not shown. The normalized excess pore pressure, $\Delta u/P_0'$ from all the sensors ranged from 1.5 to 2 during the steady penetration in test PIEZ2. The correspoding values in test PIEZ3 varied from 0.9 to 1.4. For an s_u/P_0' of 0.28 (see Table 7.3) as indicated in the reference triaxial tests, these values correspond to $\Delta u/s_u$ ranging from 5.4 to 7.1 for test PIEZ2 and from 3.2 to 5 for test PIEZ3. These values are well within the range of those predicted according to the cavity expansion theory (Vesic, 1972) where

$$4 < \frac{\Delta u}{s_u} < 7 \quad (spherical \ cavity) \tag{9.2}$$

and

$$3 < \frac{\Delta u}{s_u} < 5 \quad (cylindrical \ cavity) \tag{9.3}$$

167
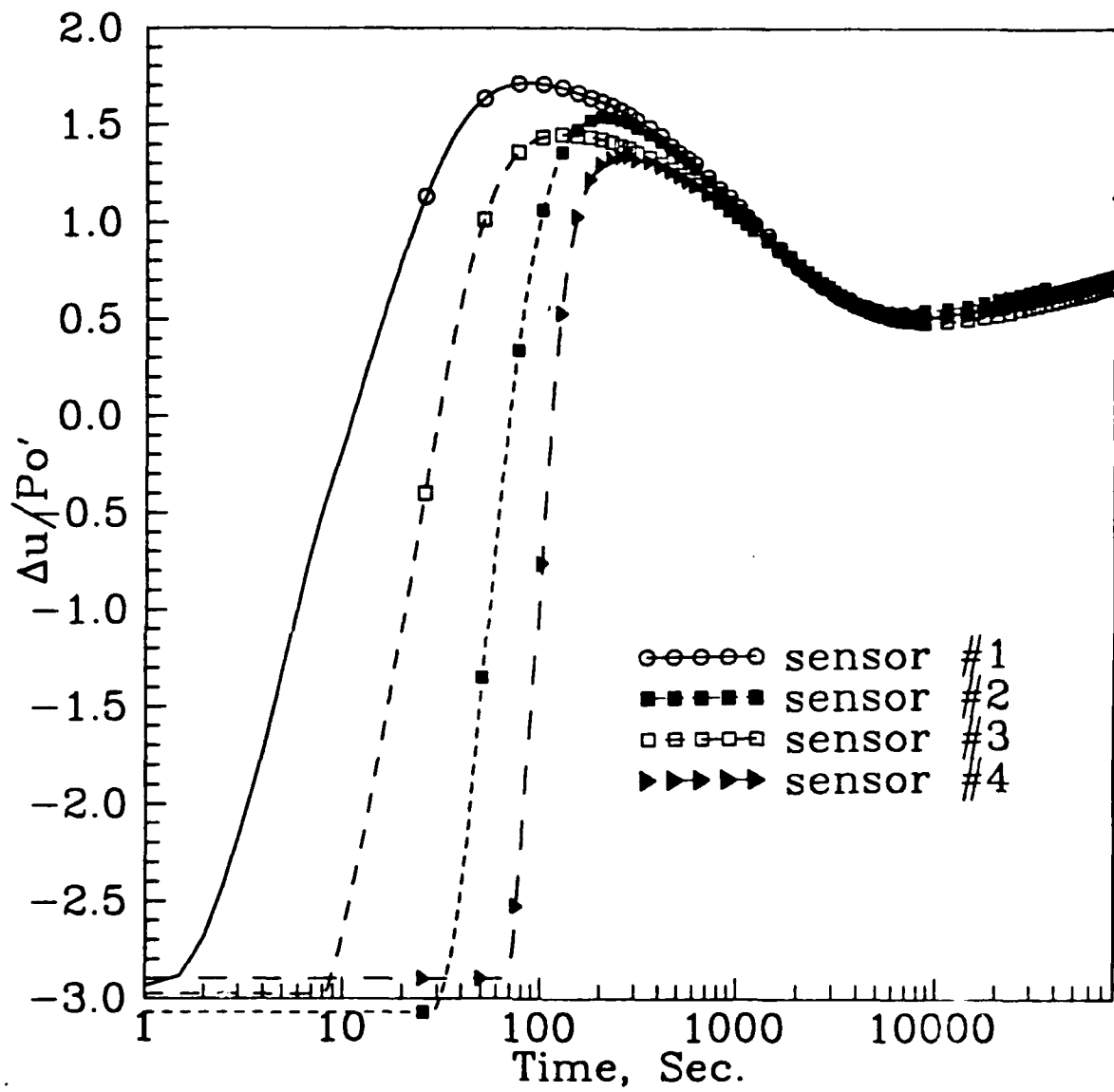
Figure 9.1: Excess pore pressure during and after penetration (PIEZ1).

The penetration induced pore pressure in the isotropically consolidated specimen (PIEZ2) was higher than that in an anisotropically consolidated specimen (PIEZ3) by as much as 43%. According to Randolph and Wroth (1979), for cylindrical penetrometers

$$\Delta u = s_u \left[ln(G/s_u) - 2ln(z/R) \right] \qquad (9.4)$$

The maximum Δu is at the boundary of the penetrometer where $z = R$. The reference triaxial tests indicate that

$$\frac{(s_u ln(G/s_u))_{CIU}}{(s_u ln(G/s_u))_{CAU}} = 2.5 \qquad (9.5)$$

for specimens normally consolidated to 218 kPa and sheared under axial extension mode. The same ratio from axial compression tests was 0.83. Soil behavior under axial extension is similar to that of lateral compression. The data would indicate therefore that the soil is mostly experiencing a lateral compression during the later stage of a flat-plate penetration and that the rigidity index in the lateral direction is the predominant factor in the development of excess pore pressure.

Figure 9.3 shows a comparison of $\Delta u/P_0'$ from chamber tests and those from SPM analyses for DMT penetration. It should be emphasized that the piezoblade has exactly the same dimensions as the model DMT. The analytical results also include $\Delta u/P_0'$ determined during a $20°$ cone penetration. Since pore pressure can only be analytically computed along the $x = 0$ plane, the chamber data shown in Figure 9.3 represent those from sensors 1 and 3. The figure shows that the analytical values are approximately 50% of those obtained in test PIEZ2 and 70% of test PIEZ3. The significant difference is most likely due to the way MCC model handles soil unload and reload. As indicated in Chapter 3, the shear octahedral strain undergoes a process of unload and reload as the soil element passes the tip of the DMT along $x = 0$ plane. The initial loading and unloading of the soil was mainly in a mode of triaxial compression as predicted in SPM studies. The MCC model considers unload-reload

as elastic and therefore there is no shear stress induced pore pressure during this stage. This is clearly not the case as indicated in reference triaxial tests with unload reload cycles. The data base regarding the post failure unload-reload behavior is very limited. It is clear that extensive experimental studies are needed to establish such a data base before the analytical model can be improved.

Despite the discrepancies, the analytical study does correctly predict the trend of excess pore distribution which shows that Δu decreases towards the end of the blade.
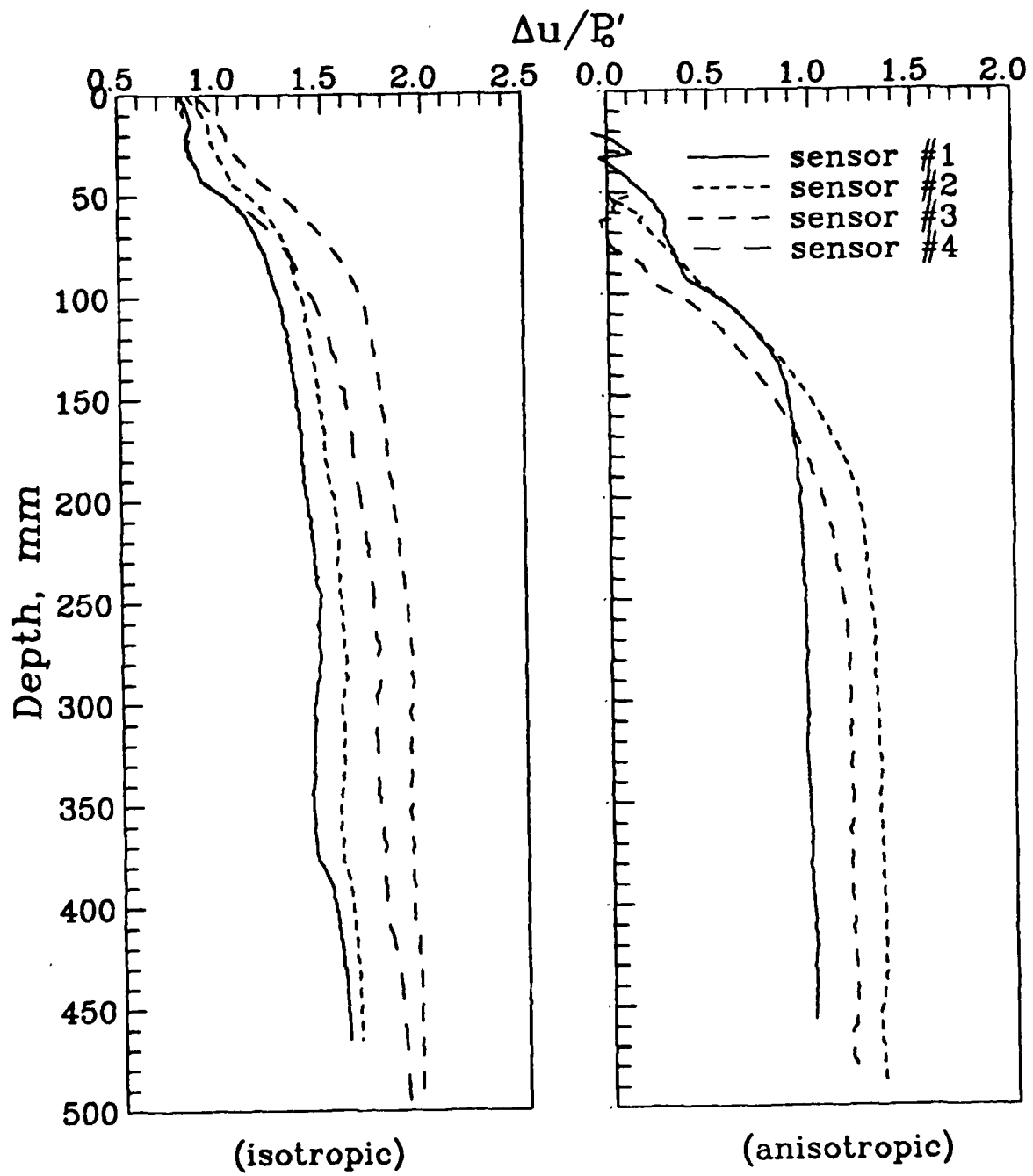
Figure 9.2: Profiles of excess pore pressure during piezo blade penetration.
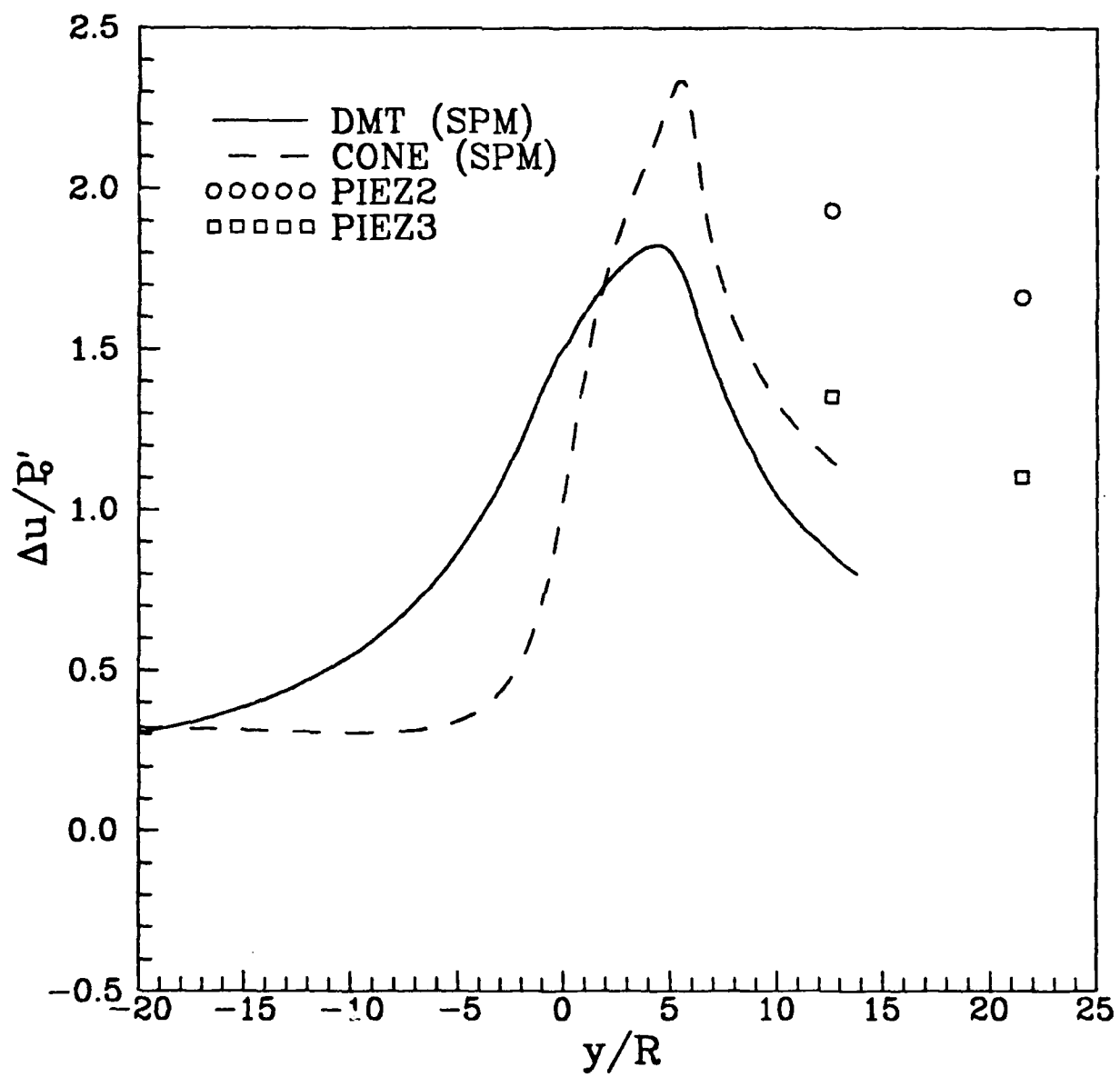
Figure 9.3: Comparison with analytical results.

9.2 Pore Pressure Distribution and Dissipation

The following discussion will concentrate on results from tests PIEZ2 and PIEZ3 because of their similarity in penetration rate and a desirable back pressure applied during the test. Piezometers were strategically located within the clay specimen to allow the pore pressure distribution to be monitored. Since the piezometers were made of relatively flexible stainless steel needles, they could be moved by the surrounding soil during the specimen consolidation. The exact location of each piezometers were therefore measured by carefully exposing them after the test was completed. The "as-measured" locations of all the piezometers along with those of the sensors (No. 3 and 4) on the piezoblade are shown in Figures 9.4 and 9.5. It should be noticed that the tip of the piezometers was at the same level as sensors 3 and 4 on the piezoblade. Although the piezometers were carefully flushed with deaired water and the specimen was under a back pressure of 690 kPa during the test, an apparent delayed response was noticed in all the piezometers. This could be caused by a combined effect of soil compressibility and the compliance of the piezometer/pressure transducer system. In any case, stable readings were obtained typically at 10 seconds after the interruption of the penetration. Tables 9.1 and 9.2 show all the piezometer readings in terms of normalized excess pore pressure ($\Delta u/P_0'$) at selected time intervals after the penetration ended. To visualize the distribution of the pore pressure, contour lines were created by interpolating these piezometer readings using a commercial software called SURFER. Contours resulted from these interpolations (Figures 9.6 to 9.17) represent the distribution of excess pore pressure in the xz plane and at the same level as pore pressure sensors 3 and 4 (y/R = 13). Based on the shapes of the contours, it appears that the pore pressure was fairly uniform across the face of the piezoblade (in the x direction) during dissipation for test PIEZ2 (isotropically consolidated specimen). For test PIEZ3 (anisotropicaly consolidated specimen) the pore pressure dissipation follows an axisymmetric pattern.
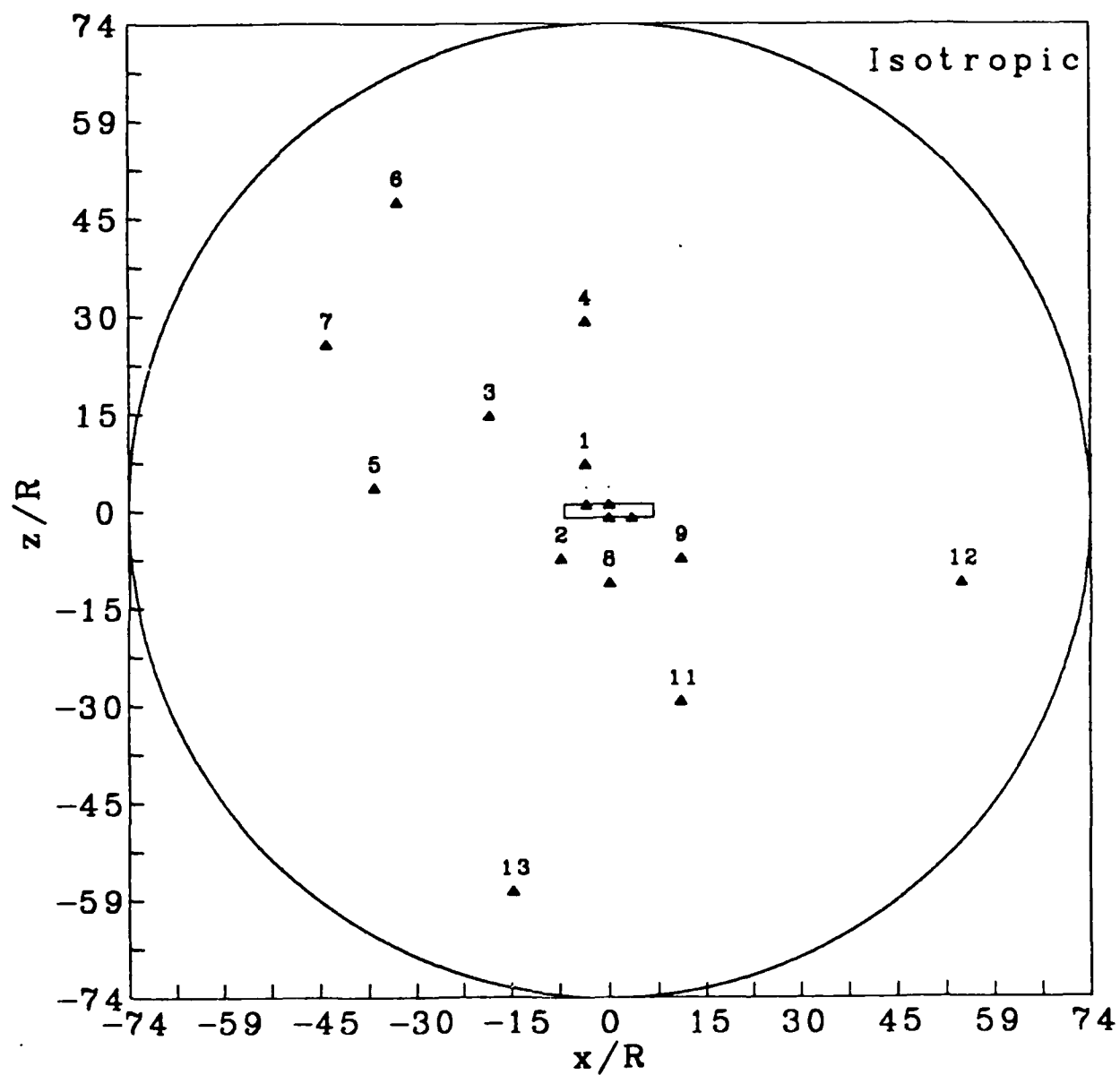
Figure 9.4: Position of piezometers after test (PIEZ2).

174
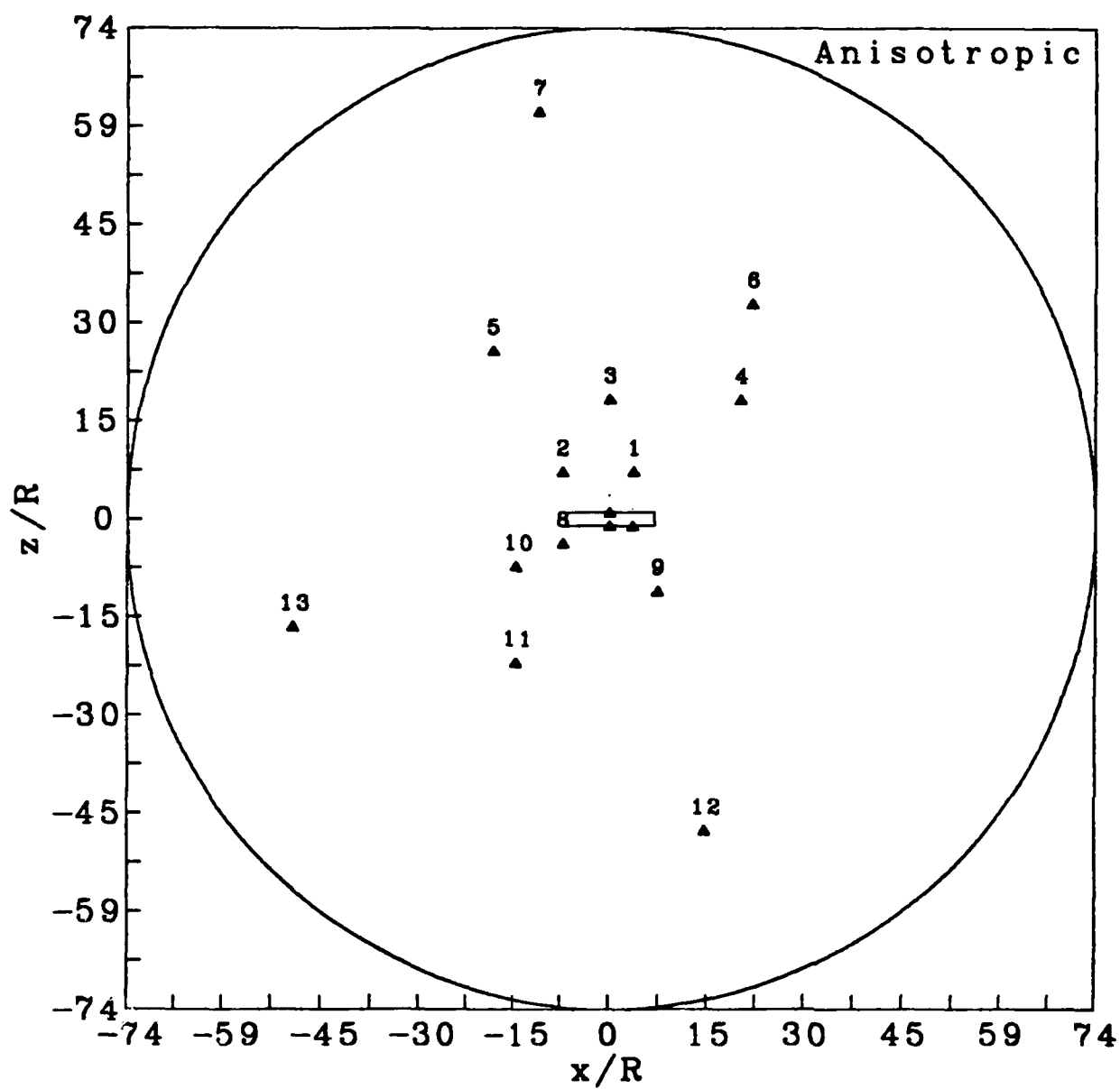
Figure 9.5: Position of piezometers after test (PIEZ3).

175

Time	Piezometer No.											
sec.	1	2	3	4	5	6	7	8	9	11	12	13
10	0.04	0.06	0.06	0.04	0.02	0.01	0.01	0.08	0.52	0.02	0.01	0.01
50	0.10	0.12	0.12	0.08	0.03	0.01	0.01	0.25	0.86	0.05	0.02	0.01
100	0.16	0.19	0.49	0.13	0.05	0.00	0.01	0.34	0.97	0.09	0.02	0.02
1000	0.51	0.54	0.49	0.37	0.20	0.08	0.08	0.72	0.69	0.31	0.10	0.13
3000	0.47	0.42	0.38	0.32	0.26	0.21	0.20	0.45	0.43	0.29	0.21	0.23
6000	0.34	0.32	0.31	0.29	0.20	0.26	0.26	0.33	0.33	0.27	0.26	0.26

Table 9.1: Table of piezometer readings for PIEZ2($\Delta u/P_o'$).

Time	Piezometer No.												
sec.	1	2	3	4	5	6	7	8	9	10	11	12	13
10	0.23	0.08	0.03	0.01	0.00	0.00	0.00	0.13	0.04	0.25	0.00	0.00	0.00
50	0.71	0.44	0.16	0.03	0.00	0.00	0.00	0.65	0.17	0.70	0.04	0.01	0.00
100	0.82	0.66	0.27	0.06	0.00	0.00	0.00	0.81	0.24	0.79	0.06	0.01	0.01
1000	0.59	0.55	0.44	0.21	0.00	0.02	0.03	0.53	0.18	0.45	0.19	0.07	0.03
3000	0.29	0.27	0.24	0.17	0.03	0.06	0.07	0.27	0.11	0.24	0.15	0.10	0.07
6000	0.17	0.17	0.16	0.13	0.06	0.09	0.09	0.17	0.09	0.17	0.12	0.10	0.09

Table 9.2: Table of piezometer readings for PIEZ3($\Delta u/P_o'$).
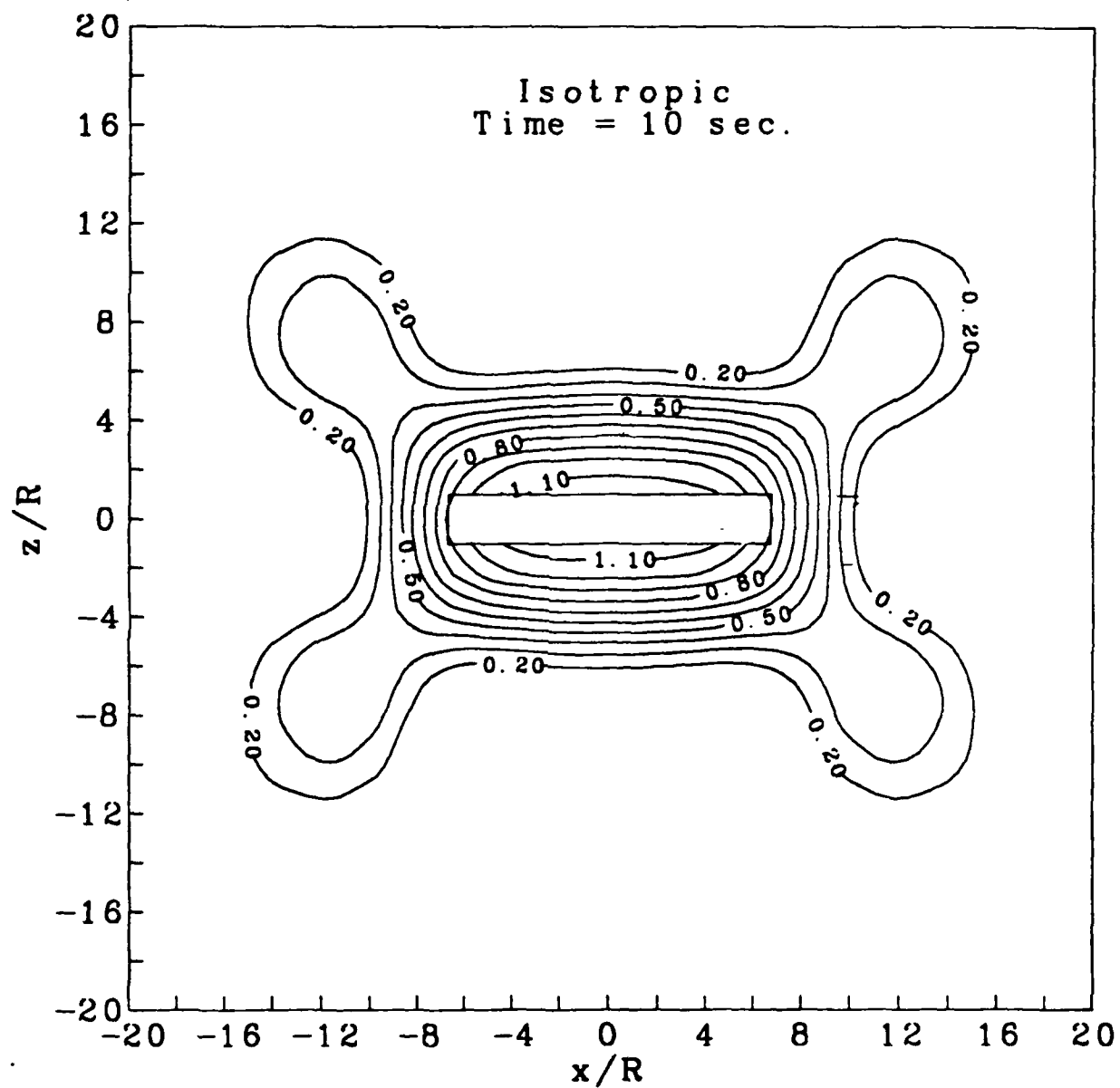
Figure 9.6: Contour of excess pore pressure 10 sec. after interruption (PIEZ2).
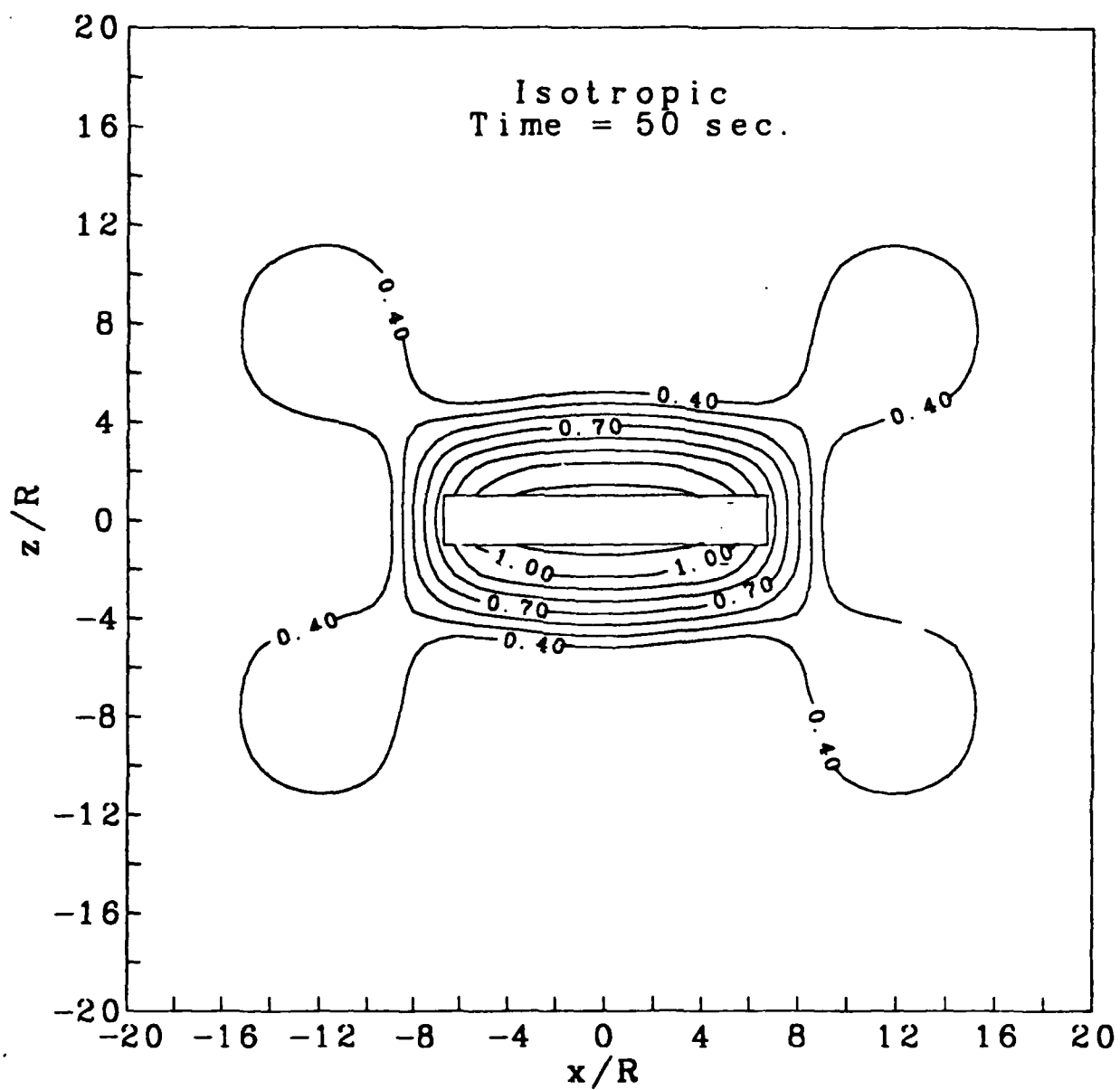
Figure 9.7: Contour of pressure 50 sec. after interruption (PIEZ2).

178
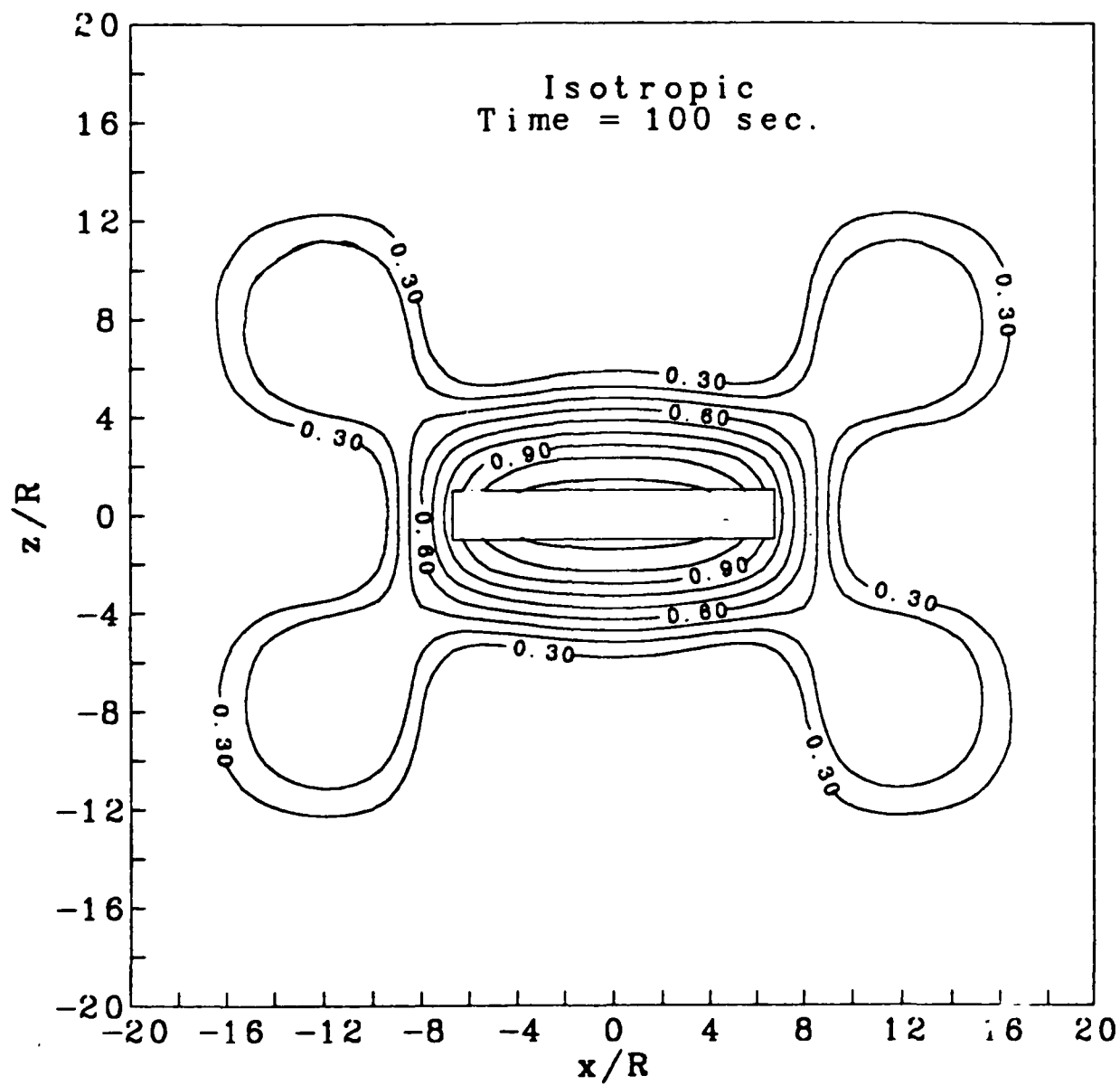
Figure 9.8: Contour of pressure 100 sec. after interruption (PIEZ2).

179
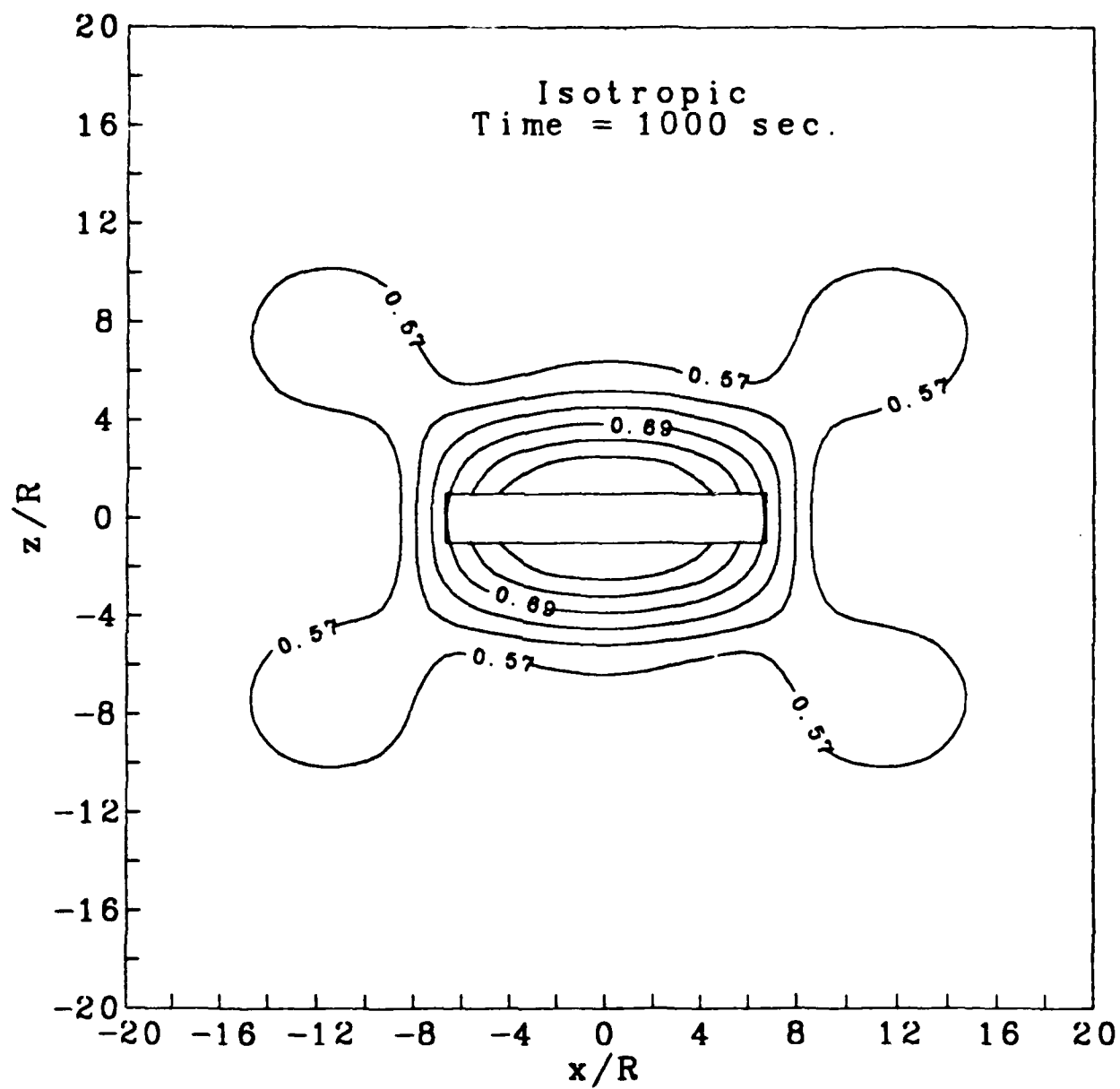
Figure 9.9: Contour of pressure 1000 sec. after interruption PIEZ2).

180
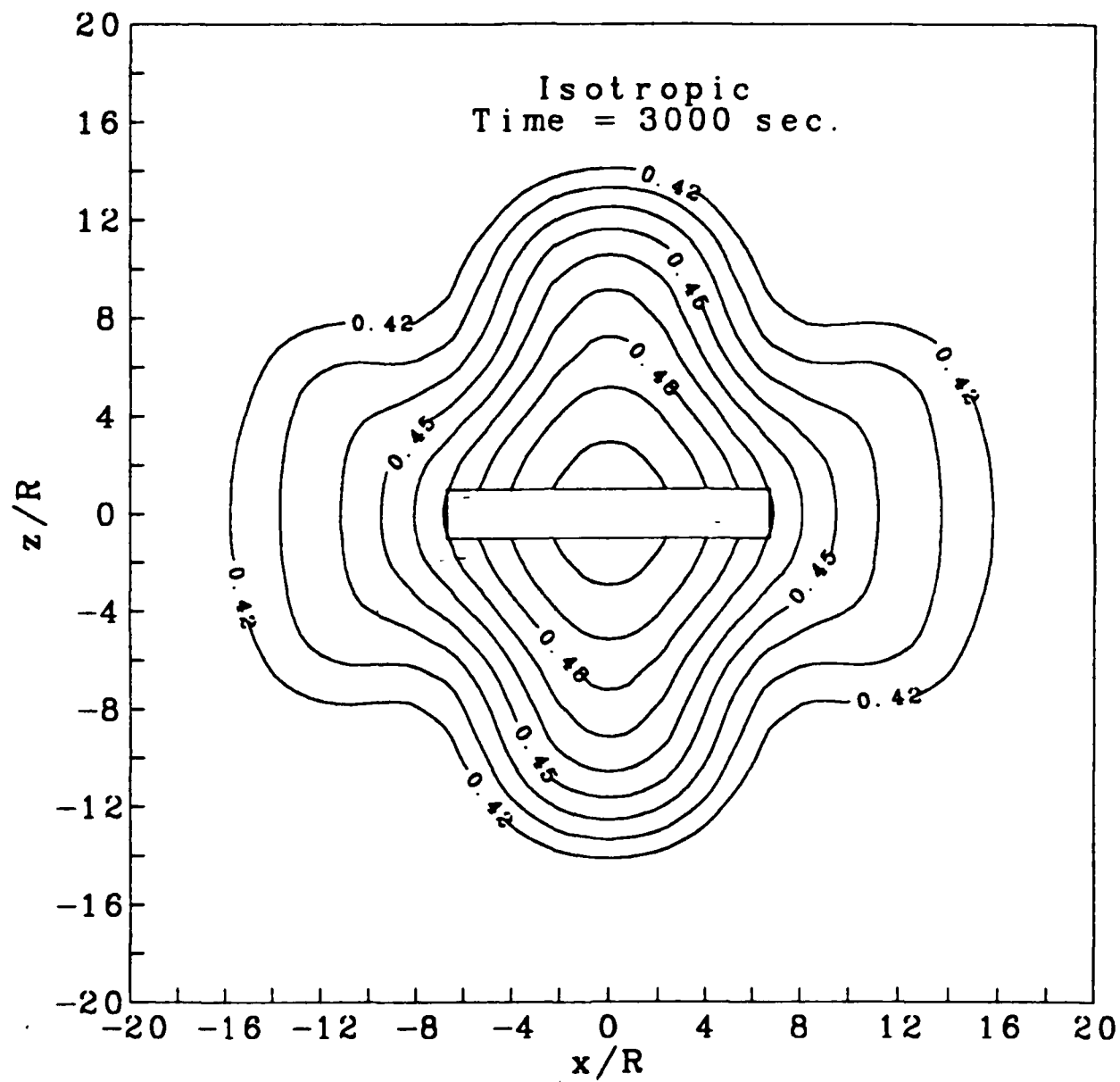
Figure 9.10: Contour of pressure 3000 sec. after interruption (PIEZ2).
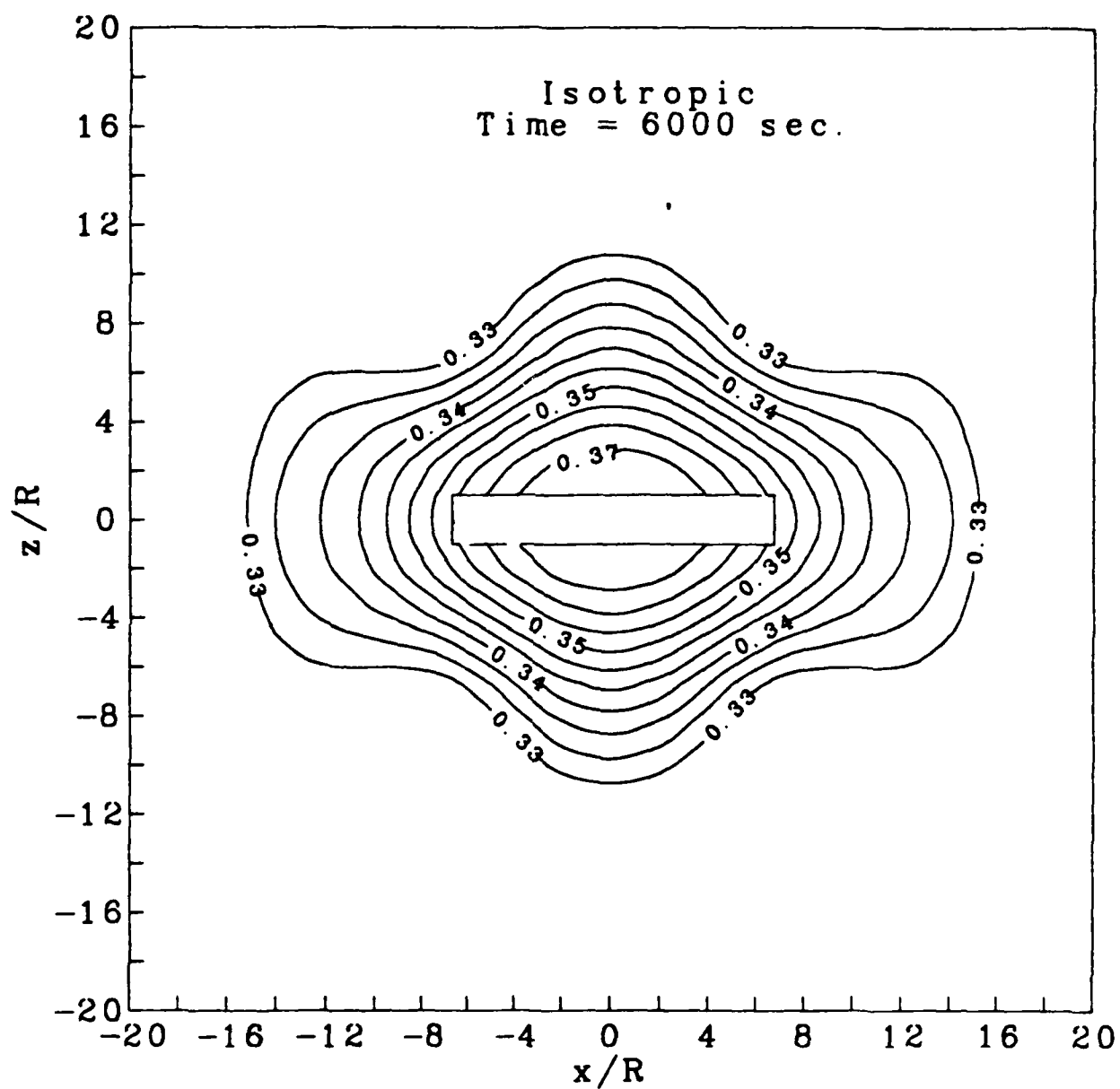
Figure 9.11: Contour of pressure 6000 sec. after interruption (PIEZ2).

182
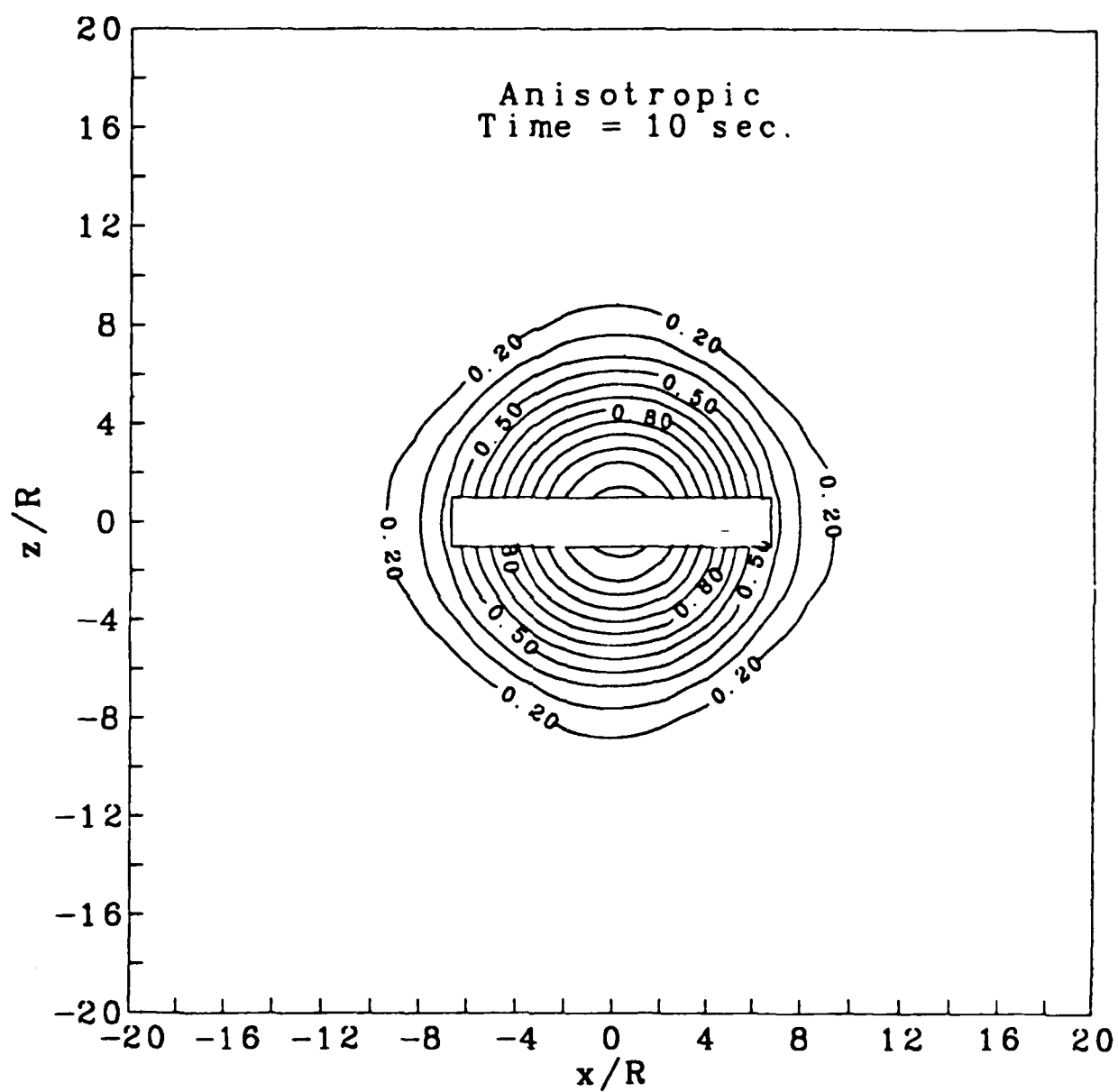
Figure 9.12: Contour of pressure 10 sec. after interruption (PIEZ3).
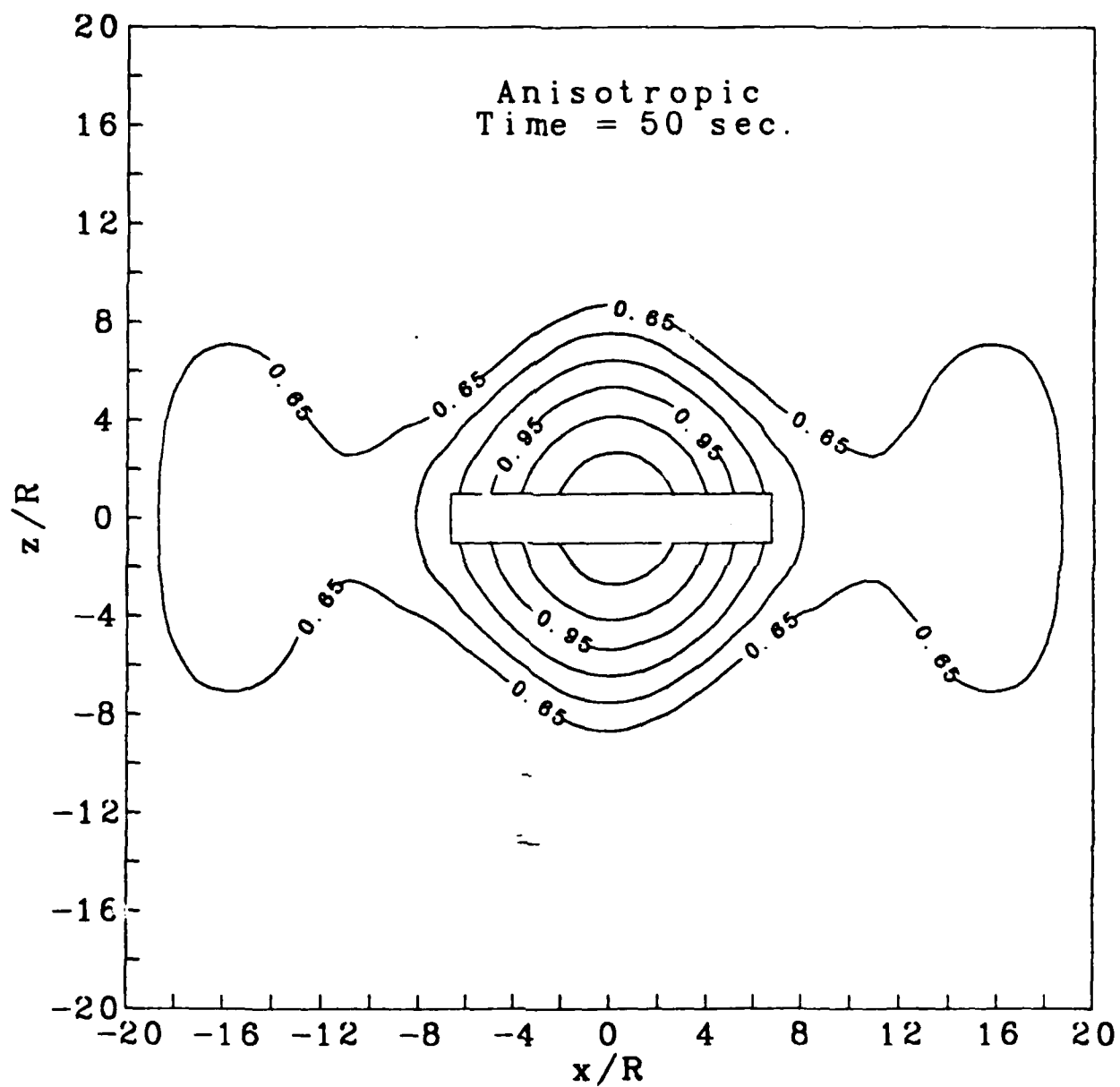
Figure 9.13: Contour of pressure 50 sec. after interruption (PIEZ3).
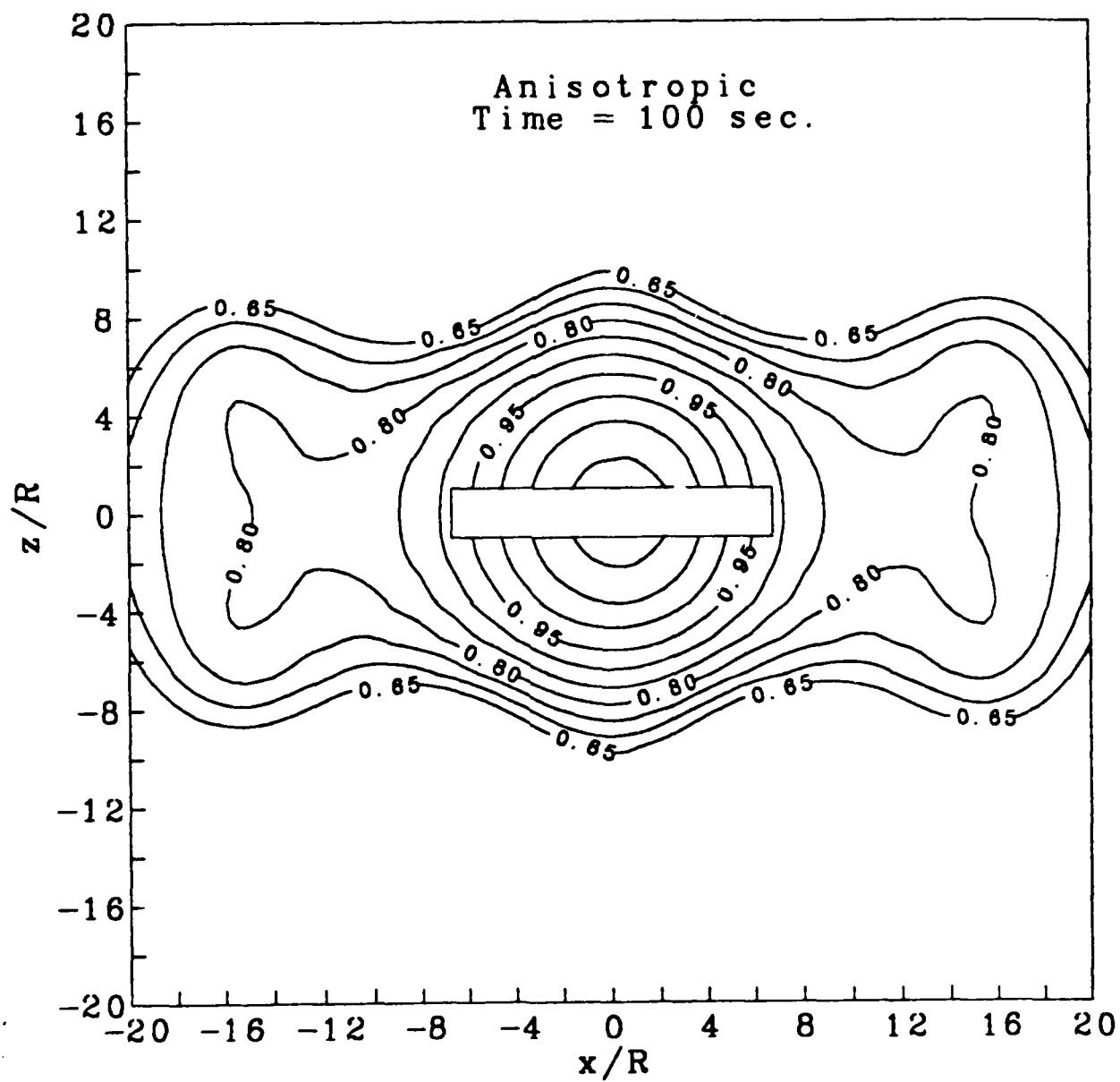
Figure 9.14: Contour of pressure 100 sec. after interruption (PIEZ3).
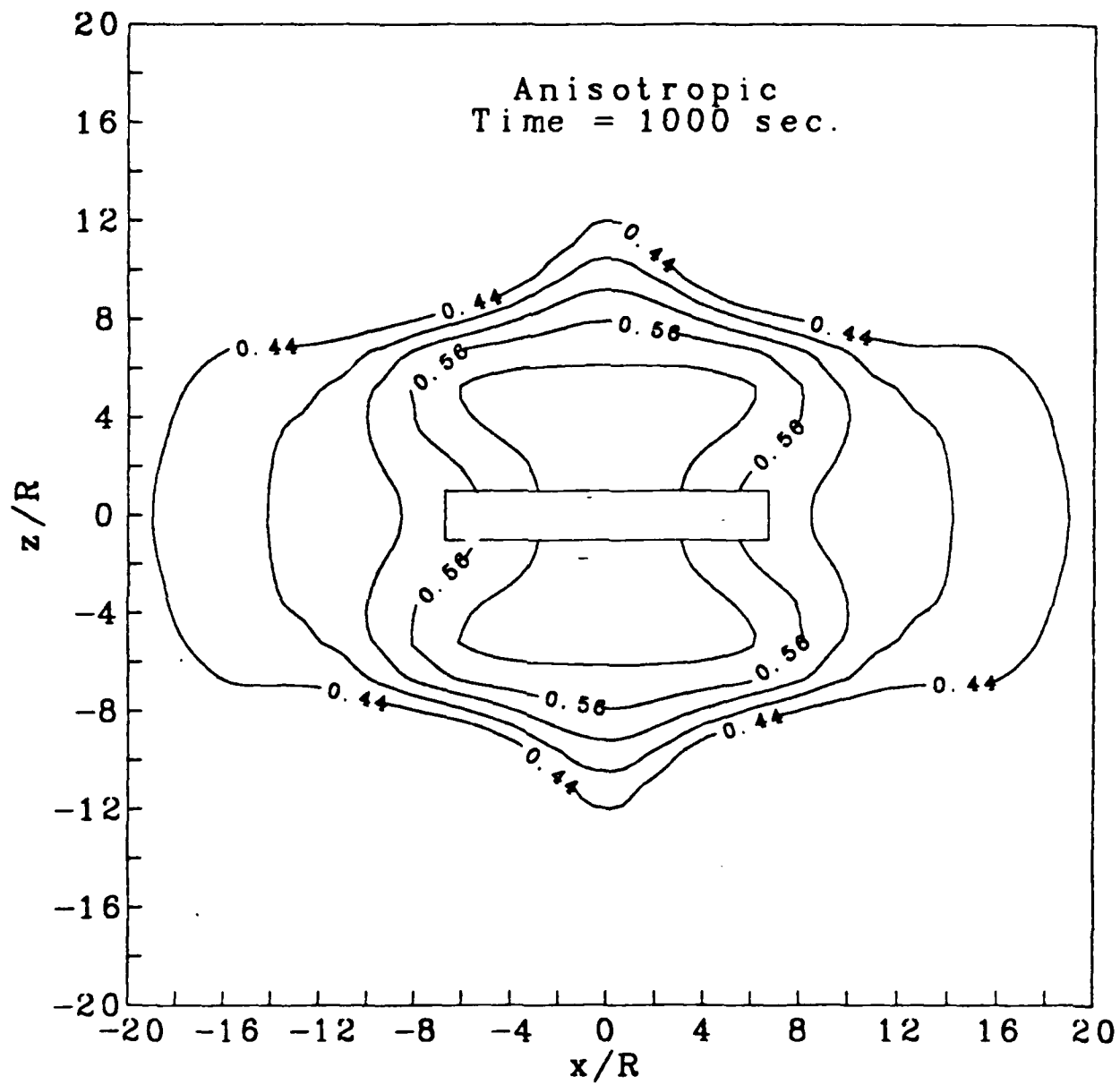
Figure 9.15: Contour of pressure 1000 sec. after interruption (PIEZ3).
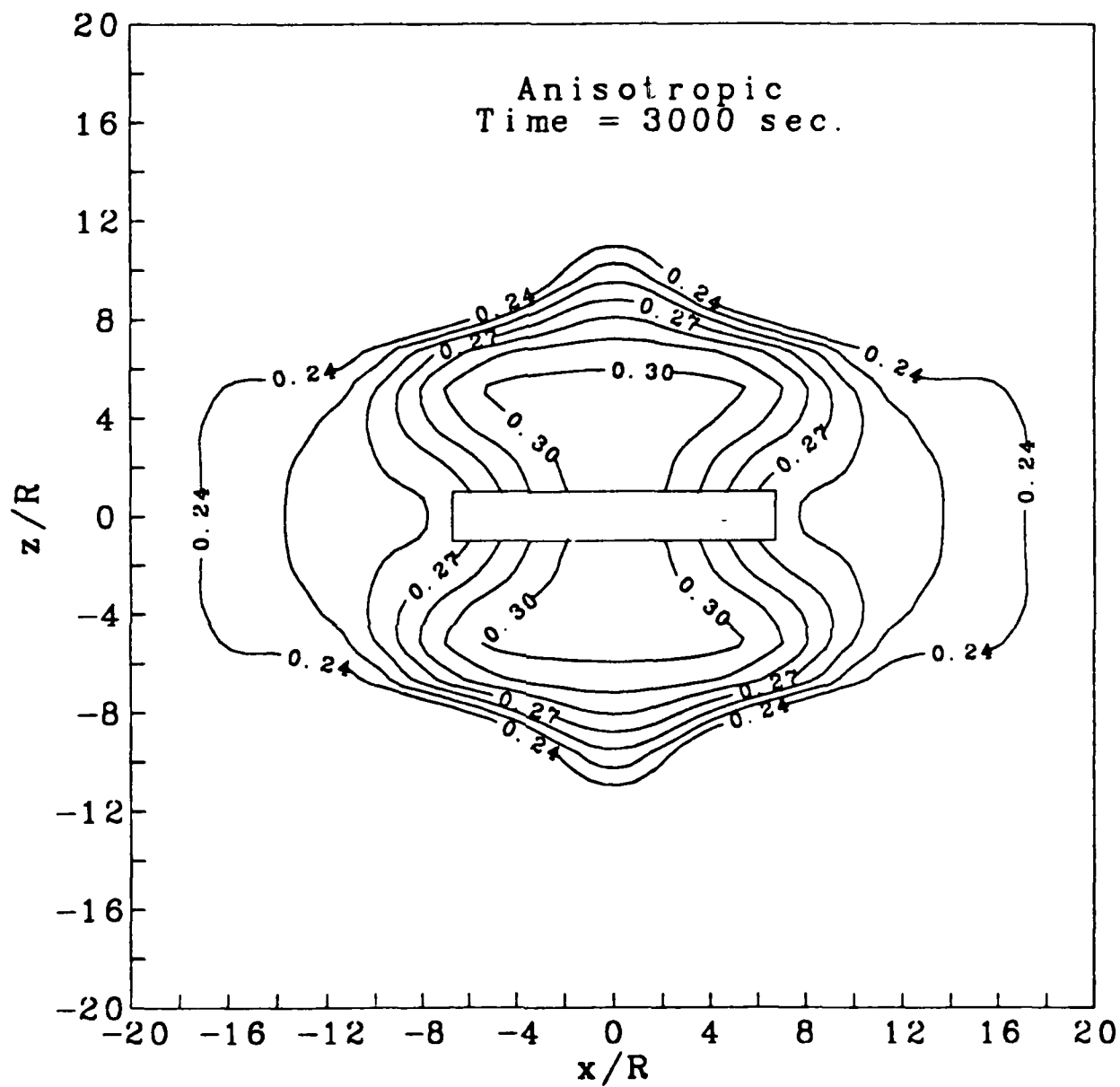
Figure 9.16: Contour of pressure 3000 sec. after interruption (PIEZ3).
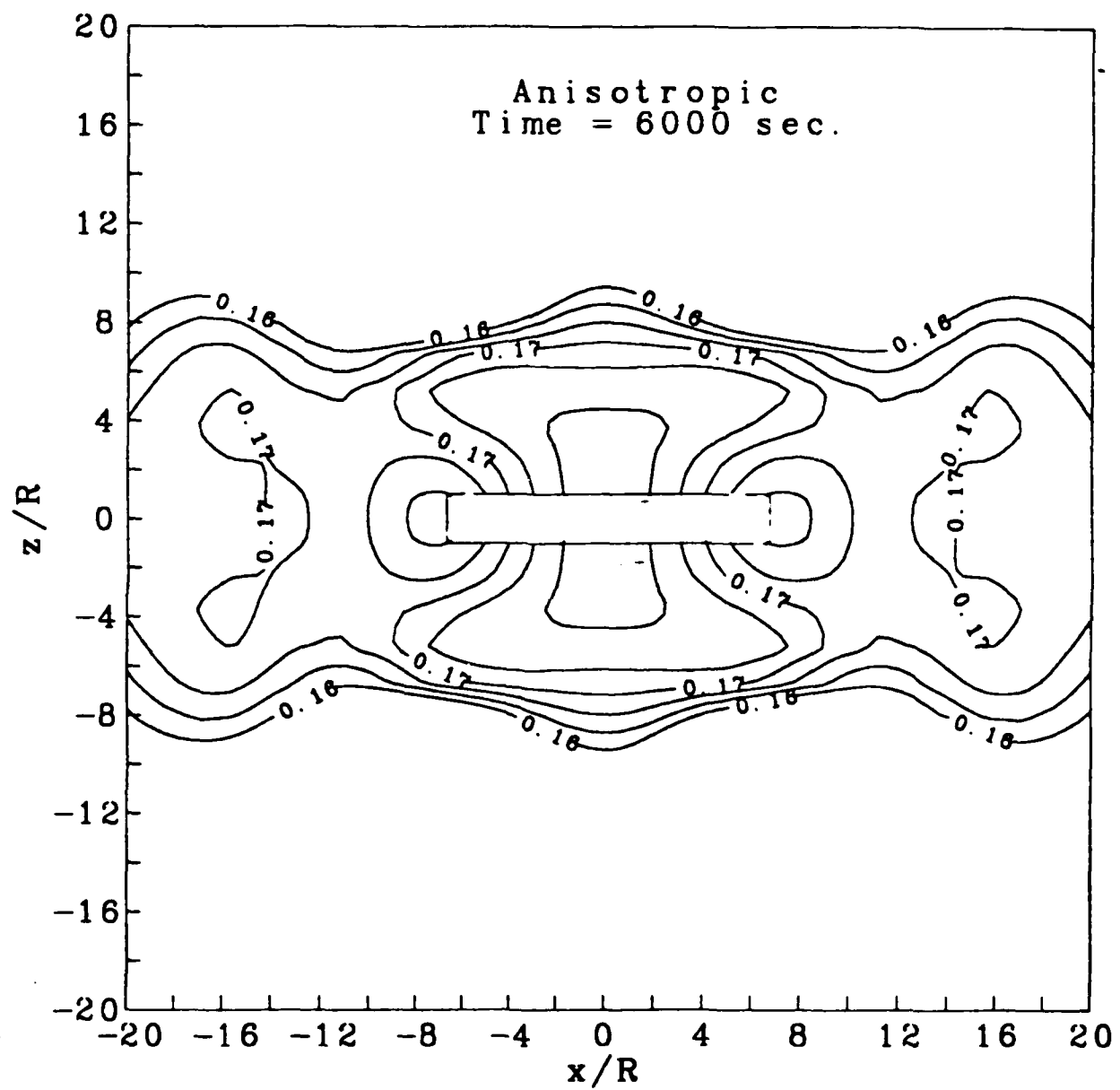
Figure 9.17: Contour of pressure 6000 sec. after interruption (PIEZ3).

188

9.2.1 Penetration Induced Excess Pore Pressure

Figure 9.18 shows the excess pore pressure in the z direction on the x = 0 plane. The figure was established based on the values depicted in the contours at 10 seconds after the penetration was interrupted. The x = 0 plane was selected as this is typically where the excess pore pressure is monitored in field flat-plate penetration tests. The amount of consolidation in 10 seconds is minimal and therefore the distribution shown in Figure 9.18 is considered the same as immediately after the penetration or at the beginning of pore pressure dissipation. According to this figure, the penetration induced excess pore pressure diminishes within a distance of 20R (R = half thickness of the piezoblade). This is significantly less than that predicted using the equation proposed for axisymmetric penetrations (Randolph and Wroth, 1979). In that sense the pore pressure measurements in the chamber agree well with the SPM analyses. The flat-plate penetration induced shear octahedral strain diminishes within a short distance (as opposed to cone penetration).

In an attempt to improve the analytical description of the pore pressure distribution, the concept proposed by Liam Finn (1963) was adopted. Considering the flat-plate penetration as a boundary value problem of a rigid plate translating laterally in an elastic half space, the normal stresses along the center line (x = 0) of the rigid plate are

$$\sigma_z = \frac{d}{b\pi} \frac{E}{(1 - \nu^2)} \left[\frac{b}{b^2 + z^2} + \frac{2by^2}{(b^2 + y^2)^2} \right] \tag{9.6}$$

$$\sigma_x = \frac{d}{b\pi} \frac{E}{(1 - \nu^2)} \left[\frac{b}{b^2 + z^2} - \frac{2by^2}{(b^2 + y^2)^2} \right] \tag{9.7}$$

where

d = R, the half thickness of the flat-plate, and

b = half width of the flat plate

189

The excess pore pressures generated may be estimated by assuming that, under undrained conditions, the mean effective stress remains constant. Thus, the excess pore pressure is equal to the change in mean total stress, giving

$$\Delta u = \frac{1}{3}(\Delta\sigma_x + \Delta\sigma_y + \Delta\sigma_z) = \frac{1}{2}(\Delta\sigma_x + \Delta\sigma_z) = \frac{d}{b\pi}\frac{E}{(1-\nu^2)}\left[\frac{b}{b^2 + z^2}\right]. \qquad (9.8)$$

The ratio of Δu at any given distance z away from the face of the blade over that on the face of the blade, Δu_o, is therefore

$$\frac{\Delta u}{\Delta u_o} = \frac{(b^2 + z^2)}{(b^2 + R^2)}. \qquad (9.9)$$

By setting Δu_o equal to that measured from sensor 3 at the end of penetration, the initial excess pore pressure distribution can be estimated based on EQ. 9.9. According to EQ. 9.9 the pore pressure distribution is independent of the rigidity of the soil provided it is elastic and Δu_o is given. In field practice, Δu_o is the measured value from the piezo unit immediately after the interruption of the penetration. Figure 9.19 plots the predicted pore pressure distribution for both the isotropically (PIEZ2) and anisotropically (PIEZ3) consolidated specimens. In general, the predicted excessive pore pressure is significantly higher than those according to chamber piezometer readings. Obviouly, it could be argued that soil is not elastic and that a plastic region is typically formed around the penetrometer which significantly reduces the area of pore pressure increase (Vesic, 1972). Also, EQ. 9.9 assumes plane strain expansion whereas the pore pressures below and above the flat-plate are much lower in real tests and therefore allows pore pressure to dissipate in the vertical direction. Despite the above problems, EQ. 9.9 does offer a basis of describing the initial pore pressure distribution and has a physical meaning. The equation shows that when z is small (relative to b value), Δu changes slowly with z as in the case of large loading area over a thin soil layer. As z increases, the effect of b diminishes and the pore pressure distribution essentially follows the ratio of $(z/R)^2$. Following this concept EQ. 9.9 can be modified as

$$\frac{\Delta u}{\Delta u_o} = \frac{(b^m + z^n)}{(b^m + R^n)}. \qquad (9.10)$$

190

where m and n are variables to be determined from curve fitting the chamber data. The values of m and n should reflect the effects of the three-dimensional and non-elastic nature of the flat-plate penetration. Also, EQ. 9.10 forms the basis of a semi-empirical approach for the interpretation of pore pressure dissipation data to be presented later. Results of the curve fitting show that for the isotropically consolidated specimen (PIEZ2)

$$\frac{\Delta u}{\Delta u_o} = \frac{(b^{1.8} + z^{2.6})}{(b^{1.8} + R^{2.6})} \tag{9.11}$$

and for anisotropically consolidated specimen (PIEZ3)

$$\frac{\Delta u}{\Delta u_o} = \frac{(b^{2.7} + z^{3.0})}{(b^{2.7} + R^{3.0})}. \tag{9.12}$$

Curves based on Eqs. 9.11 and 9.12 are also plotted in Figure 9.18.

9.2.2 Pore Pressure Dissipation and Determination of Consolidation Characteristics

Figures 9.21 and 9.22 show the dissipation of excess pore pressure after the penetration ended. The rate of pore pressure dissipation is governed mostly by the coefficient of consolidation of the surrounding soil. Attempts have been made to determine the coefficient of consolidation based on the pore pressure dissipation record from flat-plate penetration tests (Kabir and Lutenegger, 1990). All these methods assume flat-plate penetration as axisymmetric and procedures originally developed for cylindrical penetrometers have been followed. The success of such methods has been limited. One important drawback of the current approach is the lack of knowledge regarding the distribution of pore pressure around the flat-plate at different stages of pore pressure dissipation.

Analytical studies presented previously have indicated that a flat-plate penetration is a three-dimensional process. Ideally, a three-dimensional solution should be provided to properly interpret the pore pressure dissipation data and to determine the

coefficient of consolidation. However, the coefficient of consolidation is influenced by the state of stress and could vary by as much as one order of magnitude as indicated in the reference consolidation tests. In addition, a three-dimensional distribution of initial excess pore pressure would be necessary for such a solution. It would be extremely difficult to obtain such information, even in a calibration chamber. Therefore, some simplifications can be justified to determine the "approximate" coefficient of consolidation in a reasonable and practical fashion. An evaluation of the pore pressure contours shown in Figures 9.6 to 9.17 shows that for the isotropically consolidated specimen (i.e., in test PIEZ2), pore pressure was relatively uniform along the face of the plate throughout the dissipation process. For the anisotropically consolidated specimen (PIEZ3) the pore pressure distribution follows approximately an axisymmetric pattern during dissipation. If consolidation is two-dimensional (independent of y coordinate) and pore pressure is monitored at the center of the flat-plate (x=0, z=R), the pore pressure dissipation should be governed by a consolidation process which is between one-dimensional (in z direction only) and axisymmetric. These are further simplified as one-dimensional problems with a governing equation as

$$c_h \frac{\partial^2 u}{\partial z^2} = \frac{\partial u}{\partial t} \quad (one \ \ dimensional) \tag{9.13}$$

$$\frac{c_h}{r} \frac{\partial}{\partial r} \left(\frac{r \partial u}{\partial r} \right) = \frac{\partial u}{\partial t} \quad (axisymmetric) \tag{9.14}$$

where

c_h = horizontal coefficient of consolidation

u = excess pore pressure

t = time elapsed

To further explore the possibility, a finite difference program was developed to solve the above equations. Eqs. 9.11 and 9.12 were used to determine the initial excess pore pressure distribution. Boundary conditions shown in Figure 9.23 were used in the finite difference computation. They consider the penetrometer surface

192

and the specimen outer boudary as impermeable which are comparable to the cases of chamber testing. It was assumed that the consolidation was linear and uncoupled so that c_h and the total stress remain constant. Computational results in terms of $\Delta u / p_o'$ at the flat-plate surface ($x=0$, $z=R$) versus time factor $\tau(c_h t / R^2)$ are shown in Figure 9.24. Notice that Δu does not necessarily reach 0 at large τ. This is because of the limited and impermeable outer boundary used in the analyses which is also the case in chamber testing (see Figures 9.21 and 9.22).

The c_h value can be determined by comparing the pore pressure dissipation data (i.e., Figures 9.21 and 9.22) and the analytical solution (i.e., Figure 9.24). t_{50} is taken as the time elapsed when 50% of the excess pore pressure on the flat-plate surface has dissipated according to the dissipation data. The corresponding τ_{50} is selected from the analytical solution. c_h is then calculated as

$$c_h = \frac{\tau_{50} R^2}{t_{50}} \tag{9.15}$$

Table 9.3 shows the estimated c_h values following the above procedure. In general, c_h values based on axisymmetric solutions are higher than those from one-dimensional solutions. The results of controlled gradient consolidation tests performed on samples taken from the chamber specimens are summarized in Table 9.4. For the isotropically consolidated specimen, the estimated c_h is at least one order of magnitude smaller than those in Tables 9.4 and c_v values in Table 7.2. For the anisotropically consolidated specimen, the estimated c_h based on axisymmetric solution is within the order of magnitude but close to the lower bound of the corresponding values in Table 9.4. The SPM study indicated a significant decrease of pore pressure between the tip of the flat-plate ($y=0$) and the location of sensor 3 ($y=13$) which is typically where the pore pressure is monitored in the field piezoblade tests. Because of this, there is also a tendency for the pore pressure to increase towards the center of the flat-plate as the pore pressure dissipates away from it after an interruption of penetration. This is a likely reason as to why typically excess pore pressures from piezoblade tests dissipate

193

much slower than those obtained from piezocone tests. For piezocone tests, the pore pressure is generally monitored within the region of the cone tip where the excess pore pressure is usually the highest.

It appears that for isotropically consolidated specimens, a reasonable analysis of pore pressure dissipation around a flat-plate would have to consider the components in the y direction. For anisotropically consolidated soil, a lower bound c_h can be estimated considering the pore pressure dissipation as axisymmetric and the initial excess pore pressure distribution follows that described by EQ. 9.12.

Consolidation	$C_h, 10^{-3} cm^2/sec$	
	One-Dimensional	Axisymmetric
Isotropic	0.48	0.20
Anisotropic	0.50	1.50

Table 9.3: Estimated c_h from the piezoblade tests.

Tests	$C_h, 10^{-3} cm^2/sec$		C_c
	Reload	Virgin Loading	
Isotropic	6.9 to 67.4	4.6 to 8.6	0.15 to 0.26
Anisotropic	11.1 to 72.5	4.5 to 9.7	0.19 to 0.23

Table 9.4: Summary of the controlled gradient consolidation tests conducted on chamber specimens.
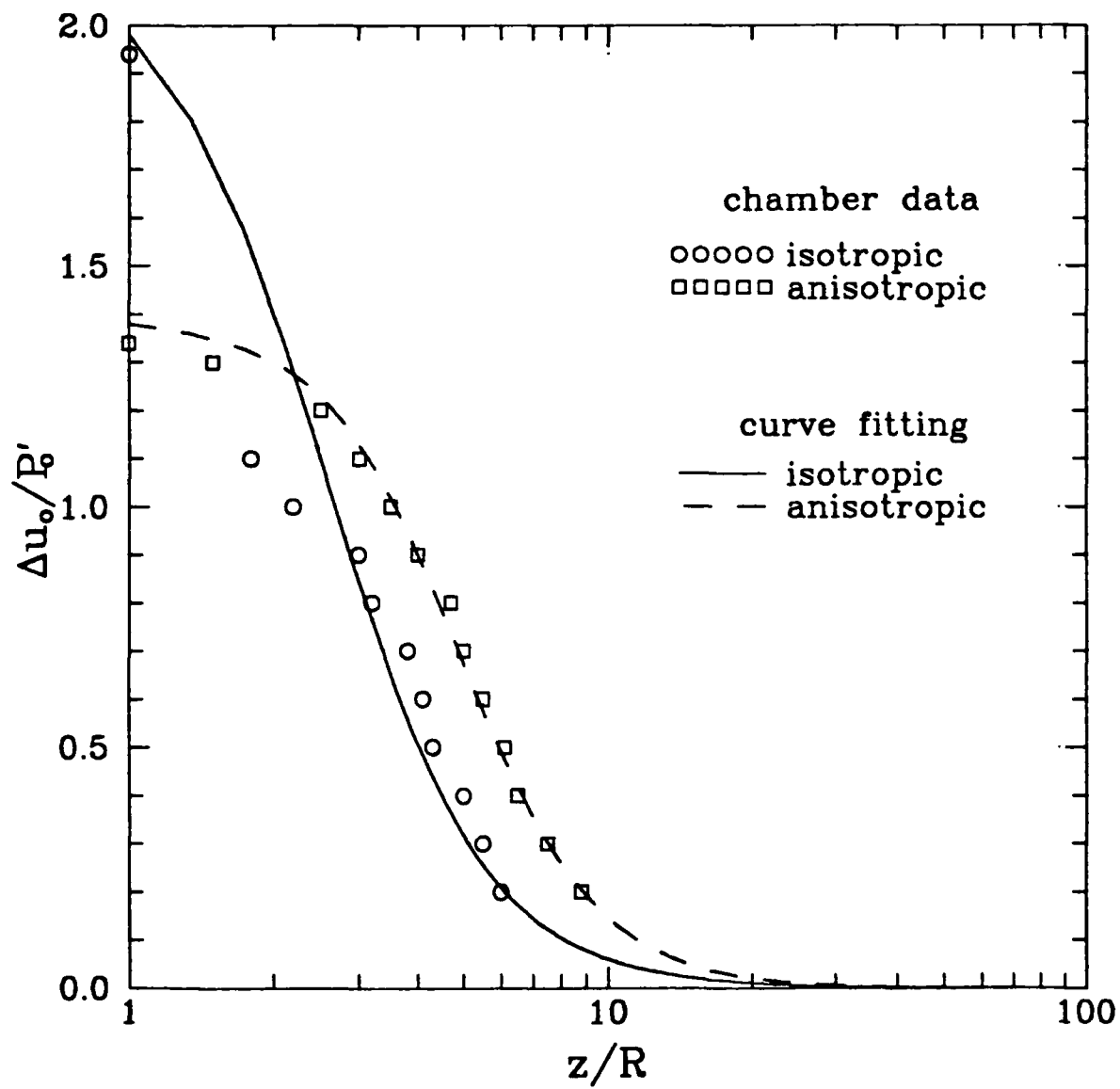
194

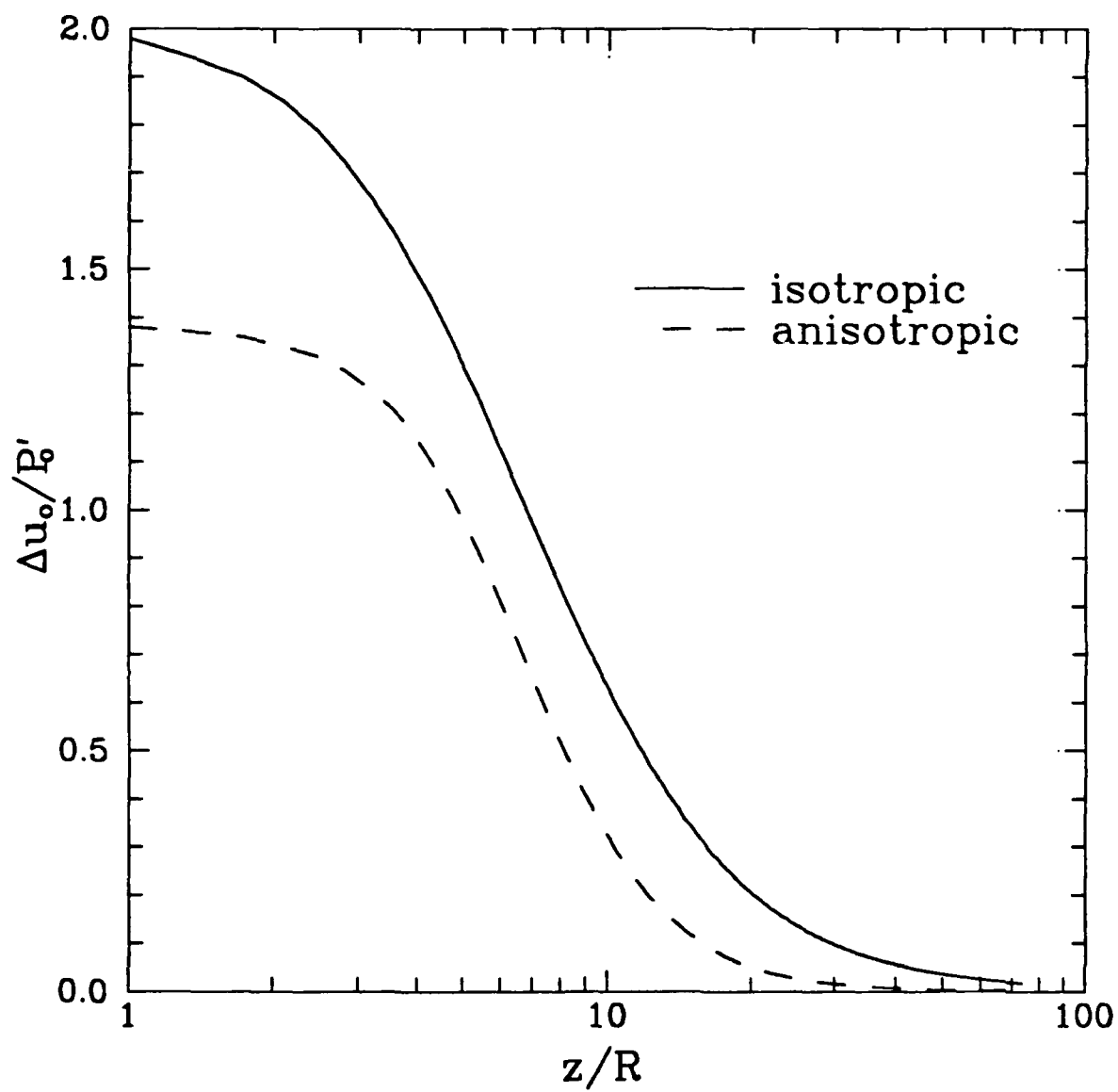Figure 9.18: Distribution of pore pressure in z direction.

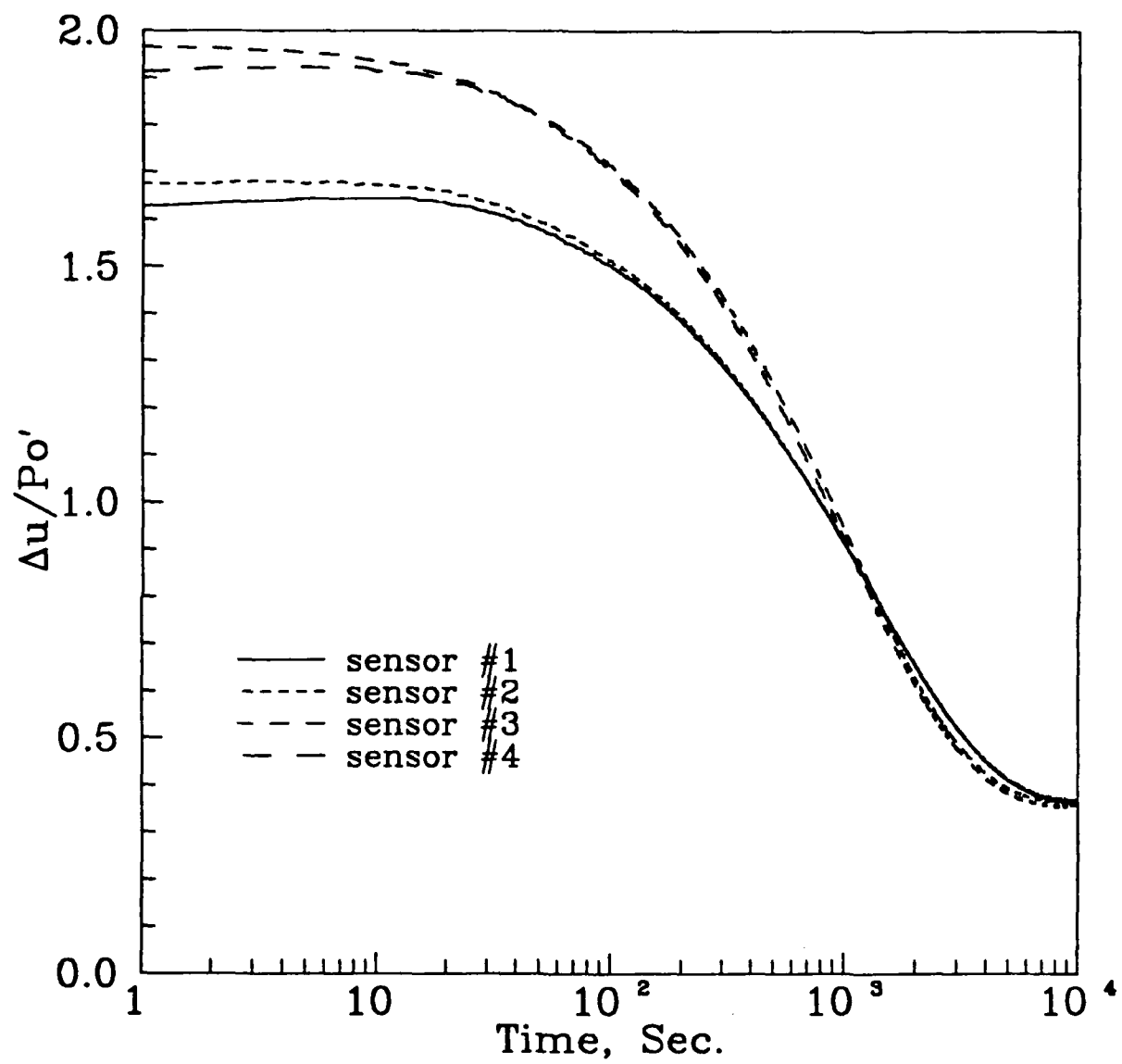Figure 9.19: Excess pore pressure distribution based on elastic theory.

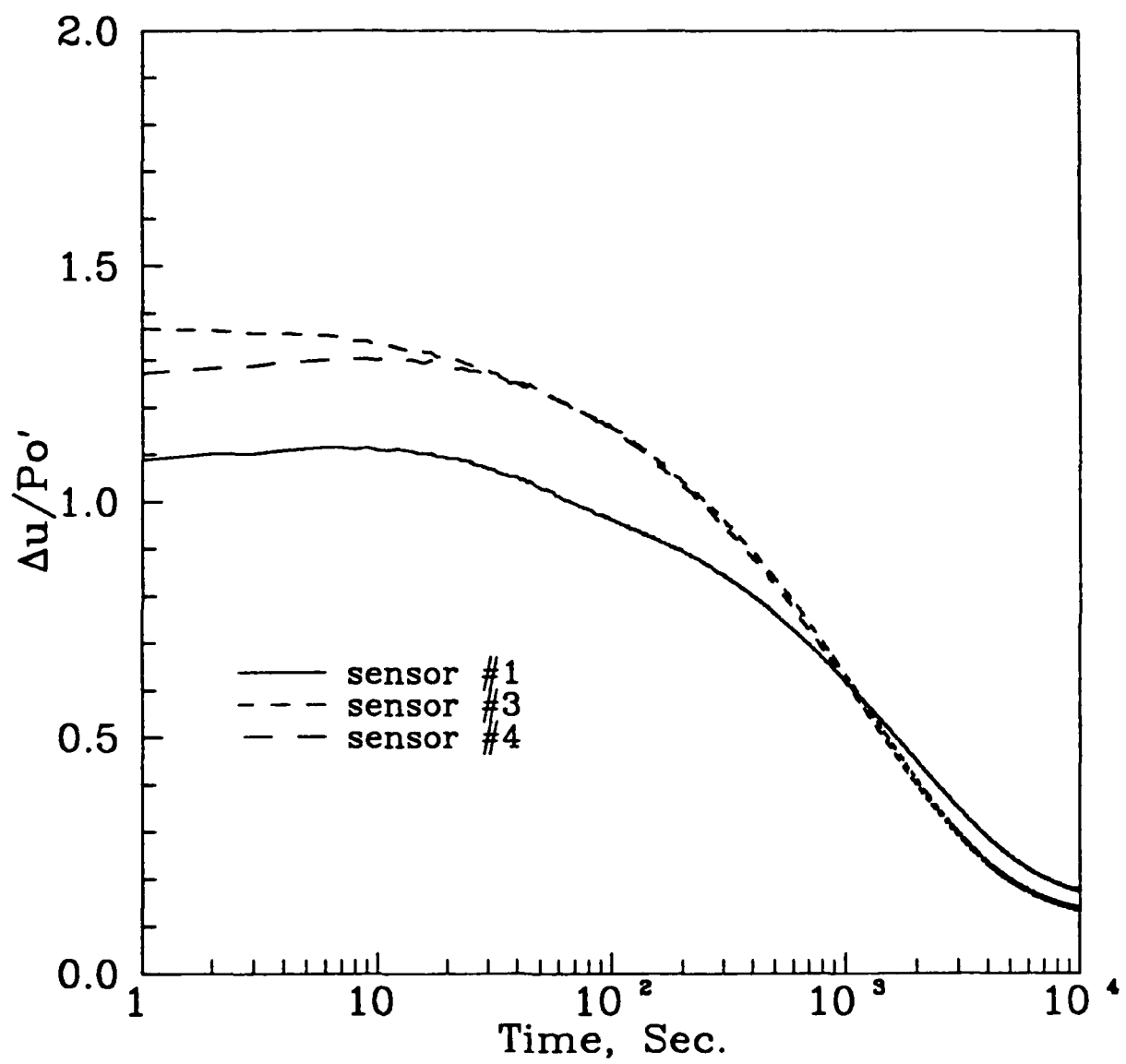Figure 9.20: Dissipation results from PIEZ2.
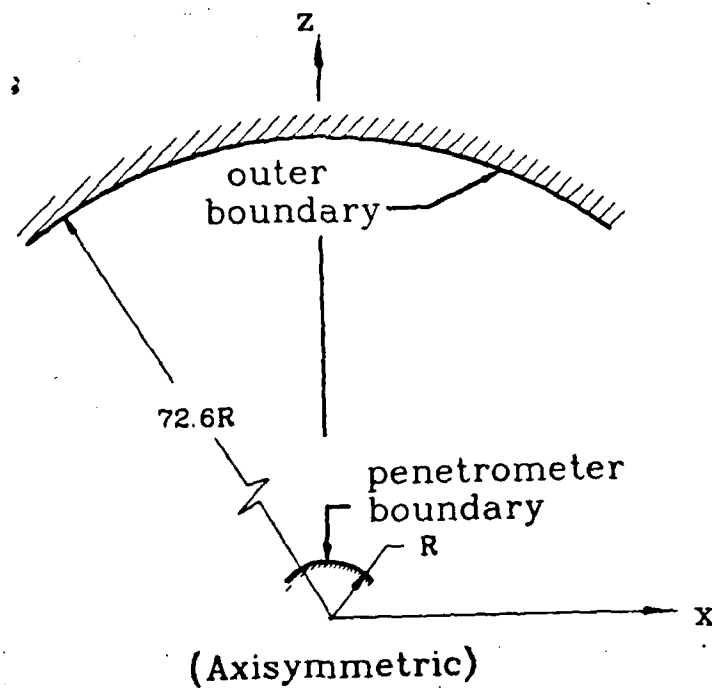
Figure 9.21: Dissipation results from PIEZ3.
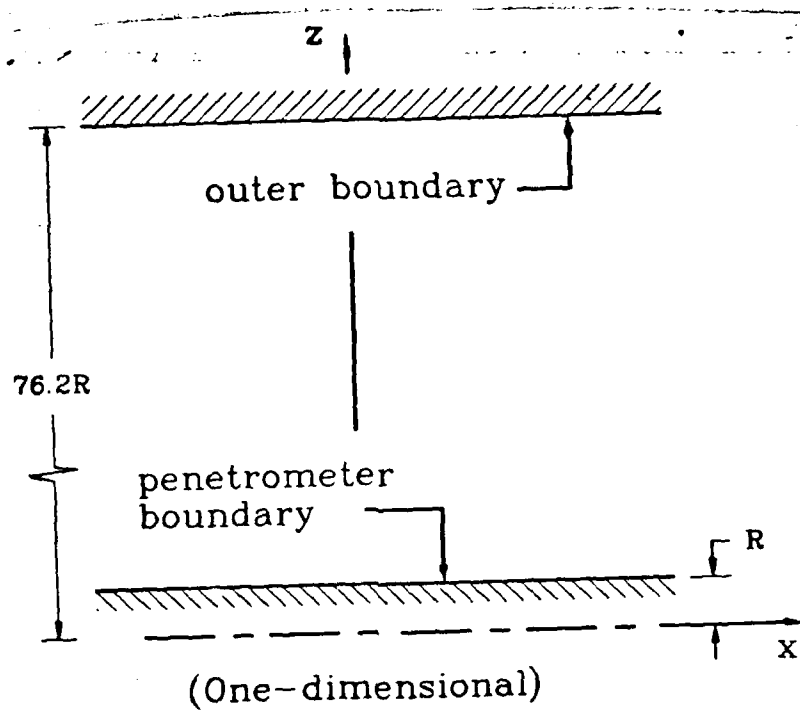
Figure 9.22: Boundary conditions used in the finite difference computation.
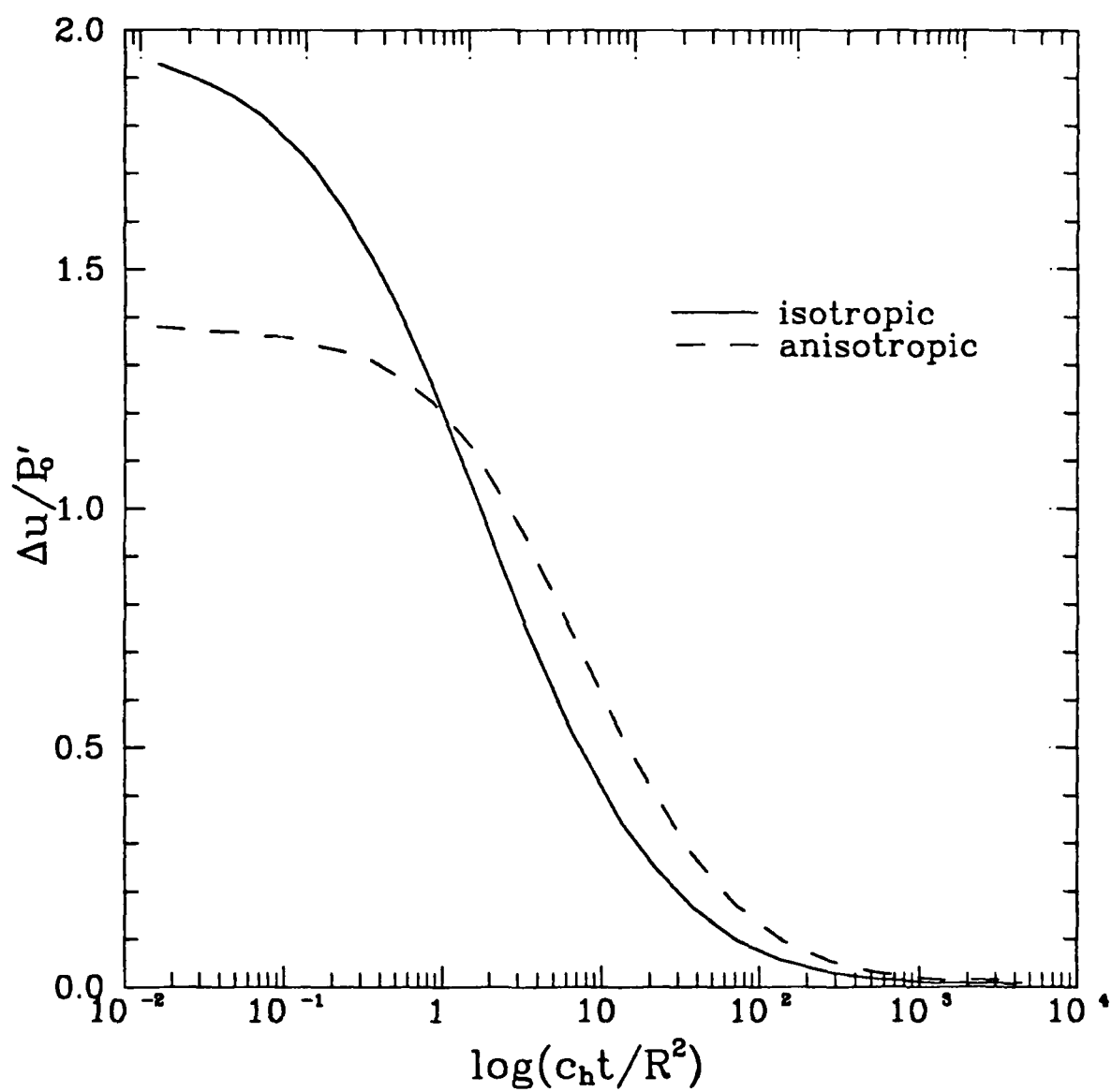
Figure 9.23: Results from finite difference computation.

9.3 Results of the Model DMT Tests

Results from two model DMT tests are presented in the following sections. In test DMT2, the diaphragm was ruptured during penetration and therefore no results wil be presented. Test DMT1 was conducted in an isotropically consolidated specimen and DMT3 was performed in an anisotropically consolidated specimen. In both tests the diaphragm was expanded shortly after the DMT penetration was interrupted. In test DMT1 the diaphragm was inflated to roughly 0.5 mm and then vented to its original position. A second inflation to 1 mm was then performed with the subsequent return to the original position. These were the only full inflation tests that were performed in DMT1. In test DMT3, the diaphragm was inflated to roughly 0.5 mm and then vented to its original position, no further full expansion was applied until the excess pore pressure was fully dissipated. Notice that DMT1 was performed under a back pressure of 218 kPa and a back pressure of 550 kPa was applied in DMT3. Figures 9.25 and 9.26 show the applied pressure versus diaphragm expansion from these two tests and stiffness of the diaphragm membrane according to the calibration tests performed in the blade housing unit under the back pressure. For each DMT test, a set of P_0, P_1 and P_2 pressures were computed where

P_o = pressure required to expand the diaphragm off the face of the DMT blade

P_1 = pressure at which the diaphragm inflated 1 mm away from the face of the blade

P_2 = pressure at which the diaphragm regains its contact with the DMT blade following an expansion.

The above pressures were corrected by subtracting the membrane stiffness according to the calibration curves which included back pressure.

While the pore pressure in the specimen was dissipating a succession of diaphragm inflations and deflations were performed to obtain a series of equivalent DMT P_o and P_2 readings. The inflation of the diaphragm was just enough to find the lift-off and

201

the return pressure. Care was taken not to induce excessive membrane expansion.

Because of the different dimensions of the model DMT used in this research and a conventional DMT blade, the interpretation of the test had to be modified. The value of P_1 was considered to be the pressure at which the diaphragm inflated 0.5 mm away from the face of the blade and not 1 mm. This number was chosen because the model blade dimensions including the diaphragm are all exactly half of the conventional DMT dimensions.

Table 9.5 summarizes the parameters derived from the two model DMT tests following the procedure established by Marchetti (1980). According to Marchetti's soil classification scheme the I_D values from both tests would indicate that the soil tested is clay. This result correlates well to the actual soil type which was silty-clay. Marchetti (1980) suggested that

$$OCR = (0.5K_D)^{1.56} \tag{9.16}$$

Test No.	P_0, kPa	P_1, kPa	P_2, kPa	I_D	K_D	E_D, kPa	U_D
DMT1	396	436	285	0.10	1.91	1532	0.79
DMT3	309	337	226	0.09	1.49	972	0.73

Table 9.5: Summary of DMT derived Parameters.

According to EQ. 9.16 the OCR value is 0.93 for DMT1 and 0.63 for DMT3. The actual soil was normally consolidated with an OCR of 1. Considering the significant differences in dimensions between the model and the Marchetti DMT, these empirical rules perform relatively well.

Figures 9.27 and 9.28 show a comparison between the P_0 and P_2 readings and the excess pore pressures taken from the piezoblade tests (PIEZ2 and PIEZ3). All variables are normalized with respect to the preconsolidation pressure P'_o. In the corresponding piezoblade tests, the same boundary conditions and stress history were applied as in the model DMT tests. The same excess pore pressures measured in the piezoblade tests are therefore expected to occur during the model DMT tests. For tests performed both in the isotropically and anisotropicaly consolidated specimens, P_0 was higher than the excess pore pressure in the very beginning of the pore pressure dissipation process. This indicates that the total stress around the DMT is somewhat higher than the pore pressure. During the majority of the pore pressure dissipation, P_0 remained close to the excess pore pressure readings. Towards the end of dissipation, however, P_0 was higher than the corresponding excess pore pressures. This further confirms the existence of a compressive effective stress adjacent to the DMT. The P_2 values follow closely or slightly below the excess pore pressure readings. A suction could be developed during deflation of the DMT diaphragm. This is most likely the reason for the lower P_2 readings from test DMT3. In any case, the trend of P_2 readings versus time is very close to that of the excess pore pressure dissipation. Therefore, it would be possible to use P_2 readings in the determination of c_h value.

Figures. 9.29 to 9.32 show the moisture content distribution down the front and side of the flat-plate path from four separate specimens all isotropically consolidated. There is no marked differences in the moisture contents taken from the four specimens. This would indicate the reasonable repeatability of specimen preparation procedure adopted in the research project.

Figures. 9.33 and 9.34 show the moisture content distribution from the front and side of the flat-plate of an anisotropically consolidated specimen. All the profiles indicated a consistent decrease of moisture content by as much as 2% adjacent to

the DMT blade. This corresponds to a change of void ratio of 0.054. If flat-plate penetration induces strictly a one-dimensional lateral compression, the reduction of such void ratio would mean an increase of lateral consolidation stress on the order of 200 to 300 kPa based on the C_c values from consolidation tests on samples taken from the chamber specimens (Table 9.4). These are significantly higher than the P_0 readings after the pore pressure dissipation. It is possible therefore that significant creeping had occurred in the process of pore pressure dissipation.
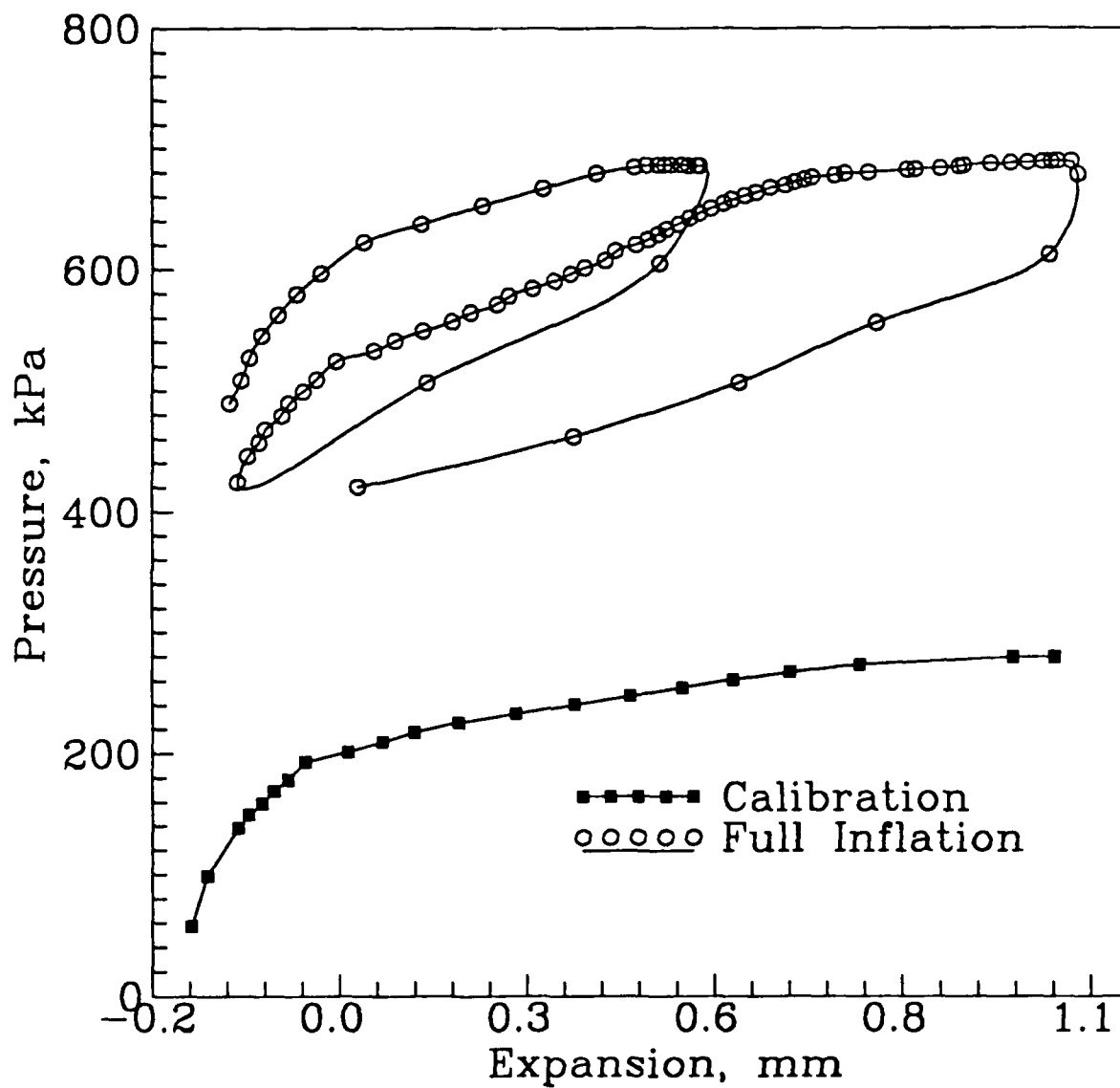
Figure 9.24: Expansion curves of test DMT1.
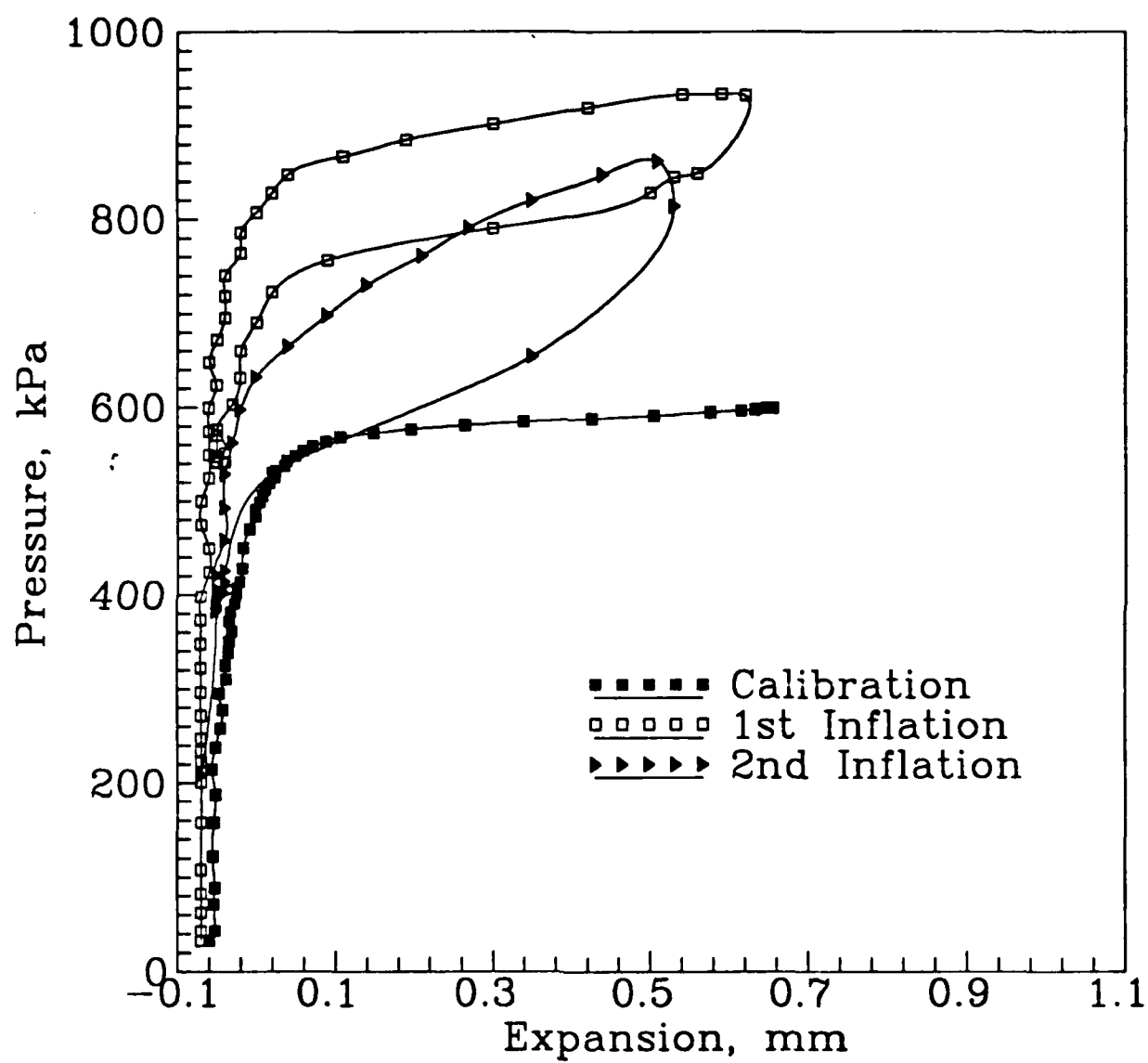
Figure 9.25: Expansion curves of test DMT3.
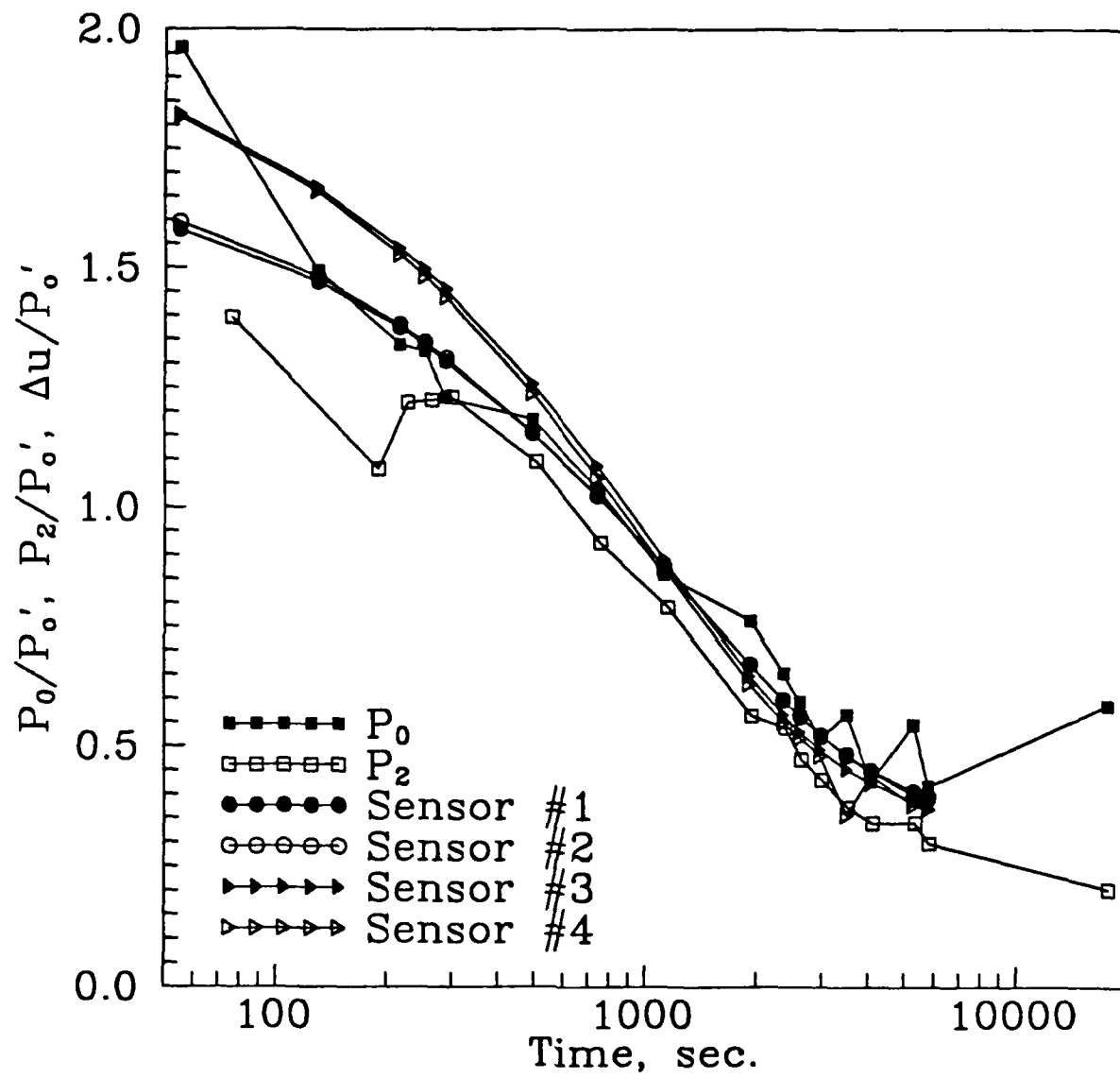
Figure 9.26: Normalized P_0 and P_2 readings (DMT1) and piezoblade dissipation (PIEZ2) data.
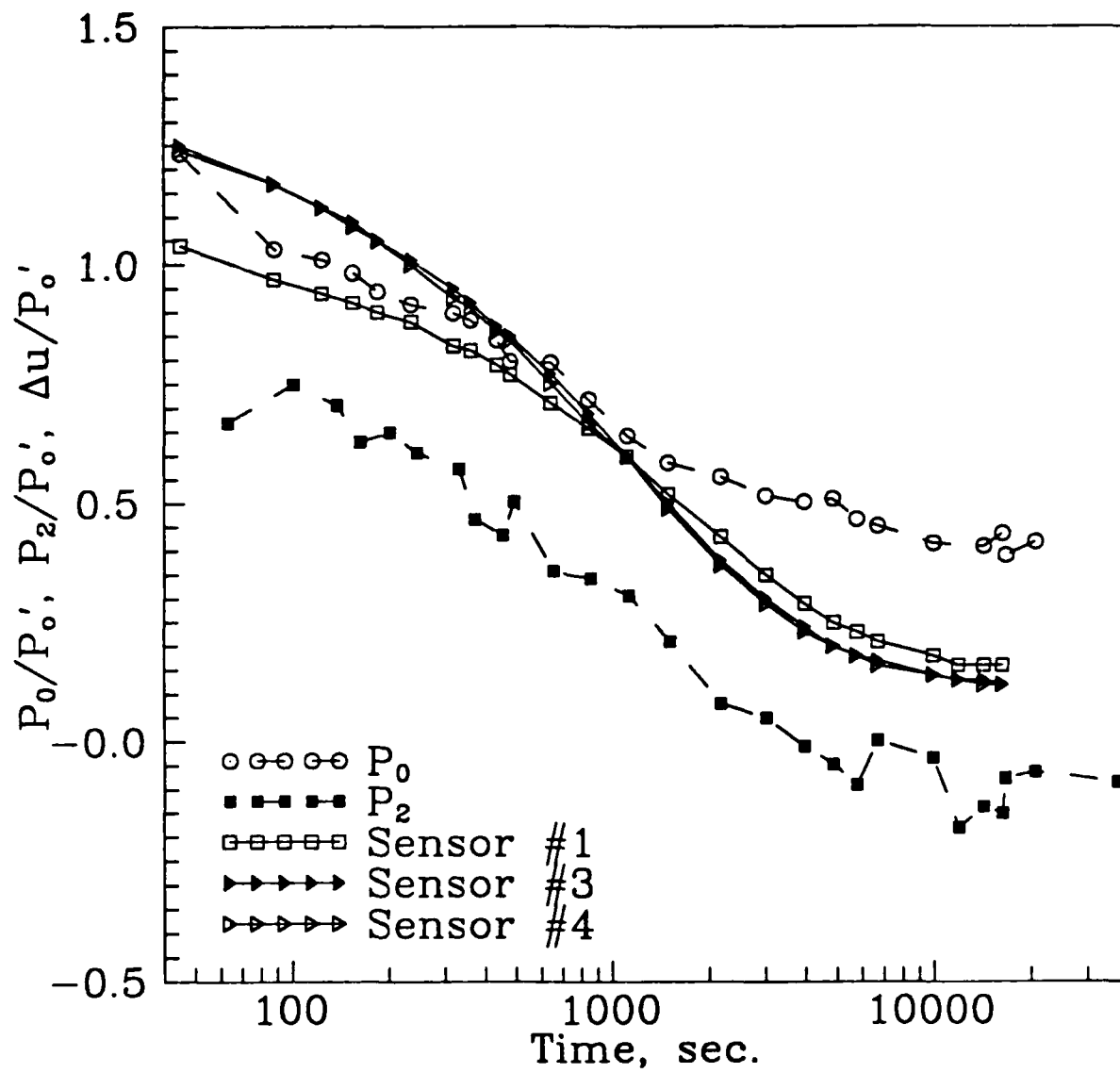
Figure 9.27: Normalized P_0 and P_2 readings (DMT3) and piezoblade dissipation (PIEZ3) data.
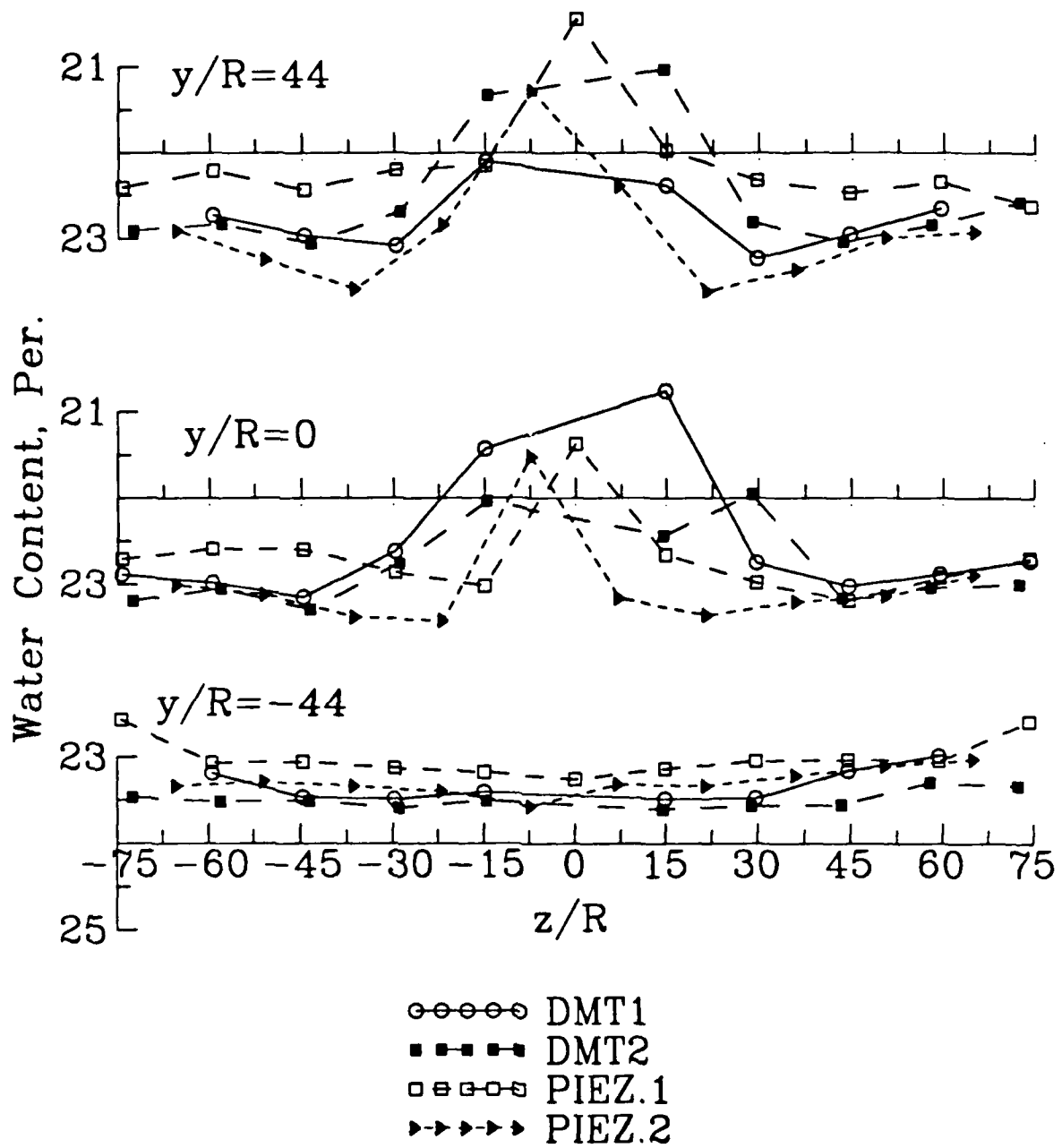
Figure 9.28: Moisture contents from the isotropically consolidated specimens (across the front of the blade).
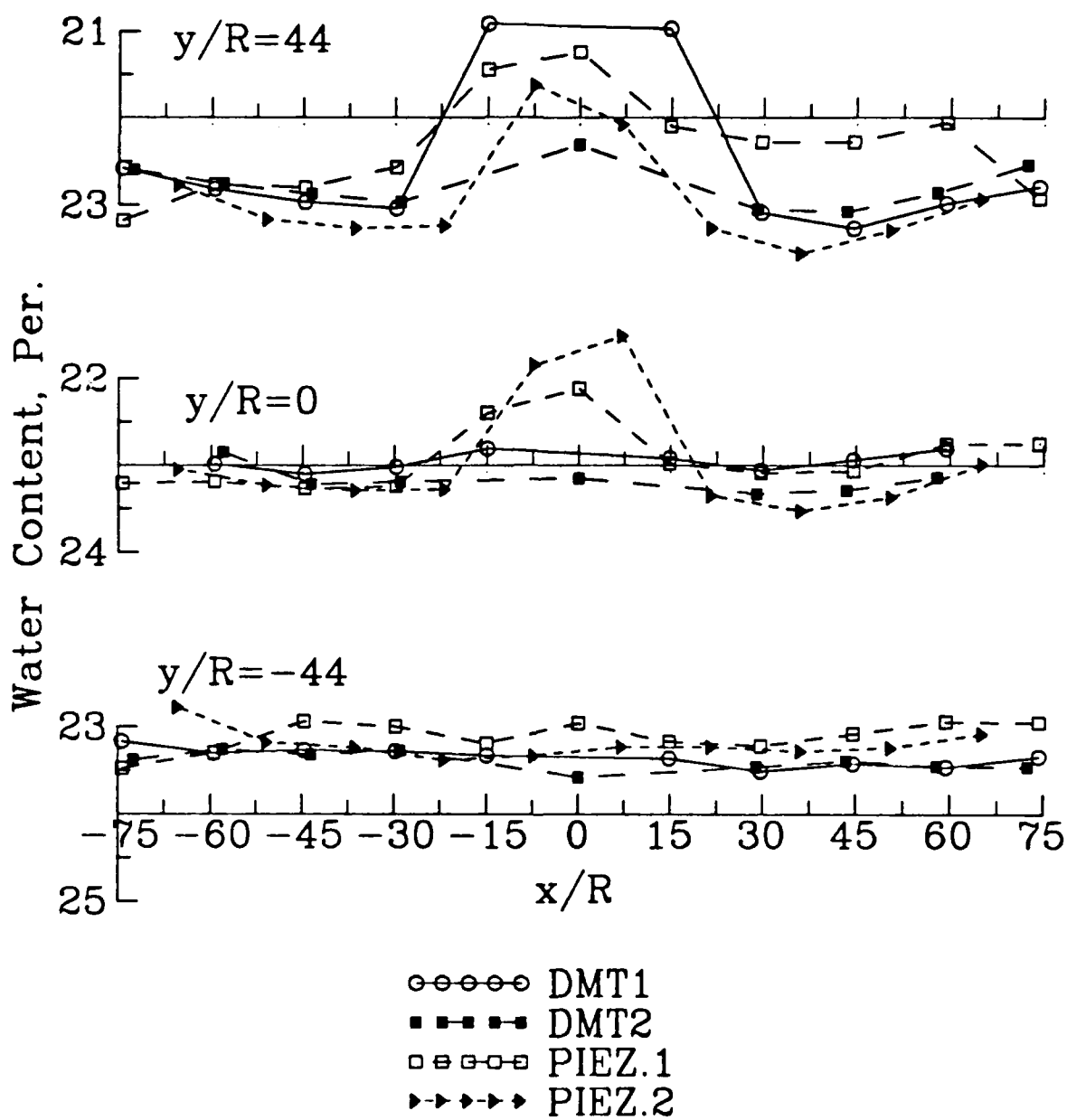
Figure 9.29: Moisture contents from the isotropically consolidated specimens (across the side of the blade).
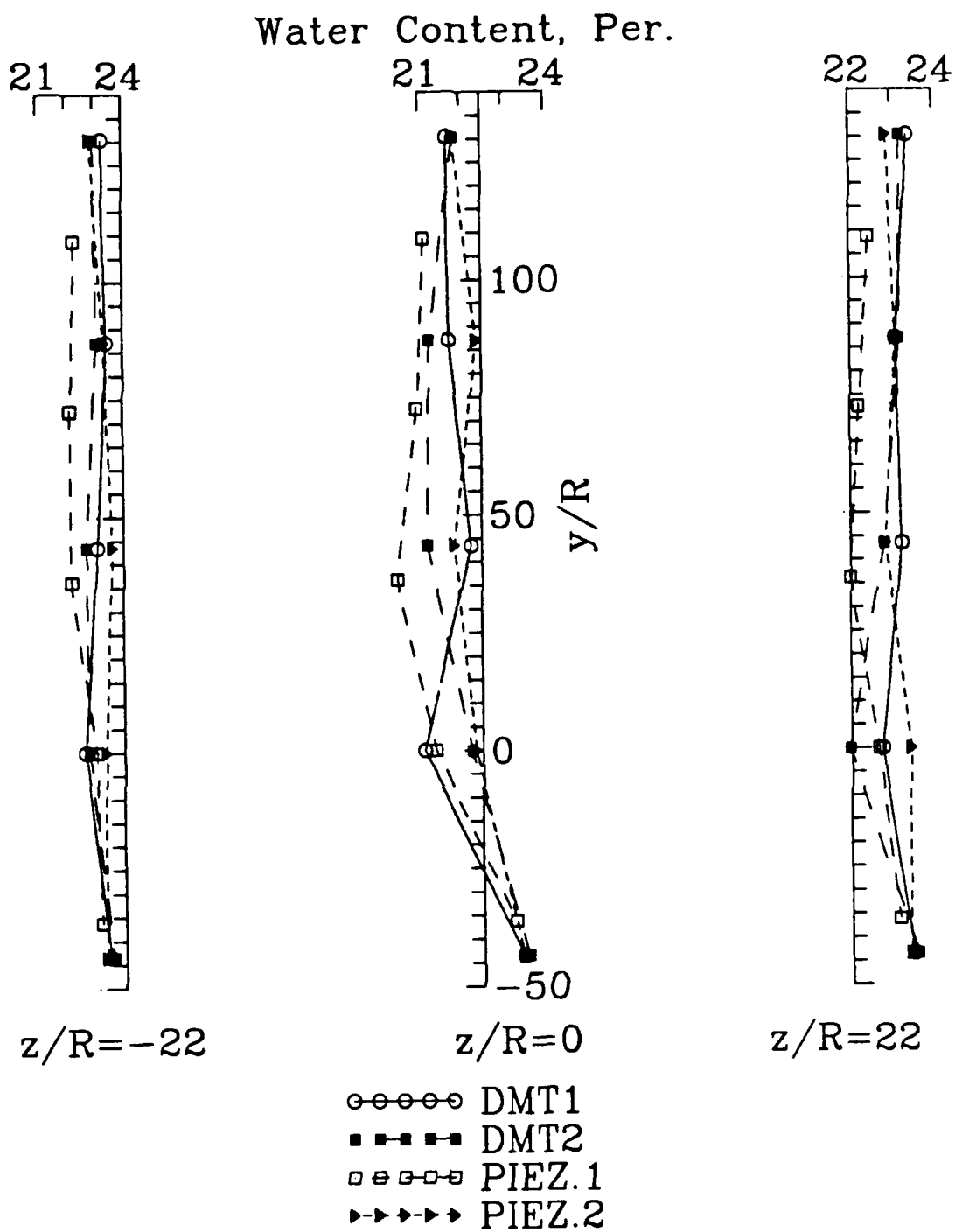
Figure 9.30: Moisture contents from isotropically consolidated specimens (down the front of the blade).
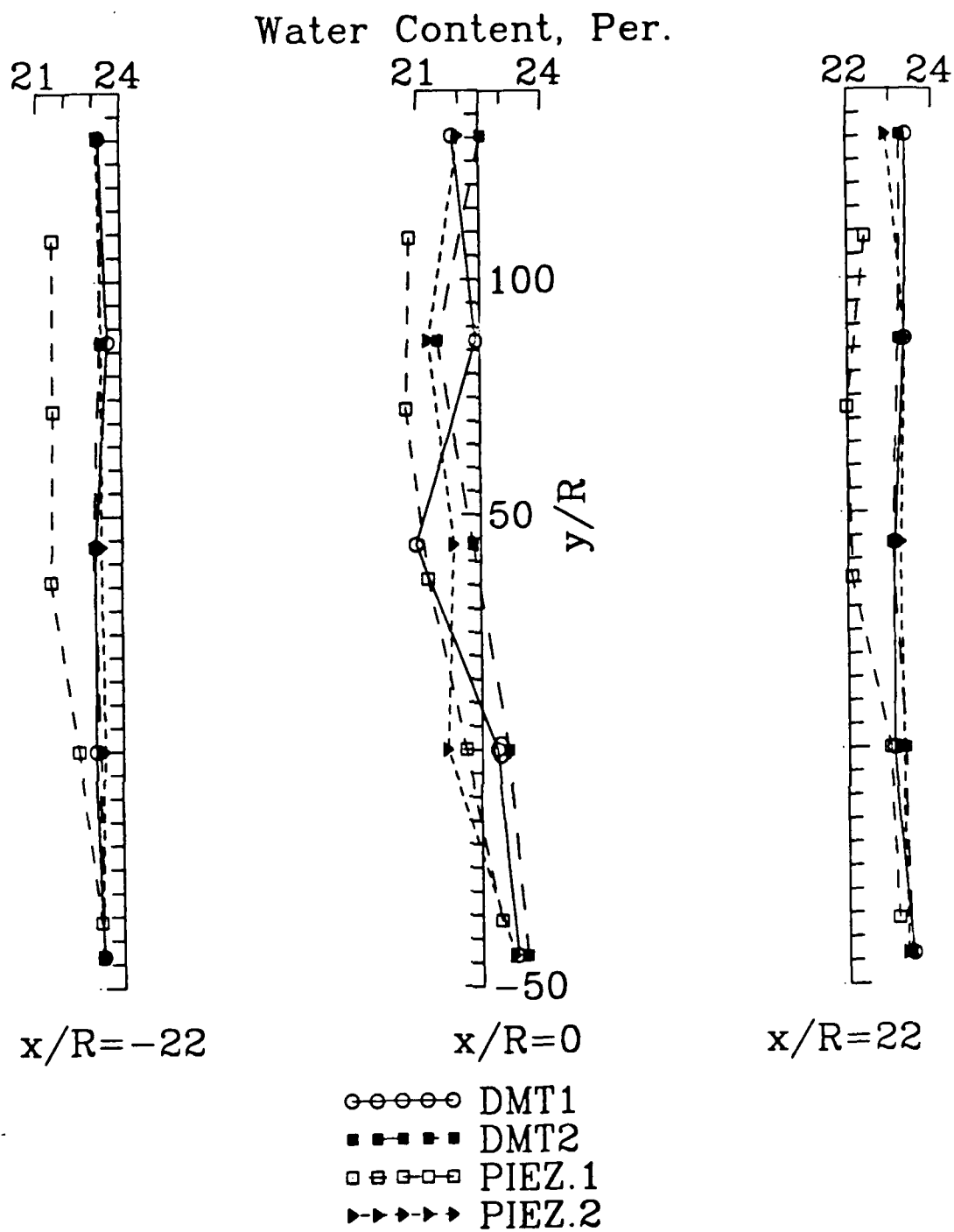
Figure 9.31: Moisture contents from isotropically consolidated specimens (down the side of the blade).
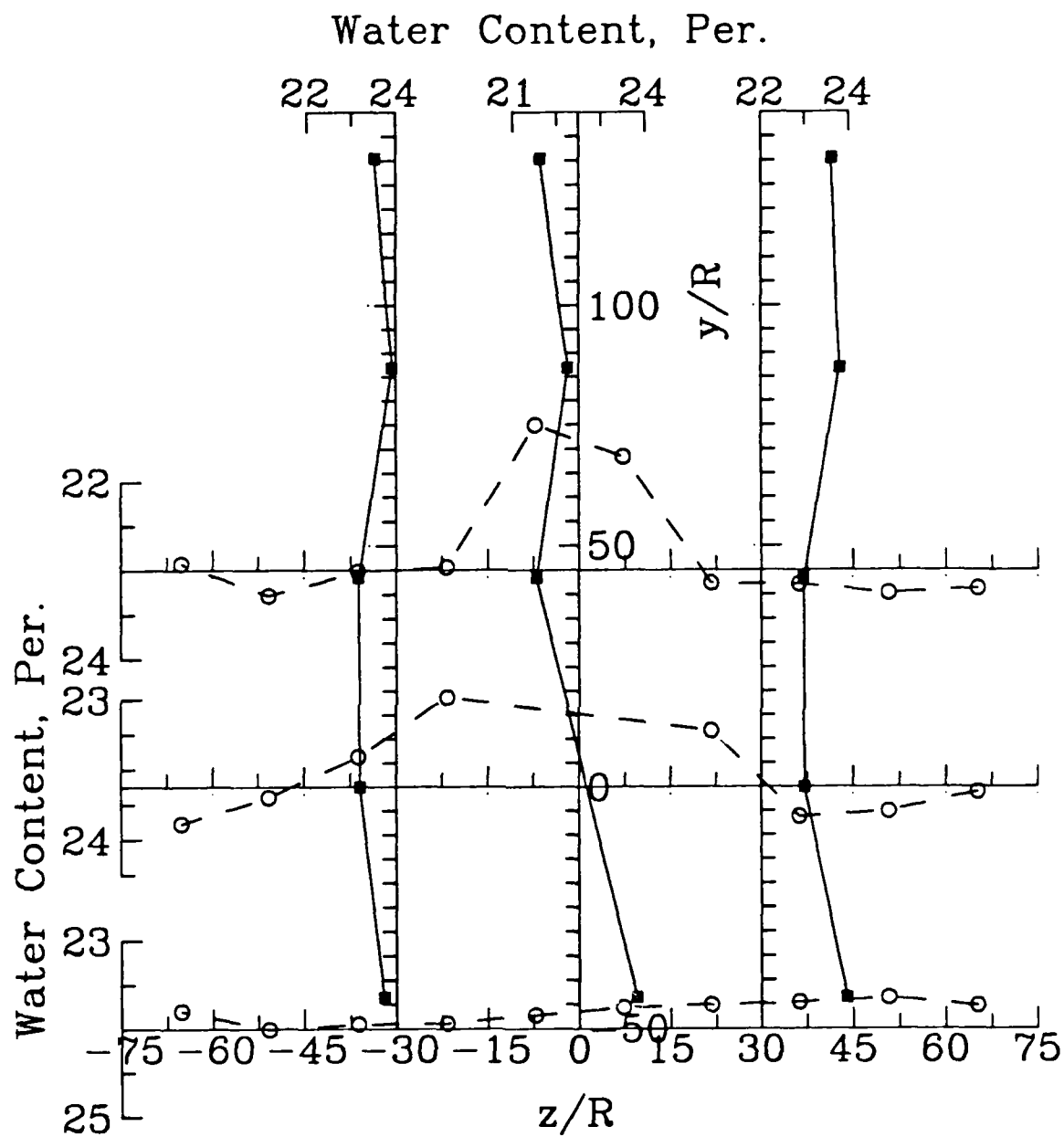
Figure 9.32: Moisture contents from anisotropically consolidated specimens (front of the blade).
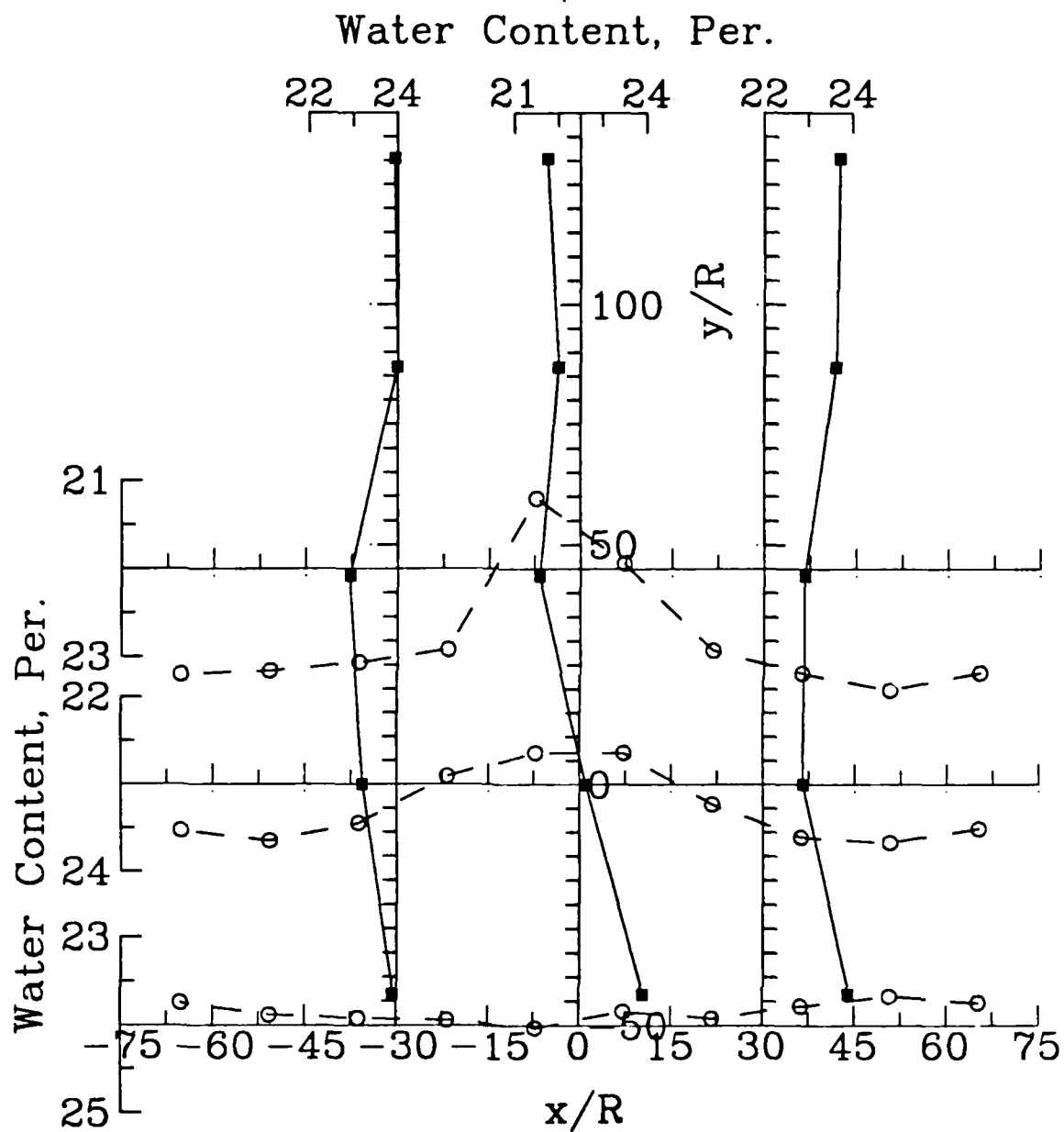
Figure 9.33: Moisture contents from anisotropically consolidated specimens (side of the blade).

Chapter 10

Comparisons with Field Tests

A comparison was made of the results obtained from the various flat-plate penetrometers by conducting field tests which included DMT, K_o-Stepped Blade and tapered blade tests. The test site is located east of the town of Massena, New York, which is within the southern extent of the Champlain sea. The soils consist of approximately 12 m of a marine clay deposit underlain by glacial till. Below a highly weathered and fissured crust of 1.5 m thick, the marine clay is soft and lightly overconsolidated (OCR = 1.5 to 3) . In addition to conventional laboratory classification tests, reference insitu tests performed at the test site included Self-Boring Pressuremeter (SBPM), Full-Displacement Pressuremeter (Pencel), Field Vane Shear (FVT) and Piezocone (CPTU) tests. Figure 10.1 shows profiles of the available test results.

The interpretation of the K_o-Stepped and tapered blade followed the procedures by Handy, et al. (1982) which uses linear regression to fit the data to EQ. 1.4 with assumed value $a = 1$. A coefficient of correlation is also computed during the linear regression. The results are shown in Figure 10.2 and plots of the normalized pressure versus blade thickness for all the data are included in Figure 10.3. The DMT results in terms of the net pressures at the beginning (P_0^{DMT}) and end of the membrane

expansion (P_1^{DMT}) versus depth are plotted in Figure 10.4 along with the SBPM and Pencel lift off and limit pressures. In essence, the field flat-plate test results support the SPM studies substantially. The pressure readings from the first sensor are consistently higher than those from the second one in most of the stepped and tapered blade tests. These results are similar to those obtained at other sites (Lutenegger and Timian, 1986a; 1986b) using the same K_o-Stepped Blade and are consistent with results obtained using a widened blade (Handy, et al. , 1987). These penetrometers have relatively large apex angles. Strain path analyses indicated that there is a large reversal of the E_3-strain as the soil passes the blade tip. Computations of pore pressure and total stress presented earlier indicated that there is sharp increase and subsequent decrease of pore pressure at the tip of a penetrometer, regardless of its geometry. Due to the proximity of the first pressure sensor to the blade tip, the sensor is likely to be influenced by such a high pore pressure thus yield high pressure readings. This abnormality is responsible for some of the negative slopes for the K_o-Stepped Blade tests and undesirable coefficients of correlation for all as shown in Figure 10.2. Neglecting the first pressure reading is not preferable as it would jeopardize the statistical validity of the data especially for the K_o-Stepped Blade. The test data shown in Figures refkoblade and 10.3 indicate that for the tapered-blade, the measured lateral pressures are rather insensitive to the blade thickness in this clay. This is consistent with the analytical studies which indicate that the pore pressure and total lateral stress (σ_{zz}) remain relatively constant beyond the tip of the blade, as the blade thickness increases.

The flexible membrane on the DMT extends to approximately $x = 4.2R$ (30 mm radius). Based on SPM analyses, the E_2-strain within the membrane area should be between those of plane strain and CPT penetrations. The P_0^{DMT} value should therefore reflect an effect between plane strain and cylindrical cavity expansions.

216

This is consistent with the P_0^{DMT} values shown in Figure 10.4 which are very close to the SBPM limit pressures. Similar results were also reported by Lutenegger (1988) for other DMT tests performed in the same marine clay deposit.
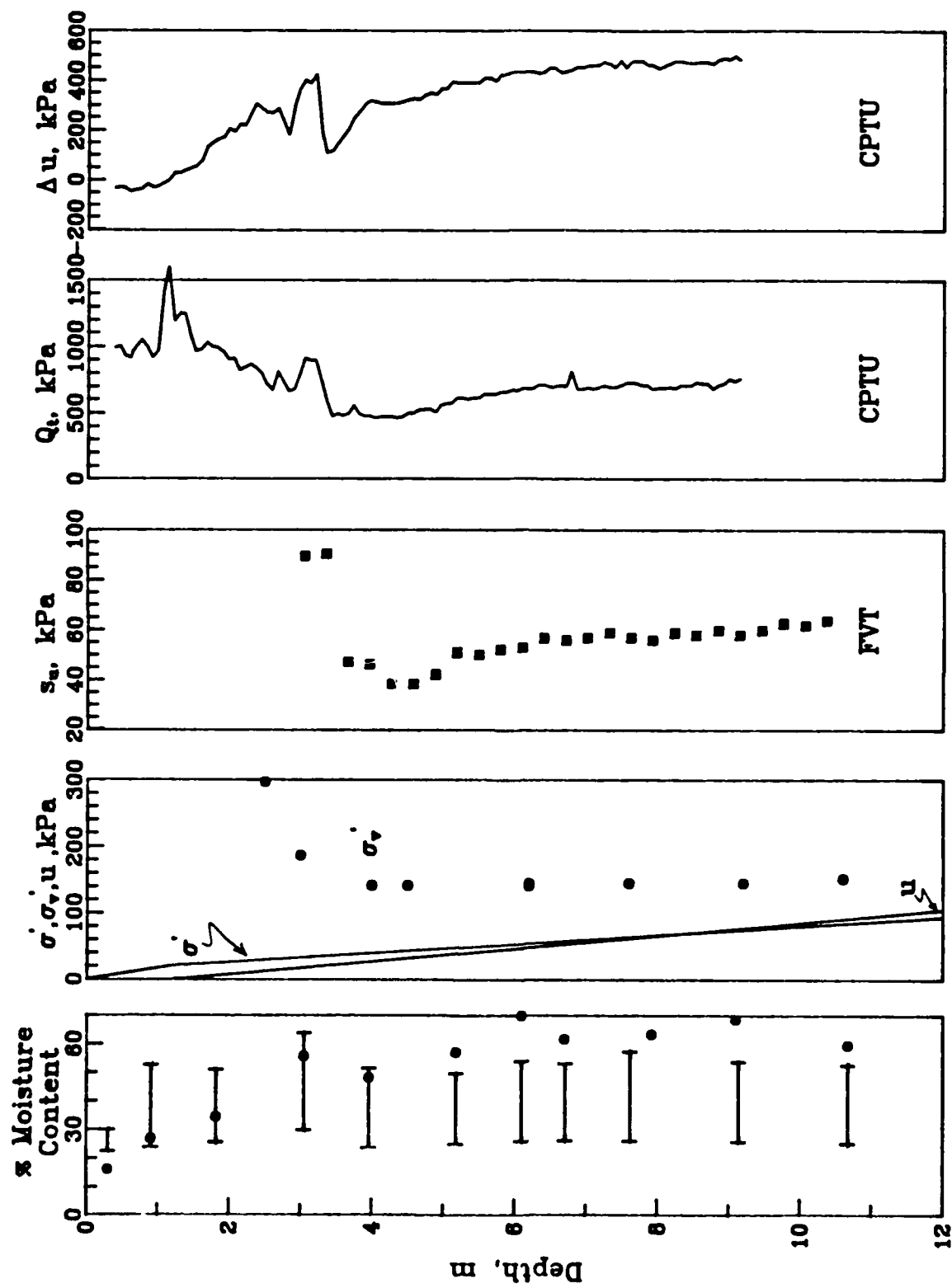
Figure 10.1: Soil profiles at the test site.
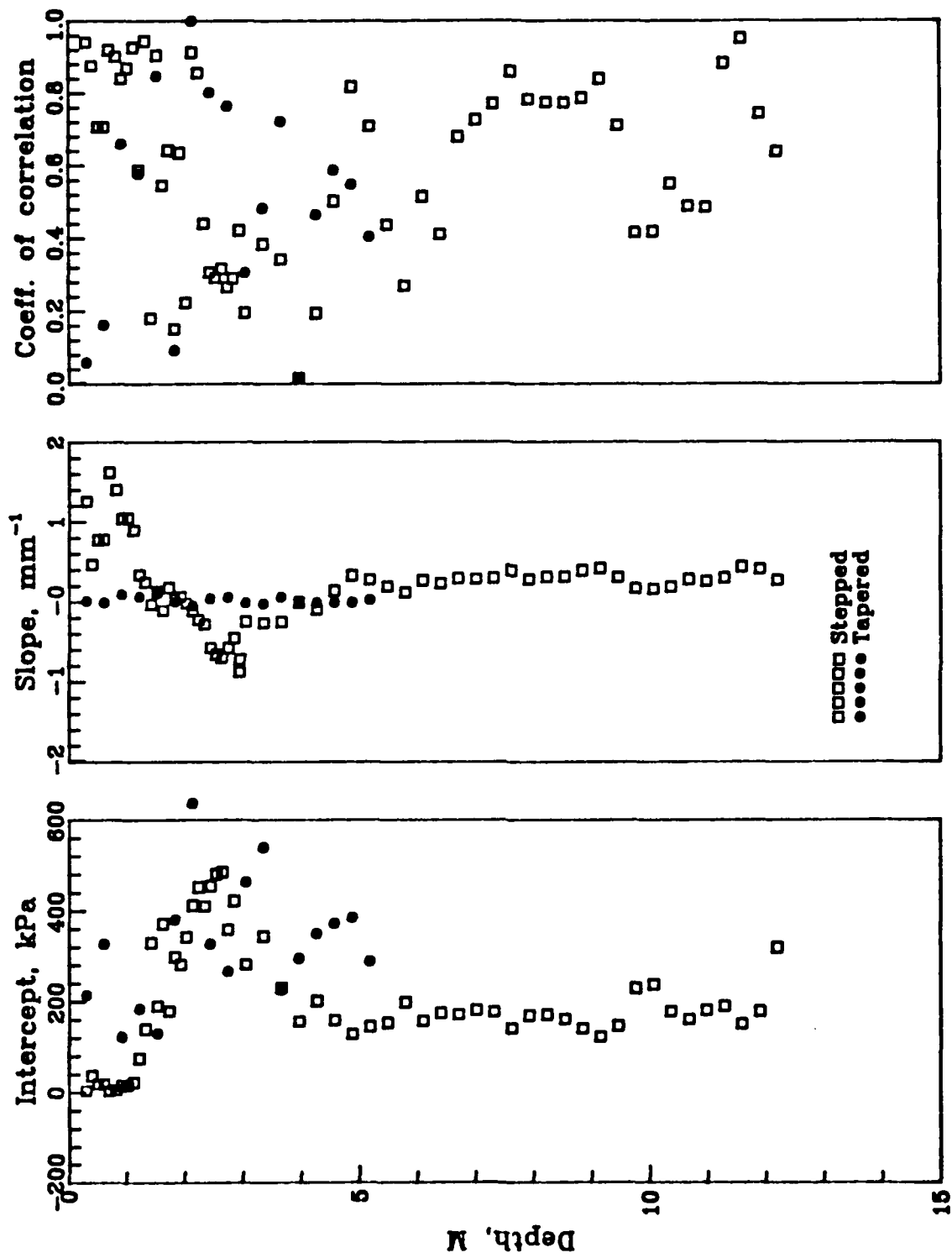
Figure 10.2: Interpretations of the stepped and tapered blade tests.

219
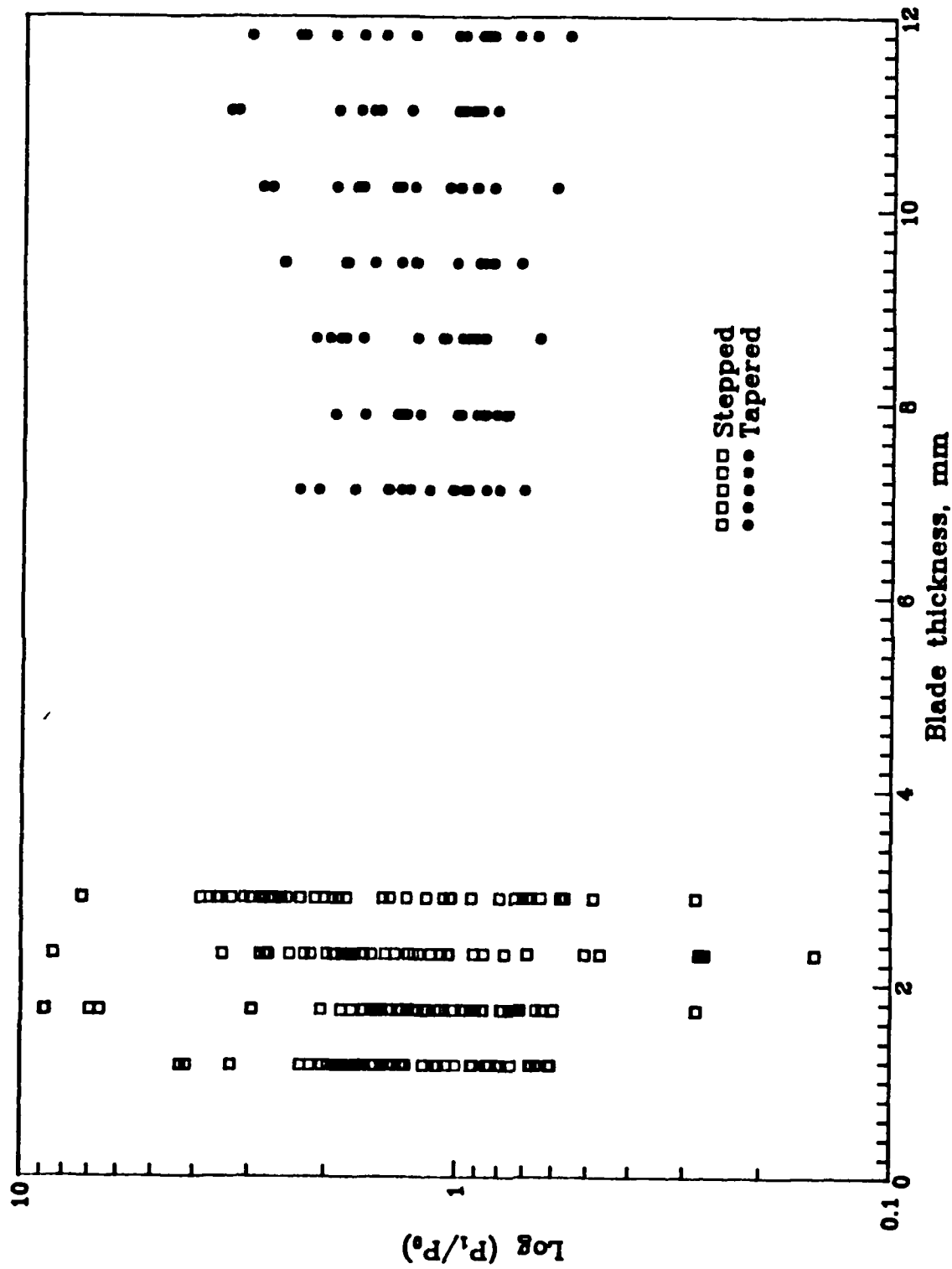
Figure 10.3: Normalized stepped and tapered blade test results.
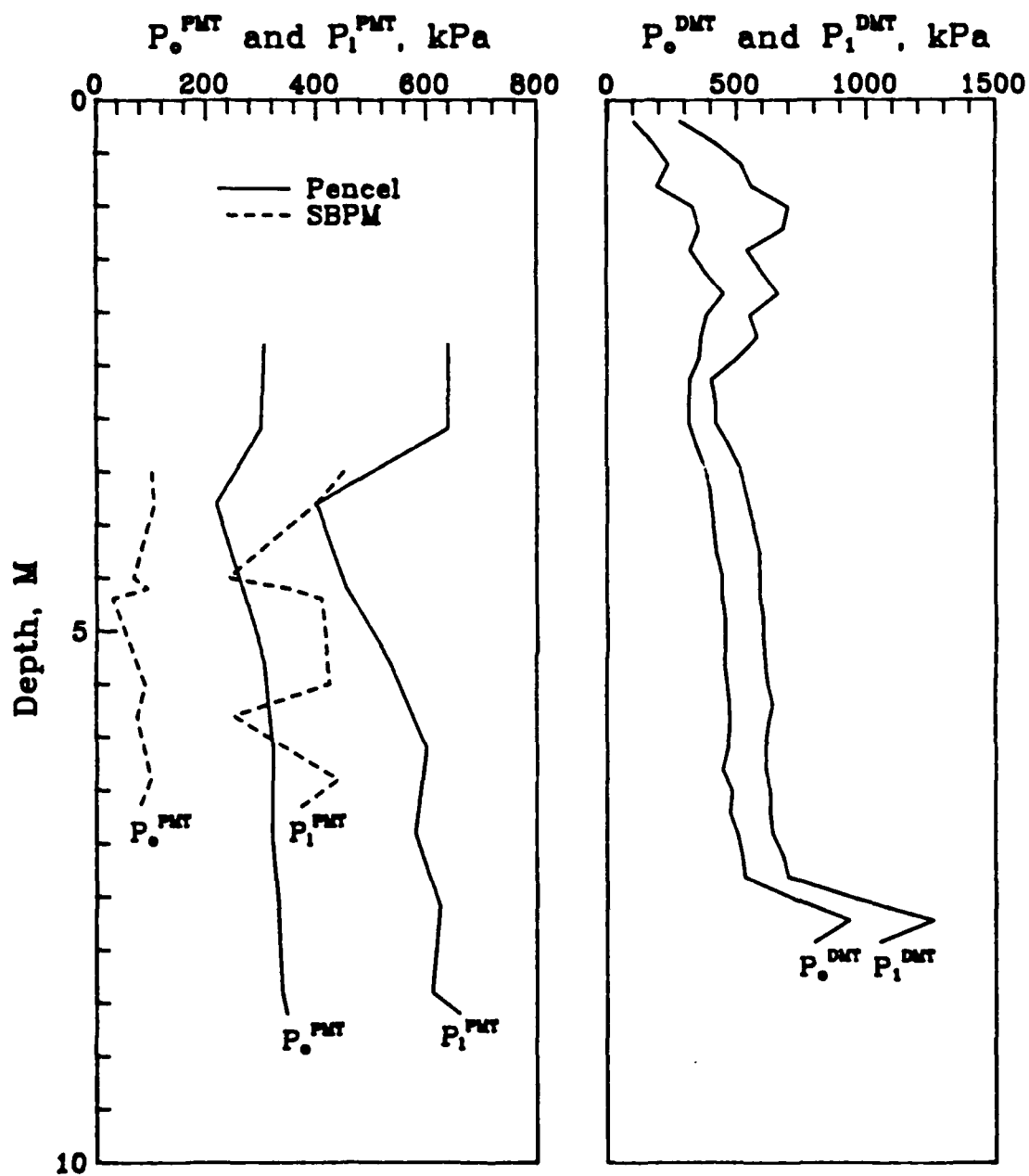
Figure 10.4: SBPM and DMT test results.

Chapter 11

Conclusions

In this research, a numerical technique capable of computing strain paths for three-dimensional penetrometers was developed. It provided a systematic way of elucidating the soil strain and displacement induced by the insertion of a flat-plate which we had limited knowledge hitherto before. A strain based Modified Clay model was used to estimate the associated stress field. The pore pressure distribution was computed based on considerations of stress equilibrium. Laboratory experiments were conducted concurrent with the analytical studies. A calibration chamber system and model flat-plate penetrometers were fabricated. Model flat-plate penetration tests were performed in laboratory prepared clay specimens using the chamber system. Triaxial and consolidation tests were conducted on the same clay to provide reference properties of the soil. Field flat-plate penetration test results from a Clarkson University research test site were evaluated. Based on the findings, the following conclusions are made:

- A three-dimensional flat plate penetration, as in cone penetration, results in strains and strain rates much higher than those encountered in common laboratory experiments. Strain rates as high as 20% per second are encountered in the tip region of all penetrometers analyzed, as compared to the 0.015% per second value which is typical to laboratory triaxial testing. The soil in the vicinity of the flat-plate penetrometer is subject to large strains and strain reversals;

- For cylindrical penetrometers, E_2-strain is the predominant component as previous studies (Baligh, 1985) had indicated. This is, however. not necessarily the case for flat-plate penetrometers. The characteristics of the strain field during a flat-plate penetration is influenced by both the w/t ratio and the tip apex angle. The combination of a blunt tip angle (i. e. , larger than 20 degrees) and a w/t of approximately 10 or larger could result in E_3-strain as the predominant strain component during penetration. This would render the lateral compression theory irrelevant to the problem it intends to solve;

- The basic concept of linearly relating lateral pressure measurements to the exponential of plate thickness is highly questionable. The SPM analyses indicated that the predominant strains induced by the penetration of a K_o-Stepped Blade resembles that during a cyclic direct simple shear test. The tapered design is an improvement as it eliminates such cycles. However, a more serious drawback lies with the requirement of varying w/t ratios. As w/t decreases the strain paths deviates further away from those of plane strain penetrations, which is required for a linear exponential relationship between the lateral pressure measurements and the plate thickness. For the current designs, the w/t ratios are far from being desirable. This implies that there is no theoretical basis for such a linear exponential relationship between pressure and plate thickness, even if the soil is linear elastic. Analytical studies further indicated that the pore pressure and total normal stress (σ_{zz}) peak at the tip of the penetrometer regardless of the penetrometer geometry. The tip apex angle affects the peak values but does not alter the trend of a sharp decrease of pore pressure and total stress as soil element passes the tip of the penetrometer. Computations showed that the total stress remains more or less constant as the soil element passes the flat-plate with increasing thickness. Field stepped-blade and tapered blade tests confirmed these findings;

- The flat-plate penetration induced excess pore pressure as predicted by the SPM/Modified Cam Clay model system is significantly lower than those measured in the calibration chamber. The plane strain simplification for the pore

pressure computation is obviously a part of the reason for this discrepancy. The lack of a more appropriate consideration of the shear stress related pore pressure development under a mixed mode of strain reversals is probably a more serious drawback in the current approach. Knowledge and available data base in this area are very limited at present;

- For a simple flat-plate penetration (i.e., the DMT) in normally consolidated clay, the magnitude of pore pressure increase is positively related to the soil rigidity index in the lateral direction. This may have an important implication in the interpretation of DMT tests in clays to obtain shear modulus and/or undrained shear strength;

- The analytical and experimental studies showed that the magnitude of flat-plate penetration induced excess pore pressure is comparable to that of cylindrical penetration. In the case of chamber piezoblade penetration tests, the excess pore pressure diminishes much faster with distance than expected for a cylindrical penetrometer with comparable dimensions;

- The dissipation of pore pressure at the center of a flat-plate is significantly slower than expected for a cylindrical penetrometer. The same has also been reported for field piezoblade tests (Kabir and Lutenegger, 1990). This is mostly due to a concurrent pore pressure dissipation from the tip towards the center of the plate. It is apparent that placing the piezo unit within the tip region of flat-plate would make the interpretation for c_h much simpler;

- Despite the three-dimensional nature of the piezoblade, the excess pore pressure dissipation followed an axisymmetric pattern for the chamber test performed in an anisotropically consolidated specimen. Interpretation of the chamber piezoblade pore pressure dissipation data using an axisymmetric solution resulted in a c_h value comparable with but lower than those obtained from consolidation tests;

- The P_2 readings follow the same trend as the excess pore pressure dissipation after the penetration is interrupted. It is therefore possible to use P_2 directly

224

from DMT tests for the interpretation of c_h;

- The strain path studies confirm what Hvorslev (1949) found out forty years ago that as far as disturbance is concerned, it is the geometry not the size that matters. Any attempt to improve the design of penetrometers should concentrate on the geometries. Based on the studies presented herein, a good flat-plate penetrometer should have a w/t exceeding 20 and a tip apex angle less than 20 degrees. The diameter of the pressure sensor should be less than $1/4$ of the plate width. The sensor lift-off pressure can then be related to lateral compression under a plane strain condition. Spade cells (see Figure 3.1) used in the past have had w/t ratios varying from 12.7 to 25 (Massarsch, 1975; Ladd et al. ,1979; Tedd and Charles, 1981; Fukuoka and Imamura, 1983). Unfortunately, most designs did not take full advantage of the relatively favorable w/t ratios as the pressure sensors extended the full width of the blade. Studies presented herein showed that strains around the blade corners are far from plane strain and would undoubtedly affect the pressure measurements.

- If a flat-plate penetrometer (e. g. , DMT) has any advantage over a cylindrical one (e. g. , CPT), it has to be mechanical or in operation efficiency. A cone with a sharper apex angle could induce strains which are axisymmetric and with levels comparable to that of DMT.

225

Bibliography

[1] Baligh, M. M. (1985). "Strain Path Method," Journal of Geotechnical Engineering Division ASCE Vol. 111, No. GT9, pp. 1108-1136.

[2] Baligh, M. M. (1986a). "Undrained Deep Penetration, I: Shear Stresses," Géotechnique Vol. 36, No. 4, pp. 471-485.

[3] Baligh, M. M. (1986b). "Undrained Deep Penetration, II: Pore Pressures," Géotechnique Vol. 36, No. 4, pp. 487-501.

[4] Baligh, M. M. , Azzouz, A. S. , and Chin, C. T. (1987). "Disturbance Due to 'Ideal' Tube Sampling," Journal of Geotechnical Engineering Division, ASCE, Vol. 113, No. GT7, pp. 739-757.

[5] Chen, W. F. , and Saleeb. , A. F. (1982). "Constitutive Equations for Engineering Materials, Volume 1: Elasticity and Modeling," John Wiley and Sons, New York, N. Y.

[6] Davis, R. O. and Mullenger, G. (1978). "A Rate Type Constitutive Model for Soils with a Critical State," International Journal for Numerical and Analytical Methods in Geomechanics, Vol. 2, No. 3, pp. 255-282.

[7] Fukuoka, M. and Imamura, Y. (1983). "Earth Pressure Measurements in Retaining Wall Backfill", Proc. of International Symposium on In Situ Testing of Soil and Rock, Paris, Vol.2, pp. 49-53.

[8] Fukuoka, M. , and Imamura, Y. (1983). "Earth Pressure Measurement in Retaining Wall Backfill," Proceedings, International Symposium on Soil & Rock Investigations by In Situ Testing," Vol. 2, pp. 49-53.

[9] Handy, R. L. , Briaud, J. L. , Gan, K. C. , Mings, C. L. , Retz, D. W. , and Yang, J. -F. (1987). "Use of the K_0-Stepped Blade in Foundation Design," Report No. FHWA/RD-87-102. Federal Highway Administration, Washington, D. C. .

[10] Handy, R. L. , and Lutenegger, A. J. (1985). "Tapered Blade in Situ Testing Device," U. S. Patent No. 4543820.

[11] Hess, J. L. , and Smith, A. M. O. (1962). "Calculation of Non-Lifting Potential Flow about Arbitrary Three-Dimensional Bodies," Douglas Aircraft Company Report No. ES-40622.

[12] Handy, R. L. , Remmes, B. , Moldt, S. , Lutenegger, A. J. , and Trott, G. (1982). "In Situ Stress Determination by Iowa Stepped Blade," Journal Of Geotechnical Engineering Division, ASCE Vol. 108, GT11, pp. 1405-1422.

[13] Hess, J. L. and Smith, A. M. O. (1964). "Calculation of Non-Lifting Potential Flow about Arbitrary Three-Dimensional Bodies," Journal of Ship Research, Vol. 8, No. 2, pp. 22-44.

[14] Hess, J. L. (1975). "Review of Integral-Equation Techniques for Solving Potential-Flow Problems with Emphasis on The Surface-Source Method," Computer Methods in Applied Mechanics and Engineering, Vol. 5, pp. 145-196.

227

[15] Huang, A. -B. (1986). "Laboratory Pressuremeter Experiments in Clay Soils," Ph. D. Thesis, Purdue University.

[16] Huang, A. -B. , Holtz, R. D. , and Chameau, J. -L. (1988). "A Calibration Chamber for Cohesive Soils," Geotechnical Testing Journal, Vol. 11, No. 1, pp. 30-35.

[17] Hvorslev, M. J. (1949). "Subsurface exploration and sampling of soil for civil engineering purposes," ASCE. , New York, N. Y. , pp. 126-127.

[18] Janbu, N. (1967). "Settlement calculations based on the tangent modulus concept," Institute for Soil Mechanics and Foundation Engineering, The Technical University of Norway, Trondheim, Norway.

[19] Kabir, M. G. (1990). "In Situ Estimate of the Coefficient of Consolidation in Clays," Canadian Geotechnical Engineering, Vol. 27, pp. 58-67.

[20] Kavvadas, M. (1982). "Non-Linear Consolidation Around Driven Piles in Clays," Doctor of Science Thesis, Massachussetts Institute of Technology.

[21] Kellog, O. D. (1929). "Foundations of Potential Theory," Frederick Ungar Publishing Company, New York, N. Y.

[22] Krizek, R. J. and Sheeran, D. E. (1970). "Slurry Preparation and Characteristics of Samples Consolidated in the Slurry Consolidometer," Technical Report No. 2, Contract No. DACW 39-70-C-0053, U.S. Army Corps of Engineers Waterways Experiment Station, Vicksberg, Mississippi.

[23] Ladd, C. C. , Germaine, J. T. , Baligh, M. M. and Lacasse, S. (1979). "Evaluation on Self-Boring Pressuremeter Tests in Boston Blue Clay," Interim Report, DOT contract FH-11-9264.

[24] Levadoux, J. -L. and Baligh, M. M. (1980). "Pore Pressure during Cone Penetration in Clays," Report No. MITSG 80-12, MIT.

[25] Liam Finn, W. D. (1963). "Boundary Value Problem of Soil Mechanics," Journal of Soil Mechanics and Foundation Engineering Division, ASCE Vol. 89, No. SM1, pp. 39-72.

[26] Lutenegger, A. J. , and Timian, D. (1986a). "Flat-plate Penetrometer Tests in Marine Clays," Proceedings, 39th Canadian Geotechnical Conference, pp. 301-309.

[27] Lutenegger, A. J. , and Timian, D. (1986b). "In Situ Tests with K_0-Stepped Blade," Proceedings, Conference on Use of In Situ Tests in Geotechnical Engineering, Blacksburg, Virginia, pp. 730-751.

[28] Lutenegger, A. J. (1988). "Current Status of The Marchetti Dilatometer Test," Proceedings, 1st ISOPT, Florida, pp. 137-155.

[29] Marchetti, S. (1975). "A New in Situ Test for Measurement of Horizontal Soil Deformability," Proceedings, Conference on In Situ Measurement of Soil Properties, Raleigh, North Carolina, pp. 255-259.

[30] Marchetti, S. (1980). "In Situ Tests by Flat Dilatometer," Journal of Geotechnical Engineering Division, ASCE Vol. 106, No. GT3, pp. 299-321

[31] Marchetti, S. (1981). "Closure of In Situ Tests by Flat Dilatometer," Journal of Geotechnical Engineering Division ASCE, Vol. 107, pp. 832-837.

[32] Massarsch, K. R. (1975). "New Method for Measurement of Lateral Earth Pressure in Cohesive Soils," Canadian Geotechnical Journal, Vol. 12, pp. 142-146.

[33] Mitchell, J. K. (1976). "Fundamentals of Soil Behavior," John Wiley and Sons, Inc., New York, pp. 84-99, 303-305.

[34] Prevost, J. H. (1978). "Anisotropic Undrained Stress-Strain Behavior of Clays," Journal of Geotechnical Engineering Division, ASCE Vol. 104, No. GT8, pp. 1075-1090.

[35] Prevost, J. H. (1978). "Plasticity Theory for Soil Stress-Strain Behavior," Journal of Engineering Mechanics Division, ASCE Vol. 104, EM5, pp. 1177-1194.

[36] Randolph, M. F. and Wroth, C. P. (1979). "An Analytical Solution for the Consolidation around a Driven Pile," International Journal for Numerical and Analytical Methods in Geomechanics, Vol. 3, pp. 217-229.

[37] Roscoe, K.H. and Burland, J.B. (1968). "On the Generalized Behavior of Wet Clays", Eng. Plasticity. Eds. J. Heymann and F.A. Leckie, Cambridge, University press, pp. 535-609.

[38] Schmertmann, J. S. (1981). "Discussion of In Situ Tests by Flat Dilatometer," Journal of Geotechnical Engineering Division, ASCE Vol. 107, pp. 831-832.

[39] Scott, R. F. (1987). "Failure," The Rankine Lecture, Géotechnique Vol. 37, No. 4, pp. 423-466.

[40] Skempton, A.W. (1954). "The Pore Pressure Coefficients A and B," Géotechnique, Vol. 4, pp. 143-147.

[41] Tedd, P. , and Charles, J. A. (1981). "In Situ Measurement of Horizontal Stress in Overconsolidated Clay Using Push-in Spade-Shaped Pressure Cells," Géotechnique Vol. 31, No. 4, pp. 554-558.

[42] Tedd, P. , and Charles, J. A. (1983). "Evaluation of Push-in Pressure Cell Results in Stiff Clay," Proceedings, International Symposium on In Situ Testing, Paris, Vol. 2, pp. 579-584.

[43] Teh, C.I. (1987). "Analytical Study of the Cone Penetration Test," PhD Thesis, University of Oxford, England.

[44] Tumay, M. T. Acar, Y. B. Cekirge, M. H. and Ramesh, N. (1985). "Flow Field Around Cones in Steady Penetration," Journal of Geotechnical Engineering Division, ASCE Vol. 111, pp. 193-204.

[45] Vesic, A. S. (1972). "Expansion of Cavities in Infinite Soil Mass," Journal of Soil Mechanics and Foundation Engineering Division, ASCE Vol. 98, No. SM3, pp. 265-290.